Aeroacoustic Simulation of Turbulent Boundary Layer Induced Automotive Gap Noise

A thesis accepted by the
Faculty of Aerospace Engineering and Geodesy
of the University of Stuttgart
in partial fulfilment of the requirements for the degree of
Doctor of Engineering Sciences (Dr.-Ing.)

by
Lars Erbig
born in Berlin-Lichtenberg

Main-referee: Prof. Dr. rer. nat. Claus-Dieter Munz
Co-referee: Prof. Dr.-Ing. Jan Delfs

Date of defence: 27 May 2020

Institute of Aerodynamics and Gas Dynamics
University of Stuttgart
2021

Acknowledgments

This thesis was developed during my employment as a PhD student at the department for Aerodynamics, Aeroacoustics and Wind Tunnels, RD/ANA of the Daimler AG, Sindelfingen.

Foremost I would like to thank my advisor Prof. Dr. Claus-Dieter Munz from the Institute for Aerodynamics and Gasdynamics (IAG) of the University of Stuttgart for his assistance. Similarly, I would like to thank Prof. Dr. Jan-Werner Delfs from the Institute of Aerodynamics and Flow Technology of the German Aerospace Center (DLR) for participating to this thesis committee.

I would like to thank Dr. Teddy Woll and Dr. Volker Schwarz for giving me the chance to work on the challenging topic of automotive gap acoustics, for providing me with the necessary equipment for successful measurements and numerical simulations and for giving me the opportunity to share my results on various conferences. Especially, this work would not have been possible without the support and commitment of my advisor Dr. Martin Maihöfer. I would like to thank Philipp Renz and Andris Riedelsheimer whose Master's theses provided a valuable contribution to my work. Finally, I would like to thank all my colleagues from RD/ANA for their discussions and attitude.

Very special thanks go to Dr. Michaela Herr, Dr. Nan Hu and the whole team of the Department Technical Acoustics of DLR for the excellent collaboration during my experimental work on the idealized rear door gap. I would also like to thank Dr. Doru Caraeni and Dr. Sylvain Lardeau from Siemens PLM Software whose ongoing support played a decisive role in the development of the numerical simulations of this thesis.

Contents

Abstract

In this work, we develop and validate a hybrid RANS/LES methodology for the numerical simulation of turbulent boundary layer induced aeroacoustic gap noise on vehicles, especially of the rear door gap. While gap noise is typically associated with strong aeroacoustic feedback modes, automotive gap noise usually does not involve self-sustained oscillations in the gap opening as the shear layer remains macroscopically stable. Instead, automotive gaps are aeroacoustically excited by attached boundary layer turbulence or turbulent wakes and vortices. The noise is then a consequence of acoustic amplification inside the gap's resonator volume. Accordingly, any numerical simulation approach requires a transient representation of the aeroacoustic excitation, the boundary layer fluctuations. Currently, such a method is not available for industrial application as scale-resolving simulations approaches are either too computationally expensive for large-scale use or depend strongly on the validity of semi-empirical target spectra and models whose applicability to car aerodynamics is not yet clear. This works' hybrid RANS/LES is based on a locally applied LES to resolve the boundary layer turbulence in the vicinity of the rear door gap. The restriction of the computational domain of the LES is achieved by synthesizing the turbulent fields via Anisotropic Linear Forcing. This method introduces an artificial volume force into the LES momentum equations that enforces the flow to govern a target state with specified mean flow velocity and Reynolds stresses. These necessary fields are determined by a RANS of the full vehicle, using the Elliptic Blending Reynolds Stress turbulence model. Accordingly, the turbulence synthetization is only implicitly affected by semi-empirical models that determine the target fields from RANS. As the Anisotropic Linear Forcing has only been applied to turbulent channel flows so far, one scope of this work is to investigate the applicability of the Anisotropic Linear Forcing to complex, industry relevant flow problems. The method is validated by comparing the results to a self-designed modular, idealized experiment. In contrast to recent experimental investigations on passive gap noise in the literature the inflowing boundary layer in our experiment develops independently from the wind tunnel's nozzle on a flat plate. Furthermore, our experiment allows precise time-synchronous measurements of the boundary layer wall pressure and the gap noise that significantly improve the possibilities for the validation of numerical simulations. Via modifications of the experiment we can additionally enforce a pressure gradient on the inflow, study the influence of design variations of the gap opening and obstacles in the inflow. On the one hand these variations help to independently confirm recently published results from the literature and on the other hand they form the basis of a systematic study of gap noise influencing parameters, the inset of shear layer instabilities with increasing opening length as well as the strengths and weaknesses of the hybrid RANS/LES. For the validation on a full-scale vehicle we apply the same techniques from the idealized experiments to a foam model of a Mercedes-Benz E-Class Estate. These experiments show that the underlying physical principles could be captured by the idealized experiment and that it is thus valid to transfer insights on relevant quantities and the applicability of the simulation method to the full-scale vehicle. With these experimental results we can show that a compressible hybrid RANS/LES is capable to accurately predict automotive gap noise approximately 70 times faster than a classical wall-resolved LES of the full-scale car. Furthermore, we can show that a common hybrid acoustic simulation using an acoustic wave equation based on incompressible flow and the Acoustic Perturbation Equations is currently not able to predict the levels of weakly excited gap resonance frequencies. Analysis indicates, that additionally accounting for the shear layer – acoustics interaction in the gap opening could improve the results of this simulation approach. A principal way to include this interaction term is discussed in the work's appendix.

Zusammenfassung

In der vorliegenden Arbeit wird eine hybride RANS/LES Methodik zur Simulation grenzschichtinduzierter Fugengeräusche an Fahrzeugen, insbesondere am Heckklappenspalt, entwickelt und mithilfe eigener experimenteller Untersuchungen validiert. Während Fugengeräusche im Allgemeinen mit aeroakustischem Feedback verbunden werden, entsteht durch die hohe Stabilität der Scherschicht in der Öffnung von Fahrzeugfugen in der Regel keine effektive, selbst-erhaltende aeroakustische Quelle. Fahrzeugfugen werden stattdessen durch anliegende Grenzschichtturbulenz oder turbulente Nachläufe und Wirbel passiv aeroakustisch angeregt und der eigentliche Lärm entsteht durch eine akustische Verstärkung der Turbulenz im Fugenhohlraum. Infolgedessen erfordert jeder numerische Simulationsansatz die Darstellung der eigentlichen aeroakustischen Anregung, der Grenzschichtturbulenz. Eine solche Simulationsmethode steht für industrielle Anwendungsfälle bisher nicht zur Verfügung, da skalenauflösende Simulationsmethoden des gesamten Fahrzeugs entweder zu rechenintensiv sind, oder aber modellierende Ansätze stark auf semi-empirischen Zielfunktionen basieren, deren Anwendbarkeit am Fahrzeug bisher nicht geklärt werden konnte. In der hybriden RANS/LES dieser Arbeit wird die Grenzschichtturbulenz ausschließlich im Bereich des Heckklappenspalts mithilfe einer lokal angewandten LES dargestellt. Die Beschränkung des LES Rechengebiets wird durch eine Turbulenzsynthetisierung durch Anisotropic Linear Forcing erreicht. Damit wird lokal eine künstliche Kraft in den Impulsgleichungen eingeführt, welche einen Zielzustand mit vorgegebener mittlerer Geschwindigkeit und vorgegebenen Reynoldsspannungen erzwingt. Die benötigten Größen werden mithilfe einer RANS des gesamten Fahrzeugs mit einem Elliptic Blending Reynolds Stress Turbulenzmodell berechnet. Die Turbulenzsynthetisierung hängt daher nur indirekt über das den Zielgrößen zugrundeliegende RANS Modell von semi-empirischen Modellen ab. Bisher wurde das Anisotropic Linear Forcing lediglich an einfachen Kanalströmungen angewendet, sodass diese Arbeit dazu dient die Anwendbarkeit der Methode an komplexeren Strömungssituationen zu untersuchen. Die Validierung dieser Simulationsmethode erfolgt an einem eigenen modularen Grundlagenexperiment. Im Gegensatz zu bisherigen Untersuchungen zu passiver Fugenakustik in der Literatur entwickelt sich in diesem Experiment die anströmende Grenzschicht unabhängig von der Düse auf einer flachen Tragflügelkonstruktion. Weiterhin ermöglicht das entwickelte Grundlagenexperiment die präzise zeitsynchrone Messung der Grenzschichtturbulenz und der Fugenakustik, was die Möglichkeiten zur numerischen Validierung stark verbessert. Über Modifikationen des Grundlagenexperiments kann zusätzlich zur normalen Anströmung ein Druckgradient aufgeprägt werden, sowie die Auswirkungen von Geometrievariationen der Fugenöffnung und Hindernissen in der Anströmung untersucht werden. Diese Variationen ermöglichen zum Einen eine unabhängige Untersuchung bereits in der Literatur veröffentlichter experimenteller Ergebnisse, sowie zum Anderen eine systematische Untersuchung der Einflussgrößen auf den in der Fuge erzeugten Schall, der mit größerer Öffnungslänge einsetzenden Scherschichtinstabilität, sowie eine Analyse der Stärken und Schwächen der hybriden RANS/LES. Zur Validierung am realen Fahrzeug wird die Technik des Grundlagenexperiments auf ein Schaummodell eines E-Klasse Kombis übertragen. Diese Experimente zeigen, dass die zugrunde liegende Physik bereits im Grundlagenexperiment abgebildet war und somit die an diesem Experiment gewonnen Erkenntnisse zu Einflussgrößen und Anwendbarkeit der Simulationsmethode Aussagekraft für die reale Fahrzeugströmung besitzen. Anhand der experimentellen Ergebnisse kann gezeigt werden, dass eine kompressible, hybride RANS/LES geeignet ist um aeroakustische Fugengeräusche am Fahrzeug etwa 70 mal schneller, als eine wandaufgelöste LES des gesamten Fahrzeugs vorherzusagen. Weiterhin wird gezeigt, dass hybride Akustiksimulationen in Form einer akustischen Wellengleichung auf Basis der Acoustic Perturbation Equations und inkompressiblen Strömungssimulationen mit Anisotropic Linear Forcing nicht in der Lage sind die Schallpegel schwach angeregter Resonanzfrequenzen der Fuge korrekt vorherzusagen. Analysen deuten darauf hin, dass eine zusätzliche Berücksichtigung der Schallinteraktion mit der Scherschichtturbulenz in der Fugenöffnung eine Verbesserung der Ergebnisse dieser Simulationsmethode erbringen könnte. Ein möglicher Weg zur Berücksichtigung dieses Einflusses wird im Anhang dargelegt.

1 Introduction

1.1 Motivation

During the past couple of years, research and development within the automobile industry has been subject to fundamental evolution and changes. In the past, power, durability and usability were perhaps the most critical parts during the development of a vehicle. But as the quality has improved in the whole market, the importance of driving comfort has dramatically increased especially for premium vehicles. Being faced with a change of concepts from combustion engines towards hybrid and electric engines, cars will become even quieter in the future. But being quiet in general is not always good. Typically, noise sources that were masked before become prominent under quiet conditions and can resemble an even more unpleasant condition than before. Consequently, especially the manufacturers of premium vehicles increased their commitment to improvements of non-powertrain noise sources, as road-tyre interactions or aeroacoustic noise.

Currently, aeroacoustic noise can be considered the dominant noise source above 100 km/h to 120 km/h and thus gained a lot of attention during the last years.[42] The driver's acoustic experience does not only rely on the exterior aeroacoustic noise but also on the acoustic transfer path through the vehicle's structure and sealings. Thus, experiment based optimization is naturally restricted to late phases of the vehicle development process, as only in these phases the technical maturity of the prototypes is sufficiently high. The major downside of this optimization is, besides temporal pressure, the limited impact on general design concepts. Numerical simulation – as an early phase opportunity of design exploration – instead requires first an accurate resolution of the turbulent and acoustic fields and second an accurate modeling of the transfer path, which makes this kind of simulation both physically challenging as well as computationally expensive. Besides these circumstances numerical approaches for the prediction of broadband side mirror noise, that is widely considered one of the major aeroacoustic noise sources, have been successfully validated and established recently, see e.g. [89].

Besides broadband and tonal side mirror noise the flow interaction with gaps and cavities resembles another major aeroacoustic noise source at vehicles. In general, gap noise has been a major topic of research in aeroacoustics for more than the last 50 years.[41,79,86,87] However, the main focus of research was set on aerospace applications with medium to high Mach numbers and self-sustained oscillations – situations where tonal gap noise bares the potential to cause significant and dangerous structural impact. Again with increasing demands on environmental noise and comfort, gap noise during take-off and landing, as well as at trains and cars received increasing attention.[41]

Especially on cars, a large variety of gap types – usually partially covered cavities that are, to some degree, filled with rubber sealings – is exposed to different local flow conditions. In the past, several primarily experimentally oriented works have been carried out by or in cooperation with different manufacturers as Audi,[12,90,91,107] Daimler,[2,74] PSA[77] and Renault[55] as well as purely by academic institutions.[22,47] Early attempts to simplify automotive gap noise to an equivalent two-dimensional problem that could be treated numerically however did not lead closer towards the industrial simulation of the problem.[48] Besides the different studied gaps and methodical differences in these works especially those that performed wind tunnel measurements of the car highlighted that automotive gap noise usually does not involve self-sustained oscillations but can be considered a passive acoustic resonance mechanism of the incoming turbulent boundary layer fluctuations instead.[2,55,90,107] As the inset of self-sustained oscillations is strongly related to the shear layer instability in the gap opening and thus to a relation between the boundary layer and the opening length, it is still unclear if aeroacoustic feedback in specific gap and cavity openings exposed to thin incoming boundary layers might happen under certain driving conditions.

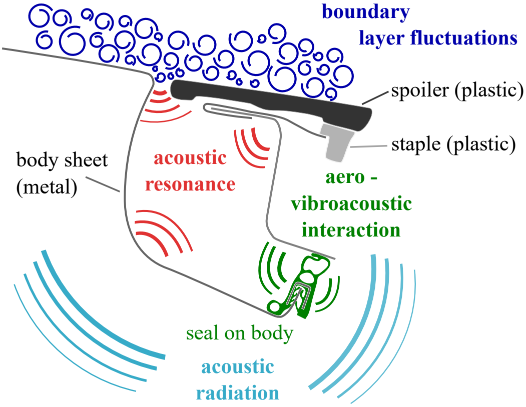

Fig. 1.1 Schematic drawing of rear door gap noise mechanisms.

Accordingly, the industrial problem of automotive gap noise can be illustrated by fig. 1.1. Turbulence, usually from an attached boundary layer, is convected over the gap's opening which might involve strong local interactions with the gap's edges under some conditions. The turbulence and local flow effects lead to an acoustic excitation of the gap that gets resonantly amplified in the partially covered resonator volume. Due to interaction with the thin metal sheets, plastic covers, glue and most importantly the rubber sealings the generated sound inside the gap is influenced due to the non-trivial acoustic wall impedance and the sound gets transported towards the vehicle cabin. The transport path through the vehicle's structure can again lead to attenuation or resonant amplification of selected frequencies. After radiating into the cabin the gap noise finally reaches the driver's ear.

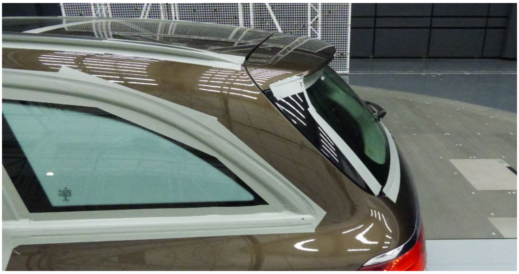

Fig. 1.2 Rear door gap of a Mercedes-Benz E-Class Estate (S213). Other visible openings or gaps are masked using cloth tape, the side windows are covered with heavy-weight mats inside the cabin.

To benefit from relatively precise inflow conditions with a very thick incoming boundary layer, the literature tends to focus on the geometrical shape and the inflow conditions of the car's rear door gap. Especially Schimmelpfennig showed that a shape variation of the gap's leading edge can lead to a noise reduction at the driver's ear by about 7 dB at the loudest resonance on their tested vehicle.[91]

In the present work we want to explore possibilities for the numerical simulation of the previously described turbulent boundary layer induced passive gap noise at cars. In accordance to the previous studies we will also focus on the physics of the rear door gap as it can be considered the most simplified gap at a car and its inflow is mainly determined by the flow over the car's roof. Although Schimmelpfennig's work already indicated the importance of the rear door gap we want to quantify the possible influence of the rear door gap on the driving experience. For this purpose we performed tests on a standard Mercedes-Benz E-Class Estate (S213) in Daimler's aeroacoustic wind tunnel[13] at the operating velocity $u_0 = 140\,\mathrm{km/h}$ using artificial head microphones at the two front seats. In these tests we removed the gap opening sealing to resemble a worst-case scenario and compared it to the gap being masked with cloth tape, see fig. 1.2.

In fig. 1.3 one can see that the noise generated in the open rear door at 1 kHz is approximately on par with the noise arising from the side mirrors. While this can be a first hint of the importance of gap noise on vehicles, fig. 1.4 shows that even at the driver's position, at least 2.5 m away from the gap, opening the rear door gap leads to a 2.5 dB(A) peak at 780 Hz and a slight increase of the sound pressure levels above this frequency. This result clearly highlights the importance of the rear door gap noise for the driver – at least at 780 Hz the influence of the gap is almost as loud as all other present aeroacoustic noise sources. The fact that even in the masked gap's pressure spectrum the 780 Hz peak can be found allows for two different interpretations: Either the influence of the rear door gap is even stronger if vibrations of the cloth tape excited the air inside the rear door gap or the rear door gap effectively excites a structural eigenfrequency of the car that is additionally excited by other mechanisms as e.g. the turbulent boundary layer fluctuations along the roof. Both interpretations encourage that an improved understanding of the underlying gap noise phenomenon can lead to significant improvements for the driver's

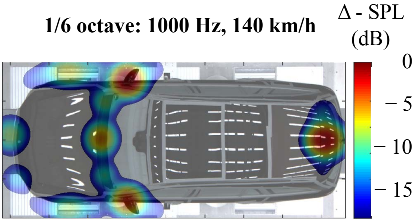

Fig. 1.3 Acoustic radiation of the rear door gap. Beamforming in 1/6 octave band at 1 kHz with open rear door gap.

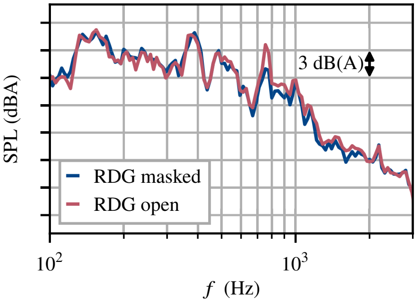

Fig. 1.4 Comparison of the masked and the open rear door gap of S213 as 1/24 octave band filtered sound pressure level at the right driver's ear.

comfort.* Thus, even an aeroacoustic simulation procedure of the exterior excitation of the gap's resonance volume might provide such insights as well as it might build an opportunity to take influence on the structural layout of the car that gets fixed during early development phases. Consequently, such actions could reduce the dependency on sophisticated sealing concepts in the gap opening.

Despite its obvious benefits, a numerical simulation of rear door gap noise imposes significant open questions and challenges. First a transient simulation of the turbulent boundary layer along the whole spanwidth of the roof would be required, second the resulting acoustic field inside the gap, its interaction with the opening's shear layer and possible compressible effects in the enclosed resonance volume need to be resolved and third the interaction of the external sound with the sealings and the structure needs to be modeled. Up to day even the very first task requires exceptional computational costs on industrially relevant scales. A generalization of the method to different gaps at the car would furthermore require to investigate if self-sustaining oscillations can occur under certain circumstances and if a numerical methodology can treat these phenomena.

1.2 Objectives

Following the brief introduction, this thesis concentrates on the external flow and the noise generated at the rear door gap without the presence of sealings and without analyzing the transport of sound towards cabin. It's the scope of this work to systematically shed more light into the physics of automotive gap noise and to develop strategies for the numerical simulation of the gap noise outside the cabin. We aim to experimentally verify Schimmelpfennig's results

---

*It is noted that the presence of a gap opening sealing, as present in the current serial version, leads to the same effective reduction of the sound pressure level as the masking of the rear door gap.

on an idealized rear door gap model that delivers high quality data that allow straightforward validation of numerical simulation approaches. The experiments on this model should be able to systematically extend the previous results to identify influencing factors on automotive gap noise. We want to understand their individual importance and if they are independent from each other. Especially, the experiments should help to understand whether any geometrical or inflow modifications could lead to the inset of self-sustained oscillations that would considerably influence the choice of numerical simulation approaches.

Based on the experimental results from the literature a numerical simulation of automotive gap noise is most-likely expected to face two substantial difficulties: First a transient representation of the turbulent boundary layer fluctuations in the vicinity of the gap is required and second the acoustic resonance in the gap's resonator and the interaction of sound and flow in the small opening need to be captured. For the first bottleneck a wide number of approaches on small-scale problems exist, ranging from synthesizing turbulence to reduce the size of the computational domain of a scale-resolving simulation, over a full transient model of the boundary layer fluctuations based on RANS or even to full semi-empirical wall pressure models. Nevertheless, neither of the available approaches has been already proven to be applicable to full-scale aeroacoustic vehicle simulations. Accordingly, we aim to identify a suitable approach from the different options and investigate its transfer to the industry relevant problem. For the second bottleneck it is currently open which kind of simulation approach is suitable for the numerical simulation of the acoustics. In principle a Direct Noise Computation (DNC) should capture all physical phenomena including self-sustained oscillations but imposes strong requirements on the mesh and non-reflecting boundary conditions. In contrast, Kreuzinger and Schimmelpfennig showed[62] that a hybrid approach based on APE-4 and an incompressible flow field is at least qualitatively suited to capture the physics of Schimmelpfennig's experiment. Despite their expected simpler usability, the quantitative accuracy of such approaches for the simulation of near-field gap noise is yet unknown. Accordingly, we will try to figure out which of the two approaches can be successfully applied to gap noise simulations.

1.3 Outline

In this thesis, we describe a detailed experimental analysis on an idealized rear door gap model and analyze a zonal hybrid RANS/LES methodology that is based on an Elliptic Blending Reynolds Stress Model[63] (EB-RSM) and Anisotropic Linear Forcing[23] (ALF). We will show that the model is capable of accurately simulating the near field gap noise of a rear door gap model of the S213 in the commercial CFD code STAR-CCM+.

The thesis consists of three parts: In the first part we briefly summarize the physical background relevant for the understanding of the mechanisms behind turbulent boundary layer gap noise, introduce the utilized numerical methods and briefly compare them to alternative choices. In the second part we present a basic experiment on the idealized rear door gap model that resembles key elements of the automotive gap noise phenomenon and that is suitable for a stringent validation of the proposed methodology. We furthermore highlight up to which degree hybrid acoustic approaches[103] that are based on APE-2 can capture the acoustic properties of the passive gap acoustics and describe the influence of different experimental variations on the measured gap noise. In the final part we will present a series of experiments on a foam model of the S213 and the application of our simulation methodology to the described cases.

2 Physical Principles of Gap Acoustics

During the last fifty years general gap noise has been studied in many works. Especially the early review article from Rockwell and Naudascher[86] and Gloerfelt's lecture notes[41] give a broad overview about the multiplicity of the different involved phenomena and the strong dependency on the inflow conditions and the gap geometry. Although we cannot even aspire to reach the amount of information given in these two reviews we want to briefly discuss the physical principles underlying gap noise in this chapter, so that we can later understand the physics of automotive gap noise and classify the latest works related to this specific topic.

Typically for the considered cases in the literature, gaps and cavities are subject to a grazing flow due to a boundary layer upstream of the gap opening. Depending on the position of the gap, the boundary layer can be either laminar or turbulent. In the gap opening a shear layer between the free stream and the initially resting air inside the gap develops. Especially if the inflowing boundary layer is turbulent the shear layer is strongly affected from the boundary layer fluctuations. Depending on the specific shear layer dynamics different gap noise mechanisms can occur due to the flow interaction with both gap opening edges. As we can assume turbulent flow at almost any automotive application, we first describe the basic principles of turbulent boundary layer fluctuations right after we briefly introduced the governing equations of fluid dynamics. Second, we summarize gap noise mechanisms from the literature. Especially, we discuss the potential inset of shear layer instabilites, interaction mechanisms with the gap opening edges and possible surface averaging effects in the gap opening.

2.1 Governing Equations

As all flow phenomena also the boundary layer fluctuations as well as the noise generated in gaps rely on the governing equations of fluid dynamics, the Navier-Stokes equations, whose particular form can be derived from mass, momentum and energy conservation in an arbitrary control mass unit by applying Reynolds' transport theorem.[36,84] For the case of an ideal gas the full Navier-Stokes equations read

$$\begin{aligned} \frac{\partial\, \varrho \boldsymbol{u}}{\partial t} + \nabla \cdot (\varrho \boldsymbol{u} \otimes \boldsymbol{u}) &= -\nabla p + \nabla \cdot \mathbf{T} + \boldsymbol{f}_b \\ \frac{\partial \varrho}{\partial t} + \nabla \cdot (\varrho \boldsymbol{u}) &= 0 \\ \frac{\partial \varrho e_t}{\partial t} + \nabla \cdot (\varrho e_t \boldsymbol{u}) &= -\nabla \cdot (p \boldsymbol{u}) + \nabla \cdot (\mathbf{T} \boldsymbol{u}) - \nabla \cdot \boldsymbol{q} + \boldsymbol{f}_b \cdot \boldsymbol{u} \end{aligned} \tag{2.1}$$

with the fluid's density ϱ, its velocity $\boldsymbol{u}$, the pressure p, the specific total energy e_t and the heat flux $\boldsymbol{q}$. External body forces, as gravity or centrifugal forces, are denoted with $\boldsymbol{f}_b$. The viscous stress tensor $\mathbf{T}$ for a Newtonian fluid is then given by

$$\mathbf{T} = 2\mu\mathbf{S} - \frac{2}{3}\mu\,(\nabla \cdot \boldsymbol{u})\,\mathbf{I} \tag{2.2}$$

with the strain rate tensor $\mathbf{S} := \frac{1}{2}\left(\nabla\boldsymbol{u} + \nabla\boldsymbol{u}^{\mathsf{T}}\right)$ and the dynamic viscosity μ. The specific total energy is defined by $e_t = e + \frac{1}{2}\boldsymbol{u} \cdot \boldsymbol{u}$ with the specific internal energy e. The heat flux is typically further specified by Fourier's law $\boldsymbol{q} = -k\nabla T$ with the temperature T and a temperature dependent material specific thermal conductivity $k = k(T)$

For an ideal gas the above system can be closed with the thermal and calorical equations of state

$$e = \frac{3}{2}\frac{RT}{M} \qquad \text{and} \qquad pV_M = RT\ , \tag{2.3}$$

respectively. Here, M denotes the molar mass of the gas, V_M the molar volume and R the universal gas constant $R = 8.314\,\mathrm{J\,mol^{-1}\,K^{-1}}$. Combining the two equations then gives

$$e = \frac{3}{2}\frac{p}{\varrho}\ . \tag{2.4}$$

A typical simplification at low Mach numbers $\mathrm{Ma} < 0.3$ is the assumption of incompressibility $\partial\varrho/\partial p = 0$ at constant temperature. This simplification implies that the fluid's density doesn't change along the streamlines of the flow and therefore

$$\frac{\partial\varrho}{\partial t} + \nabla\varrho \cdot \boldsymbol{u} = 0\ . \tag{2.5}$$

In combination with the conservation of mass from (2.1) we see that the resulting velocity is solenoidal: $\nabla \cdot \boldsymbol{u} = 0$. Especially if the fluid's density can is approximately constant at the boundaries of a certain domain it is also constant in the domain's interior, i.e. $\varrho := \varrho_0 = \text{const.}$. Under the additional assumption of a temperature independent viscosity μ even the first two equations of (2.1) form a closed system and can be solved independently from the energy equation.

2.2 Turbulent Boundary Layer Fluctuations

In this section we discuss the physical principles of turbulent boundary layer fluctuations that arise from the Navier-Stokes equations, eq. (2.1). Especially we discuss several semi-empirical models of the wavenumber-frequency spectrum and the auto power spectral density of the wall pressure fluctuations that relate these spectra to the mean boundary layer parameters.

In the following, consider the *Reynolds decomposition* of an arbitrary flow variable ϕ into its temporal average $\bar{\phi}$ and its fluctuating part $\phi' := \phi - \bar{\phi}$. Consider also an incompressible turbulent boundary layer at a wall located at $x_2 = 0$. Assuming a positive mean flow $\overline{u_1}$ in the x_1 direction, the Navier-Stokes equations, eq. (2.1) then lead to the simplified Poisson equation

$$\triangle p'(\boldsymbol{x}, t) = -\varrho_0 \left(2 \frac{\partial \overline{u_1}}{\partial x_2} \frac{\partial u_2'}{\partial x_1} + \frac{\partial^2}{\partial x_i \partial x_j} (u_i' u_j' - \overline{u_i' u_j'}) \right) \tag{2.6}$$

for the fluctuating pressure p' with the velocity $\boldsymbol{u} = (u_1, u_2, u_3)^\mathsf{T}$ and the constant fluid density ϱ_0, which we will study directly at the wall. The first right hand side term is usually considered as a contribution of the mean shear flow and the second term as a contribution from the turbulence-turbulence interaction.

In the following, let $p'(\boldsymbol{x}, t)$ denote the wall pressure at a location $\boldsymbol{x} = (x_1, x_3)^\mathsf{T}$ at the wall at time t. Then the space-time correlation of the assumed homogeneous boundary layer flow is defined by

$$R_{pp}(\boldsymbol{r}, \tau) := \overline{p'(\boldsymbol{x}, t) p'(\boldsymbol{x} + \boldsymbol{r}, t + \tau)} \tag{2.7}$$

with a temporal average $\overline{\ \cdot\ }$. Its temporal Fourier transform defines the cross power spectral density of the wall pressure fluctuations

$$S_{pp}(\boldsymbol{r}, \omega) := \frac{1}{2\pi} \int\limits_{-\infty}^{\infty} R_{pp}(\boldsymbol{r}, \tau) e^{i\omega\tau} \, d\tau \tag{2.8}$$

and a two-dimensional spatial Fourier transform of S_{pp} now provides the definition of the wavenumber-frequency spectrum Φ_{pp}

$$\Phi_{pp}(\boldsymbol{k}, \omega) := \frac{1}{(2\pi)^2} \iint\limits_{-\infty}^{\infty} S_{pp}(\boldsymbol{r}, \omega) e^{i\boldsymbol{k}\cdot\boldsymbol{r}} \, d\boldsymbol{r} \ . \tag{2.9}$$

The total power spectral density $\phi(\omega)$ at $\boldsymbol{x}$ is especially defined as $\phi(\omega) := S_{pp}(\boldsymbol{0}, \omega)$ which can be used to factorize the cross power spectral density $S_{pp}(\boldsymbol{r}, \omega)$ into the cross coherence $\Gamma_{pp}(\boldsymbol{r}, \omega)$

$$S_{pp}(\boldsymbol{r}, \omega) = \phi(\omega) \Gamma_{pp}(\boldsymbol{r}, \omega) \ , \tag{2.10}$$

which finally relates the wall pressure fluctuations to their local fluctuations and spatial decay.

By analyzing experimental data from Willmarth and Wooldridge,[109] Corcos showed that in first order approximation, the streamwise cross spectral density $S_{pp}(r_1, 0, \omega)$ and the spanwise cross spectral density $S_{pp}(0, r_3, \omega)$ can be separated.[19] Accordingly, this holds also true for the stream- and spanwise coherence and he found that it can be expressed by the non-dimensional

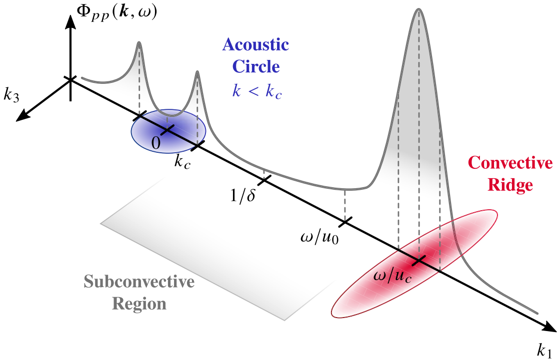

Fig. 2.1 A schematic representation of variation of the wavenumber-frequency specrum at constant frequency ($\omega\delta/u_0 \ll 1$), modified from [14].

variables $\omega r_1/u_c$ and $\omega r_3/u_c$ with the boundary layer convection velocity u_c

$$S_{pp}(\boldsymbol{r},\omega) = \phi(\omega)\, e^{-\alpha_1|\omega r_1|/u_c} e^{-\alpha_3|\omega r_3|/u_c} e^{i\omega r_1/u_c} \tag{2.11}$$

and empirical parameters α_1 and α_3. The Fourier transformation of this function yields[43]

$$\Phi_{pp}(\boldsymbol{k},\omega) = \frac{1}{2\pi^2\omega^2}\phi(\omega)\frac{\alpha_1}{\alpha_1^2 + (1 - u_c k_1/\omega)^2}\frac{\alpha_3}{\alpha_3^2 + (u_c k_3/\omega)^2}\ . \tag{2.12}$$

This simple relation clearly highlights that the total spectrum is built of the local, single point, power spectral density, a streamwise k_1 coherence including the convection and a spanwise decay of the fluctuations. The formulation by Corcos shows that maximum coherence is reached at $k_1 = \omega/u_c$. This region is typically denoted as the *convective ridge* and is most important at low Mach numbers. As discussed e.g. by Bull[14] it has been analyzed in much detail in the past that the simple Corcos model especially only applies close to the convective ridge. Several authors tried to extend the modeling to the *subconvective region* $^{\omega}/_{c} < k < {}^{\omega}/_{u_c}$ with the speed of sound c which involved considering the compressibility of the flow. During these works it became apparent that the wavenumber-frequency spectra of real boundary layer flows will feature a second finite peak at $k_c = \omega/c$, which defines the *acoustic region*. A schematic drawing of a typical wavenumber-frequency spectrum for low Mach-number flows is shown in fig. 2.1. In practice the acoustic region is not only influenced by the geometry of the boundary layer plate but also by the background noise of the experimental test facility. Although Howe derived an advanced dedicated expression for Φ_{pp} including the subconvective and acoustic region,[49] it is still common practice and feasible at relatively high frequencies to consider the total wavenumber-frequency spectrum a superposition of an acoustic diffuse field with cross spectral density

$$S_{pp,\mathrm{ac}}(\boldsymbol{r},\omega) \approx \phi(\omega) A \frac{\sin k_c|\boldsymbol{r}|}{k_c|\boldsymbol{r}|} \tag{2.13}$$

and the hydrodynamic boundary layer fluctuations.[96] This superposition leads to

$$S_{pp}(\boldsymbol{r},\omega) = \phi(\omega) \left[e^{-\alpha_1|\omega r_1|/u_c} e^{-\alpha_3|\omega r_3|/u_c} e^{i\omega r_1/u_c} + A \frac{\sin k_c|\boldsymbol{r}|}{k_c|r|} \right] . \tag{2.14}$$

In any case, the empirical parameters α_1, α_3 and A are unknown and will certainly depend on the boundary layer state, which requires fitting to experimental data. More general models try to become less dependent on such unknowns[14,49] but instead require additional knowledge about the boundary layer state itself.

Unfortunately, the wavenumber-frequency spectrum imposes severe issues when trying to measure the wall pressure spectrum $\phi(\omega)$, the coherence $\Gamma(\boldsymbol{r},\omega)$ or even to resolve $\Phi_{pp}(\boldsymbol{k},\omega)$. As every pressure sensor has a finite surface size and senses its overall surface average we cannot neglect the influence of the spatial correlation of the pressure field on the measured signal. As an example consider a plane wave of wavelength λ and a quadratic sensor with identical edge length λ. At every time the surface average on the sensor will be equal to zero and thus the sensor will be unable to detect the plane wave. Accordingly, the sensor can be interpreted as wavenumber filter $A(\boldsymbol{k})$ acting on the wavenumber-frequency spectrum $\Phi_{pp}(\boldsymbol{k},\omega)$ which leads to the measured wall pressure spectrum

$$\phi_m(\omega) = \iint\limits_{-\infty}^{\infty} |A(\boldsymbol{k})|^2 \Phi_{pp}(\boldsymbol{k},\omega)\, d\boldsymbol{k} \ . \tag{2.15}$$

When analyzing the wavenumber-frequency spectrum, Corcos was also the first to analyze the influence of the present surface attenuation by calculating the above integral for rigid rectangular and circular sensors.[18] The hydrodynamic wavenumbers in a boundary layer are typically large and thus it is impossible to use standard 1/2 inch or 1/4 inch microphones as they lead to a strong attenuation even at low frequencies. Accordingly, the quality of the measured wall pressure spectra and the coherence will be limited by the sensor size and these measurements still resemble a challenge.

Due to the Fourier transform, resolving the sharp convective ridge at low Mach numbers, and especially in the k_3 direction, requires a large array of closely spaced wall mounted pressure sensors. Consequently, the requirement of a large number of tiny sensors to get acceptable results leads to a dramatic increase of either costs or required efforts. Up to date lots of works are performed to reduce these costs and to improve their results.[6,46,96]

To bypass these issues Maidanik and Jorgensen[69] and Blake and Chase[9] developed a strategy to use a finite microphone array as additional wavenumber filter $H(\boldsymbol{k})$. Adding or subtracting the signals of several sensors (which changes $H(\boldsymbol{k})$) leads to a signal

$$\phi_H(\omega) = \iint\limits_{-\infty}^{\infty} |H(\boldsymbol{k})|^2 |A(\boldsymbol{k})|^2 \Phi_{pp}(\boldsymbol{k}, \omega)\, d\boldsymbol{k} \ . \tag{2.16}$$

If the distance of the sensors is designed well in relation to the sensor diameter this method allows to get measurement results at least for a few discrete larger wavenumbers than originally possible, see e.g. Golliard.[43] However the benefits of this bypass method reduce significantly as each sensor surface gets smaller itself and it is thus not well suited to be combined with tiny modern sensors.

A modern and relatively effective strategy for measurements of wall pressure fluctuations is thus to use flush-mounted or pinhole mounted miniature sized piezo-resistive pressure transducers in a small L-shaped array. Today, flush-mounted sensors have a minimal diameter of $d = 1.4\,\text{mm}$ (e.g. Kulite XCQ-055) while pinholes have been realized with diameters of $d = 0.5\,\text{mm}$[51] but are more difficult to manufacture. Nevertheless, both setups allow a relatively precise measurement of the wall pressure spectra $\phi(\omega)$ and one can at least fit the coherence between distinct measurement locations to a coherence model of choice, e.g. equation (2.11) of the Corcos' model. This method allows to compare the boundary layer state of different configurations and to estimate the streamwise and spanwise decay of the boundary layer fluctuations.[51]

Currently we mainly discussed the coherence properties of the boundary layer wall pressure fluctuations and their consequences on measurements. However, the measurement at any sensor directly gives $\phi_m(\omega)$ as an approximation of $\phi(\omega)$ which determines the overall levels of the wavenumber-frequency spectrum. Several semi-empirical models for these wall pressure spectra have been developed in the past, but before discussing them we first want to summarize some general considerations.

The wall pressure spectra are determined from the previous Poisson equation and thus two contributions add to the overall spectra, the mean-shear term and the turbulence-turbulence term. Solving the Poisson equation with Hockney's method and the Fast Random Particle Mesh Method (FRPM) Hu et al. could recently show that these two contributions to the wall pressure spectrum are of the same order of magnitude for a zero pressure gradient boundary layer at Mach 0.1.[53] This indicates that neither of the mechanisms can be effectively neglected when modeling the wall pressure spectra. Furthermore, they investigated the theoretical contribution from different wall-normal positions to the wall pressure spectra and could show that the fluctuations of the outermost regions of the boundary layer $x_2 > 0.61\delta$ with the boundary layer thickness δ have only little relevance to the wall pressure spectrum. The region $x_2 < 0.08\delta$ then dominates the high frequencies above 10 kHz. The frequency range below 1 kHz is then dominated from the intermediate boundary layer region. [*]

---

[*] Accordingly, it is expected that a mesh coarsening in the outer regions of the boundary layer is acceptable in aeroacoustics simulations. An under-resolution of the scales below the logarithmic layer might also be acceptable as it would

Besides these general considerations several semi-empirical models for the wall pressure spectrum have been developed in the past[†]. Especially for zero pressure gradient boundary layers Goody's model turned out to be very consistent with experimental data.[44] For its underlying considerations, Goody summarizes the experimental findings that at low frequencies, the model spectrum is proportional to ω^2 which changes to ω^{-1} at higher frequencies and finally decays with ω^{-5} at the highest frequencies. As a starting point Goody uses a model by Chase and Howe, that he states as[44]

$$\frac{\phi(\omega)u_e}{\tau_w^2\delta^*} = \frac{2(\omega\delta^*/u_e)^2}{[(\omega\delta^*/u_e)+0.0144]^{3/2}} \tag{2.17}$$

with the boundary layer edge velocity u_e, the wall friction τ_w and the displacement thickness δ^*. This simple model can at least principally describe the ω^2 and ω^{-1} proportionality but fails at the highest frequencies. As it has only a limited amount of adjustable constants Goody found it to be well suitable as a basis for an improved model that includes additional physical effects. Especially he aimed at including the high frequency decay, an improved accuracy in the overlap region between the found trends, a better agreement with overall levels and improved Reynolds number scaling. This ideas finally lead to the model equation

$$\frac{\phi(\omega)u_e}{\tau_w^2\delta} = \frac{a\cdot(\omega\delta/u_e)^b}{[(\omega\delta/u_e)^c+d]^e+\left[fR_T^g\cdot(\omega\delta/u_e)\right]^h} \tag{2.18}$$

with the boundary layer thickness δ, the time-scale ratio $R_T = \delta u_\tau^2/(\nu u_e)$ and the empirical parameters $a = 3$, $b = 2$, $c = 0.75$, $d = 0.5$, $e = 3.7$, $f = 1.1$, $g = -0.57$, and $h = 7$. While its details are well described in [44], the most notable change is the switch from δ^* to δ. This switch is based on the finding that the largest coherent structures that determine the behavior at the low frequency range are of order δ which is thus a suitable model parameter.

In the past years several authors tried to develop semi-empirical models for adverse and favorable pressure gradient boundary layers with the most recent contribution being made by Hu.[52] Based on measurements by Hu and Herr, Hu states that "*to some extent, the APG spectra have trends similar to the ZPG spectra. The spectra increase first at low frequencies, then drop at medium frequencies and roll off at high frequencies. Goody's model can represent well these trends for ZPG spectra in the three different ranges, especially at medium and high frequencies. From this point, it is appropriate to take Goody's model as the starting point.*"[51] This line of argumentation leads to the general model equation

$$\frac{\phi(\omega)u_\tau}{Q^2\theta} = \frac{a\cdot(\omega\theta/u_0)^b}{[(\omega\theta/u_0)^c+d]^e+[f\cdot(\omega\theta/u_0)]^g} \quad , \tag{2.19}$$

---

theoretically only affect the highest frequencies. However, this bares the risk to deteriorate the accuracy of the mid region fluctuations.

[†] See e.g. the summary from Goody[44]

with the dynamic pressure Q, the momentum thickness θ and empirical parameters a to g. Scaling the measured data Hu shows that scaling the right hand side by $u_e/(\tau_w^2\delta)$ does not lead to a collapse under adverse pressure gradient conditions. Instead he found that using $u_\tau/(Q^2\theta)$ and θ/u_0 leads to appropriate results. As the importance of the boundary layer outer layer increases with the adverse pressure gradient he argues that using the outer scale dynamic pressure Q is more reasonable than applying the inner wall scaling τ_w. A very detailed analysis of their data leads to the semi-empirical constants

$$\begin{aligned} a &= (81.004d + 2.154) \cdot 10^{-7} & b &= 1.0 \\ c &= 1.5 \cdot h^{1.6} & d &= 10^{-5.8 \cdot 10^{-5} \mathrm{Re}_\theta H - 0.35} \\ e &= 1.13 \cdot h^{-0.6} & f &= 7.645 \mathrm{Re}_\tau^{-0.411} \\ g &= 6.0 & h &= 1.169 \log H + 0.642 \end{aligned} \tag{2.20}$$

with the boundary layer shape factor $H = \delta^*/\theta$.[51]

2.3 Excitation Mechanisms of Gaps and Cavities

As we investigated the turbulent boundary layer fluctuations that will possibly affect the mechanics in the gap opening, we will now try to classify the dynamics of gap noise as they are described in the literature. From the hundreds of works discussed by Gloerfelt[41] it becomes obvious that the resulting gap noise depends strongly on the upstream boundary layer state, the inflow velocity and the gap's opening geometry. Besides the broad variety of results one can distinguish three different mechanisms present under turbulent inflow.

Passive excitation

The simplest mechanism is a passive excitation or so-called *turbulent rumble*. This mechanism has been described already in the early works by Plumbee[79] and Elder et al.[29] Generally, a turbulent boundary layer resembles a broadband and constant excitation source whose fluctuations get amplified in the resonator volume. Depending on the geometry of the cavity, the spectrum will show several velocity-independent resonance frequencies that can be explained by an excitation of acoustic cavity modes. In this mechanism in its purest form it is assumed that the shear layer in the opening remains macroscopically stable and does not introduce any additional noise sources. This assumption is certainly never fulfilled, but in cases where the boundary layer is thick compared to the gap or the gap opening, it is not too far away from reality. Besides this idealized assumption, Elder et al. could show that the levels in the cavity are in fact closely related to the surface averaging phenomenon when measuring turbulent boundary layer fluctuations.[29] Especially, they showed that applying the wavenumber filter from Jorgensen and Maidanik[69] to their studied gap opening could explain the experimental results in the broadband frequency ranges. The idea of wavenumber filtering has been widely expanded by Golliard, who developed a semi-empirical model for the broadband noise of flow-excited cavities.[43] Golliard assumed that the wavenumber-frequency spectrum $\Phi_{pp}(\boldsymbol{k}, \omega)$ of the turbulent boundary layer above the cavity gets filtered in the opening by a filter function $S(\boldsymbol{k})$ that leads to pressure force below the gap's orifice. As the air inside the cavity is nearly in rest and only acoustic waves propagate he assumes that the cavity acts as a linear transfer function $H_{\text{cav}}(\omega)$ function on the filtered pressure force. This model leads to a microphone pressure spectrum inside the cavity

$$\phi_{\text{mic}}(\omega) = H_{\text{cav}}(\omega) \frac{1}{S_0^2} \iint_{-\infty}^{\infty} \Phi_{pp}(\boldsymbol{k}, \omega) |S(\boldsymbol{k})|^2 \, d\boldsymbol{k} \quad , \tag{2.21}$$

where S_0 is the gap's aperture area. Obviously, the method's crux lies in finding appropriate formulations of the wavenumber filter and the transfer function under realistic geometries.

Self-sustained oscillations

In many cases gap noise involves sharp peaks whose frequencies and maximum power are strongly velocity dependent and are often detected with a ladder-type structure in a frequency-velocity diagram. In these cases, especially if the incoming boundary layer is laminar, the above mechanism cannot describe the physics of gap noise. These phenomena were first analyzed by Rossiter[87] who explained these peaks by the presence of an aeroacoustic feedback loop (self-sustained oscillations) in the gap opening. Due to his studies, these self-sustained oscillations in the opening are often called *Rossiter modes*. With the words of Gloerfelt, The mechanism can be structured into four different stages:[41]

> *(i) The feedback consists in the upstream propagation of pressure perturbations generated in the impingement region toward the region of maximum receptivity of the shear layer, as it separates from the upstream edge.*
>
> *(ii) Flow instabilities are then shed near the upstream edge.*
>
> *(iii) The amplification of the instabilities rapidly induces non-linear vortices, which continue to grow due to fluid entrainment and viscous effects.*
>
> *(iv) During the impingement, new pressure perturbations are generated, which propagate toward the upstream direction, closing the loop.*

Following Rossiter one usually considers the downstream edge as the region of maximum receptivity in gap flows. In this case, let L denote the gap's opening length, u_c the fluid's convection velocity and c the speed of sound. Then, the resulting feedback frequency f is governed by the time an integer number n of vortices needs to travel downstream and by the time the acoustic pressure wave needs to travel upstream. I.e. the feedback condition in its simplest form reads

$$f = \frac{n}{\frac{L}{u_c} + \frac{L}{c}} . \tag{2.22}$$

To agree with measurements usually an empirical phase delay α is introduced to replace n by $n - \alpha$, but this delay depends again on the specific conditions. As described by Elder, the characteristics of the incoming boundary layer has a strong influence on the feedback mechanism. The vortices rolling up in the opening are strongly coherent in the spanwise direction and superposed turbulence from the boundary layer will certainly disturb this coherence and accordingly, the levels of the feedback modes will depend on the boundary layer state.[41]

Resonant lock-on

Again, in many practical applications another mechanism needs to be taken into account. In addition to the feedback mechanism in the opening the gap certainly features some geometric eigenmodes. As soon as the feedback frequencies are getting close to these eigenmodes, the gap noise phenomenon must be seen as a system of two coupled resonators – the self-sustained flow oscillations in the opening and the geometric acoustic resonance inside the gap. Depending on the degree of matching of the subsystem's resonance frequencies the resulting resonance frequency is shifted and the amplitude varies strongly between amplification and attenuation. The case of maximum amplitude is often called *resonant lock-on*[86] or a *pipe tone* mechanism.[29]

Although the active and the passive mechanisms are principally different, the inset of the shear layer instability does not occur rapidly. In practice there exists a transition region where the shear layer becomes more and more unstable and where finally aeroacoustic feedback can be found in the opening. A necessary requirement for this inset is the excitability of the first step of the feedback loop, which is basically the Kelvin-Helmholtz instability. In his linear stability studies of an inviscid shear layer, Michalke found that it was impossible to excite disturbances above $\mathrm{St}_\theta = f\theta/u_0 > 0.04$ which was in agreement with experimental data.[72] The possible feedback frequencies are governed by equation (2.22) which allows to estimate the excitability of a certain Rossiter mode by the knowledge of θ/L. Sarohia[88] and Gharib[39] experimentally showed, that $\theta/L < 0.01$ to 0.06 needs to be fulfilled for an excitation of the Rossiter feedback in shallow flat cavities. In deep cavities, where strong acoustic eigenfrequencies become more important, the boundary layer can be much thicker to still excite a pipe tone, as the tone itself can help to trigger shear layer instabilities. Especially it was found by De Jong that in the case of deep, partially covered cavities $\theta/L < 0.16$ to 0.2 is a requirement for shear layer instabilities.[22]

Even in the early review paper by Rockwell and Naudascher[86] the influence of the gap's edge shapes on the self-sustained oscillations were analyzed. It was found that at least principally a rounded upstream edge can lead to increased broadband noise levels while the strength of the feedback mode is reduced. As the rounded upstream edge increase the small scale fluctuations in the opening, the coherent vortices of the feedback mechanism are disturbed, which leads to the findings. In the case of passive excitation, accordingly an increase of the generated noise is to be expected.

3 Status Quo: Automotive Gap Noise and its Numerical Simulation

Gap noise generally covers a wide and substantially different variety of flow excitation mechanisms. They depend on the specific case and especially the automotive application requires additional knowledge of the transfer path and the influence of sealings. Therefore, at least a few works were conducted during the last 10 years to characterize automotive gap noise. Here, we present a brief overview of the works that helped to develop a rough understanding of automotive gap noise physics and try to provide a status quo description of aeroacoustic gap noise simulations.

In general, automotive gaps differ strongly. Their design, their filling with sealings and their tendency for leakages varies between the different locations on the vehicle, between different manufacturers and it is principally prone to strong influences due to processing tolerances. In addition, also their inflow conditions vary strongly: The inflow can be either perpendicular to the gap opening or even parallel to its edges. The flow situations vary from a relatively defined inflow at the rear door gap, to a strong influence of the wheel's wake, the A-pillar vortex and the side mirror wake at the side door gaps and even to a nearly uniform inflow at the hood gap's front. A generalization is therefore difficult and most of the works concentrated on specific cases.

If the gap is subject to perpendicular inflow to its opening we will – in the following – always denote its upstream edge as the leading edge of the gap and its downstream edge as the gap's trailing edge. Accordingly, the classical leading edge noise from airfoil aeroacoustics can occur as an interaction of the shear layer with the gap's trailing edge.

First significant results to classify automotive gap acoustics were published in 2007 by Illy et al..[55] They showed experimentally that the main resonance frequency of a rear door gap does not depend on the inflow velocity. Using the Corcos model, eq. (2.11), as the flow excitation of the gap and a measured acoustic transfer function they could additionally apply Golliard's model, eq. (2.21), to the problem and were able to reconstruct the pressure signals inside the gap quite successfully. These results prove that the gap noise at their studied rear door gap is in fact independent from aeroacoustic feedback and mainly caused by an acoustic amplification and spatial filtering of turbulent boundary layer fluctuations.

In 2008 Brennberger studied gap noise at a simplified Helmholtz resonator, a simplified aluminum rear door gap model of an Audi A3 and at the hood gap of a car.[12] While the original scope of this work – the aeroacoustic simulation of automotive gap noise – turned out to be computationally unaffordable at that time he could show that the mechanism on his rear door gap model was significantly different to the Helmholtz resonator model that showed strong aeroacoustic feedback effects. He analyzed that small shear layer fluctuations led to an excitation of standing waves inside his rear door gap model, which is principally similar to the assumptions behind Golliard's model. Additionally he could show that the noise generated by his hood gap model could be characterized by typical edge-tone noise. In a consecutive study Wickern and Brennberger[107] analyzed the influence of different rear door gap designs including a vertical trailing edge offset. They used standard ½-inch microphones positioned inside the cavity and confirmed the results by Illy et al.[55] as they found a Helmholtz-resonance alike behavior with velocity independent resonance frequency in every of their studied cases. The vertical trailing edge offset led to a broadband increase of the generated noise.

Also in 2008 Müller studied the noise generated by the trunk gap of sedan cars and proved that in this case the geometry of the gap is of minor importance and instead the character of the gap's inflow dominates the generated noise.[74] The trunk gap is subject to the strong C-pillar vortices that led to leading edge noise at the upper edge of the gap. Depending on the turbulence and the direction of these vortices the trailing edge noise is significantly affected and due to the open character of the gap acoustic resonances play only a minor role.

A detailed study of the side door gaps on a Mercedes-Benz E-Class W212 was performed in 2011 by Albrecht.[2] Comparably to the rear door gap it turned out that trailing edge noise and edge-tones could be ruled out as possible excitation mechanisms and furthermore that the detected resonance frequencies in the interior of the car are velocity independent. Albrecht could show that these resonance frequencies are related to the B-pillar door gap. Also, a strong influence of some of the sealings in the gap on vibrations of the door and the window frame was present. Additional damping of the side window led to improved interior noise levels which clearly highlighted the complexity of the involved transfer paths.

Since 2012 a series of basic experiments has been performed to systematically analyze the complex features of automotive gap noise. In 2012 De Jong published detailed studies on an idealized rectangular gap with a large spanwidth compared to its opening length.[22] While his original scope was to resemble automotive gap noise and while his experiments provided many results that could be characterized by the previously described passive behavior, his main analysis concentrated on the inset of aeroacoustic feedback and the influence of the opening geometry on the shear layer instability. Especially he could show that the opening position on the downstream or upstream edge of the resonator volume has a significant influence on the stability and characteristics of the shear layer. Nevertheless he could confirm the results from linear stability theory as aeroacoustic feedback always required $\theta/L < 0.2$. Furthermore he derived a complex semi-analytical model to predict the geometric resonance frequencies of the studied partially covered rectangular gap which indicates the complexity of the eigenfrequency prediction without numerical simulations. A study on the influence of sealings showed that the resonance frequencies and levels in the gap are only minimally affected by their presence. However no significant results regarding the acoustic transfer through the sealing could be found.

The extension of this work was carried out by Hazir who especially studied the influence of sealings on gap noise and the acoustic transport through them.[47] Using a basic experiment for noise transmission he could prove that in fact the influence of the sealings on the exterior sound levels is comparably small and accordingly, that a one-way coupling between a highly resolved CFD simulation and a FE simulation of the acoustic transport through the sealing was principally sufficient to treat the phenomenon on his test cases. He could furthermore show that the influence of the sealings on the interior noise is much more complex than only a damping function. Especially it turned out that a small external excitation could lead to high levels inside the cabin at certain frequencies while at most frequencies a classical damping occurred. Besides his studies the influence of other transfer path components is still unknown and the knowledge of the correct position and shape of the sealing at a closed door as well as the treatment of leakages remains a significant limitation of these simulations.

The latest contribution to the field of automotive gap noise has been published by Schimmelpfennig in 2015.[90] He developed a basic experiment of an exemplary rear door gap in a small-scale wind tunnel that led to a passive gap noise phenomenon. In his experiments the gap was positioned shortly downstream of the wind tunnel's nozzle and he additionally influenced the boundary layer state with different turbulator strips. Varying the leading and the trailing edge of the gap Schimmelpfennig could show that both of broadband levels and the excitation of some cavity modes are strongly affected by its edge shapes. Based on these findings he proved that a surface averaging effect is present in the gap opening. Accordingly, the inflowing boundary layer fluctuations dominate the gap noise spectra up to a geometry dependent frequency range, while the frequencies above this range are mostly influenced by interactions with the gap's trailing edge. Using flow visualization paint he could also prove that the separation line is not stationary for a rounded leading edge which leads to strongly increased turbulence in the opening. In his work he additionally studied the influence of different geometry modifications but gave only a brief summary of the results. Experiments on a real vehicle showed a similar behavior to the study by Wickern and Brennberger and thus confirmed the applicability of the small-scale experiment.[107]

In summary, it appears from this range of works that automotive gaps tend to act mostly as passive amplifiers of external turbulence and not as active noise source due to aeroacoustic feedback in their respective openings. The results furthermore indicate that gaps with perpendicular inflow generate more noise than gaps with parallel inflow. In special cases the interaction of the inflow turbulence with the edges of the gap is even more significant for the maximum

Table 3.1 Comparison of the inflow conditions at several gaps of a Mercedes-Benz A-Class W176 at $u_0 = 140\,\mathrm{km/h}$.

Gap	Type	u_e (m/s)	θ (mm)	f_{inst} (Hz)	L_0 (mm)	θ/L_0
Windscreen / Roof	quasi flat	40	0.64	2500	2	0.32
Rear Door Gap	partially covered	44	8.42	210	7	1.2
B-pillar gap	partially covered	42	8.19	205	5	1.63

noise levels than the amplification mechanism. Although a generalization remains difficult we can at least principally compare the results from linear stability theory ($\mathrm{St}_\theta > 0.04$ for the inset of shear layer instabilites,[72] $\theta/L_0 < 0.01$ to 0.06 for flat cavities,[39,88] $\theta/L_0 < 0.16$ to 0.2 for partially covered cavities[22]) with the situation at different car gaps. In table. 3.1 we evaluated the momentum thickness θ from a standard $k - \varepsilon$ CFD simulation at several gaps of a Mercedes-Benz A-Class W176 and compare it to the respective opening length of the gaps (data from [1]). The critical instability frequency according to $\mathrm{St}_\theta = 0.04$ depends on the gap type and is called f_{inst}. Although linear stability theory can only be a very rough criterion for the prediction of the inset of aeroacoustic feedback, it is seen that all cases are far off from the assumed instability limits and the findings are in good agreement with the previously discussed experimental studies. Consequently, we assume that the passive gap noise mechanism usually plays a decisive role on any car gap and not only on the rear door gap studied in this work.

This analysis bares several strong consequences for the numerical simulation of automotive gap noise: While feedback dominated gap noise is generated by a local flow phenomenon in the gap's opening, a strong influence of the passive amplification requires a transient representation of the inflowing turbulence. Even if feedback occured, Schimmelpfennig's results showed that the turbulent boundary layer fluctuations play a decisive role until the surface averaging effect sets in. This effect depends only on the gap's opening length and not on the presence of feedback. Accordingly, even in such a case, the generated noise at gaps would be a superposition of acoustically amplified turbulence and the self-sustained oscillation in the gap opening. Even an ideal detached eddy simulation without grey-area at the gap's leading edge could not provide this information. The numerical costs associated with the resolution of the turbulent boundary fluctuations are excessive and close to a true direct numerical simulation.[16] Therefore it is necessary to develop specific strategies if the numerical simulation of gap noise is desired.

In the literature at least a few simulation strategies for such phenomena are described. Golliard's semi-empirical model[43] could, at least in principle, be applied for numerical simulation procedures. The model needed to be based on e.g. a Corcos (eq. 2.11) or a Chase-Howe spectrum (see e.g. [43]) at the gap opening from a steady RANS, assume an appropriate wavenumber filter in the opening and finally transport the resulting acoustic field in the gap's resonator. While this approach provides the advantage to easily couple the resulting acoustic fields to sealings or structural interaction it also introduces severe limitations. First, the validity of a semi-empirical wavenumber-frequency spectrum along the opening is highly questionable in case of non-uniform flows in the opening. Second local flow effects e.g. due to rounding of the leading edge would not be included in the model but only its geometric effect on the wavenumber filtering. And third it is impossible to capture possible inflow into the cavity or to handle eventual self-sustaining oscillations in the opening. Although Illy showed that the model is principally applicable to the rear door gap,[55] its general applicability to automotive gaps remains highly unlikely due to the strongly varying inflow conditions and the uncertainties under design changes.

In 2012 De Jong described a two-step simulation strategy for his experiments based on the Lattice-Boltzmann Code PowerFLOW:[22] First he resolved the experimentally used turbulator strip which led to a transient turbulent boundary layer. Downstream of this strip he stored the fluctuating velocity and pressure fields and used it as an unsteady inlet for the aeroacoustic simulation of the gap. While this methodology delivered principally good results in his experiments it is still computationally expensive, as the turbulator strip is extremely small and furthermore certainly not applicable in general situations with varying inflow and complex geometries upstream of the gap. Simplified numerical simulations using a URANS method with an average representation of the boundary layer turbulence led to a strong over-prediction of the feedback levels. De Jong concluded that additionally the strongly coherent shedding vortices in the opening are significantly influenced by the small-scale boundary layer fluctuations which causes an attenuation of the resulting noise.

Comparable simulation attempts have been performed by Mercier[71] for an experimental study by PSA[77] and Kreuzinger and Schimmelpfennig[62] for the experimental results from Schimmelpfennig.[90] Instead of resolving a turbulator strip both approaches synthesized turbulence for local LES of the gap flow. Mercier used a stochastic modal approach by Kraichnan[61] and Kreuzinger and Schimmelpfennig applied a simple recirculation inlet by Manhart and Friedrich.[70] Although both approaches in their described state are principally restricted to simple flow situations synthesizing turbulence can outline a path towards industrially applicable gap noise simulations. As the computational domain for the gap acoustics can be kept relatively small, the restrictions of a wall-resolved LES are reduced. By synthesizing the boundary layer there exists a chance to somehow reduce its resolution requirements. The challenge for these approaches remains to find a formulation that is robustly applicable to a wide range of flow situations as well as it is applicable to complex underlying geometries. In the following chapter we dill discuss potential candidates for these kinds of simulations and present a simulation strategy that will be applied in this thesis.

4 Numerical Methodology

The previous analysis of the literature indicates that most importantly external turbulence and noise gets amplified in automotive (door) gaps and consequently, an accurate representation of these sources is required to capture the principal physical effects.* In order to develop a widely applicable method, that is not restricted to cases where detached turbulence masks the principally present turbulent boundary layer at the wall, this situation requires a transient representation of the turbulent boundary layer at the gap opening – even before considering the acoustic propagation. Due to the physics of the attached turbulence at the wall most commonly this task requires either a Direct Numerical Simulation (DNS) of all turbulent scales or a wall-resolved Large Eddy Simulation (LES) where only the smallest scales of turbulent motion are modeled. As such methods are extremely computationally expensive[3,17] their application is typically limited to small-scale problems or pilot tests. To reduce the computational requirements of this task we are thus investigating methods that – based on a Reynolds Averaged Navier Stokes (RANS) simulation of the full-scale vehicle – synthesize the turbulence in a local, bounded sub-domain around the desired gap. The cheapest available methods for such approaches are likely stochastic reconstruction methods as the wavenumber-frequency based *Fast Random Particle Mesh Method*[33] (FRPM) that has been applied to synthesize turbulent boundary layer fluctuations[53] or the energy based *Stochastic Noise Generation and Radiation* method[7] (SNGR) that has also been modified to account for anisotropic boundary layer turbulence.[99] Both methods were developed to act as true aeroacoustic noise models based on RANS input data and both intrinsically rely on the validity of their underlying target spectra of free turbulence and accordingly their applicability to complex flow situations might be limited. At least FRPM is currently also under development to serve as inlet turbulence generator for LES based aeroacoustic simulations in a small computational domain[8] that are more expensive than the original scope of the stochastic methods. Several other synthetic inlet turbulence methods, ranging from systematically straightforward *Recycling Inlet* approaches[5,68,70] to *Digital Filtering*[59] and the relatively well-known *Synthetic Eddy Method*[56] are discussed in some detail by Dhamankar et al..[24] However, all these approaches still require specific flow conditions or a typical inlet. Thus their modification to true three-dimensional cases is not straightforward. In contrast, *Volume Forcing* approaches[23,94] try to synthesize turbulence by simply enforcing e.g. the mean velocity or the turbulent kinetic energy through an artificial force in the LES momentum equation. Accordingly, these methods rely strongly on the assumption that the enforced Navier-Stokes equations still resemble realistic physics. Nevertheless they depend neither on specific flow conditions, standard two-dimensional inflow, nor on specific semi-empirical target spectra. For an application to aeroacoustic simulations it is additionally

---

[*] The experimental analysis of an idealized rear door gap in chapter 6 and the rear door gap of a Mercedes-Benz S213 in chapter 8 confirm these findings.

required that the turbulence synthetization methods do not only resemble correct physics but that they also produce an acceptable amount of numerical noise.

Due to the potential flexibility of volume forcing approaches we especially investigate the applicability of a specific two-step hybrid RANS/LES methodology based on De Laage de Meux' *Anisotropic Linear Forcing*[23] (ALF) to automotive gap noise. In this method first an Elliptic Blending Reynolds Stress Model RANS[63] of the whole setup is performed. The data from these simulations are used as target fields for ALF that synthesizes turbulence for a LES in a small computational sub-domain around the gap of interest.

In addition to the capability of this approach to resolve the turbulent boundary layer fluctuations we still need to model the sound propagation in the gap. For this purpose we study the applicability of a classical compressible Direct Noise Computation (DNC) and a hybrid acoustic analogy approach based on an acoustic wave equation[103] that was derived from the *Acoustic Perturbation Equations*[34] (APE). While the presence of self-sustained oscillations in the gap opening certainly requires a compressible simulation due to the two-way coupling of flow and acoustics, the passive acoustic amplification mechanism might be captured by acoustic analogies based on an incompressible flow simulation, but the influence of additional compression or scattering effects in the small gap opening is still unknown. These acoustic analogies could be advantageous as spurious noise due to spatial under-resolution and interactions with the artificial flow boundaries of the small sub-domain could be controlled much better with separated scales.

All simulations are performed with the commercial finite volume CFD code STAR-CCM+. In the following we will give a brief introduction to the basic ideas and properties of the applied methods.

4.1 A Hybrid RANS/LES

The hybrid RANS/LES method described here, is one of the many available approaches to effectively treat the wide variety of length and time scales in turbulent motion that range from the smallest scales, where eddies dissipate into heat, to large energy containing eddies shedding from obstacles. Due to these different scales a DNS of the full Navier-Stokes equations is currently restricted to small academic cases and any industrial application requires modeling of at least some of the involved scales. Here, we first want to provide a very brief insight into the different involved scales and the concept of the *energy cascade* and then describe the LES, ALF and the EB-RSM RANS in more detail.

Usually, turbulence is quantified by its statistical moments. Common representations therefore utilize the *Reynolds decomposition* of flow variables $\phi = \bar{\phi} + \phi'$ from chapter 2.2 into a temporally averaged part $\bar{\phi}$ and a fluctuating part ϕ', where the temporal average is defined as

$$\bar{\phi} := \lim_{T\to\infty} \frac{1}{T} \int_{t_0}^{t_0+T} \phi \, dt \ . \tag{4.1}$$

Due to the complexity of turbulence often simplified models as *homogeneous* and *isotropic* turbulence are considered. The statistical properties of homogeneous turbulence are invariant under arbitrary translations of the coordinate axes while those of isotropic turbulence are invariant under arbitrary rotations of the coordinate axes. Besides the mathematical simplification arising from these definitions, homogeneous isotropic turbulence can be realized experimentally by using grids in a wind tunnel and is thus well studied for detailed studies.

Lots of research has been conducted to understand the spatio-temporal characteristics of turbulence, its production, convection and dissipation mechanisms. Especially spectral analysis of the total kinetic energy $k := \frac{1}{2}\overline{u_i' u_i'}$ provides many insights into the processes and the interaction between the different scales of turbulence. A typical spectrum of the contribution $E(\kappa)$ at wavenumber κ to the total turbulent kinetic energy, i.e.

$$k = \int_0^\infty E(\kappa)\, d\kappa \,, \tag{4.2}$$

depicting a classical *energy cascade* can be seen in fig. 4.1. Due to the presence of viscous shear stresses any vortical disturbance within a mean flow gets rapidly dissipated into internal energy. Therefore a continuous source of energy is required to maintain any turbulent flow. The generated turbulence consists of many different length scales (wavenumbers) but most of the turbulent kinetic energy k is contained in its largest structures. These structures are generally anisotropic and strongly affected by the surrounding geometry or the turbulence generation mechanism. Inertial forces, still independent from viscous effects, deform and transport these large eddies which leads to smaller and smaller structures. As the vortex size decreases, the respective Reynolds number decreases as well, and suddenly dissipation due to the viscous forces and molecular diffusion occurs and dominates the inertial forces. In these ranges the turbulence can again be assumed universally homogeneous and isotropic. In addition to this typically dominant energy cascade in many cases turbulent and stochastic backscatter from

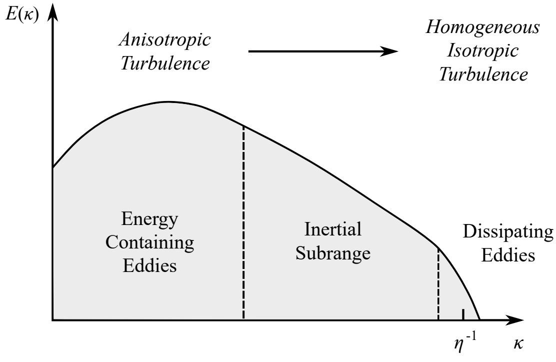

Fig. 4.1 Schematic energy spectrum for a turbulent flow, log-log scales. Anisotropic large scale eddies carry most of the turbulent kinetic energy k. Driven by inertial forces the size of the eddies decreases in the inertial subrange and finally molecular diffusion and viscous forces begin to dominate at the largest wavenumbers which leads to dissipation of the eddies into internal energy.

small to large scales happens and the importance of these phenomena depends on the considered cases.

Especially at sufficiently high Reynolds numbers it is possible to characterize the different scales of motion by typical length-scales, see e.g. Pope.[80] The energy containing range may be represented by *integral length and time scales* estimating the correlation distance and time of the turbulence. Due to the strong anisotropy in this wavenumber range different longitudinal and transverse length scales are necessary – nevertheless most often classical definitions from homogeneous (sometimes even isotropic) turbulence are utilized in the literature. Furthermore the inertial subrange is often characterized by the *Taylor microscale* λ that is defined from the curvature of the respective longitudinal and transversal autocorrelation functions. Although a true physical interpretation of this eddy size is not available, these scales are well defined and lie within the inertial subrange. According to Pope, a typical approximation of the Taylor microscale is given by

$$\lambda := \sqrt{15 \frac{\nu}{\varepsilon} u_i' u_i'} \tag{4.3}$$

with $\nu := \mu/\varrho$ the fluid's kinematic viscosity and ε the mean turbulent dissipation rate.[80] This formulation is again exact in isotropic turbulence. The dissipation range is finally described by the *Kolmogorov microscales*. The length, time and velocity scales

$$\eta := \left(\frac{\nu^3}{\varepsilon}\right)^{1/4}, \qquad \tau_\eta := \left(\frac{\nu}{\varepsilon}\right)^{1/2}, \qquad u_\eta := (\nu\varepsilon)^{1/4} \tag{4.4}$$

describe the smallest, dissipative eddies in turbulent flows and in fact, the Reynolds number based on the Kolmogorov microscales is equal to 1 which indicates that viscous dissipation becomes effective in this range.

While a DNS principally requires to resolve all these turbulent scales down to the Kolmogorov scales, LES aims to model the scales below the inertial subrange, or equivalently below the Taylor microscales. In contrast, the scope of a steady RANS is to model the full energy cascade of turbulence. While these approaches introduce modeling uncertainties and new equations, resolution and time step restrictions are typically significantly reduced.

4.1.1 Large Eddy Simulation

As we require a transient representation of the turbulent boundary layer fluctuations, the key element of our simulations approach is an LES around the gap of interest. In order to model the smallest scales of turbulence, the equations that are solved for LES are obtained by spatial filtering of the variables. Let ϕ be a solution variable like velocity components, pressure or energy, and $G(\boldsymbol{x}, \boldsymbol{\Delta})$ a spatial filter kernel with filter width $\boldsymbol{\Delta}$. Then in the LES each solution variable is decomposed as $\phi = \tilde{\phi} + \phi^{\mathrm{s}}$ into a filtered value

$$\tilde{\phi}(\boldsymbol{x}, t) := \iiint G(\boldsymbol{x} - \boldsymbol{x}')\phi(\boldsymbol{x}', t)\; d\boldsymbol{x}' \tag{4.5}$$

and a sub-grid value $\phi^{\mathrm{s}} := \phi - \tilde{\phi}$. Applying this filtering to the compressible Navier-Stokes equations yields the LES momentum and continuity equations

$$\begin{aligned} \frac{\partial\, \varrho\tilde{\boldsymbol{u}}}{\partial t} + \nabla \cdot (\varrho\tilde{\boldsymbol{u}} \otimes \tilde{\boldsymbol{u}}) &= -\nabla\tilde{p} + 2\mu\nabla \cdot \tilde{\mathbf{S}} - \frac{2}{3}\mu \triangle \tilde{\boldsymbol{u}} + \nabla \cdot \mathbf{T}^{s} + \boldsymbol{f}_b \\ \frac{\partial\varrho}{\partial t} + \nabla \cdot (\varrho\tilde{\boldsymbol{u}}) &= 0\;. \end{aligned} \tag{4.6}$$

with the resolved strain rate tensor

$$\tilde{\mathbf{S}} = \frac{1}{2}\left(\nabla\tilde{\boldsymbol{u}} + \nabla\tilde{\boldsymbol{u}}^{\mathsf{T}}\right)\;. \tag{4.7}$$

The filtered viscous stress tensor components $T^{s}_{ij} := -\widetilde{\varrho u^{\mathrm{s}}_i u^{\mathrm{s}}_j}$ are unknown and require additional modeling. In STAR-CCM+ an implicit filter is used, which means that the computational grid is interpreted as the spatial low-pass filter determining the scales of the filtered eddies. While it is not possible to precisely state the filter kernel G this approach takes full advantage of the grid resolution and is, in general, computationally less expensive than explicit filtering.[97]

As the filter length and the mesh resolution needs to be chosen such that the limiting wavelength is well in the inertial subrange, LES makes typically use of the Bousinessq approximation

$$\mathbf{T}^{s} = 2\mu_t\tilde{\mathbf{S}} - \frac{2}{3}\mu_t\,(\nabla \cdot \tilde{\boldsymbol{u}})\,\mathbf{I}\,, \tag{4.8}$$

that assumes that subgrid scale stresses, resulting from the interaction between the larger, resolved eddies and the smaller, unresolved eddies, are linearly dependent on the resolved strain rate tensor $\tilde{\mathbf{S}}$. The subgrid scale turbulent viscosity μ_t must be described by a subgrid scale model that accounts for the effects of small eddies on the resolved flow.[97]

In this work we typically use the Wall-Adapting Local-Eddy Viscosity (WALE) subgrid scale model.[76] This model can be considered as a development of the Smagorinsky subgrid scale model[98] and the Dynamic Smagorinsky subgrid scale model.[38,67] In the Smagorinsky models the subgrid scale viscosity is modeled via an algebraic mixing-length formula

$$\mu_t = \varrho\Delta^2 S \tag{4.9}$$

where Δ is an appropriate filter width and $S := \sqrt{2\tilde{\mathbf{S}} : \tilde{\mathbf{S}}}$ the modulus of the resolved strain rate tensor. The length scale Δ of the original Smagorinsky model is then directly related to the cell volume V and the centroid wall distance d by

$$\Delta = f_v \min\{\kappa d, C_s V^{1/3}\} := \left(1 - \exp\left\{-\frac{y^+}{25}\right\}\right) \min\{\kappa d, C_s V^{1/3}\} . \tag{4.10}$$

Here, $\kappa = 0.41$ is the Von Kármán constant, $y^+ = y u_\tau / \nu$ and C_s is a non-universal model coefficient that depends on the local flow conditions. The damping function f_v is needed to obtain proper results in wall-bounded flows. The Dynamic Smagorinsky Subgrid Scale model has the same basic form as the Smagorinsky model, however instead of using a single user-defined C_s coefficient, the model computes a local time-varying coefficient by test-filtering the flow field at a length scale greater than the grid length scale. This dynamic variation of the constant gives the model its name, and allows it to compute the correct result for wall-bounded flows without the use of damping functions.[97] In the WALE subgrid scale model the mixing-length formula is modified by

$$\mu_t = \varrho \Delta^2 S_w := \varrho \Delta^2 \frac{\mathbf{S}_d : \mathbf{S}_d{}^{3/2}}{\mathbf{S}_d : \mathbf{S}_d{}^{5/4} + \tilde{\mathbf{S}} : \tilde{\mathbf{S}}^{5/2}} . \tag{4.11}$$

Here, S_w is typically called a deformation parameter and the tensor $\mathbf{S}_d$ is defined by

$$\mathbf{S}_d = \frac{1}{2} \left[\nabla \tilde{\boldsymbol{u}} \cdot \nabla \tilde{\boldsymbol{u}} + (\nabla \tilde{\boldsymbol{u}} \cdot \nabla \tilde{\boldsymbol{u}})^\mathsf{T} \right] - \frac{1}{3} \mathrm{tr} \left(\nabla \tilde{\boldsymbol{u}} \cdot \nabla \tilde{\boldsymbol{u}} \right) \mathbf{I} . \tag{4.12}$$

Due to this reformulation the WALE model does not require any form of near-wall damping but automatically gives accurate scaling at walls, independent of laminar or turbulent flow conditions. Accordingly the determination of the grid filter width

$$\Delta = \min\{\kappa d, C_w V^{1/3}\} \tag{4.13}$$

in this model does not require a dynamic variation of its model coefficient C_w. Although this model coefficient is again non-universal, the WALE model has been applied successfully to a wide range of applications and seems to be relatively insensitive to the value of C_w, that is typically chosen as $C_w = 0.544$.

While LES leads to a significant reduction of the numerical costs compared to a DNS when it comes to free turbulence, the benefits reduce close to the wall. Due to the strong anisotropy of the wall bounded eddies and their low Reynolds numbers the grid size needs to be strongly refined not only in the wall-normal direction but also in the tangential direction. In 1979 Chapman[15] provided a first estimate of the grid resolution requirements of LES that has been revisited by Choi and Moin in 2009.[17] According to their analysis, the degrees of freedom N_{LES} required for the LES of a zero pressure gradient boundary layer of length x fulfills $N_{\text{LES}} \sim \mathrm{Re}_x^{13/7} \approx \mathrm{Re}_x^{1.86}$ while $N_{\text{DNS}} \sim \mathrm{Re}_x^{39/14} \approx \mathrm{Re}_x^{2.79}$. Although this represents a clear benefit compared to DNS, the wall resolved LES becomes increasingly expensive as the size of the studied objects increases. Typically, resolutions of $\Delta x^+ := u_\tau \Delta x / \nu \approx 50 \sim 130$, $\Delta z^+ := u_\tau \Delta z / \nu \approx 10 \sim 30$, $y^+ \approx 1$

and approx. 10 ~ 30 layers in the wall-normal direction have been used successfully in wall resolved LES of zero pressure gradient boundary layers.[17,37] In a parameter study Choi and Moin could also show that a temporal resolution of $\Delta t^+ := \Delta t u_\tau^2/\nu = 0.4$ is required for accurate LES or DNS of wall bounded flows with implicit time-stepping schemes as they are used in STAR-CCM+.[16]

As these resolution requirements cannot be adapted to full industrial scales either some kind of wall-modeling based on the universal laws of the wall is required or reducing the computational domain of the LES to a smaller sub-domain which then requires to synthesize the boundary layer turbulence in an appropriate manner.

4.1.2 Anisotropic Linear Forcing

In our approach we decided to apply the LES only in a constrained sub-domain around the gap, which implies that an appropriate boundary layer state including transient fluctuations needs to be provided at the velocity inlet. As discussed in the introduction into this chapter several more or less general approaches are described in the literature. In this work the volume forcing approach *Anisotropic Linear Forcing* (ALF)[23] is used to synthesize turbulent boundary layer fluctuations in the LES sub-domain. In general, volume forcing approaches require a set of target fields that represent the desired turbulence state.

For ALF, let $\overline{\boldsymbol{u}}^\dagger$ denote an arbitrary average velocity target field and $\overline{u_i'u_j'}^\dagger$ corresponding target Reynolds Stresses. Furthermore let $\tilde{\boldsymbol{u}} = \langle\tilde{\boldsymbol{u}}\rangle + \boldsymbol{u}'$ denote the LES filtered velocity, with $\langle\cdot\rangle$ an estimation of the Reynolds average and $\boldsymbol{u}'$ its resulting approximated fluctuating part.

In ALF a linear volume force $\boldsymbol{f} = \mathbf{A}\langle\tilde{\boldsymbol{u}}\rangle + \boldsymbol{b}$ with unknown coefficents $\mathbf{A} = \left(A_{ij}\right)$ and $\boldsymbol{b} = (b_i)$ is introduced into the LES momentum equation

$$\frac{\partial\, \varrho\tilde{\boldsymbol{u}}}{\partial t} + \nabla\cdot(\varrho\tilde{\boldsymbol{u}}\otimes\tilde{\boldsymbol{u}}) = -\nabla\tilde{p} + 2\mu\nabla\cdot\tilde{\mathbf{S}} - \frac{2}{3}\mu\,\triangle\,\tilde{\boldsymbol{u}} + \nabla\cdot\mathbf{T}^s + \boldsymbol{f}_b + \varrho\boldsymbol{f}\;. \tag{4.14}$$

Let furthermore $\langle u_i'u_j'\rangle$ the resolved stress tensor of the LES. Then, De Laage de Meux showed that the linear system (in component notation)

$$A_{ij}\langle\widetilde{u_j}\rangle + b_i = \frac{1}{\tau_v}\left(\overline{u_i}^\dagger - \langle\widetilde{u_i}\rangle\right) \tag{4.15}$$

$$A_{ik}\langle u_j'u_k'\rangle + A_{jk}\langle u_i'u_k'\rangle = \frac{1}{\tau_r}\left(\overline{u_i'u_j'}^\dagger - \langle u_i'u_j'\rangle\right) \tag{4.16}$$

for the matrix and vector coefficients A_{ij} and b_i leads to

$$\langle\widetilde{u_i}\rangle \to \overline{u_i}^\dagger \qquad\qquad \langle u_i'u_j'\rangle \to \overline{u_i'u_j'}^\dagger \tag{4.17}$$

for an appropriately chosen averaging operator $\langle\cdot\rangle$ and relaxation times τ_ν, τ_r. Furthermore he showed, that the matrix coefficients A_{ij} can be calculated analytically from the resolved stresses and the ALF target fields, which makes the computation cheap.

In this work an exponential filter $\mathcal{G}_T(\phi)$ with

$$\frac{\partial \mathcal{G}_T(\phi)}{\partial t} = \frac{\phi - \mathcal{G}_T(\phi)}{N_{\mathrm{EWA}}\Delta t}\,, \qquad N_{\mathrm{EWA}} \in \mathbb{N} \tag{4.18}$$

has been used to approximate the Reynolds averaging $\langle\cdot\rangle$. The relaxation time definitions from De Laage de Meux[23] have been extended to

$$\tau_\nu = \frac{C_\nu}{S^\dagger} \qquad \text{and} \qquad \tau_r = \max\left\{2\Delta t,\ \max\left\{\frac{C_r}{C_\mu},\ \frac{k^\dagger}{\varepsilon^\dagger},\ C_t\sqrt{\frac{\nu}{\varepsilon^\dagger}}\right\}\right\} \tag{4.19}$$

where in addition $S^\dagger$ denotes the modulus of the target velocity field's strain rate tensor, $k^\dagger$ the target turbulent kinetic energy and $\varepsilon^\dagger$ the target turbulent dissipation rate. $C_\mu = 0.22$, $C_\nu = 0.1$, $C_r = 1.0$, $C_t = 1.0$ are dimensionless model parameters.

In our simulations the target fields used for the ALF are calculated from the RANS as

$$\overline{u_i}^\dagger = \overline{u_i}_{\mathrm{RANS}} \qquad\qquad \overline{u_i'u_j'}^\dagger = \overline{u_i'u_j'}_{\mathrm{RANS}} - \frac{2}{3}\delta_{ij}k^{\mathrm{s}}\,, \tag{4.20}$$

with the Kronecker symbol δ_{ij} and the subgrid kinetic energy k^{s} modeled by the LES. In the LES subgrid scale model the total stresses from the LES will be composed from the resolved turbulence and the subgrid scale contribution, which explains the correction term in eq. (4.20). The ALF target fields from the EB-RSM are mapped onto the mesh using a shape function based weighting scheme that gives accurate results even close to the wall.

De Laage de Meux especially applied the Anisotropic Linear Forcing to a classical turbulent channel flow in a channel of height h. Such flow can be treated either by periodic boundary conditions or with the Synthetic Eddy Method (SEM).[56] He analyzed the influence of the different length and time scales in much detail and could especially show that ALF could be used successfully for a zonally forced RANS/LES. His studies showed that the length L of the ALF region influences the accuracy of the forcing in the whole channel. Already at $L/h = 5.0$ the quality of the calculated Reynolds stresses and the skin friction coefficient C_f at the wall was on par or better than the SEM results. Nevertheless, the quality still improved with $L/h = 7.5$. Furthermore, the computational costs were approximately 3.8 times smaller than with the SEM and relatively independent from L. Applying ALF in the whole channel, he also evaluated the velocity fluctuations at different positions and found that no spurious noise was introduced in comparison to the periodic LES. Although he did not evaluate any pressure signals and although the influence of linear forcings on spectral data is still not clarified analytically, these results indicate that wall pressure spectra generated by ALF could possibly reach a good degree of accuracy – however a precise validation at turbulent boundary layer flows is required and the optimal length of the ALF region still needs to be studied under different conditions.

Applying ALF on an industrial scale thus requires the knowledge of the mean velocity, the mean Reynolds stresses and the mean turbulent dissipation rate from the RANS. Additionally, the mean pressure information will be required to set accurate boundary conditions. While these requirements impose only small restrictions, applying a Reynolds stress RANS model to a full-scale vehicle can be a challenge as typically their convergence and robustness is weak and the computational costs are high. Compared to the savings of a true wall resolved LES at least this last point is still relatively negligible.

4.1.3 Elliptic Blending Reynolds Stress Model RANS

To calculate accurate boundary conditions for the sub-domain LES as well as the target fields and stresses required for ALF we globally apply a RANS using the Elliptic Blending Reynolds Stress Model[63] (EB-RSM). In contrast to the LES a steady RANS approach aims to model all scales of turbulent motion and not only the smallest homogeneous isotropic scales. Consequently, here the Reynolds decomposition $\phi = \bar{\phi} + \phi'$ is directly applied to the Navier-Stokes equations, eq. (2.1), in order to separate all steady and unsteady scales, resulting in the RANS equations

$$\begin{aligned} \frac{\partial \varrho\bar{\boldsymbol{u}}}{\partial t} + \nabla\cdot(\varrho\bar{\boldsymbol{u}}\otimes\bar{\boldsymbol{u}}) &= -\nabla\bar{p} + 2\mu\nabla\cdot\bar{\mathbf{S}} - \frac{2}{3}\mu \triangle \bar{\boldsymbol{u}} + \nabla\cdot\mathbf{T}^{\mathrm{RANS}} + \boldsymbol{f}_b \\ \frac{\partial \varrho}{\partial t} + \nabla\cdot(\varrho\bar{\boldsymbol{u}}) &= 0 \\ \frac{\partial \varrho\bar{e}_t}{\partial t} + \nabla\cdot(\varrho\bar{e}_t\bar{\boldsymbol{u}}) &= -\nabla\cdot(\bar{p}\bar{\boldsymbol{u}}) + \nabla\cdot\left(\bar{\mathbf{T}}\bar{\boldsymbol{u}}\right) + \nabla\cdot\left(\bar{\mathbf{T}}^{\mathrm{RANS}}\bar{\boldsymbol{u}}\right) - \nabla\cdot\bar{\boldsymbol{q}} + \boldsymbol{f}_b\cdot\bar{\boldsymbol{u}}\ , \end{aligned} \tag{4.21}$$

with the mean strain rate tensor $\bar{\mathbf{S}} = \frac{1}{2}\left(\nabla\bar{\boldsymbol{u}} + \nabla\bar{\boldsymbol{u}}^{\mathsf{T}}\right)$ that are formally equivalent to the previous LES equations but now require modeling of the six independent Reynolds stresses $T_{ij}^{\mathrm{RANS}} = -\varrho\overline{u_i'u_j'}$ and not only of the subgrid scale stresses. Although such a modeling increases the uncertainties and potential errors, it significantly reduces the computational costs associated with identifying the mean flow. The most popular available RANS turbulence models are eddy viscosity models as the Spalart-Allmaras model,[100] many different k-ε models or Wilcox' k-ω model.[108] These models again employ the Boussinesq approximation and model the Reynolds stresses linearly dependent on the mean strain rate tensor:

$$\left(\overline{u_i'u_j'}\right)_{ij} = 2\mu_t\bar{\mathbf{S}} - \frac{2}{3}\mu_t\left(\nabla\cdot\bar{\boldsymbol{u}}\right)\mathbf{I}\ . \tag{4.22}$$

In these models the eddy viscosity μ_t needs to be modeled. As the RANS turbulence models do not only model the smallest turbulent scales, more complex models are necessary to produce good approximations of μ_t. As they are principally based on the assumption of isotropic turbulence, which is certainly invalid in many situations, each model works well under certain conditions but fails at other. To account for the anisotropy and low Reynolds numbers close to the wall, all of these models incorporate specific wall-treatments that are based on the universal wall laws and require different wall-normal mesh refinements.

In cases where anisotropic effects play a significant role or a dedicated knowledge of the Reynolds stresses close to the wall is required, as it is the case when using ALF, typically the Reynolds stresses are modeled directly by deriving their six equations of motion:

$$\begin{aligned} \frac{\partial \overline{u_i'u_j'}}{\partial t} + \bar{u}_k \frac{\partial \overline{u_i'u_j'}}{\partial x_k} = & \overbrace{-\frac{1}{\rho}\left(\overline{u_j'\frac{\partial p'}{\partial x_i}} + \overline{u_i'\frac{\partial p'}{\partial x_j}}\right)}^{\text{redistribution } \phi^*_{ij}} \overbrace{-2\nu\left(\overline{\frac{\partial u_i'}{\partial x_k}\frac{\partial u_j'}{\partial x_k}}\right)}^{\text{dissipation } \varepsilon_{ij}} \\ & \underbrace{-\frac{\partial \overline{u_k'u_i'u_j'}}{\partial x_k}}_{\substack{\text{turbulent}\\ \text{transport } \mathcal{D}^t_{ij}}} \underbrace{-\overline{u_j'u_k'}\frac{\partial \bar{u}_i}{\partial x_k} - \overline{u_i'u_k'}\frac{\partial \bar{u}_j}{\partial x_k}}_{\text{production } P_{ij}} + \underbrace{\nu\left(\frac{\partial^2}{\partial x_k^2}\right)\overline{u_i'u_j'}}_{\substack{\text{molecular viscous}\\ \text{transport } \mathcal{D}^\nu_{ij}}} \quad . \end{aligned} \tag{4.23}$$

Again, these equations cannot be solved directly and all terms besides the turbulence production P_{ij} and the molecular viscous transport D^ν_{ij} require additional modeling. For further reading see e.g. Andersson et al.[4] or Wilcox.[108]

The Elliptic Blending Reynolds Stress Model (EB-RSM) in the formulation of Manceau and Lardeau[63] tries to improve the modeling of the anisotropic near-wall effects compared to standard eddy viscosity models and other quadratic or linear pressure strain Reynolds stress models like the SSG models[102] by focusing especially on the redistribution and dissipation terms $\phi^*_{ij} - \varepsilon_{ij}$. It is based on observations that nonlocal pressure wall effects on the redistribution term are of elliptic nature.[27] Accordingly, to close the system an elliptic blending parameter $\alpha \in [0, 1]$ is introduced that fulfils the elliptic equation

$$\alpha - L^2 \Delta \alpha = 1 \tag{4.24}$$

with a turbulent length scale L, $\alpha = 0$ at the wall and $\alpha \longrightarrow 1$ in the free stream. The parameter α does not introduce any artificial damping close to the wall and is then used to blend $\phi^*_{ij} - \varepsilon_{ij}$ between a near-wall formulation $\phi^w_{ij} - \varepsilon^w_{ij}$ and a free stream formulation $\phi^h_{ij} - \varepsilon^h_{ij}$ by

$$\phi^*_{ij} - \varepsilon_{ij} = \left(1 - \alpha^3\right)\left(\phi^w_{ij} - \varepsilon^w_{ij}\right) + \alpha^3\left(\phi^h_{ij} - \varepsilon^h_{ij}\right) \quad . \tag{4.25}$$

Following Durbin, the wall boundary condition of ϕ^w_{ij} is approximated by a near-wall Taylor expansion that leads to an exact second order near-wall condition for all Reynolds stresses except of $\overline{u_1'u_2'}$ and $\overline{u_1'u_3'}$.[25,26] The wall boundary condition of ε^w_{ij} and the free stream calculation of

$\phi_{ij}^h - \varepsilon_{ij}^h$ follows the quadratic pressure strain SSG model.[102] A detailed discussion of the EB-RSM turbulence model can be found e.g. in the Master's thesis by Renz.[83]

4.2 Acoustic Modeling

In addition to the scales of turbulent motion, also the acoustic propagation needs to be captured accurately in our simulations. Typically, the acoustic pressure fluctuations are much smaller than the hydrodynamic fluctuations and especially at low Mach numbers their wavelength and propagation velocity is much larger than the typical scales of the flow. In this section we thus briefly describe the concepts of the utilized DNC and the hybrid acoustic wave equation approach whose applicability to gap noise is studied in the following chapters.

4.2.1 Direct Noise Computation

The term Direct Noise Computation is typically used for compressible flow simulations that intrinsically include acoustic waves. Due to the differences between sound and flow scales it is essential in DNCs to keep a small time-step, an accurate mesh resolution for both sound and flow, to control numerical dissipation and dispersion errors and to strictly avoid spurious noise sources. In our case we use the synthetic turbulence generated by ALF within a compressible LES based on the described WALE subgrid scale model or the Dynamic Smagorinsky subgrid scale model. Accordingly, the resulting pressure field p_{DNC} is a superposition of the mean pressure $\overline{p}$, hydrodynamic pressure fluctuations p' and the acoustic pressure p^{ac}

$$p_{\mathrm{DNC}} = \overline{p} + p' + p^{\mathrm{ac}} \quad . \tag{4.26}$$

While this approach is principally straightforward, DNCs are prone to spurious noise due to mesh transition regions and acoustically reflecting flow boundary conditions. Typical approaches to improve these issues are either acoustic suppression zones that are applied inside the domain to damp acoustic waves before they impinge the boundary[10] or to use so called free stream boundary conditions that are based on the method of characteristics to reduce the reflectivity for perpendicularly impinging acoustic waves.[40] While acoustic suppression zones can be very effective[58] they require a large computational domain if damping of low frequencies is desired. In contrast free stream boundary conditions can be principally positioned closer to the object of interest but it is well known that these conditions tend to generate spurious noise as turbulent eddies impinge and that they lose their effectiveness if the incoming acoustic waves are non-perpendicular to its surface. The free stream boundary conditions can be interpreted as a modification of standard pressure and velocity boundary conditions and can thus be used to impose the mean velocity, the mean pressure and the mean temperature with moderate accuracy.

As the LES sub-domain typically needs to be as small as possible and as mean flow similarity between the global RANS and the LES is essential for our approach, we use free stream boundary conditions for the Direct Noise Computations, although the requirements for minimal reflectivity are certainly not fulfilled within the turbulent boundary layer. To reduce the potential effects of spurious noise generated at the boundary we typically apply a mesh coarsening close to the boundary. Nevertheless a comparison of different sub-domain designs and a validation of the external turbulence spectra will be necessary to study the effectiveness of these boundary conditions.

4.2.2 Hybrid Acoustics: Wave Equations based on the Acoustic Perturbation Equations

In general, hybrid acoustic simulation approaches try to separate the acoustic field from the flow field. Typically, they benefit from an improved efficiency at low Mach numbers, where the fluid flow and the acoustic scales differ strongly, and an improved treatment of spurious acoustic noise due to mesh under-resolution or artificial acoustic reflections at the flow boundaries. These hybrid approaches can be divided into two classes: aeroacoustic analogies and perturbation approaches. A broader overview of these approaches and their historical development than provided here was given by Schoder and Kaltenbacher in [95].

The main idea behind the aeroacoustic analogies is a reformulation of the compressible Navier-Stokes equations into a wave equation for the fluctuating density. This was first done by Lighthill[65,66] and since then was widely studied in several works. Although Lighthill's reformulation is generally valid without additional assumptions, the equation's source term needs to be simplified in order to obtain computational efficiency for specific Mach numbers and flow situations. Typically, the simplified Lighthill equations are capable of predicting far field noise in a resting acoustic medium but don't deliver valid results in the core flow regions.

In contrast to the aeroacoustic analogies, perturbation approaches aim for a systematic decomposition of the fields into mean and fluctuating vortical and acoustic components. Therefore, these approaches also try to provide information about the acoustic fields in the core flow regions. Hardin and Pope were the first to propose such a split of the flow into viscous and acoustic variables that could be calculated by an incompressible flow simulation and an additional perturbation equation.[45] Bogey et al. derived Linearized Euler Equations with aerodynamic source terms to compute the acoustic far field.[11] They could show that the introduced source terms were suited for the simulation of free sheared flows and that the influence of the mean flow was taken into account. Munz et al. extended these approaches for weakly compressible low Mach number flows with variable density and temperature by replacing the incompressible flow solution by interpreting it as the limit $\mathrm{Ma} \to 0$.[75] This approach resembles a more general representation of the regime and allows a detailed discussions of relevant source terms.

Another prominent representative of the perturbation approaches are the Acoustic Perturbation Equations (APE) by Ewert[34] which are based on solenoidal source filtering of the Linearized Euler Equations. For low Mach numbers and nearly incompressible flows, the APE-2 variant is especially suitable. The APE-2 equations are primarily based on the unique Helmholtz decomposition of the velocity $\boldsymbol{u} = \overline{\boldsymbol{u}} + \boldsymbol{u}' + \boldsymbol{u}^{\mathrm{ac}}$ into the solenoidal hydrodynamic velocity fluctuations $\boldsymbol{u}'$ and the irrotational acoustic velocity $\boldsymbol{u}^{\mathrm{ac}}$. This decomposition results in a pressure decomposition $p \approx \overline{p} + p' + p^{\mathrm{ac}}$, where p^{ac} denotes the approximation of the acoustic pressure.[†] Neglecting temperature and entropy noise sources the APE-2 system reads

$$\frac{\partial \varrho'}{\partial t} + \nabla \cdot \left\{ \varrho' \bar{\boldsymbol{u}} + \bar{\varrho} \boldsymbol{u}^{\mathrm{ac}} \right\} = - \nabla \bar{\varrho} \cdot \boldsymbol{u}' \tag{4.27}$$

$$\frac{\partial \boldsymbol{u}^{\mathrm{ac}}}{\partial t} + \nabla \left\{ \bar{\boldsymbol{u}} \cdot \boldsymbol{u}^{\mathrm{ac}} \right\} + \nabla \frac{p^{\mathrm{ac}}}{\bar{\varrho}} = \nabla q_{\bar{\omega}} \tag{4.28}$$

$$\frac{\partial p^{\mathrm{ac}}}{\partial t} - c^2 \frac{\partial \varrho'}{\partial t} \approx - \frac{\partial p'}{\partial t} \tag{4.29}$$

with the density $\varrho = \overline{\varrho} + \varrho'$ and $q_{\bar{\omega}}$ the interaction of the acoustic field with the mean vorticity of the flow, governed by

$$\Delta q_{\bar{\omega}} := -\nabla \cdot \left(\bar{\omega} \times \boldsymbol{u}^{\mathrm{ac}} \right) . \tag{4.30}$$

Starting from the APE-2 system, additionally neglecting the vorticity and mean shear interactions one can derive the convective wave equation

$$\begin{aligned} \frac{1}{c^2} \frac{\partial^2 p^{\mathrm{ac}}}{\partial t^2} + \frac{2}{c^2} \bar{\boldsymbol{u}} \cdot \nabla \frac{\partial p^{\mathrm{ac}}}{\partial t} + \frac{(\bar{\boldsymbol{u}} \cdot \nabla)}{c^2} \left[\nabla \cdot \bar{\boldsymbol{u}} p^{\mathrm{ac}} \right] - \triangle p^{\mathrm{ac}} & \\ = - \left[\frac{1}{c^2} \frac{\partial^2 p'}{\partial t^2} + \frac{2}{c^2} \bar{\boldsymbol{u}} \cdot \nabla \frac{\partial p'}{\partial t} + \frac{(\bar{\boldsymbol{u}} \cdot \nabla)}{c^2} \left[\nabla \cdot \bar{\boldsymbol{u}} p' \right] \right] & \end{aligned} \tag{4.31}$$

that is used in STAR-CCM+.[103] Assuming $\overline{u_i} = 0$ it is possible to further neglect the influence of the mean convection on the acoustic propagation and one finally arrives at a classic acoustic wave equation[89]

$$\frac{1}{c^2} \frac{\partial^2 p^{\mathrm{ac}}}{\partial t^2} - \triangle p^{\mathrm{ac}} = - \frac{1}{c_0^2} \frac{\partial^2 p'}{\partial t^2} \quad . \tag{4.32}$$

Both equations, (4.31) and (4.32), are solved simultaneously on the same mesh as the incompressible LES equations. The hydrodynamic pressure fluctuations p' and the mean velocity $\overline{u_i}$ from the LES are used as input quantities for the wave equations. The flow boundaries of the sub-domain are treated as non-reflecting boundaries within the utilized wave equation.

4.3 Summary

In this chapter we introduced the concept of a hybrid RANS/LES based on ALF and its usage as either a DNC or in combination with a hybrid acoustic wave equation approach. According

---

[†] Especially, Hüppe showed that it is not necessary to derive the APE-2 equations by source filtering that requires homogeneous flow but that they can be derived directly from the compressible Navier-Stokes equations using only the above assumptions.[54]

to first studies on turbulent channel flows by De Laage de Meux[23] this approach should be principally applicable to aeroacoustic simulations on industrial scales as it significantly reduces the computational costs of a wall resolved LES without introducing new semi empirical assumptions. The resulting simulation approaches for the DNC and the hybrid acoustic approach are summarized in table 4.1.

Table 4.1 Summary of the steps of the studied numerical procedures.

	DNC	**Hybrid Approach**	**Computational Domain**
(i.)	Steady RANS using the EB-RSM turbulence model		Wind tunnel
(ii.)	ALF synthesizes turbulent fluctuations with mean statistics from the EB-RSM RANS		Aeroacoustic Sub-domain
(iii.)	Compressible LES including acoustics	Incompressible LES + acoustic wave equation	Aeroacoustic Sub-domain

Although this procedure should be principally applicable to automotive gap noise simulations a precise validation procedure is absolutely necessary. First we need to investigate the capabilities of the hybrid RANS/LES to predict turbulent boundary layer fluctuations and especially their wall pressure spectra and develop application strategies for complex problems. Second we need to investigate if automotive gap noise can be simulated by either of the two acoustic simulation approaches and if the achieved inflow quality is sufficient for its simulation. If the computational costs of these studies on simplified cases are promising, the applicability of the method to a full-scale vehicle needs to be investigated in a final step.

5 Turbulent Boundary Layer Simulations with Hybrid RANS/LES

In the following four chapters we will present the details of an experimental and numerical investigation of turbulent boundary layer induced automotive gap noise. A stringent and precise validation of the methods described in the previous chapter for the numerical simulation of the phenomenon must consist of three independent steps: (i) validation of the generated inflow, (ii) validation of a simplified small-scale gap noise case with precise boundary conditions, (iii) application and validation on a full-scale vehicle model. The first and eventually most severe bottleneck for such simulations in the past was an adequate scale-resolving representation of the attached inflowing turbulent boundary layer upstream of the gap. While De Laage de Meux originally provided a detailed application of ALF to the LES of a turbulent channel flow[23] the simulation of a free turbulent boundary layer is even more challenging. Although scale-resolving simulations of turbulent boundary layers have been performed for many years,[28,92,101,110] such simulations of industry-relevant external flows remain difficult and exceptionally expensive.[3] The main limitations stem from the fact that using classical techniques it is necessary to physically resolve the turbulence production at the wall as well as it is necessary to include the whole industrial configuration – even if scale-resolving is only important in a small sub-domain. These requirements add not only to the costs of the simulation, but also to the uncertainties associated with the numerical treatments (resolution, time-steps) and required modeling to overcome these limitations (e.g. grey area mitigation). Thus it is necessary to study the capabilities of the ALF based hybrid RANS/LES methodology to simulate turbulent boundary layer flows under different conditions in terms of signal quality, computational costs and application strategies.

For this purpose we perform simulations with our approach of a series of experiments by Hu and Herr.[51] In these experiments the turbulent boundary layer above a flat plate configuration in the Acoustic Windtunnel Braunschweig (AWB) was studied using pinhole mounted piezo-resistive pressure transducers (Kulite LQ-062), static pressure ports as well as single-wire and cross-wire anemometry at different locations. The base configuration of this experiment generates a zero pressure gradient boundary layer and will be referred to as *ZPG*. In a variant of this case, a rotatable NACA-0012 airfoil was positioned above the flat plate to manipulate the boundary layer by introducing a pressure gradient. Our studied variant will be referred to as *APG-10* as the airfoil's geometric angle of attack was 10°. The setup of their experiments is well comparable to the gap noise measurements described in chapter 6 but offers more precise measurements of the boundary layer. Their experiments are thus ideally suited to validate the inflow conditions for the numerical simulation of the gap noise experiments performed in the framework of this thesis.

The following description of Hu's and Herr's experiments as well as the numerical analysis of the simulation of their APG-10 case are based on the conference publication *Hybrid RANS/LES* *of an Adverse Pressure Gradient Turbulent Boundary Layer Using an Elliptic Blending Reynolds Stress Model and Anisotropic Linear Forcing* published in the conference proceedings in *Notes on Numerical Fluid Mechanics and Multidisciplinary Design*,.[31]

5.1 Test Case: Experiments by Hu and Herr

The open-jet wind tunnel AWB has a rectangular nozzle with a height of 1200 mm and a width of 800 mm, and a maximum operating velocity $u_0 = 65\,\mathrm{m/s}$. In the experiment by Hu and Herr,[51] a 42 mm thick, 1350 mm long and 1300 mm wide flat-plate was positioned symmetrically 10 mm downstream of the nozzle. To generate an attached ZPG turbulent boundary layer the flat-plate featured a super-elliptic nose and a 12° beveled trailing edge. Above the flat-plate a NACA-0012 airfoil with chord length $c = 400\,\mathrm{mm}$ and spanwise length 1800 mm could be installed with a variable geometric angle of attack (AOA). At 0°AOA the leading edge of the NACA-0012 airfoil was positioned 850 mm downstream of the flat-plate's leading edge and 120 mm above its upper surface, see fig. 5.1.1 and fig. 5.1.2. Both the NACA-0012 airfoil and the flat-plate were wide enough to avoid vertical mixing in the open-jet shear layer.

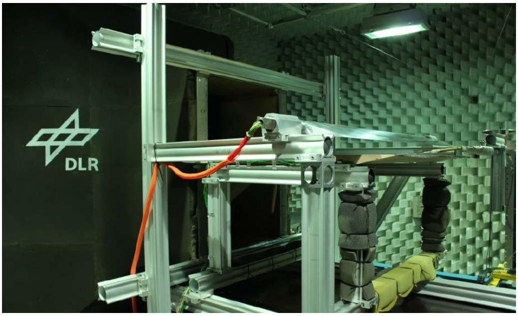

Fig. 5.1.1 Experimental Setup in the AWB with the NACA-0012 airfoil at +12°AOA, from [51].

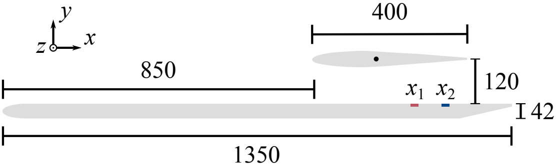

Fig. 5.1.2 Schematic drawing of the experimental flat-plate setup with NACA-0012 airfoil at 0° AOA. Measurement positions x_1 and x_2 indicated. (Measures in mm)

The upper surface of the flat-plate includes a measurement module with 25 static pressure ports ($d = 0.6\,\mathrm{mm}$) and 12 pinhole mounted Kulite LQ-062 pressure transducers that are positioned in an L-shaped array allowing measurements of the spanwise and streamwise correlation of the wall pressure spectra, see fig. 5.1.3. The pinholes have a diameter of 0.5 mm and their resonance

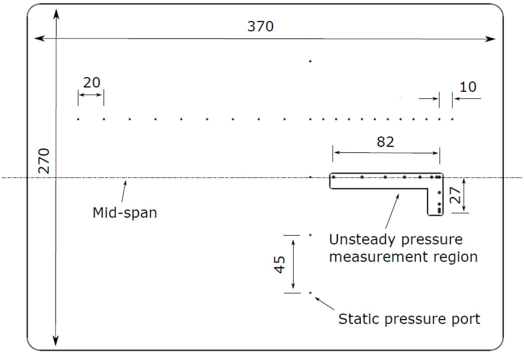

Fig. 5.1.3 Schematic drawing of the measurement module in the upper surface of the flat plate, from [51]. Left corresponds to the upstream direction and the most upstream Kulite sensor in the L-shaped array is positioned at x_1.

frequency lies above 15 kHz, thus the influence of the pinhole impedance on the measured signals can be neglected below 10 kHz. Due to the surface averaging of the turbulent boundary layer fluctuations in the opening of the pinhole, the sensors can only provide unattenuated results up to $\omega\delta/u_e = 20$.[50]

In the following, let $x = 0$ at the flat plate's nose, $y = 0$ at its upper surface and $z = 0$ in the spanwise symmetry plane of the setup. The most upstream Kulite sensor of the L-shaped array is positioned at $x_1 = 1128$ mm downstream of the flat plate's leading edge and the central Kulite sensor at $x_2 = 1210$ mm. At these two measurement locations additional single-wire measurements of the turbulent boundary layer profiles were performed and at x_2 also cross-wire anemometry data are available. To validate our simulation we study two cases. The first is called ZPG, without the optional airfoil at $u_e(x_2) = 30.2\,\mathrm{m/s}$. The second case is called APG-10 and includes the airfoil at a geometric angle of attack of 10° with $u_e(x_2) = 30.4\,\mathrm{m/s}$. The characteristics of the two cases are shown in table 5.1. We compare our results with the static pressure, the data available at x_1 and x_2, and the cross-correlation measured with the L-shaped array of Kulite sensors.

Table 5.1 Experimental results of the ZPG and APG-10 cases used for the validation of the numerical simulations (data from [51]).

	x (mm)	u_e (m/s)	δ (mm)	δ^* (mm)	θ (mm)	H	u_τ (m/s)	Re_τ	Re_θ
ZPG	1210	30.2	19.7	3.51	2.49	1.41	1.125	1439	4889
APG-10	1128	32.0	23.0	5.09	3.12	1.63	0.88	1314	6492
	1210	30.4	28.7	7.68	4.39	1.75	0.745	1388	8670

5.2 Numerical Setup

As outlined in chapter 4 the numerical simulations in this work generally consist of two parts: In this chapter especially a steady incompressible RANS of the whole wind tunnel using the EB-RSM model described in chapter 4.1.3 is followed by an incompressible LES in a small sub-domain located around the experimental measurement module (see fig. 5.2.1).

In our RANS we use a 2nd order segregated flow solver that leads to converged results within approx. 5000 iterations under both ZPG and APG-10 conditions. The setup and the meshes are chosen very similarly to [83], especially we utilize a wall-function formulation everywhere except of the flat-plate's surface and the upper-surface of the flat-plate is anisotropically refined in order to smoothly resolve the gradients within the boundary layer of interest. To simplify the mesh generation process the same mesh refinement boxes are used for both the ZPG and the APG-10 case (see fig. 5.2.2).

The EB-RSM results (velocity, pressure, stresses and turbulent dissipation rate) are then mapped onto the fine mesh of the designated LES sub-domains using a shape-function based weighting scheme. Based on these RANS target fields, ALF is used in the LES sub-domain to synthetically produce the inflow turbulence as described in chapter 4.1.2. For the LES we use the WALE subgrid scale model, c.f. chapter 4.1.1, a 3rd order MUSCL/CD3 scheme in space with blending factor 0.02 and a five-step 2nd order backward differencing scheme in time with 10 inner iterations per time-step, c.f. appendix A. To ensure similarity of the flow between the EB-RSM RANS and the LES, the mean velocity from the RANS is prescribed as a boundary condition at all sub-domain boundaries besides the downstream surface, where we utilize a pressure outlet with prescribed mean pressure from the RANS.

The basic LES sub-domain used for the ZPG case is defined as $700\,\mathrm{mm} \le x \le 1350\,\mathrm{mm}$, $0 \le y \le 300\,\mathrm{mm}$, $|z| \le 100\,\mathrm{mm}$ and ALF is applied at $x \le 1028\,\mathrm{mm}$. Assuming a boundary layer growth rate $\delta \sim x/\log x$ as described in Schlichting et al.[93] in this case ALF is applied over a length of approximately 22δ which is well above the 5δ length used by [23] for a channel flow. In relation to the experimental data from $x = 1210\,\mathrm{mm}$ from table 5.1 the sub-domain is approximately 10δ wide and thus the core of sub-domain should not suffer from side interaction effects. To study the influence of the ALF application length for the ZPG case we additionally

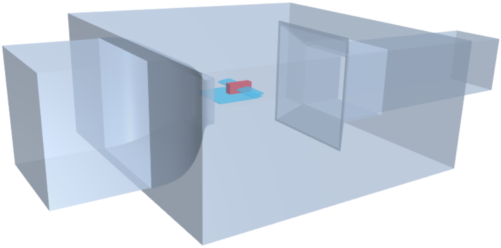

Fig. 5.2.1 Three dimensional view of the AWB geometry used for the numerical simulations. The flat plate and the NACA-0012 airfoil are shown in blue, the RANS domain boundaries in grey and the LES sub-domain boundaries in red.

compare the results of three modified domains where ALF is applied over 15δ, 10δ and 5δ which matches De Laage de Meux's determined value. These domains are realized by moving the inlet plane to 938 mm, 860 mm and 790 mm, respectively.

For the base case with the longest ALF region we also compare the influence of mesh and time-step resolution. We use the three time-steps $\Delta t_1 = 2 \times 10^{-5}$ s, $\Delta t_2 = 1 \times 10^{-5}$ s and $\Delta t_3 = 5 \times 10^{-6}$ s corresponding to $t_1^+ = \Delta t_1 u_\tau^2/\nu = 1.64$, $t_2^+ = 0.82$ and $t_3^+ = 0.41$ based on the measured velocity profiles at x_2. For all three meshes 30 geometrically growing prism layers are used close to the wall. The prism layers extended up to 3.5 mm and the near wall thickness is 0.01 mm, corresponding to $y^+ = 0.7$ at x_2. Outside of the prism layer zone we use a trimmed mesh with isotropic cells. The $z = 0$ cross section of the three meshes is shown in fig. 5.2.3 and its different span- and streamwise resolutions can be found in table 5.2. The near-wall resolution of the three meshes thus correspond to $\Delta_1^+ = 72$, $\Delta_2^+ = 36$, $\Delta_3^+ = 18$ with $\Delta^+ := \Delta x u_\tau/\nu = \Delta z u_\tau/\nu$ based on the measured quantities at x_2. According to Choi and Moin[16,17] at least time-step t_3 and mesh M3 can be considered adequate for an implicit wall-resolved LES on the entire computational domain. Due to its isotropy the trimmed mesh M2 needs to be considered slightly under-resolved in the spanwise direction while M1 is generally under-resolved. The baseline case of our study is based on mesh M2 using the time-step Δt_2.

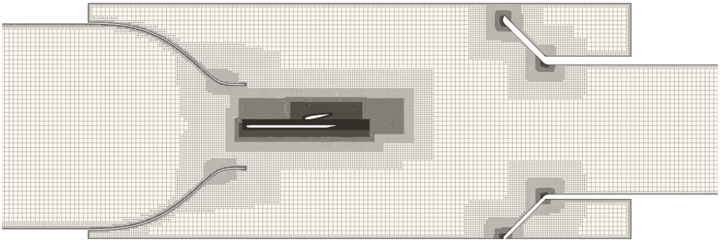

Fig. 5.2.2 $z = 0$ cross section through the RANS mesh of the APG-10 case.

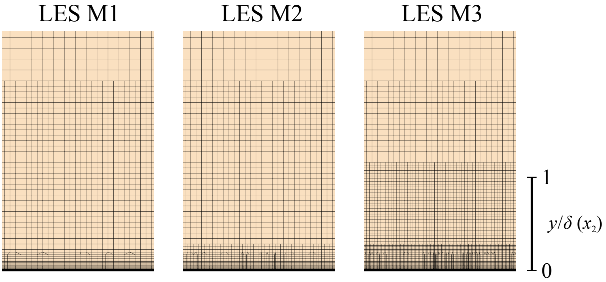

Fig. 5.2.3 Comparison of the three meshes used for the LES of the ZPG cases.

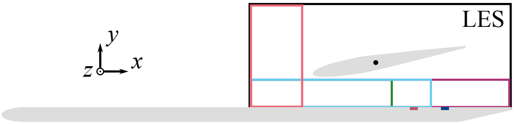

Fig. 5.2.4 Outline of the LES subdomain and the ALF forcing regions, $x \leq 830\,\mathrm{mm}$ (coral), $x \leq 1028\,\mathrm{mm}$ (green), $x \leq 1169\,\mathrm{mm}$ (light-blue), $x \leq 1350\,\mathrm{mm}$ (violet), edited from [31].

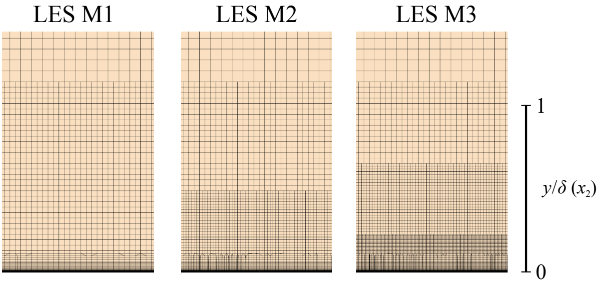

Fig. 5.2.5 Comparison of the three meshes used for the LES of the APG-10 cases.

Table 5.2 Parameters of the three meshes used in the LES sub-domain of the ZPG case. (Δ is the isotropic cell size parallel to the wall)

	Mesh M1	Mesh M2	Mesh M3
Total no. of cells	10.7×10^6	20.1×10^6	72.0×10^6
$\Delta^+ \approx 72$ if y/δ is less than	1.77	1.77	1.77
$\Delta^+ \approx 36$ if y/δ is less than	—	0.25	1.00
$\Delta^+ \approx 18$ if y/δ is less than	—	—	0.25

The LES sub-domain for the APG-10 case is defined very similar to the ZPG case as $650\,\text{mm} \leq x \leq 1350\,\text{mm}$, $0 \leq y \leq 300\,\text{mm}$, $|z| \leq 100\,\text{mm}$ around the experimental measurement points, see fig. 5.2.4. As the application strategy of ALF for such cases was not studied in the past we compare different ALF regions inside the sub-domain (see fig. 5.2.4). Furthermore we also compare the performance of the LES on three different meshes with the three different time-steps from the ZPG case, which now correspond to $t_1^+ = 0.72$, $t_2^+ = 0.36$ and $t_3^+ = 0.18$ based on the measured velocity profiles at x_2.

The three meshes now solely differ on the upper-surface of the flat-plate, while the surface of the NACA-0012 profile is treated identically. Again the same prism layer structure, corresponding to a wall-normal resolution of $y^+ = 0.5$ at x_2, was used on all meshes. The different span- and streamwise resolutions used in the three meshes are summarized in table 5.3 and visualized in fig. 5.2.5. The near-wall resolution of the APG-10 case thus corresponds to $\Delta_1^+ = 48$, $\Delta_2^+ = 24$, $\Delta_3^+ = 12$ based on the measured quantities at x_2. Although all these values (except of the spanwise resolution of mesh M1) fall in the recommended range for implicit wall-resolved LES[16,17] it is very important to keep in mind that the boundary layer thickness varies strongly below the NACA-0012 profile and a significant acceleration is present. This leads to drastically increased values of u_τ below the airfoil's stagnation point and therefore space and time are under-resolved in this area. Consequently the compared ALF regions cannot be classified systematically by their streamwise dimension compared to the boundary layer thickness.

The baseline case of the APG-10 study is again based on mesh M2 using the time-step size Δt_2 and ALF is applied in the region $x \leq 1028\,\text{mm}$, $y \leq 80\,\text{mm}$, see fig. 5.2.4. The physical time simulated for both ZPG and APG-10 is 0.3 s and the wall pressure spectra are evaluated during the last 0.25 s using Welch's method[106] with a Hann window and an overlap of 75 %.

Table 5.3 Parameters of the three meshes used in the LES sub-domain of the APG-10 case. (Δ is the isotropic cell size parallel to the wall)

	Mesh M1	Mesh M2	Mesh M3
Total no. of cells	12.5×10^6	30.6×10^6	93.6×10^6
$\Delta^+ \approx 48$ if y/δ is less than	1.11	1.11	1.11
$\Delta^+ \approx 24$ if y/δ is less than	—	0.52	0.70
$\Delta^+ \approx 12$ if y/δ is less than	—	—	0.24

5.3 Analysis

In the following section we study the general behavior of the previously described hybrid RANS/LES based on ALF, analyze the quality of its results and develop application strategies by applying the method to the cases ZPG and APG-10 of Hu and Herr's experiment and by comparing the numerical results to their experimental data. For simplicity we focus on the LES part of the method. For a detailed discussion of the simulation quality of the first step of the method, the EB-RSM RANS, we refer to Renz[83] whose Master's thesis covers the two cases.

5.3.1 ZPG

The simpler of the two cases is the ZPG case. Running the LES in the base configuration (M2, Δt_2) first the general behavior of ALF becomes visible. As an artificial force in the momentum equation ALF is expected to introduce disturbances that lead to a fully developed synthetic turbulence field after some time steps. One of the central elements to control the behavior of ALF is the filter length T_{EWA} of the exponential weighted average which we apply over $N_{\mathrm{EWA}} = 750$ time-steps, see also equation (4.18). It turns out that the choice of T_{EWA} controls how fast turbulence is imposed. This onset of turbulence is shown in fig. 5.3.1. Starting from an undisturbed mean boundary layer profile first disturbances are introduced within 0.5 T_{EWA} and the boundary layer appears turbulent inside the ALF region within T_{EWA}. Until 8 T_{EWA} turbulence develops and is convected downstream to the outlet of the computational domain. Depending on the distance between the downstream edge of the ALF region, the outlet of the computational sub-domain and the present convection velocity an adequate offset needs to be chosen before results are evaluated. In this case we drop the first 0.05 s of the signal which correspond to $6.66 T_{\mathrm{EWA}}$. It has been shown by De Laage de Meux that reducing T_{EWA} can cause stability issues but also reduces the quality of the synthesized turbulence.[23]

As already discussed in the numerical setup section the base configuration cannot be considered fully resolved in terms of a wall-resolved LES. In addition to the near wall resolution, the mesh is even coarsened towards the outer layer of the boundary layer. To judge the capabilities of the hybrid RANS/LES it is therefore crucial to study the mesh-resolution capabilities throughout the boundary layer. In fig. 5.3.2 one can see the fraction between the wall-normal resolution Δy,

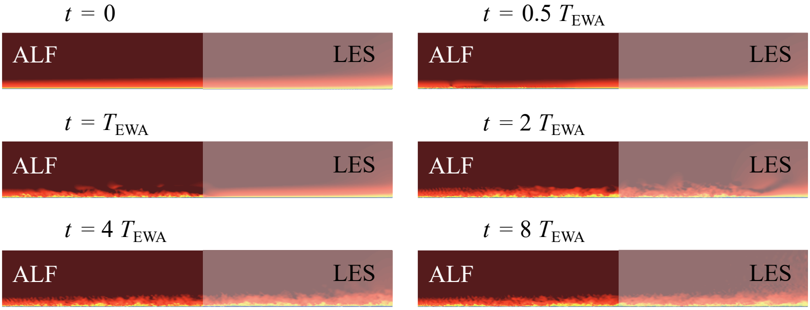

Fig. 5.3.1 Inset of the boundary layer turbulence by applying ALF.

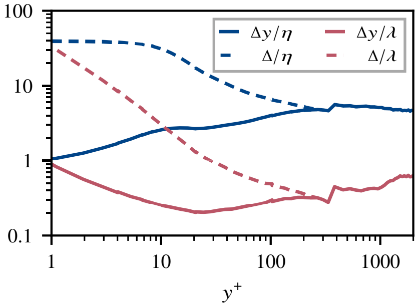

Fig. 5.3.2 Resolution capabilities of the base configuration of the hybrid RANS/LES (mesh M2, Δt_2).

the stream-/spanwise resolution Δ and the Taylor microscale λ and the Kolmogorov scale η, respectively. In these evaluations the length scales and the turbulent dissipation rates are based on the effective viscosity instead. Accordingly the result is only an approximation to the actual resolution capabilities. While the wall-normal resolution Δy of the used mesh is able to resolve the Taylor microscale in the whole boundary layer, the stream- and spanwise resolution Δ can only resolve these scales above $y^+ \approx 20$. As usually a resolution of the Taylor microscales is considered to be required for a wall-resolved LES we can thus assume that the under-resolution is especially present in the viscous sublayer and the lower region of the buffer layer. Nevertheless comparable mesh resolutions are sometimes even used for DNS. Consequently the apparent mesh coarsening in the outer layers of the boundary layer are adequate to resolve these turbulent scales. Comparing the mesh resolution to the Kolmogorov scale it is clear that this mesh is not suited for a DNS as the mesh resolution is typically five times too coarse to resolve the Kolmogorov scales. As mesh M3 uses a doubled stream-/spanwise resolution below the logarithmic layer one can additionally assume that this mesh is suited to resolve the Taylor

Table 5.4 Relative errors of the boundary layer parameters of the base configuration (mesh M2, Δt_2) at x_2 compared to the experiment.

	u_e	δ	δ^*	θ	H	u_τ
Experiment	30.2 m/s	19.7 mm	3.51 mm	2.49 mm	1.41	1.125 m/s
RANS	+0.3 %	+1.5 %	−2.5 %	+0.4 %	−2.7 %	+4.6 %
LES	+0.3 %	+1.5 %	−2.8 %	−0.4 %	−2.1 %	−3.3 %

microscales above $y^+ = 10$, which is now very close to the viscous sublayer and thus this mesh will match the typical resolution requirements.

Besides this discussion, the aim of using this hybrid RANS/LES is of course not to perform simulations on fully resolved meshes but to get good results and a consistent behavior on coarse meshes. Accordingly, mesh M3 can be treated as a reference mesh where a typical wall-resolved LES should produce good results. In fact it is found that already the base configuration using mesh M2 leads to accurate results.

The first criterion for the accuracy of the boundary layer flow is the quality of its mean velocity profile. In table 5.4 one can see, that first the EB-RSM RANS can predict the shape of the mean velocity profile with 3 % accuracy and that only the friction velocity u_τ is over-predicted by 4.6 %. The LES is then able to nearly reproduce the results of the RANS target fields but now the friction velocity, that is not imposed by ALF, is under-predicted by 3.3 %, i.e. a loss of approximately 8.0 % occurs between RANS and LES. This behavior is well confirmed by fig. 5.3.3 and fig. 5.3.4. While the unscaled velocity profiles nearly coincide, the wall-unit scaling highlights a mismatch of the log-layer due to the relatively large errors of u_τ. In fig. 5.3.5 one can see that three effects lead to these errors: First the streamwise u_τ development of the RANS shows overall high values (higher than the experimental result at $x_2 = 1210\,\mathrm{mm}$), second the mean friction velocity inside the ALF region $x \leq 1028\,\mathrm{mm}$ is lower than the RANS results and third a significant drop occurs at the transition from ALF to the unforced LES region. It has been found that a smooth blending between ALF and unforced LES does not improve these issues. Although the drop becomes smoother its absolute height remains unchanged, which supports the previous explanation. Finally it is seen that the mean friction velocity varies much stronger in the unforced LES region than in the ALF region. It is well known in the literature that the present SGS models lead to an under-prediction of u_τ on under-resolved meshes and accordingly a log- or buffer layer mismatch which is thus due to the LES and not necessarily due to ALF.

The next quality criterion that is enforced by ALF and strongly related to the wall pressure spectra are the mean stress profiles. Fig. 5.3.6 shows that first the EB-RSM RANS calculates slightly too high values for all four non-zero stress components in comparison to the experiment. Despite this small issue of the ALF target fields the mean stresses from the LES, except the $\overline{u_1'u_1'}$ component which is now under-predicted, collapse well with the experimental data. A convergence study needs to clarify whether this accordance is by coincidence or systematic. In terms of turbulence production and the quality of the wall pressure spectra the influence of the under-predicted $\overline{u'_1 u'_1}$ stress component is expected to be relatively weak as the first is significantly driven by the $\overline{u'_1 u'_2}$ component and the latter by the $\overline{u'_2 u'_2}$ component of the stresses. Normalizing the stresses is obtained with the anisotropic tensor $\mathbf{C} = (c_{ij})$ with

$$c_{ij} = \frac{\overline{u'_i u'_j}}{2k} - \frac{1}{3}\delta_{ij} \tag{5.1}$$

and the mean turbulent kinetic energy k in fig. 5.3.7 accordingly highlights that despite the small differences the anisotropy of the generated turbulence is well matched with the RANS and the experimental data inside the boundary layer. Only in the outermost regions of the boundary layer strong differences set in and indicate different turbulent states of the free stream within the two approaches and the experiment. However, any differences in these regions are expected to influence the wall pressure spectra only at very low frequencies, if they influence them at all. In agreement with these findings the wall pressure spectrum calculated by the LES at x_2 in fig. 5.3.8 is in excellent agreement with the experimental data up to 3.5 kHz. Above this frequency turbulent structures are not resolved and the power spectral density drops steeply. Besides the quality of the mean flow that potentially leads to this well matched wall pressure spectrum this result also shows that ALF is suited for these types of application and does not introduce a significant amount of numerical noise.

Another common measure to characterize the boundary layer state by the wall pressure in terms of second order statistics is the coherence, see also chapter 2.2. If the LES performs well an asymptotic fit of the coherence between different positions of the L-shaped array to the Corcos model, eq. (2.11), should be possible. In fig. 5.3.9a one can find the calculated streamwise coherence and in fig. 5.3.9b the spanwise coherence, respectively. Indicated in black is the exponential fit to the experimental data proposed by Hu.[51] For best comparison we calculate the frequency dependent convection velocity $u_c(\omega)$ for the spanwise coherence as in their apparent paper. It appears that the streamwise coherence drops a little bit faster than the experimentally found decay rate of 0.15 but the spanwise coherence is in generally good agreement with the experimental decay. Although these results indicate the good quality of the LES results they should be taken with care as the evaluated time signal is short.

Given the good quality of the baseline LES three questions need further clarification. (i) How do the results depend on the length of the ALF region? (ii) How is the drop and the overall level of the mean friction velocity affected by resolution and discretization? (iii) How good is convergence and can the hybrid RANS/LES deliver consistent results on under-resolved meshes? To answer these questions we present the results of a convergence study for the ALF length, the discretization schemes, the spatial resolution and the temporal resolution.

ALF region length

In [23] it was shown that an ALF region with length $L_{\mathrm{ALF}} = 5\delta$ can produce good

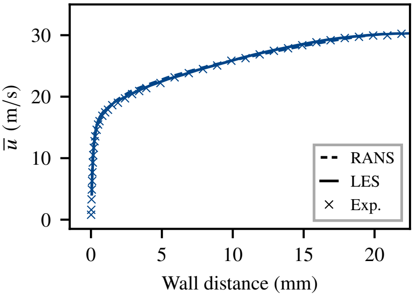

Fig. 5.3.3 Unscaled mean velocity profiles of the ZPG baseline LES at $x_2 = 1210\,\mathrm{mm}$.

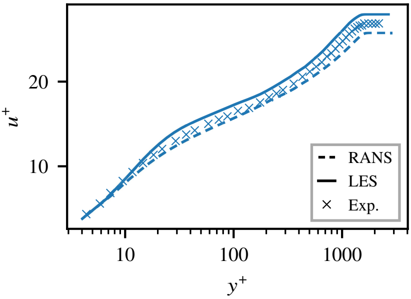

Fig. 5.3.4 Mean velocity profiles of the ZPG baseline LES at $x_2 = 1210\,\mathrm{mm}$ scaled with the mean friction velocity u_τ.

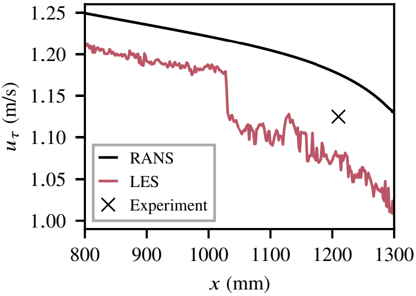

Fig. 5.3.5 Streamwise distribution of the mean friction velocity u_τ of the ZPG baseline LES.

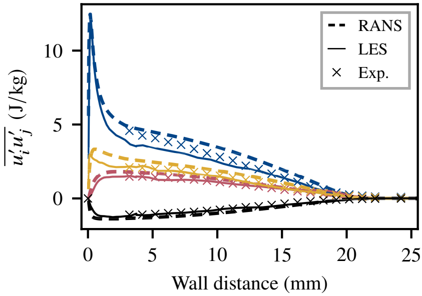

Fig. 5.3.6 Reynolds stresses of the ZPG baseline LES at $x_2 = 1210\,\mathrm{mm}$.

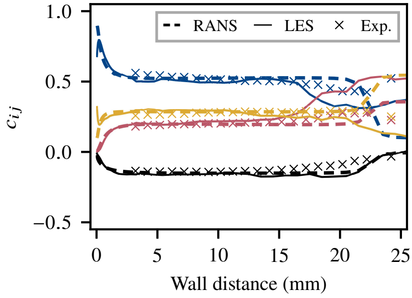

Fig. 5.3.7 Anisotropic tensor components c_{ij} of the ZPG baseline LES at $x_2 = 1210\,\mathrm{mm}$.

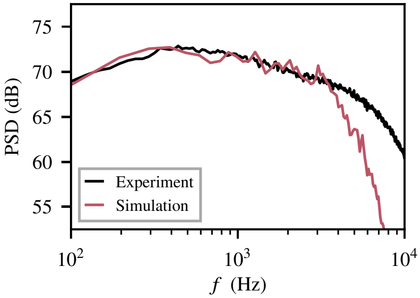

Fig. 5.3.8 Wall pressure spectrum of the ZPG baseline LES at $x_2 = 1210\,\mathrm{mm}$.

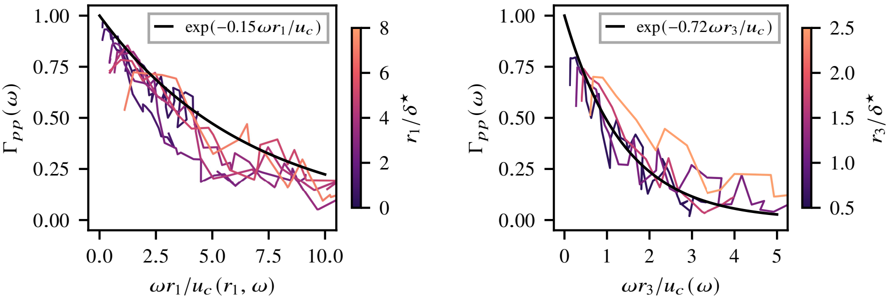

(a) Streamwise coherence.

(b) Spanwise coherence.

Fig. 5.3.9 Coherence of the baseline LES between different positions of the L-shaped array. Lines are colored by their underlying sensor distance normalized with the displacement thickness δ^*

results for a turbulent channel flow. In the case of a growing ZPG boundary layer it is still possible to estimate the boundary layer thickness depending on the streamwise position. As described before we compare four different cases with $L_{\mathrm{ALF}} \in \{5\delta, 10\delta, 15\delta, 22\delta\}$ with the longest being the previous baseline case. In fig. 5.3.10 one can see, that the level of the friction velocity inside the ALF region is not affected by its length, however the levels downstream depend on the ALF length L_{ALF} with smaller values tending to a larger drop. Although the mean friction velocity is not completely converged this indicates that the state of the synthetic turbulence differs between the different variants. In fig. 5.3.12 one can see, that turbulent kinetic energy is lost above the logarithmic layer for short ALF region lengths while the level of the near wall peak remains constant at all variants. Although there is still a difference between $L_{\mathrm{ALF}} = 15\delta$ and $L_{\mathrm{ALF}} = 22\delta$ the results are already quite similar. As the local mean flow velocity changes rapidly within the boundary layer one can conclude, that the time a particle that follows a mean streamline of the boundary layer is exposed to the artificial volume force depends on the wall distance of the streamline. While the effective time might be sufficient in the viscous sublayer this is not necessarily true further away from the wall. Such significant losses above the logarithmic layer are expected to significantly affect the wall pressure spectra. Fig. 5.3.14 shows that in fact the level of the frequencies below 2 kHz depends significantly on L_{ALF} with larger losses of turbulent kinetic energy leading to lower power spectral densities. Again a length of $L_{\mathrm{ALF}} = 15\delta$ already produces good and accurate results. In contrast to [23] it is thus found that L_{ALF} is not universal and needs to be prolonged compared to turbulent channel flows.

Discretization scheme

The CFD code Star-CCM+ gives the possibility to use different temporal and spatial discretization schemes. While the baseline LES utilizes a 3$^{\mathrm{rd}}$ order MUSCL/CD3 scheme

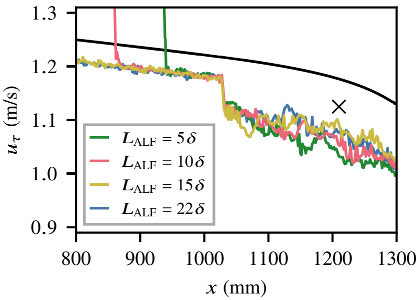

Fig. 5.3.10 Streamwise distribution of the mean friction velocity u_τ. Comparison of different ALF lengths L_{ALF} to RANS (black) and experiment (×).

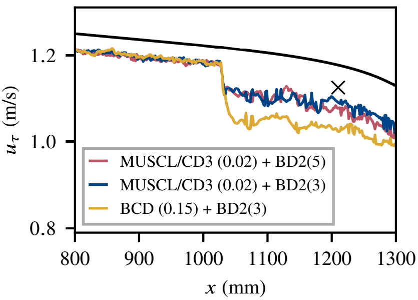

Fig. 5.3.11 Streamwise distribution of the mean friction velocity u_τ. Comparison of discretization schemes to RANS (black) and experiment (×).

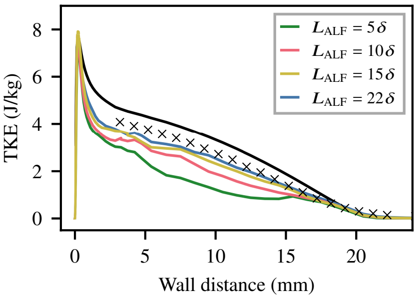

Fig. 5.3.12 Turbulent kinetic energy profiles at x_2. Comparison of different ALF lengths L_{ALF} to RANS results (black) and experiment (×).

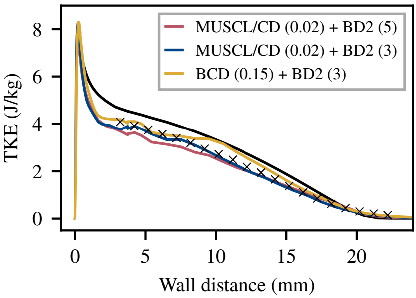

Fig. 5.3.13 Turbulent kinetic energy profiles at x_2. Comparison of discretization schemes to RANS results (black) and experiment (×).

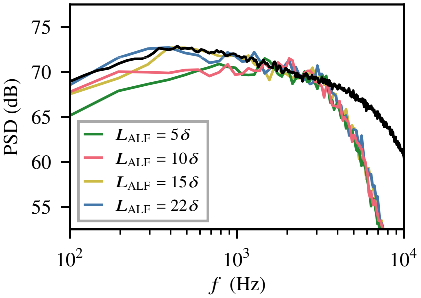

Fig. 5.3.14 Wall pressure spectra at x_2. Comparison of different ALF lengths L_{ALF} to experimental data (black).

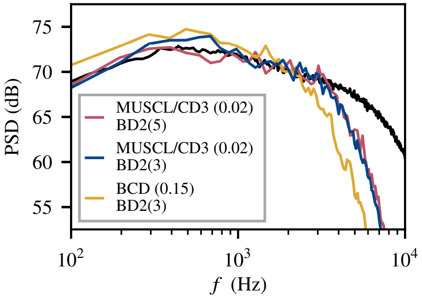

Fig. 5.3.15 Wall pressure spectra at x_2. Comparison of discretization schemes to experimental data (black).

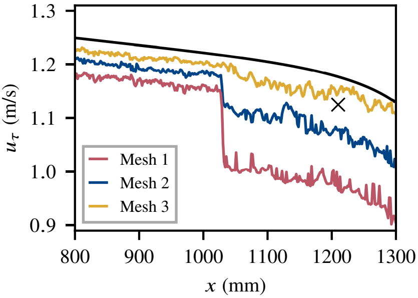

Fig. 5.3.16 Streamwise distribution of the mean friction velocity u_τ. Comparison of the different meshes to RANS (black) and experiment (×).

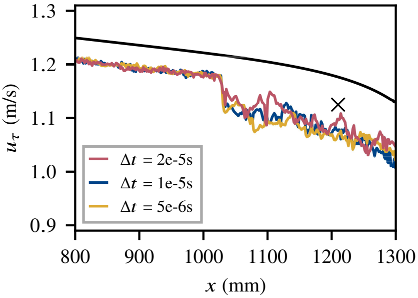

Fig. 5.3.17 Streamwise distribution of the mean friction velocity u_τ. Comparison of the different time-steps to RANS (black) and experiment (×).

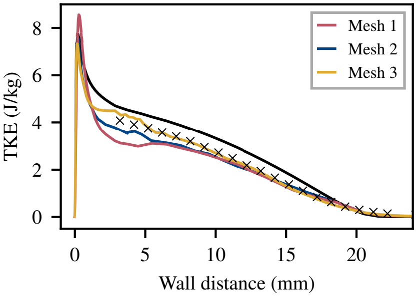

Fig. 5.3.18 Turbulent kinetic energy profiles at x_2. Comparison of the different meshes to RANS (black) and experiment (×).

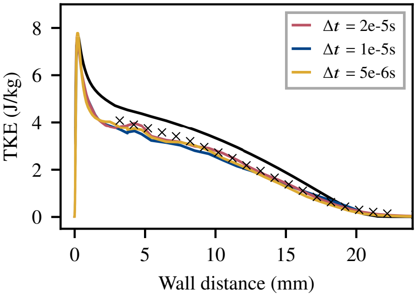

Fig. 5.3.19 Turbulent kinetic energy profiles at x_2. Comparison of the different time-steps to RANS (black) and experiment (×).

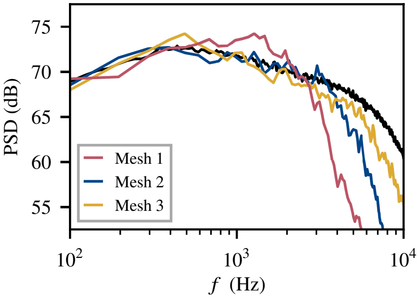

Fig. 5.3.20 Wall pressure spectra at x_2. Comparison of the different meshes to experimental data (black).

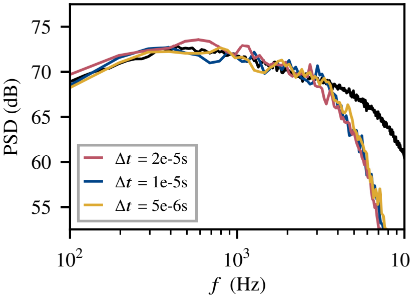

Fig. 5.3.21 Wall pressure spectra at x_2. Comparison of the different time-steps to experimental data (black).

with blending factor 0.02 in space and a five step 2$^{\mathrm{nd}}$ order backward differencing scheme in time we additionally compare the results to a standard three-step BD2 scheme in time and a 2$^{\mathrm{nd}}$ order bounded central scheme (blending factor 0.15) in space based on mesh M2 and time-step Δt_2. For a description of the schemes see also appendix A. While the temporal discretization does not significantly affect the friction velocity, the lower order spatial discretization yields a doubled drop height at the ALF/LES transition, see fig. 5.3.11. Interestingly the lower order scheme leads to slightly increased turbulent kinetic energy levels above the logarithmic region 5.3.13. Consequently the wall pressure levels below 2 kHz are slightly higher than those of the baseline LES, see fig. 5.3.15. Additionally the high-frequency drop of the 2$^{\mathrm{nd}}$ order BCD scheme is lowered to approximately 2 kHz, i.e. the resolution capabilities of the turbulent eddies is reduced. Nevertheless the influence of the discretization scheme is much smaller than the ALF length and switching to more stable schemes seems appropriate if better stability is required.

Spatial and temporal resolution

In this section we compare the results from the three meshes M1, M2 and M3 and the three time-steps Δt_1, Δt_2 and Δt_3, which generally show a very consistent picture. In fig. 5.3.16 it is seen that both the level of the mean friction velocity inside the ALF region as well as the drop at the ALF/LES transition depend strongly on the mesh resolution. Overall the levels get much closer to the results from the EB-RSM RANS and the experimental data as the resolution increases towards the fully resolved mesh M3. Contrarily the time-step influence on u_τ can be neglected, see fig. 5.3.17. Again the turbulent kinetic energy increases with increased mesh resolution and matches the experimental data at mesh M3 (fig. 5.3.18) but the influence of the time-step size is negligible (fig. 5.3.19). As found in fig. 5.3.20 the wall pressure spectra however depend strongly on the mesh resolution. While the overall levels of mesh M2 and mesh M3 are very comparable, the high-frequency drop of mesh M3 is shifted to much higher frequencies. As more turbulence is resolved by this mesh the spectrum seems to be a bit more noisy and thus a longer evaluation time might be indicated, which would again increase the computational costs. In contrast the wall pressure spectrum of the coarsest mesh M1 does not match the experimental data. Again the influence of the time-step size is negligible (see fig. 5.3.21).

In summary the hybrid RANS/LES based on ALF introduces three degrees of flexibility for the simulation of ZPG boundary layers, N_{EWA}, τ_v and τ_r. It can be run stably and consistently on slightly under-resolved meshes, a much coarser time-step can be used than indicated by Choi and Moin[16] and the size of the computational domain for the LES is significantly reduced as the region of interest needs to be extended upstream by approximately 15δ.

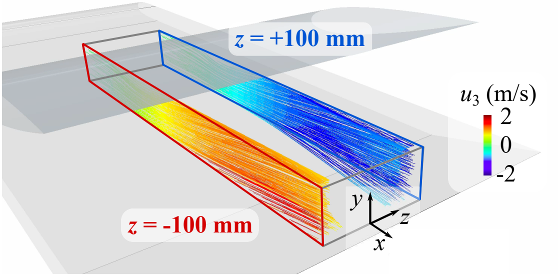

Fig. 5.3.22 Streamlines of EB-RSM showing the non-negligible three dimensional inflow into the outlined LES sub-domain with a maximum spanwise velocity magnitude up to $0.1u_0$. (Geometry is clipped for visualization), edited from [31]

5.3.2 APG-10

In this section we will analyze the performance of the EB-RSM/ALF hybrid RANS/LES method for the APG-10 case by again comparing the calculated Reynolds stresses and wall pressure spectra to the experimental data measured at x_2.

Running the EB-RSM RANS of the APG-10 case an important characteristic observed is the three-dimensionality of the flow in the APG region below the NACA-0012 airfoil (see fig. 5.3.22), with significant inflow from the sides into the LES sub-domain, which increases the complexity of the case. As shown in fig. 5.3.23, the boundary layer is subject to very different flow conditions. Starting nearly from ZPG conditions, the flow first gets significantly accelerated and then slows down leading to a thickening of the boundary layer. The main purposes of this analysis are thus the questions how ALF can be applied to such a more complex situation and how accurate and robust the results will be, respectively.

Besides this complexity the hybrid RANS/LES based on mesh M2 and time-step Δt_2 gives relatively accurate predictions of the mean velocity boundary layer profiles summarized in table 5.5 and fig. 5.3.24. While the data of the EB-RSM RANS show some significant errors of the momentum and displacement thickness, especially at x_1, the results of the LES are much

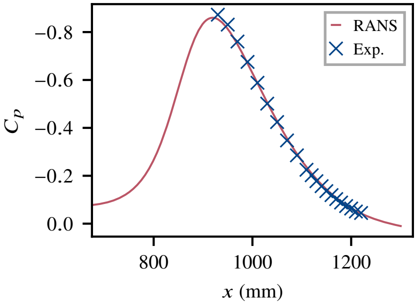

Fig. 5.3.23 Pressure distribution along of the upper surface of the flat-plate ($z = -45$ mm).

improved and, especially at x_2, excellently match the experimental values. Nevertheless in this case the accuracy of the method is reduced compared to the ZPG case and especially changes of the side inflow between RANS and LES could lead to mass changes inside the boundary layer and help to explain the drastic changes between RANS and LES. We thus forego an analysis of the wall scaled velocity profiles.

The streamwise distribution of the mean friction velocity from fig. 5.3.27 shows a comparable behavior as in the ZPG case. The EB-RSM tends to over-predict the experimental data at x_1 and x_2, the LES does not reach the RANS level inside the ALF region and at the ALF/LES transition an immediate drop occurs. However downstream of this transition the gradient of the LES results is less steep than the RANS result and the LES also over-predicts the experimental data. Additionally it is found that the calculated wall pressure spectra at both x_1 and x_2 as well as the stream- and spanwise coherence of the wall pressure field match the experimental data very well, see fig. 5.3.25, 5.3.28, 5.3.29. Under-resolution of the boundary layer fluctuations leads to a steep high-frequency cut-off of the wall pressure spectra at 2.5 kHz. As shown in fig. 5.3.26 the Reynolds Stresses of the LES match the experimental data very well, but the stresses from the EB-RSM, that are used more upstream as target fields for the ALF, significantly over-predict the experimental data. It might thus be possible that a compensation effect between the EB-RSM over-prediction and possible LES under-resolution leads to the present results.

Table 5.5 Relative errors of the boundary layer parameters of the base configuration (mesh M2, Δt_2) at x_1 and x_2 compared to the experiment.

	u_e	δ	δ^*	θ	H
Experiment (x_1)	32.0 m/s	23.0 mm	5.09 mm	3.12 mm	1.63
RANS	+1.0 %	0.0 %	−10.0 %	−7.0 %	−3.0 %
LES	+0.5 %	0.0 %	−5.9 %	−3.8 %	−1.8 %
Experiment (x_2)	30.4 m/s	28.7 mm	7.68 mm	4.39 mm	1.75
RANS	−0.3 %	+1.0 %	−5.2 %	−3.3 %	−1.1 %
LES	−1.1 %	+1.0 %	+1.0 %	−0.5 %	+1.1 %

Due to the different flow conditions and the severe acceleration below the airfoil an explanation of the EB-RSM and LES differences is not trivial. As shown previously the quality of the EB-RSM stresses is much better under ZPG conditions which are present upstream of the flow's acceleration area and the quality of the data inside this area is simply unknown. As ALF is applied upstream of the APG area it is thus at least principally possible that its target fields are more accurate than the stresses at x_2 indicate. Consequently the results of the LES must not necessarily be affected by the APG area EB-RSM simulation results.

To understand the interaction between EB-RSM and LES we perform a time-step, mesh and discretization scheme convergence study of the LES cases. Fig. 5.3.30 and 5.3.31 show again a similar behavior of u_τ to the ZPG case. While increased mesh resolution reduces the drop height at the ALF/LES transition and increases the levels in the ALF region, the distribution is independent from the time-step size. It is found that the gradient $\partial u_\tau / \partial x$ in the unforced LES region is also depending strongly on the mesh resolution and gets steeper as resolution increases. Fig. 5.3.32 and 5.3.33 prove that the turbulent kinetic energy (TKE) calculated from the LES is also completely independent from the time-step size and that the results from the meshes M2 and M3 are already very close to each other. Convergence of the common resolved frequency range of the wall pressure spectra, fig. 5.3.34 and 5.3.35, is also very good, which indicates that our results with the base setup is in fact mesh and time-step independent in this range. Analysis of a discretization scheme convergence study similar to the ZPG case shows that both TKE, see fig. 5.3.38, and wall pressure spectra, see fig. 5.3.40, are independent from the order of accuracy. Only the streamwise u_τ distribution shows a similar behavior as for changed mesh resolutions which thus can be considered consistent (fig. 5.3.36). As in the unforced LES region both the time-step sizes and the mesh resolution fall into the recommended ranges for wall-resolved LES from the literature[16,78] we can thus assume that numerical dissipation and dispersion can be ruled out as the main reasons for the improved results from the base LES compared to the EB-RSM.

Another factor possibly influencing the quality of our LES results is the position of the ALF region. To study the influence of different forcing types we introduced two additional alternative forcing regions shown in fig. 5.2.4. In the first, ALF is only applied upstream of the NACA-0012 profile, thus both acceleration and relaxation of the boundary layer must be resolved by the LES, while in the second, the ALF region is prolonged until $x \leq 1169\,\text{mm}$. Fig. 5.3.37, 5.3.39 and 5.3.41 show that the prolonged ALF region leads to equivalent results for the streamwise u_τ distribution, the wall pressure spectra as well as the TKE as our base case. But it is also seen that forcing only upstream of the NACA-0012 profile is not sufficient to capture the physics of the flow. A significant reduction of the Reynolds stresses and thus reduced levels of the wall pressure spectra occur.[53] It is seen that the unforced LES in this case is not capable to reach correct friction velocity levels in the acceleration area, which is achieved if ALF is applied in this area. Thus it seems that ALF helps to overcome the spatial and temporal resolution issue in the area of high friction velocities but the results are independent of the position of the ALF region.

Apart from the particular choice of the ALF region and the spatial and temporal resolution it is necessary to study how the ALF target fields, calculated with the EB-RSM, influence the LES results. To understand this influence, we study two different test cases: First we also apply ALF globally (see fig. 5.2.4) and second we linearly scale the ALF target fields such that they match the experimental data at x_2 and compare the results of both the base case as well as the globally forced case. Using global forcing the TKE of the LES is much closer to the original EB-RSM result although its level is not fully reached, see fig. 5.3.39. As the TKE is much higher than the experimental value, an over-prediction in the frequency range below 2 kHz is found in fig. 5.3.41. If the target levels are scaled to the experimental data (see fig. 5.3.42) one can see, that for the globally forced case the realized TKE is significantly lower, with the total loss of energy

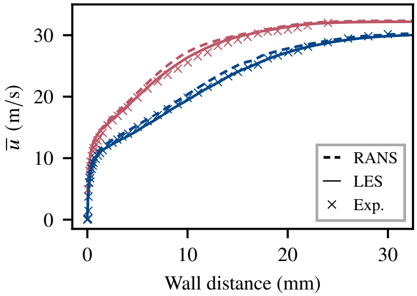

Fig. 5.3.24 Mean velocity profiles of the APG-10 baseline LES at x_1 (red) and x_2 (blue).

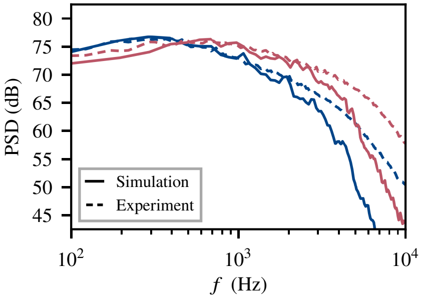

Fig. 5.3.25 Wall pressure spectra of the APG-10 baseline LES at x_1 (red) and x_2 (blue).

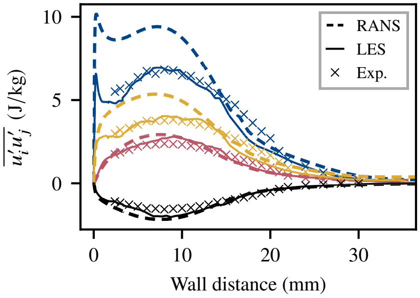

Fig. 5.3.26 Reynolds stresses of the APG-10 baseline LES at x_2.

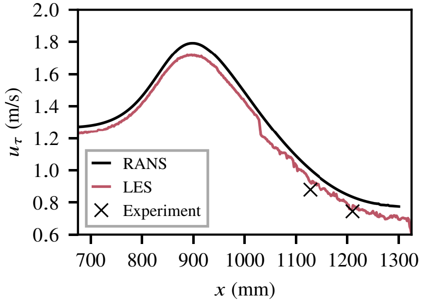

Fig. 5.3.27 Streamwise distribution of the mean friction velocity u_τ of the APG-10 baseline LES.

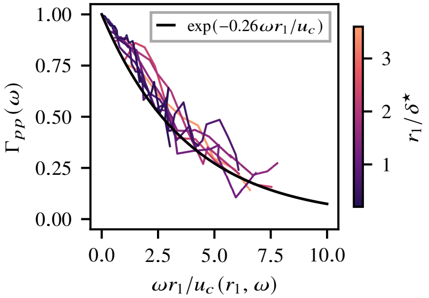

Fig. 5.3.28 Streamwise coherence of the APG-10 baseline LES.

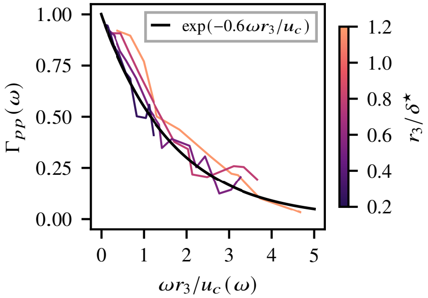

Fig. 5.3.29 Spanwise coherence of the APG-10 baseline LES.

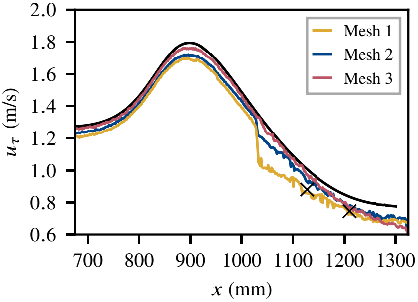

Fig. 5.3.30 Streamwise u_τ distribution from LES variants with $\Delta t = 1 \times 10^{-5}$ s, EB-RSM (black) and experiment (×) at x_2.

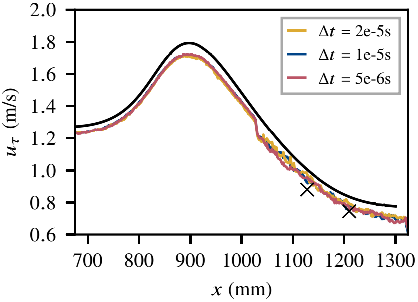

Fig. 5.3.31 Streamwise u_τ distribution from LES variants with Mesh 2, EB-RSM (black) and experiment (×) at x_2.

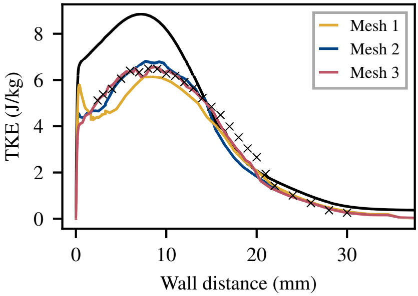

Fig. 5.3.32 TKE from LES variants with $\Delta t = 1 \times 10^{-5}$ s, EB-RSM (dashed) and experiment (×) at x_2.

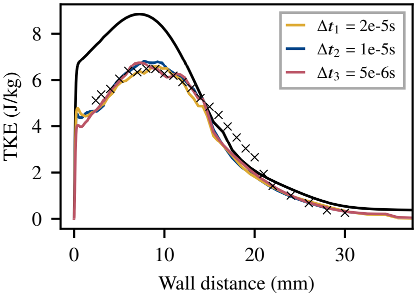

Fig. 5.3.33 TKE from LES variants with Mesh 2, EB-RSM (dashed) and experiment (×) at x_2.

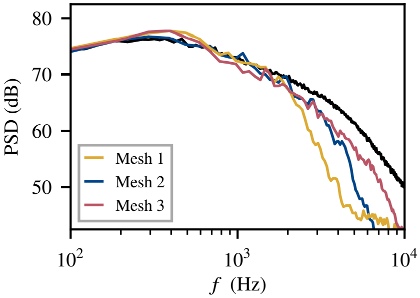

Fig. 5.3.34 Wall pressure spectra from LES variants with $\Delta t = 1 \times 10^{-5}$ s and experiment (black) at x_2.

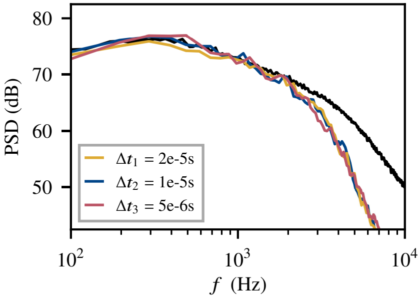

Fig. 5.3.35 Wall pressure spectra from LES variants with Mesh 2 and experiment (black) at x_2.

corresponding to the original behavior, but the TKE of the base LES remains nearly unchanged. This indicates, that the influence of relaxation due to the diffuser effect of the NACA-0012 airfoil on the LES solution at x_2 is much stronger than the influence of the ALF target fields more upstream. This behavior is supported by the fine mesh in the unforced LES region that would be sufficient to run a wall-resolved LES. Consequently, the wall pressure spectrum at x_2 (fig. 5.3.43) barely changes at all while the globally forced spectrum is lowered by about 3 dB.

We can thus summarize that the boundary layer at x_2 calculated with the base setup of our EB-RSM/ALF method is not influenced by compensation effects between EB-RSM stress over-prediction and an LES under-prediction due to poor mesh-resolution and that the studied method provides good results. The relaxation due to the diffuser effect of the NACA-0012 airfoil dominates the boundary layer development in the APG area in this particular case and thus introduces some robustness against uncertainties in the forcing. Accordingly, ALF can be used to overcome resolution restrictions due to strong acceleration regions.

However requiring the knowledge of all Reynolds stresses imposes a strong constraint for the application of the method to industrially relevant cases, as the EB-RSM is difficult to handle on such cases.[83] We thus also applied the forcing to our base case in an isotropic manner, only prescribing the isotropic components of the turbulent kinetic energy on the diagonal elements of the stress tensor, which is certainly more unphysical than the original formulation. It can be seen in fig. 5.3.44 and fig. 5.3.45 that this kind of forcing introduces an over-prediction of turbulent kinetic energy in the middle height of the boundary layer and that the wall pressure spectrum is thus slightly too high at low frequencies. Surprisingly these differences are not extremely severe, indicating that the isotropic synthetic turbulence relaxes towards a more physical state downstream of the ALF region. The friction velocity u_τ in fig. 5.3.46 nevertheless shows a clear difference between the two forcing types as in case of isotropic forcing u_τ is drastically over-predicted inside the ALF region. At the transition between ALF and pure LES a severe drop occurs and the level relaxes towards the values of the other simulations more downstream.

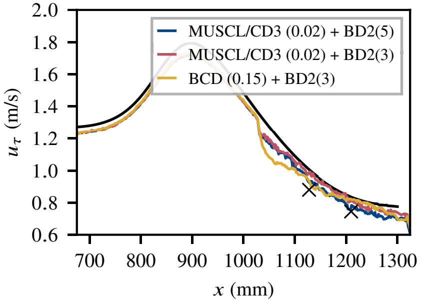

Fig. 5.3.36 Streamwise u_τ distribution from LES variants, EB-RSM (black) and experiment (×) at x_2.

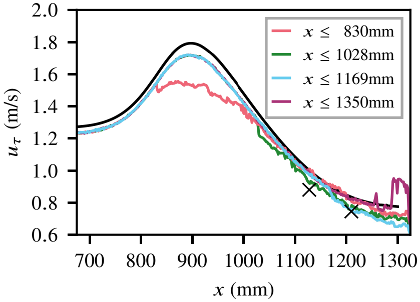

Fig. 5.3.37 Streamwise u_τ distribution from LES variants, EB-RSM (black) and experiment (×) at x_2.

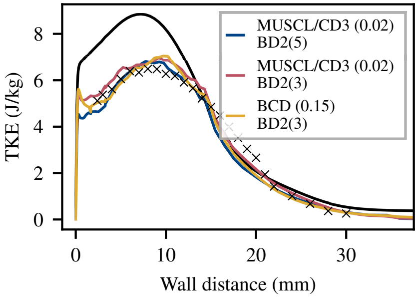

Fig. 5.3.38 TKE from LES variants, EB-RSM (dashed) and experiment (×) at x_2.

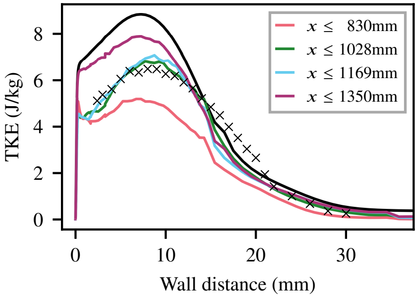

Fig. 5.3.39 TKE from LES variants, EB-RSM (dashed) and experiment (×) at x_2.

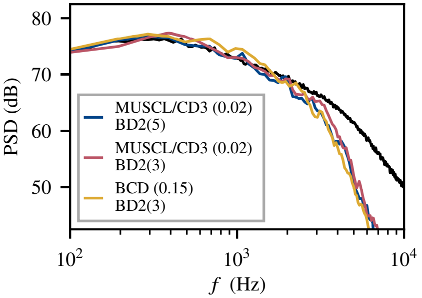

Fig. 5.3.40 Wall pressure spectra from LES variants and experiment (black) at x_2.

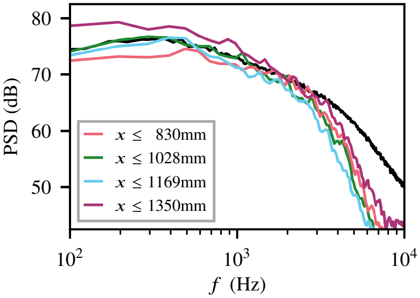

Fig. 5.3.41 Wall pressure spectra from LES variants and experiment (black) at x_2.

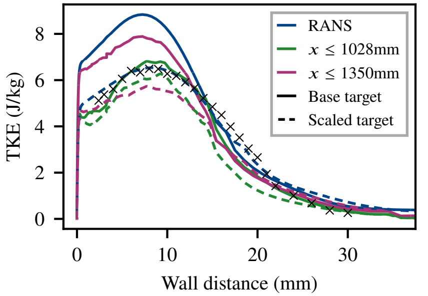

Fig. 5.3.42 TKE comparison of EB-RSM and LES with original (solid) and scaled (dashed) target stresses with experiment (×) at x_2.

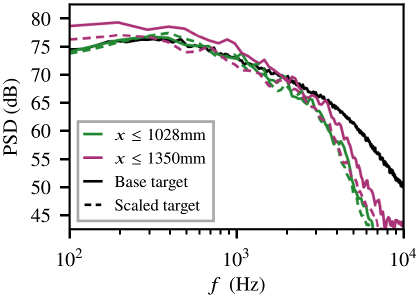

Fig. 5.3.43 Wall pressure spectra of experiment (black) and LES with original (solid) and scaled (dashed) ALF target stresses at x_2.

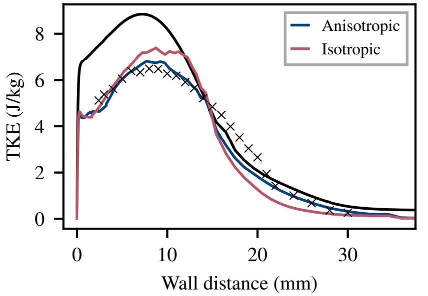

Fig. 5.3.44 TKE comparison of base LES with ALF, base LES with isotropic linear forcing EB-RSM (dashed) and experiment (×) at x_2.

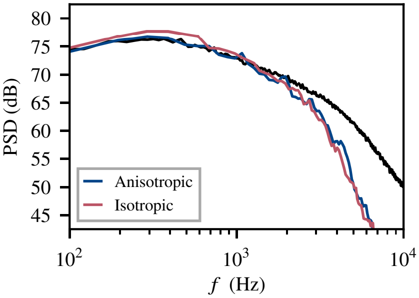

Fig. 5.3.45 Wall pressure spectra comparison of base LES with ALF, base LES with isotropic linear forcing and experiment (black).

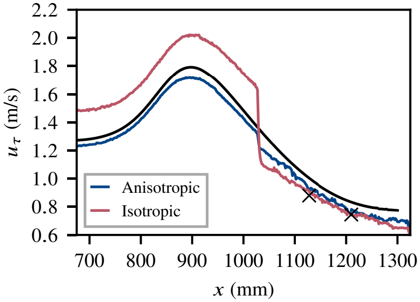

Fig. 5.3.46 Streamwise u_τ distribution from isotropic and anisotropic forcing, EB-RSM (black) and experiment (×) at x_2.

5.4 Summary

In this chapter we studied the applicability of a hybrid RANS/LES method based on ALF to typical turbulent boundary layer dominated ZPG and APG cases from experiments by Hu and Herr.

Based on the preliminary works by de Laage de Meux[23] application of ALF to ZPG boundary layer cases is rather straightforward. On meshes that must be considered slightly under-resolved in terms of a wall-resolved LES we found that the methodology produces accurate results for forcing lengths $L_{\mathrm{ALF}} \geq 15\delta$. Additionally, if the ALF region is close to the region of interest a relatively large time-step size can be chosen to achieve consistent results. A present restriction of the method is a potential mismatch of the log-layer compared to experimental data as both the friction velocity does not reach correct levels inside the ALF region if under-resolved meshes are used and as a significant drop at the ALF/LES transition occurs due to the LES subgrid scale models' sensitivity towards under-resolution. However these errors were limited to the log layer region and did not influence the boundary layer parameters too significantly. In cases where a precise prediction of the log layer is required we want to stress that results must be taken with caution if coarse meshes are used.

In our study of the APG-10 case we found that the stresses calculated by the EB-RSM are not accurate in the APG zone – nevertheless the LES produced very good results. Analysis of the LES confirmed that compensation effects between EB-RSM and LES errors can be ruled out as a reason. Our analysis indicates both that the EB-RSM stresses upstream of the NACA-0012 airfoil are more accurate and that the LES itself is quite robust to errors in the acceleration region below the airfoil as the airfoil's influence on the downstream development is strong and the mesh resolution in this area was sufficient. In our case ALF helps to consistently overcome spatial resolution issues in the acceleration area of the LES sub-domain and thus we conclude that ALF should be applied in such regions. The resulting wall pressure spectra are mesh-independent in the common resolved frequency range. Even if the forcing is applied isotropically, the resulting fields rapidly relax towards an anisotropic behavior.

In summary the utilized EB-RSM/LES method can be applied successfully and consistently to ZPG cases as well as three-dimensional APG cases and produces very good results even under robust low order discretization schemes. Additionally, the method drastically reduces the resolution restrictions of a typical wall-resolved LES and the required size of the LES domain without introducing too many arbitrary case-dependent model parameters.

6 Study of an Idealized Rear Door Gap Model I – Analysis and Simulation of the Reference Case

In the previous chapter we showed that the proposed hybrid RANS/LES methodology based on the EB-RSM turbulence model and ALF can be used to simulate unsteady turbulent boundary layer flows in an efficient manner, which is a mandatory property to capture the inflow conditions for automotive door gaps. Nevertheless the method's applicability to simulate the gap noise depending on the boundary layer fluctuations is still an open question. As the computational costs of a full-scale vehicle simulation are expected to be high and the flow situation in this case will be difficult we will now describe an idealized gap noise experiment that was carried out in DLR's acoustic wind tunnel AWB and numerical simulations of different cases.

With the idealized experiment described in this chapter we want to address three major tasks and open questions: (i) The experiment should principally resemble automotive gap noise physics on a smaller scale while providing as simple flow conditions as possible. (ii) The experiment should allow a direct validation of aeroacoustic gap noise phenomena without introducing new modeling uncertainties. (iii) The experimental setup should be modular such that different relevant inflow conditions as well as common geometrical variations of the gap can be studied separately. It should thus provide precise insights into the physical mechanisms of automotive gap noise and establish a first connection to the full-scale application. Consequently, such an experiment will be suited to precisely study the general capabilities of numerical methods for gap noise simulations and especially to develop a simulation setup for the proposed hybrid RANS/LES that can be applied to the more complex full-scale vehicle model. Furthermore it should then be possible to understand the method's capabilities to predict relevant design modifications, which will be an essential requirement for industrial application.

The following experimental analysis of the experiment's base case in chapter 6.2 and the numerical simulations shown in chapter 6.3 are based on the conference paper *Experimental and Numerical Study of Passive Gap Noise* published in the proceedings of the 2018 AIAA/CEAS Aeroacoustics Conference.[30]

6.1 Experimental Setup and Measurement Techniques

The experimental study was carried out in the anechoic test section of the Acoustic Windtunnel Braunschweig (AWB). As described in chapter 5 the wind tunnel has a rectangular nozzle with a height of 1200 mm and a width of 800 mm. Its general aeroacoustic properties are described in [81].

Comparable to the experiment by Hu and Herr, [51], the central element of this study is an 80 mm thick flat plate that was placed 10 mm downstream of the nozzle's exit in the mid-height nozzle position. On the upper surface of the flat plate one can find the opening of a modular, aluminum built 50 mm deep cavity gap as well as two additional pressure measurement modules. The plate itself was made from Ureol MB 600 and it was 1775 mm long, 1400 mm wide and its surface was aligned with the flow direction. The nose of the flat plate had a super-elliptic shape ($n = 3$) and both sides of the plate were tripped 100 mm downstream of the leading edge using 0.2 mm thick zigzag tape. The bottom side of the plate had a 12° beveled trailing edge that was extended with foam serrations. Compared to the experiments by Hu and Herr our flat plate is thicker to ensure enough space for the cavity, it is longer as the microphones used inside the cavity require relatively much space downstream of the cavity and it is wider as we still want to avoid vortical mixing of the open-jet's shear layer. In their experiments this setup led to an attached zero pressure gradient turbulent boundary layer on the upper surface of the plate. As we maintained the general shape of the plate's nose this behavior is also expected in our experiment. The setup of the plate model inside the wind tunnel can be found in fig. 6.1.1.

In addition to this basic setup we also used the technique from their paper to enforce pressure gradients on the upper surface of the plate: A rotatable NACA-0012 airfoil with chord length $c = 400$ mm and spanwidth 1800 mm was placed above the plate.[51] Its rotation axis was located at $0.41c$ and the airfoil was movable in the streamwise direction. During all measurements that involved the NACA-0012 profile the flat plate's vertical position was increased by 30 mm and the airfoil's rotation axis was placed 100 mm above the plate's upper surface. The configuration with the NACA-0012 airfoil can be seen in fig. 6.1.2.

In the following we will always describe the streamwise direction by the coordinate x, with the leading edge of the flat plate positioned at $x = 0$, the spanwise direction by z, with $z = 0$ in the symmetry plane and the wall-normal direction with y, where $y = 0$ at the upper surface of the flat plate.

In the experiment we measured the pressure inside the cavity, the hydrodynamic wall pressure spectra, and the static pressure in stream- and spanwise directions with the three independent

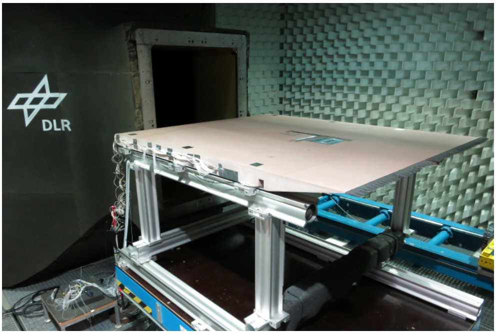

Fig. 6.1.1 Setup of the flat plate including the aluminum measurement modules inside the anechoic test section of AWB.

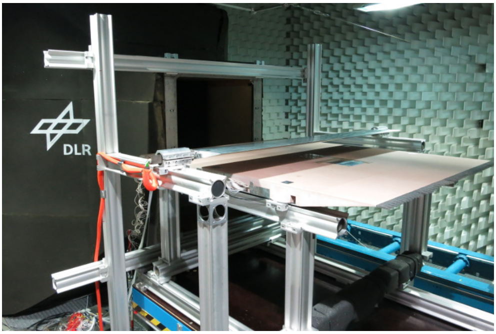

Fig. 6.1.2 Setup of the flat plate and the NACA-0012 airfoil for measurements including pressure gradients inside the anechoic test section of AWB.

aluminum panels mounted in the upper surface of the flat plate whose exact layout and position is shown in figure 6.1.3.

Gap module

The cavity had a spanwise dimension $W = 100\,\mathrm{mm}$ with its leading edge located at $x = 1200\,\mathrm{mm}$ downstream of the plate's leading edge. A cross section with all relevant labels, measures and shapes is presented in fig. 6.1.5a. The edges forming the cavity's opening are interchangeable and thus different opening lengths L_0, rounded and sharp edges, vertical offsets of the downstream edge and a change of the opening position can be realized, see fig. 6.1.4. Three B&K Type 4954-A microphones were flush-mounted 10 mm above the cavity's bottom at a middle, quarter, and edge position of the downstream wall of the cavity's resonator volume (see fig. 6.1.5b).

Wall-pressure module

Directly upstream of the cavity nine differential Kulite pressure transducers, model XT-140M with B-screen, with an outer diameter of 2.54 mm were flush-mounted in an L-shaped array. The sensors in the spanwise direction were evenly spaced with a distance of 8 mm while the sensors in the streamwise directions had a distance of 8, 10, and 12 mm, respectively. The nine Kulite sensors in the wall-pressure module are numbered sequentially from 1-9 from the bottom right to the top left position (fig. 6.1.6a).

As the XT-140M pressure transducers are designed for threaded mounting we used Loctite 222 threadlocker to seal potential leakages below the surface of the aluminum module. The differential pressure tubes of the sensors were covered with silicone tubes to avoid the influence of slow pressure fluctuations inside of the flat plate, see fig. 6.1.6b. While the thread mounting gives the advantage of greater flexibility and a precise vertical mounting the thread opening and chamfer of the aluminum module introduces additional uncertainties to the relatively large diameter of the sensor itself. To address these specific uncertainties measurements have been performed that allowed a direct comparison to the measurements of Hu and Herr. It has been shown in much detail that good agreement with these measurements can be reached and that it is even possible to introduce an empirical correction to extend the reliable frequency range of the sensors up to $\omega\delta/u_0 = 20$ under zero pressure gradient conditions.[50] A brief overview of this correction and the comparison is shown in the following experimental analysis.

Static pressure ports module

The static pressure was measured in the span- and streamwise direction using pressure ports with a diameter of 0.6 mm (see fig. 6.1.3).

The sampling rate of the time-synchronous measurement of the Kulite sensors and the microphones was set at 50 kHz and the data were recorded for 60 s. A preamplifier with a gain factor of 250 and a high pass filter with cut-off frequency at 200 Hz was applied to the Kulite sensors and their data are corrected using the filter frequency response curve. The power and coherence spectra are calculated by Welch's method:[106] The total discrete signal length is composed of N successive windows of sample length M that overlap by $D < M$ samples. For all calculations a Hann window function

$$w(m) = \frac{1}{2}\left(1 - \cos\frac{2\pi m}{M-1}\right) \tag{6.1}$$

and the acoustic reference pressure $p_\text{ref} = 2 \times 10^{-5}$ Pa is used. Usually we show the spectra with a density scaling (power spectral density, PSD). While this approach leads to constant levels of broadband data, independent from the frequency resolution, the levels of sharp peaks will depend on the resulting frequency resolution. Using unscaled power spectra instead leads to an opposite behavior with frequency dependent broadband levels and constant peak levels. As the gap acoustics spectra are expected to incorporate both types of data neither choice is ideal. Consequently, the number of samples per window M and their overlap ${}^{D}/_{M}$ is stated separately any time experimental data is analyzed or compared to simulated data and compared spectra will always have identical frequency resolution.

The boundary layer mean flow velocity was measured 1 cm besides Kulite sensor no. 4 by a single-wire anemometer, see fig. 6.1.7. The measurement was performed along the wall normal line, with the first point being approximately 1 mm above the plate's surface. The data at each point were recorded for 20.4 s and we utilized a sampling rate of 50 kHz and a 20 kHz low pass filter. The first point was chosen such, that it was deep inside the logarithmic layer of the boundary layer for all flow configurations. For the further analysis of the boundary layer profile we extrapolated the data into the buffer layer and the viscous sublayer by following Knopp[60] who suggests that fitting

$$u^+ = (1-\phi)\, u^+_\text{Rei} + \phi u^+_\text{log}\,, \quad \text{with} \quad \phi = \tanh\left(\text{arg}^4\right) \quad \text{and} \quad \text{arg} = \frac{y^+}{27} \tag{6.2}$$

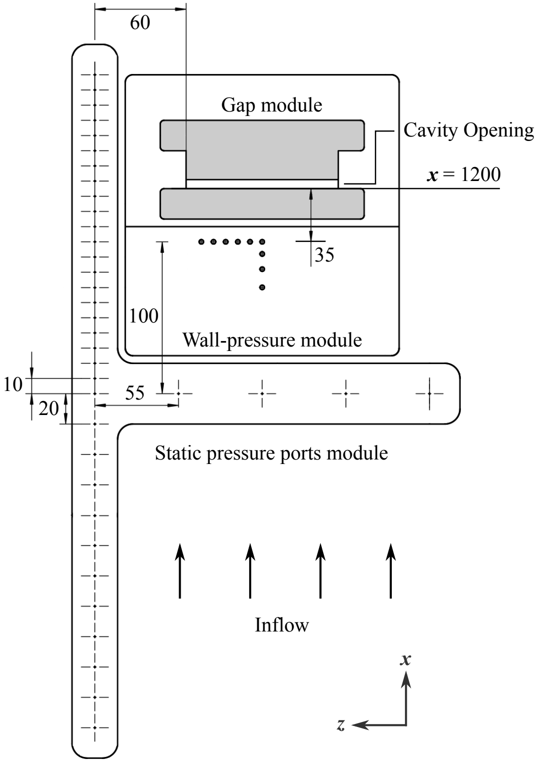

Fig. 6.1.3 Schematic drawing of the measurement modules. Measures are in millimeter. The nine Kulite sensors in the Wall-pressure module are numbered sequentially from 1-9 from the bottom right to the top left position.

Fig. 6.1.4 View of the gap's opening in a configuration with 2 mm vertical offset of the downstream edge. The mounting threads and gaps are masked with aluminum tape.

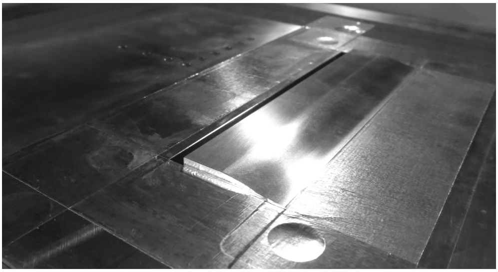

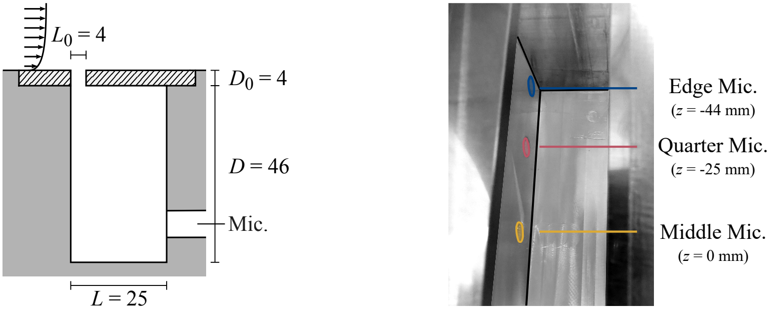

(a) Cross section of the studied cavity in a configuration with opening length $L_0 = 4$ mm and sharp edges. The boundary layer thickness corresponds to the measured δ value. Measures are in millimeter.

(b) View through a long gap opening on the three flush-mounted microphones.

Fig. 6.1.5 Experimental setup of the cavity module.

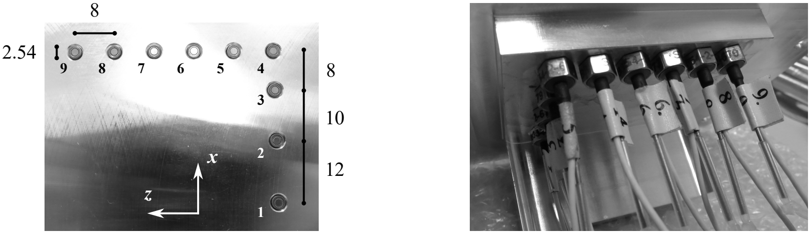

(a) Top view of the L-shaped Array of Kulite XT-140M sensors. Measures are in millimeter, bold numbers indicate the used enumeration of the sensors.

(b) Bottom side of the wall pressure module. The threads of the sensors are sealed with Loctite-222 and the reference pressure tubes are covered with silicone tubes.

Fig. 6.1.6 Experimental setup of the wall pressure module.

Fig. 6.1.7 View of the hot wire measurements close to Kulite sensor no. 4. The hot wire system is mounted on a traverse system with a long aluminum support cone.

with the log law

$$u^+_{\log} = \frac{\log y^+}{\kappa} + 5.1 \tag{6.3}$$

and Reichardt's law of the wall[82]

$$u^+_{\mathrm{Rei}} = \frac{\log\left(1 + \kappa y^+\right)}{\kappa} + 7.8\left[1 - e^{-y^+/11.0} - \frac{y^+}{11.0} e^{-y^+/3.0}\right] \tag{6.4}$$

to the measured data points inside the logarithmic layer leads to excellent matches with experimental data. Here $\kappa = 0.41$ denotes the Von Kármán constant.

6.2 Experimental Results

As a first step we analyze the physics of a defined base configuration at different free stream velocities u_0. In this base case we use the zero pressure gradient setup, the gap opening length $L_0 = 4\,\mathrm{mm}$ and sharp edges. The case provides very defined and simple flow conditions (zero pressure gradient, no pressure driven separation at the gap opening) but still resembles the geometric relations typically present at a vehicle. While the experimental opening length is a bit smaller than expected on a car also the boundary layer thickness in the experiment is much smaller than in reality ($\delta = 18.8\,\mathrm{mm}$, $\theta = 2.28\,\mathrm{mm}$ at $u_0 = 39.2\,\mathrm{m\,s^{-1}}$ in Hu's and Herr's comparable experiment[51]). In summary we thus expect $\theta/L_0 \approx 0.5$ at the gap's opening which should lead to a similar excitation mechanism than discussed in chapter 3 and described previously by Schimmelpfennig,[90] Wickern and Brennberger[107] and Illy et al..[55]

The measurements were performed at an operating velocity range $25\,\mathrm{m\,s^{-1}} \leq u_0 \leq 45\,\mathrm{m\,s^{-1}}$. To specify the flow conditions in front of the gap, its opening was masked with aluminum tape to avoid any influence of the gap on the upstream boundary layer development and the dimensionless static pressure c_p was measured with the static pressure ports module. It is found, that c_p has a maximum spreading $\Delta c_p \leq 0.01$ in the streamwise direction which indicates a zero pressure gradient condition. The spreading of c_p in the spanwise direction is below $\Delta c_p \leq 0.005$ confirming the two-dimensionality of the flow in the vicinity of the cavity. In addition, the hot wire measurement was performed at $u_0 = 40\,\mathrm{m\,s^{-1}}$ and further confirms that the inflow conditions are well described by a turbulent ZPG boundary layer (compare e.g. Eitel-Amor et al.[28]): $H = 1.38$, $\delta_{99} = 18.7\,\mathrm{mm}$, $\delta^* = 3.21\,\mathrm{mm}$, $\theta = 2.33\,\mathrm{mm}$, $u_\tau = 1.51\,\mathrm{m\,s^{-1}}$ with $\mathrm{Re}_\theta = 6310$ and $\mathrm{Re}_\tau = 1820$. Due to blockage effects, the chosen nozzle velocity leads to the local boundary layer edge velocity $u_e = 41.7\,\mathrm{ms^{-1}}$. Normalized velocity profiles of this measurement can be found in fig. 6.2.1.

With the data of the two-dimensional ZPG boundary layer it is possible to validate the signal of the utilized Kulite sensors that is influenced by the chosen mounting and the finite sensor size.[50] Therefore fig. 6.2.2a shows a comparison of the measured wall pressure spectrum at $u_0 = 40\,\mathrm{m\,s^{-1}}$ and two different corrections of the measured data with experimental results by

Hu & Herr[51] and Hu's empirical model,[52] eq. (2.19)

$$\frac{\phi(\omega)u_\tau}{Q^2\theta} = \frac{(81.004d + 2.154)\cdot 10^{-7}\cdot(\omega\theta/u_e)}{\left[(\omega\theta/u_e)^{1.5/h^{0.6}} + 0.07\right]^{1.13/h^{0.6}} + \left[7.645\mathrm{Re}_\tau^{-0.411}\cdot(\omega\theta/u_e)\right]^6} \quad , \qquad (6.5)$$

where $Q = 0.5\rho u_e^2$ denotes the dynamic pressure, $\log_{10} d = -5.8\cdot 10^{-5}\cdot \mathrm{Re}_\theta H - 0.35$ and $h = 1.169\log H + 0.642$ (c.f. section 2.2). The setup of Hu & Herr's experiments is very comparable to our setup (plate length 3.7 % longer, u_e 6.0 % smaller compared to our experiment) and thus a direct comparison of the data is valid. The two correction methods are the classical Corcos correction briefly discussed in chapter 2.2 that addresses a signal attenuation due to spatial averaging on a sensor's finite circular surface with uniform sensitivity.[18] For the Corcos correction assumptions of the effective radius of the sensor (in this case Kulite's B-screen) and the convection velocity are necessary. Under all possible combinations the results do not reach better accuracy than shown in fig. 6.2.2a where an over-prediction of the mid-frequencies is present and higher frequencies are still severely under-predicted in comparison to the reference data. The second correction method was developed in the framework of this comparison and discussed in [50]. It was found that the attenuation ϕ_m/ϕ of the measured spectrum ϕ_m in comparison to the actual spectrum ϕ (in this case the data from Hu & Herr) can be reasonably well described by

$$10\log_{10}\frac{\phi_m}{\phi} = 10\log_{10}\frac{a}{a+(\omega r/u_c)^b}\ , \quad \text{with} \quad a = 0.427 \quad \text{and} \quad b = 2.85. \qquad (6.6)$$

With this correction excellent agreement of the measured data with Hu's model and the data by Hu & Herr is reached, see fig. 6.2.2a. In addition, the streamwise coherence $\Gamma_{pp}(\omega, \boldsymbol{r})$ of the inflowing boundary layer should asymptotically follow Corcos' semi-empirical model, eq. (2.11)

$$\Gamma_{pp}(\omega, r_1, r_3) = \exp\left\{-\alpha_1\omega r_1/u_c\right\}\exp\left\{-\alpha_3\omega r_3/u_c\right\} \quad , \qquad (6.7)$$

where r_1 denotes the streamwise distance, r_3 the spanwise distance, u_c the frequency dependent convective velocity, $\omega = 2\pi f$ the angular frequency and α_1, α_3 are semi-empirical parameters.[19] It can be seen in fig. 6.2.2b that the measured data of the streamwise positioned Kulite sensors at $u_0 = 40\,\mathrm{m\,s^{-1}}$ collapse well with this model for the fitting parameter $\alpha_1 = 0.133$. Despite the finite diameter of the Kulite sensors it can be concluded that this experimental setup can be used to study the pressure fields resulting from the superposition of the incoming boundary layer and the acoustic radiation of the cavity. It is suitable to validate both the wall pressure and coherence spectra of our numerical simulations and in the following we will always show the wall pressure spectra corrected by eq. (6.6).

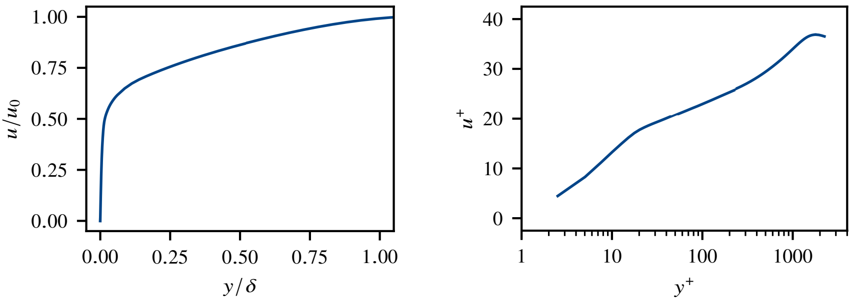

Fig. 6.2.1 Measured dimensionless velocity boundary layer profiles at the operating velocity $u_0 = 40\,\mathrm{m\,s^{-1}}$ scaled by the free stream (left) and wall (right) variables.

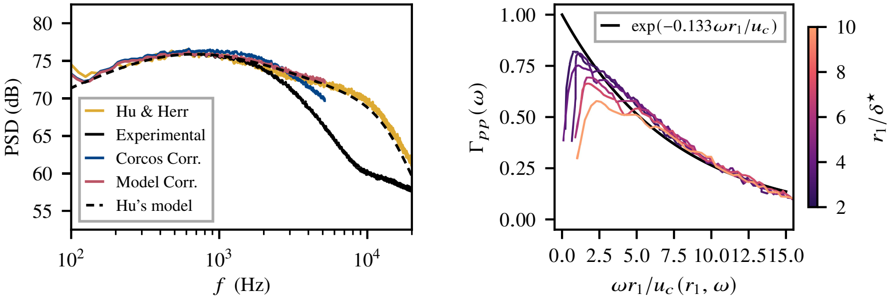

(a) Wall pressure spectrum of Kulite sensor 8 at $u_0 = 40\,\mathrm{ms^{-1}}$ in comparison to experimental data by Hu & Herr[51] and Hu's model.[52] The attenuation due to the sensor size is visible above 2 kHz. ($M = 2^{12}$, $D/M = 0.5$)

(b) Streamwise coherence $\Gamma_{pp}(\omega)$ at $u_0 = 40\,\mathrm{m\,s^{-1}}$ of the four longitudinal Kulite sensors in comparison to the Corcos model, eq. (6.7), with $\alpha = 0.135$. ($M = 2^{10}$, $D/M = 0.5$)

Fig. 6.2.2 Spectral analysis of the incoming boundary layer and comparison with experimental and semi-empirical data.

In the following the acoustic behavior of the cavity is analyzed: In fig. 6.2.3 the pressure spectrum of the edge microphone at five different operating velocities is shown. Positioned at the edge of the acoustically reflecting cavity, every possible resonance frequency of the cavity is detected by this microphone. It can be seen that all resonance frequencies below 10 kHz remain constant within the operating velocity range, thus confirming the results of Schimmelpfennig for a similar cavity.[90] Consequently, the presence of aeroacoustic feedback in the cavity opening can be ruled out and the detected velocity-independent resonance frequencies can be assigned to geometrical eigenfrequencies of the cavity that get excited by the turbulent boundary layer. In fig. 6.2.4 the pressure spectra of the three microphones are compared at $u_0 = 40\,\mathrm{m\,s^{-1}}$. As discussed by Wickern and Brennberger[107] and Schimmelpfennig[90] one can expect the Helmholtz resonance as well as different standing modes inside such types of rectangular cavities. The standing waves are usually roughly approximated by the eigenmodes of a fully reflecting cuboid with dimension $L \times D \times W$ and the speed of sound c

$$f = \frac{c}{2}\sqrt{\left(\frac{n_x}{L}\right)^2 + \left(\frac{n_y}{D}\right)^2 + \left(\frac{n_z}{W}\right)^2} \quad . \tag{6.8}$$

The Helmholtz frequency can be approximated by a spring-mass model with an empirical neck-length correction

$$f_H = \frac{c}{2\pi}\sqrt{\frac{L_0}{A \cdot \left(D_0 + \frac{\pi}{2}L_0\right)}} \quad , \tag{6.9}$$

where A denotes the cross section area of the cavity's resonance volume.[107] Using these formulas one can calculate approximate model resonance frequencies that are given in table 6.1 and compare these results with the measured frequencies and detection positions. Due to inevitable differences of the acoustic impedance at the gap opening, the model frequencies differ systematically from the measured values, but still match the resonance detection positions. Accordingly, the first five resonance frequencies in fig. 6.2.4 are numbered with the titles from table 6.1.

Table 6.1 Assignment of detected resonance frequencies to spatial mode structures.

Mode index	f (Hz) exp.	Detected at	Model	f (Hz) model
f_H	850	Edge, Quarter, Middle	Helmholtz	930
f_1	1950	Edge, Quarter	$n_z = 1$	1720
f_2	3585	Edge, Middle	$n_z = 2$	3450
f_3	3970	Edge, Quarter, Middle	$n_y = 1$	3750
f_4	4335	Edge, Quarter	$n_y = n_z = 1$	4130

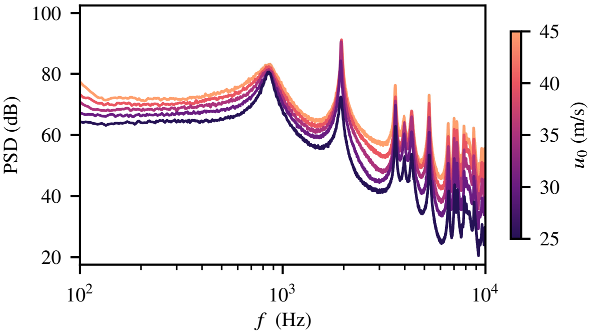

Fig. 6.2.3 Power Spectral Density at the five different operating velocities measured at the edge microphone inside the cavity's resonance volume. ($M = 2^{14}$, $D/M = 0.5$)

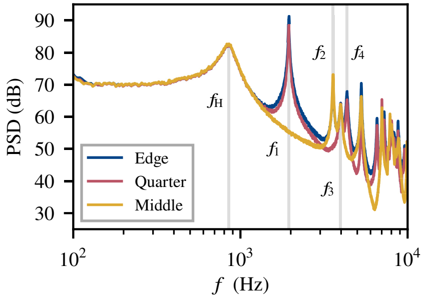

Fig. 6.2.4 Power Spectra at $u_0 = 40\,\mathrm{m\,s^{-1}}$ at the three different microphones. ($M = 2^{14}$, $D/M = 0.5$)

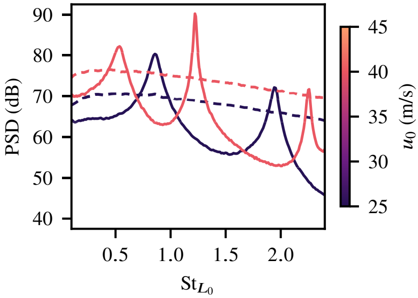

Fig. 6.2.5 Power Spectra of Kulite sensor 8 (dashed) and the edge microphone (solid) scaled by the opening length Strouhal number. (Kul.: $M = 2^{10}$, $D/M = 0.5$, Mic.: $M = 2^{12}$, $D/M = 0.5$)

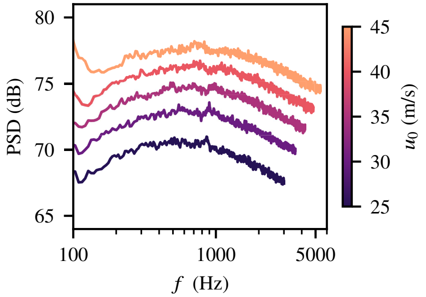

Fig. 6.2.6 Power Spectra of Kulite sensor 8 time-synchronously measured to the gap acoustics. ($M = 2^{13}$, $D/M = 0.5$)

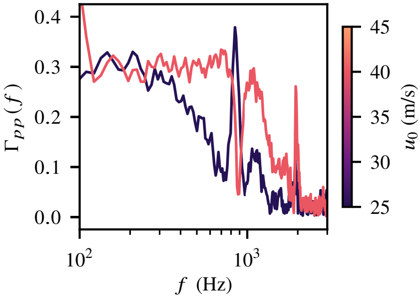

Fig. 6.2.7 Coherence between the edge microphone and Kulite sensor 8. ($M = 2^{12}$, $D/M = 0.75$)

In addition, it can be seen in fig. 6.2.3 that the measured levels increase with increasing velocity: While at most frequencies the level increment per velocity is smooth and comparable to the increment of the boundary layer wall pressure spectra, the level at the Helmholtz frequency f_H remains merely constant and the level at the first standing wave rises very inconsistently within the velocity range. This difference can be studied in more detail in fig. 6.2.5, where we show the pressure power spectra of both Kulite sensor 8 and the edge microphone at $u_0 = 25\,\mathrm{m\,s^{-1}}$ and $u_0 = 40\,\mathrm{m\,s^{-1}}$ over their Strouhal number $\mathrm{St}_{L_0} = \omega L_0/u_0$. In the shown Strouhal number range one can find the Helmholtz frequency f_H and the first standing wave for both velocities. One can thus compare the acoustic excitation of the cavity with the hydrodynamic excitation due to the turbulent boundary layer. As summed up in table 6.2 excitation is strong if the Strouhal number is close to 1.0 and comparably low at the two resonance frequencies at $\mathrm{St}_{L_0} = 0.5$ and $\mathrm{St}_{L_0} = 1.95$, respectively. A high pressure level inside the cavity's resonance volume in combination with a comparably low level of the external hydrodynamic excitation indicates a higher acoustic impedance of the opening in the Strouhal range close to 1.0 than in the other regions. These findings correspond to results of a study by Golliard[43] on slit openings, who found that - due to the grazing flow caused by an incoming boundary layer - the acoustic impedance of the studied openings varied between attenuation and amplification at low Strouhal numbers.

Table 6.2 Excitation Δ dB of the gap's acoustic resonance frequencies compared to the hydrodynamic excitation from fig. 6.2.5.

Mode	u_0 (m/s)	St_{L_0}	Δ dB
f_H	40	0.5	5
f_H	25	0.85	10
f_1	40	1.2	16
f_1	25	1.95	5

Accordingly the classical classification of a true passive resonator, c.f. chapter 2.3 and Plumbee,[79] whose acoustic impedance relies only on its geometry is not sufficient for this case. While many parts of the spectrum behave passively, the impedance of the opening depends on the flow and changes the excitation of the Helmholtz frequency and the first standing mode. The changing acoustic impedance of the opening can be caused by several reasons. Amongst these reasons one can especially think of the following ones:

(a) Inset of aeroacoustic feedback in the opening,

(b) Inset of strong compressibility in the opening as described by the classical derivation of the Helmholtz frequency,

(c) Change of the acoustic radiation direction of the opening,

(d) Increased or decreased acoustic dissipation at the boundary layer.

While this list may not be complete finding answer for these possibilities is essential to assess the applicability of hybrid acoustic simulations that are restricted to certain cases depending on their formulation. At least some of these possibilities could be addressed by extending the formulation of the models.

If aeroacoustic feedback sets in, single tones are amplified in the opening. If these tones correspond to an acoustic resonance frequency of the cavity they lead to a strong resonant lock-on of the two oscillation modes as described in chapter 2.3 and thus to a drastically changed impedance of the gap. As the resonance frequencies in our measurements are constant, this option could already be ruled out.

Changing compressibility as supposed in option (b) is also a possible explanation. While the Helmholtz frequency itself is only an acoustic eigenfrequency of the cavity that can be equally excited by an acoustic noise source, Helmholtz' classical derivation of the resonance frequency utilizes a flow based spring-mass analogy. Compressibility of the gap opening can thus play a major role in the excitation of the Helmholtz resonance it is however yet unknown how strongly the compressibility in the opening varies.

If one assumes that the acoustic propagation can be described by a plane wave mechanism, option (c) seems possible: If the scattering of the acoustic wave at the mean boundary layer in the gap's opening depends on the free stream velocity, the main angle of acoustic transmission can change. Assuming classical plane wave scattering, the reflection angle at the boundary layer changes with the transmission angle and thus also the reflected intensity, which leads to different levels inside the cavity.

Option (d) on the other hand is quite intuitive: If a changing mean vorticity or convection velocity of the shear layer leads to increased or decreased dissipation of the acoustics, the level inside the cavity changes with the opening's absorption rate. Although the consequences of this behavior are relatively clear it is not yet known which parameters of the boundary layer influence this behavior. Additional gap acoustics measurements with different boundary layers, c.f. chapter 7.1, and different opening lengths indicate, that the critical Strouhal number range is more influenced by the shear layer stability (and thus accordingly θ and u_τ) than by the boundary layer thickness δ. As we did not perform the hot-wire measurements at every operating velocity it is not possible to clearly indicate the reasons from our measurements.

Analyzing the time-synchronously measured signals of Kulite sensor 8 in fig. 6.2.6 one can see a slight indentation at $u_0 = 40\,\mathrm{m\,s^{-1}}$ and a small bump at $u_0 = 25\,\mathrm{m\,s^{-1}}$ at the Helmholtz frequency. As these features were not present when the cavity was masked they can be assumed to be caused by acoustic radiation of the cavity and thus indicate changes as proposed by mechanisms (c) and (d). While the difference of the Kulite spectra is small, changes become obvious when looking at the coherence between Kulite sensor 8 and the edge microphone, fig. 6.2.7. While there is a sharp peak visible at f_H with high coherence at $u_0 = 25\,\mathrm{m\,s^{-1}}$, the coherence sharply drops at $u_0 = 40\,\mathrm{m\,s^{-1}}$. This finding might indicate a changing acoustic radiation directivity of the cavity due to different scattering at the mean boundary layer. However it is also possible, that due to the shorter correlation length inside the boundary layer at $u_0 = 25\,\mathrm{m\,s^{-1}}$ compared to $u_0 = 40\,\mathrm{m\,s^{-1}}$, only at the higher velocity an effective interaction between the hydrodynamic fluctuations and the acoustics can occur. Besides both interpretations, an additional change of the acoustic dissipation at the boundary layer cannot be excluded from this analysis.

As the experimental analysis does not give distinct results for this question, a comparison of a DNC with different hybrid acoustic simulation approaches that include different levels of interaction between the acoustics and the flow, might shed some light into the driving mechanisms of the changing excitation strength of the cavity and can deliver answers on the general applicability of hybrid acoustic simulations to gap noise.

6.3 Numerical Simulation

In this chapter we describe different numerical simulations of the previously described base case of the experimental study on an idealized rear door gap model. Based on the hybrid RANS/LES using ALF we try to develop a simulation strategy for the simulation of automotive gap noise. For this purpose this model experiment is used as an ideal and simple test case which helps to identify potentials of the methods but also possible issues and bottlenecks. Especially we study the quality and applicability of a DNC based on ALF, that principally covers all possible physical phenomena but is known to be sensitive to numerical disturbances and the applicability of hybrid acoustic approaches based on an Acoustic Wave Equation[103] derived from the APE-2 equations[34] that are known to be applicable to broadband side mirror noise simulations.[89]

6.3.1 Setup

The simulation approaches are again based on the hybrid RANS/LES scheme described in chapter 4 and applied to turbulent boundary layer simulations in chapter 5. While these simulations were performed with an incompressible solver the application to gap noise requires changes to this procedure. By definition a DNC is a fully compressible simulation and a hybrid approach needs to add a wave equation solver that uses source terms from an incompressible simulation. In total we compare three approaches, the DNC, an acoustic wave equation where the acoustic waves are propagated in the resting air and a convective wave equation which additionally allows a non-zero mean velocity field.

In the computational domain of the EB-RSM RANS not only the flat plate itself was included, but also the geometry of the nozzle and the collector of the wind tunnel. Although it has been shown, that in ZPG cases a correct boundary layer can be produced without the wind tunnel geometry[53] in this configuration possible three-dimensional effects from the nozzle's shear layer are included and thus boundary conditions for the aeroacoustic subdomain can be accurately mapped. For the simulation, a mass flow inlet has been defined upstream of the nozzle and a pressure outlet was positioned several meters behind the collector. To solve the steady problem we use a segregated flow solver with a second order discretization in space. The used unstructured hexahedral trimmed mesh consists of approximately 55 million cells, the base size of the mesh is 32 mm in the free stream and is refined at the edges of the wind tunnel geometry. At all walls of the wind tunnel a wall-function formulation with $y^+ > 30$ was used. The volume mesh above the upper plate of the flat plate is anisotropically refined to 4 mm × 4 mm × 1 mm and the wall at all faces of the flat plate was resolved with $y^+ = 1$. In the gap opening, the mesh is additionally refined to capture possible vortices. The $z = 0$ cross section of the mesh can be seen in fig. 6.3.1. A converged solution is reached within 5000 iterations.

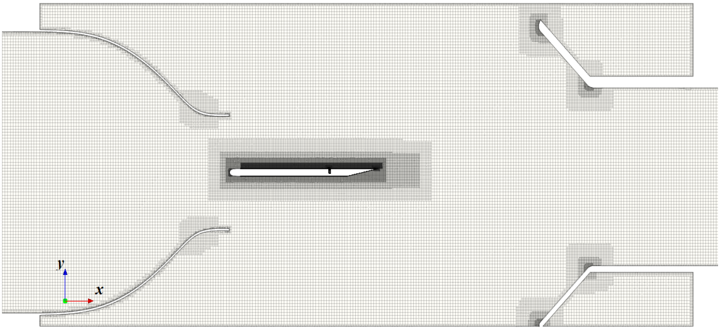

Fig. 6.3.1 $z = 0$ cross section of the mesh used for the EB-RSM RANS (Note that the wind tunnel geometry is deformed for visualization).

Both the DNC and the hybrid acoustic simulation are then performed on the same LES sub-domain and the same mesh. The computational domain contains a small region around the cavity: Its streamwise dimension is $750\,\text{mm} \leq x \leq 1400\,\text{mm}$, where again $x = 0$ is located at the flat plate's leading edge, its spanwise expanse is $-150\,\text{mm} \leq z \leq 150\,\text{mm}$ and the maximum height is $y = 300\,\text{mm}$. For our simulations we used an unstructured hexahedral trimmed mesh inside the computational domain with 21.3 million cells in total. At all walls, except of the cavity's bottom and its downstream wall, 25 prism layers with a near-wall thickness of 0.01 mm and a total thickness of 3 mm are used. The boundary layer was refined in several areas: Within the range $x \leq 1250\,\text{mm}$, $|z| \leq 75\,\text{mm}$ and up to a wall distance of 6 mm (which is inside the logarithmic layer) the mesh's base edge length was set to 0.5 mm. Above and outside of this area a size of 1 mm was used up to the wall distance 27 mm (outside the boundary layer). Outside of these boxes, the maximum cell size in the domain was limited to 4 mm. Inside the cavity the volume mesh base size was restricted to 0.5 mm. A cross section through the finest boundary layer mesh and the cavity can be seen in fig. 6.3.2b and fig. 6.3.2c respectively.

In the range $x \leq 1000\,\text{mm}$ (see fig. 6.3.2a), corresponding to a streamwise length of at least 15δ based on the experimental results at $x = 1165\,\text{mm}$, the assumption $\delta \sim x/\log x$ for the boundary layer growth rate[93] and depending on the velocity. ALF was applied again using the

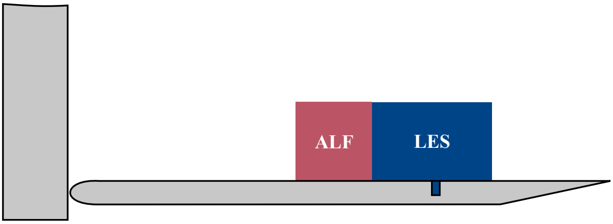

(a) Relative position and size of the aeroacoustic subdomain in comparison to the flat plate. Application region of ALF ist indicated.

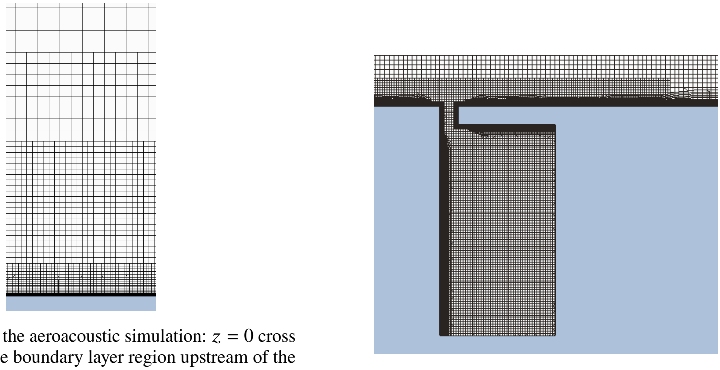

(b) Mesh used for the aeroacoustic simulation: $z = 0$ cross section through the boundary layer region upstream of the cavity. The largest visible cell size corresponds to an edge length of 4 mm

(c) Mesh used for the aeroacoustic simulation: $z = 0$ cross section through the cavity.

Fig. 6.3.2 Geometrical setup of the aeroacoustic simulations.

relaxation parameters $C_v = 1.0$, $C_r = 0.1$ and $N_{\mathrm{EWA}} = 750$. The ALF target fields from the EB-RSM are mapped onto the mesh using a shape function based weighting scheme that gives accurate results even close to the wall. At the artificial boundaries of the subdomain the mean flow fields from the EB-RSM are used to impose physically meaningful boundary conditions. The freestream boundary condition used in the DNC requires knowledge of the mean velocity field, the mean pressure and the temperature at the boundary. In the incompressible simulations only velocity and pressure boundaries are used. An overview of the boundaries is given in table 6.3.

In the flow simulation of both, the DNC and the incompressible simulation, we use a segregated flow solver based on the WALE subgrid scale turbulence model with a third order MUSCL/CD3 scheme with upwind blending factor 0.15 in space and an implicit three-step second order backward differencing scheme in time (c.f. appendix A). In comparison to the boundary layer simulations from chapter 5 the stability of the schemes has been slightly increased as the

Table 6.3 Overview of the flow boundary conditions used for the aeroacoustic simulation.

	DNC	Hybrid Simulation
Velocity	Inlet	Inlet, Sides, Top
Pressure	—	Outlet
Freestream	Sides, Top, Outlet	—

application on a car possibly requires more dissipative schemes and the simulation methods should be studied close to their required usage. The temporal discretization of the temperature equation used in the DNC is identical to the flow equations. To avoid spurious pressure oscillations near the artificial flow boundaries, additional Rhie-Chow type dissipation with limiting acoustic CFL 3.0 is used. The simulation is performed for a total physical time of $T = 0.6\,\mathrm{s}$ using the time step $\Delta t = 1 \times 10^{-5}\,\mathrm{s}$ with 10 inner iterations per time step. The acoustic wave equation, or equivalently the convective wave equation, are calculated after $T_0 = 0.075\,\mathrm{s}$ using a Newmark Delta scheme with $\delta = 0.502$ in time.

6.3.2 Analysis: Potentials of DNC and Hybrid Approaches

The numerical simulations of our study are performed at $u_0 = 25\,\mathrm{m\,s^{-1}}$ and $u_0 = 40\,\mathrm{m\,s^{-1}}$. Similar to the experiment, a validation of the inflow conditions is necessary to interpret the gap acoustics results and to establish a proper level of expectations. As the accuracy of the method for boundary layer flows has been shown previously we want to discuss this only briefly but emphasize the effects of different flow velocities and of the compressible LES. In table 6.4 we compare calculated boundary layer parameters from the experiment and the simulations at $u_0 = 40\,\mathrm{m\,s^{-1}}$. Very similar to chapter 5 it is found that especially the integral parameters δ^*, θ and the shape factor H are very well matched, with a maximum deviation to the experimental results below 3 %. As expected both LES do not differ significantly. Again a mismatch of the friction velocity u_τ can be seen: While the EB-RSM RANS tends to over-predict the friction velocity by about 7.3 %, both LES under-predict u_τ by about 4.0 %. Accordingly, the friction velocity drops by about 13.0 % between the target fields from the RANS and the realized LES solutions. This behavior again leads to a log-layer mismatch, see fig. 6.3.3. The streamwise development of u_τ is shown in 6.3.4 where we can see again that both the level of the RANS is not reached inside the ALF region and that a significant drop occurs at the transition between ALF and unforced LES. In chapter 5 we proved that this behavior depends on the mesh resolution and the spatial discretization scheme and improves as the mesh resolution gets closer to a wall-resolved LES mesh. At $u_0 = 25\,\mathrm{m\,s^{-1}}$ the friction velocity drops only about 7.7 % between the RANS and the LES, which is even smaller than at Hu's ZPG case from the previous chapter. As the mesh resolution remained fixed and the convection velocity increases, this phenomenon obviously gets worse at higher free stream velocities and accordingly the log-layer mismatch of the boundary layer profiles gets larger.

However it can be concluded that the used hybrid RANS/LES method produces good quality mean velocity profiles. As the stresses in chapter 5 were slightly under-predicted in comparison to the experimental results we also expect this behavior in these simulations. Nevertheless we assume that the classical indicator for the cavity response θ/L_0 is well matched in our simulations.[22,86] In both LES $\theta/L_0 > 0.5$ and thus one can assume a macroscopically stable shear layer in the gap's opening. In general special care must be taken of the log-layer mismatch due to the skin friction drop that could severely influence the shear layer. Due to its high stability in the gap opening the influence on the gap acoustics and the cavity flow is assumed to be negligible in our case and even a stronger mismatch in the log-layer would not be expected to cause significant unphysical shear layer instabilities.

Table 6.4 Experimental and numerical characteristic boundary layer parameters at $x = 1165\,\mathrm{mm}$ and $u_0 = 40\,\mathrm{m\,s^{-1}}$.

	u_0 (m/s)	δ_{99} (mm)	δ^* (mm)	θ (mm)	H	u_τ (m/s)	$\mathrm{Re}_\theta = u_0\theta/\nu$
Experiment	41.7	18.7	3.21	2.33	1.38	1.51	6310
EB-RSM RANS	+2.8 %	+1.6 %	+0.9 %	+2.6 %	−1.4 %	+7.3 %	+5.4 %
LES Comp.	+2.8 %	+1.6 %	−0.9 %	−0.4 %	−0.7 %	−4.0 %	+2.5 %
LES Inc.	+2.8 %	+1.6 %	−1.8 %	−0.8 %	−0.7 %	−4.6 %	+2.4 %

At least as important for the gap acoustics as the mean velocity profiles are the boundary layer wall pressure spectra, that can be seen in fig. 6.3.6a. It is found that besides the under-resolution compared to a wall-resolved LES, the wall pressure spectrum at $u_0 = 25\,\mathrm{m\,s^{-1}}$ of both the incompressible and the compressible LES is well matched with the (corrected) experimental data up to 3 kHz and lies well within an 80 % confidence interval around the experimental reference.* At $u_0 = 40\,\mathrm{m\,s^{-1}}$ the simulated signal up to 5.5 kHz lies within the experimental confidence interval, only the frequency region close to the spectrum's maximum is slightly over-predicted. Surprisingly the limiting frequencies of the simulation correspond quite well to the experimental sensor resolution limits. Above these limiting frequencies numerical dissipation and dispersion lead to a steep drop of the simulated pressure levels. In fig. 6.3.6b it is seen that both limiting frequencies correspond to the characteristic wavelength $\omega/u_0 = 750\,\mathrm{m^{-1}}$ and thus the method scales with the Strouhal number and leads to consistent results at different free stream velocities. Consequently, the levels of the gap acoustics simulation cannot be expected to match the experimental values above these limiting frequencies. Additionally, the coherence of the wall pressure spectra at $u_0 = 40\,\mathrm{m\,s^{-1}}$ is found to decay slightly too fast compared to the

---

*While the experimental data has been measured for 60 s, the evaluated time of the simulations is only 0.5 s, thus much higher statistical scattering must be expected. To estimate the quality of the simulated signals, the experimental signal has been divided into 120 intervals of length 0.5 s and the power spectral density of each interval was calculated. If normal distribution of the data is assumed, the standard deviation σ of these experimental results gives a 67 % confidence interval, (1.28σ produces the 80 % interval) around the experimental signal with signal length 60 s.

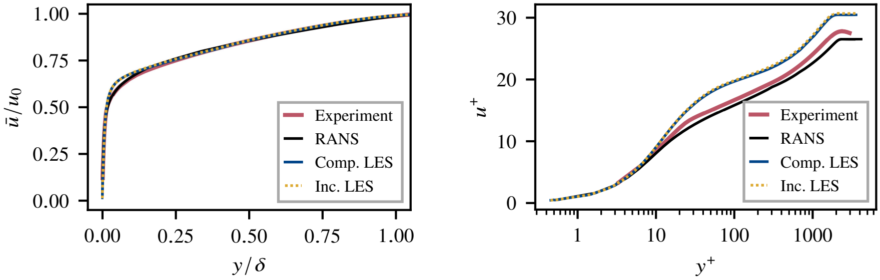

Fig. 6.3.3 Comparison of mean boundary layer velocity profiles at $x = 1165$ mm ($u_0 = 40\,\mathrm{m\,s^{-1}}$).

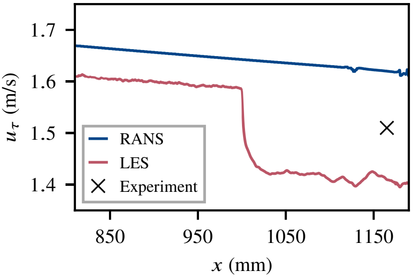

Fig. 6.3.4 Streamwise development of u_τ at the upper surface of the flat plate ($u_0 = 40\,\mathrm{m\,s^{-1}}$).

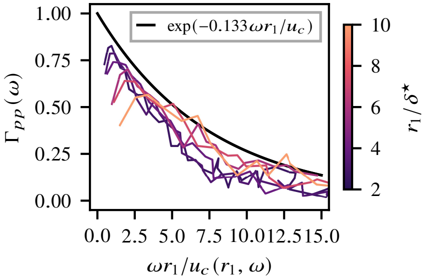

Fig. 6.3.5 Streamwise coherence of the simulated wall pressure spectra in comparison to the experimental decay ($M = 2^9$, $^D/_M = 0.9$).

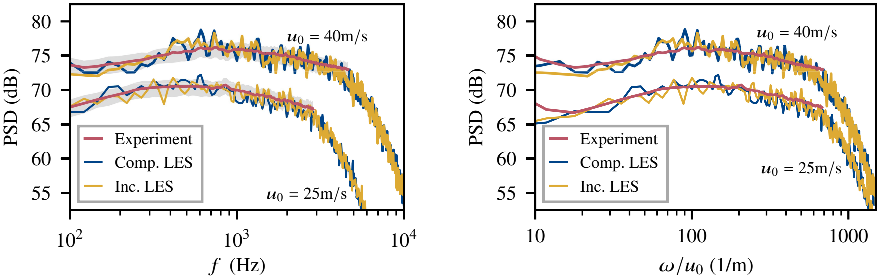

(a) Unscaled wall pressure spectra, experimental 80 % confidence intervals indicated in grey.

(b) Velocity scaled wall pressure spectra.

Fig. 6.3.6 Simulated and measured wall pressure spectra at Kulite position 8. ($M_{\mathrm{exp}} = 2^{11}$, $M_{\mathrm{sim}} = 2^{12}$, $^D/_M = 0.75$, both corresponding to FFT frequency resolution $\Delta f \approx 24$ Hz) experimental results, see fig. 6.3.5. Taking into account the results from Hu's ZPG case (see fig. 5.3.9a) we can assume that the increased under-resolution due to the higher free stream velocity causes this issue. Nevertheless the result is still reasonable and in the typical range of ZPG boundary layers.

In fig. 6.3.7a and 6.3.7b the simulation results of the DNC, the acoustic wave equation and the convective wave equation at the edge microphone position are compared to the experimental data. It is found, that above 300 Hz and below 700 Hz the levels of all three approaches compare very well and the results can even match the experimental confidence interval at both operating velocities. Below 300 Hz the influence of background noise in the experimental data increases. It has been shown by Hu and Herr,[51] that below 200 Hz the wind tunnel's background noise is present even at low velocities. It is assumed, that at higher operating velocities this effect might extend up to 300 Hz.

Close to the Helmholtz frequency f_H differences between the approaches can be seen: While the DNC is able to match the experimental confidence interval at both velocities quite well, neither of the hybrid approaches can fulfill this criterion. At $u_0 = 25\,\mathrm{m\,s^{-1}}$ the simulated levels are still relatively close to the experimental data, but at $u_0 = 40\,\mathrm{m\,s^{-1}}$ the simulation results are more than 10 dB too high and also the shape of the resonance frequency is not matched. It should be noted, that f_H at $u_0 = 40\,\mathrm{m\,s^{-1}}$ could be experimentally assigned to a low excitation range, while the cavity's excitation at $u_0 = 25\,\mathrm{m\,s^{-1}}$ was strong (see table 6.2). This indicates that the used hybrid approaches have systematic difficulties to predict the level at f_H, that increase if the excitation of the cavity is weak.

Again, all three approaches give good results in the broadband frequency range between f_H and f_1 with the levels being slightly too high at $u_0 = 40\,\mathrm{m\,s^{-1}}$. The correct simulation of the pressure level at f_1 itself is difficult for all three approaches, but the DNC delivers the best results for both velocities. However the level of the hybrid approaches seems to be closer to the experimental data at $u_0 = 40\,\mathrm{m\,s^{-1}}$ than at $u_0 = 25\,\mathrm{m\,s^{-1}}$, which supports the assumption that especially strong interaction of the acoustics with the flow leads to difficulties for the hybrid approaches.

Above f_1, the characteristics of the numerical results change: At $u_0 = 25\,\mathrm{m\,s^{-1}}$ the levels of the DNC compared to the experiment drop right above 2 kHz, corresponding to a characteristic limiting wave length $\omega/u_0 \approx 500\,\mathrm{m^{-1}}$, which can be seen in fig. 6.3.8a. Nevertheless, the shape of the higher resonance frequencies f_2 to f_4 are still well predicted but the frequencies are already shifted due to numerical dispersion. Above f_5 dissipation and dispersion are so strong that the resonance frequencies do not get excited any more and cannot be distinguished. In comparison, the hybrid approaches give relatively accurate levels up to 9 kHz, only the resonance frequency f_3 is merely excited at all. Besides this positive impression, the results of the hybrid simulations above 3 kHz must be taken with care, as the pressure spectra of the incoming boundary layer significantly drop. Schimmelpfennig showed that spatial averaging in the gap's opening reduces the direct influence of the incoming boundary layer fluctuations on the pressure levels inside the cavity in this frequency range.[90] Therefore the importance of the interaction of the turbulent boundary layer with the downstream edge of the gap's opening increases. Nevertheless, even this excitation mechanism still strongly depends on the spectral accuracy of the interacting boundary layer and only if the boundary layer is described well, correct characteristics of this interaction mechanism can be expected. It is thus assumed, that the level above 3 kHz is influenced by numerical effects and does not represent the physics.

At $u_0 = 40\,\mathrm{m\,s^{-1}}$ the levels of the DNC match the experimental data up to approximately 4.2 kHz, corresponding to $\omega/u_0 \approx 615\,\mathrm{m^{-1}}$ (see fig. 6.3.8b), with a drop of the levels between the resonance frequencies f_3 and f_4. While the wall pressure spectra at both velocities dropped at the same characteristic wavelength $\omega/u_0 \approx 750\,\mathrm{m^{-1}}$, here the drop at the two velocities differs by $\Delta\omega/u_0 \approx 115\,\mathrm{m^{-1}}$. One can see that at $u_0 = 25\,\mathrm{m\,s^{-1}}$ the frequency range above $\omega/u_0 = 500\,\mathrm{m^{-1}}$ is dominated by broadband noise whereas this frequency range at $u_0 = 40\,\mathrm{m\,s^{-1}}$ is dominated by acoustic resonances. Thus we can assume that the wavenumber-frequency spectrum at $u_0 = 40\,\mathrm{m\,s^{-1}}$ in this frequency range is dominated by acoustic modes with relatively large wave length, while at $u_0 = 25\,\mathrm{m\,s^{-1}}$ the influence of the small scale hydrodynamic fluctuations is important. This effect would lead to smaller numerical dissipation and thus a higher limiting frequency at $u_0 = 40\,\mathrm{m\,s^{-1}}$ as observed in the simulations. In contrast to the $u_0 = 25\,\mathrm{m\,s^{-1}}$ case, the results of the hybrid approaches are not as promising above 2.2 kHz. Between 2.2 kHz and 5 kHz the levels are much higher compared to the experiment. This finding supports the former analysis, that the hybrid simulations above 3 kHz, or in this case even above 2.2 kHz, are dominated by numerical effects and don't represent the physics in this frequency range. Above 5 kHz the levels first drop to the experimental values and then slightly under-predict the experiment results. As the inflow turbulence levels in this frequency range are severely under-predicted these results are more of numerical nature than they are representing actual physics. However obviously the acoustic wave equation approaches are much less dissipative than the DNC with approximately identical computational costs.

Although the hybrid acoustic simulations have strong limitations, the decomposition of the total fluctuating pressure field into the acoustic pressure p^{ac} and the hydrodynamic pressure fluctuations p' can provide additional insights. Especially the $u_0 = 25\,\mathrm{m\,s^{-1}}$ case is well suited for such an analysis as the agreement with the experimental data is good. In fig. 6.3.9 one can see that the low frequencies of the total spectrum is dominated by the hydrodynamic fluctuations p'. This finding corresponds well with theoretical transfer functions H of Helmholtz resonators that usually have $|H| \approx 1$ below their Helmholtz frequency f_H. Then, up to the Helmholtz frequency the acoustic pressure dominates the spectrum. In the frequency region between f_H and f_1 an interesting behavior is found: While the total spectrum matches the experimental results, the pure acoustic levels are approximately 10 dB higher. The hydrodynamic levels are instead on par with the total level. Consequently some kind of cancellation takes place in this frequency region of this simulation. The resonance frequency f_1 is then again dominated by the acoustic pressure. Above f_1 results cannot be trusted anymore and in fact a distinctive hump is

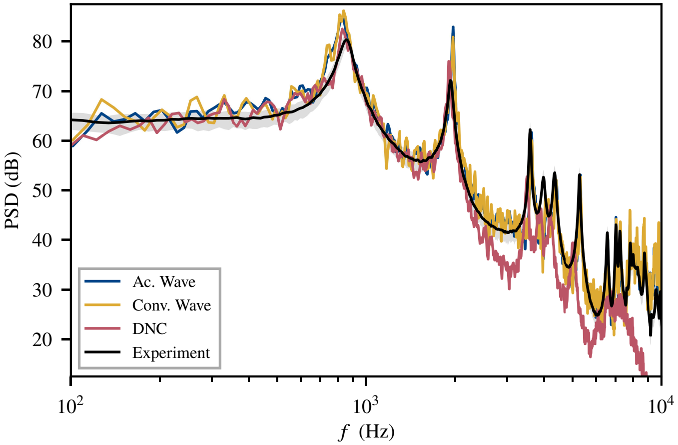

(a) $u_0 = 25\,\mathrm{m\,s^{-1}}$

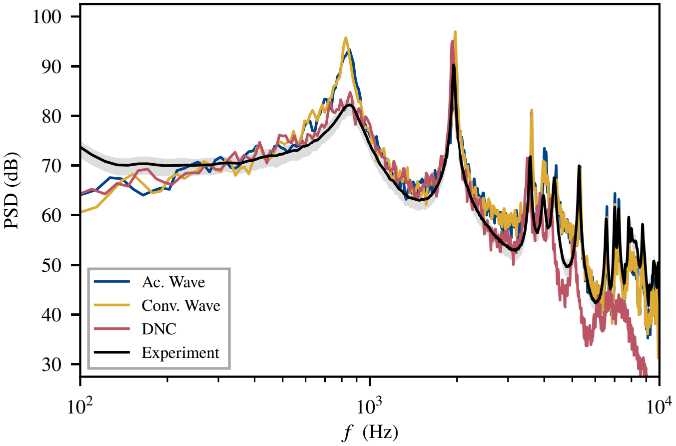

(b) $u_0 = 40\,\mathrm{m\,s^{-1}}$

Fig. 6.3.7 Simulated and measured pressure spectra at the edge microphone position. The grey area indicates the 67 % confidence interval of the experiment. ($M_{\mathrm{exp}} = 2^{12}$, $M_{\mathrm{sim}} = 2^{13}$, $D/M = 0.75$, both corresponding to FFT frequency resolution $\Delta f \approx 12\,\mathrm{Hz}$)

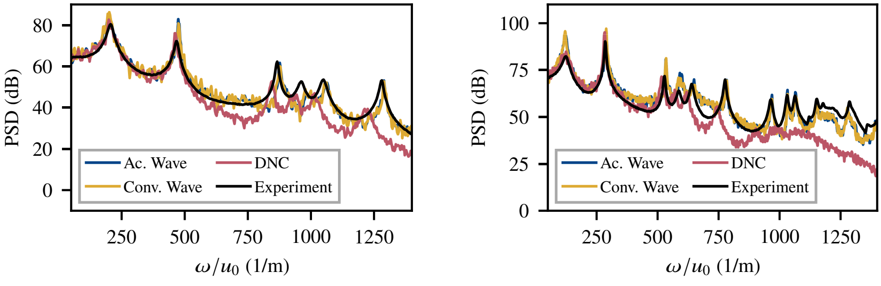

(a) $u_0 = 25\,\mathrm{m\,s^{-1}}$ (b) $u_0 = 40\,\mathrm{m\,s^{-1}}$

Fig. 6.3.8 Simulated and measured pressure spectra at the edge microphone position scaled with the free-stream velocity. ($M_{\mathrm{exp}} = 2^{12}$, $M_{\mathrm{sim}} = 2^{13}$, $D/M = 0.75$, both corresponding to FFT frequency resolution $\Delta f \approx 12\,\mathrm{Hz}$)

found at 4 kHz whose nature is yet unclear.[†] As the hydrodynamic pressure levels drop above this hump the highest frequency range up to 10 kHz is again dominated by the acoustic pressure. Although the inflow is drastically under-resolved in this frequency range this general behavior seems conclusive as the gap opening certainly acts as a wave length filter comparable to the high frequency attenuation when measuring wall pressure spectra.

As the DNC's signals match the experimental data very well it is possible to assume that, up to the corresponding frequency limit, the physics of the studied gap acoustics problem are well captured by this method. In fig. 6.3.10 surface fourier transforms in the $x = 1202\,\mathrm{mm}$ plane (in the middle of the gap's opening) are shown close to the five measured resonance frequencies at $u_0 = 40\,\mathrm{m\,s^{-1}}$. The calculated modes correspond to the simple used resonance models in the experimental analysis from table 6.1 and confirm their results. In addition, one can clearly see, how the opening and the boundary layer itself act as an impedance boundary condition on the acoustics and effectively damp any modal acoustic resonance structure in the opening. As the geometry of a real rear door gap is much more complicated and simple formulas won't be applicable such an analysis offers a great value for an industrial application. The modal structure of resonance frequencies could be studied and possibilities to influence these frequencies could be developed.

From the experimental analysis it was still unclear why the excitation strength of the cavity changes with the Strouhal number. In our simulations, we showed that all three methods can produce acceptable levels in the broadband ranges up to 2.2 kHz well above the Helmholtz resonance frequency f_H, but that only the DNC gave correct levels at f_H. Especially if the excitation of f_H is weak, both hybrid approaches fail. This situation allows a deeper analysis of

---

[†] We could show that the frequency and the level of this hump strongly depend on the chosen discretization scheme and mesh setup in the corners of the gap and did not converge with mesh resolution which indicates that this peak cannot be considered physical but a numerical artefact.

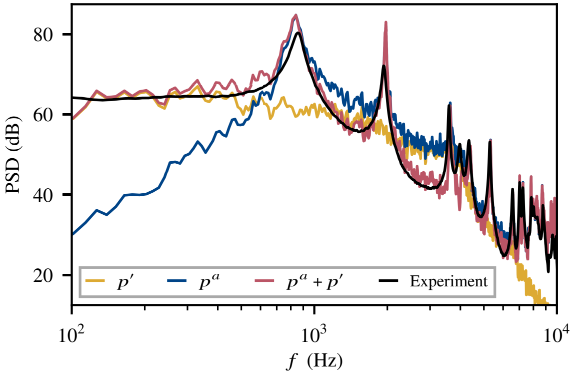

Fig. 6.3.9 Simulated spatial mode structure of the first five resonance frequencies in the $x = 1202$ mm cross section. Results from DNC at $u_0 = 25\,\mathrm{m\,s^{-1}}$. ($M_{\mathrm{exp}} = 2^{12}$, $M_{\mathrm{sim}} = 2^{13}$, $D/M = 0.75$, both corresponding to FFT frequency resolution $\Delta f \approx 12$ Hz)

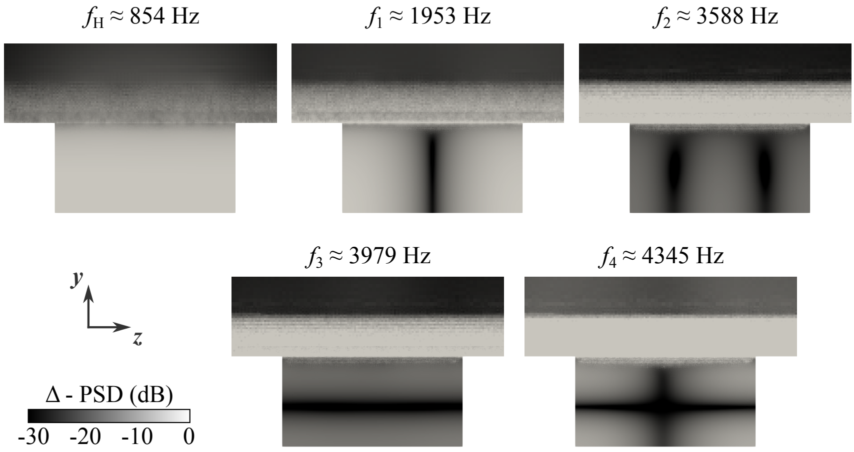

Fig. 6.3.10 Simulated spatial mode structure of the first five resonance frequencies in the $x = 1202$ mm cross section. (Results from DNC at $u_0 = 40\,\mathrm{m\,s^{-1}}$)

the underlying excitation mechanism. In fig. 6.3.11a and fig. 6.3.11b it is found, that despite the much higher degree of noise in the simulations and the different levels at f_H all three simulation approaches can reproduce the principal shape of the experimental coherence between Kulite sensor 5 and the microphone at the edge position. Accordingly, the main cause for the velocity dependent excitation of f_H is not yet covered in the hybrid simulation and thus the phenomenon itself might not be explained completely from the prior proposed option (c), a changing acoustic radiation direction due to different scattering at the mean velocity boundary layer. As both hybrid approaches produce nearly identical results, the influence of convection by the mean velocity on the acoustic propagation in this problem can be neglected. Thus the different shapes of the coherence spectra can be assumed to be related to the different phase velocities at the different free stream velocities. If a changing acoustic radiation direction plays a role in this mechanism it must either be caused by scattering at the small scale fluctuating velocity fields instead of the mean velocity boundary layer (d) or by changing compressibility in the gap's opening (b).

In fig. 6.3.12a and 6.3.12b we plot the relative density fluctuations $\varrho'/\bar{\varrho}$ as a measure for the flow compressibility at three different points over time: at the edge microphone, in the gap opening and at the Kulite sensor position 4. While the compressibility overall increases with increasing velocity (which is expected as incompressible simulations are usually considered acceptable below Mach 0.3 or equivalently $\varrho'/\bar{\varrho} < 5\,\%$) the maximum amplitude nowhere exceeds a value of 0.1 %. However a significant increase of the opening compressibility is visible. At $u_0 = 25\,\mathrm{m\,s^{-1}}$ the amplitude of the opening density fluctuations are comparable to the the fluctuations inside the gap due to acoustic propagation but at $u_0 = 40\,\mathrm{m\,s^{-1}}$ they are on par with the hydrodynamic boundary layer fluctuations. Although the relatively small amplitudes of the compressibility indicate that an incompressible flow simulation should be valid for both cases the influence of the changes on the acoustic wave equation is not yet understood.

Reviewing the derivation of the acoustic wave equation, see Ewert and Schröder[34] and chapter 4.2 one can see, that the interaction term between the acoustic velocity and the mean vorticity of the flow was neglected. It is known that this effect is of special importance in shear layers. It is assumed that this interaction changes the acoustic transmission and dissipation in the opening as described in option (d). Therefore this simplification might be a reason for the failure of the hybrid approaches. It should be noted, that including the vorticity in a hybrid acoustic simulation can also be interpreted as first step in including the small scale fluctuating velocity field in the acoustic propagation. In appendix B we sketch a possibility to consistently include the flow's mean vorticity field in the acoustic wave equation.

We finally conclude, that despite the nearly passive character of the studied gap noise phenomenon a precise numerical simulation currently requires a DNC. The DNC based on a hybrid RANS/LES using ALF can produce excellent results up to a resolution dependent limiting frequency. Implementing a proper vorticity interaction term into the acoustic wave equation could provide new insights into the physics of the changing gap opening impedance.

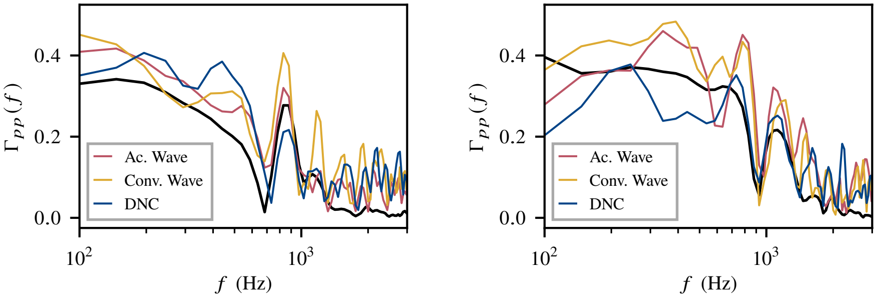

(a) $u_0 = 25\,\mathrm{m\,s^{-1}}$ (b) $u_0 = 40\,\mathrm{m\,s^{-1}}$

Fig. 6.3.11 Simulated and measured coherence between the edge microphone position and Kulite sensor 5. To reduce the noise in the simulated data but still resolve the steep gradients, zero padding was used (×2). ($M_{\mathrm{exp}} = 2^9$, $M_{\mathrm{sim}} = 2^{10}$, $^D/_M = 0.75$, both corresponding to FFT frequency resolution $\Delta f \approx 48\,\mathrm{Hz}$)

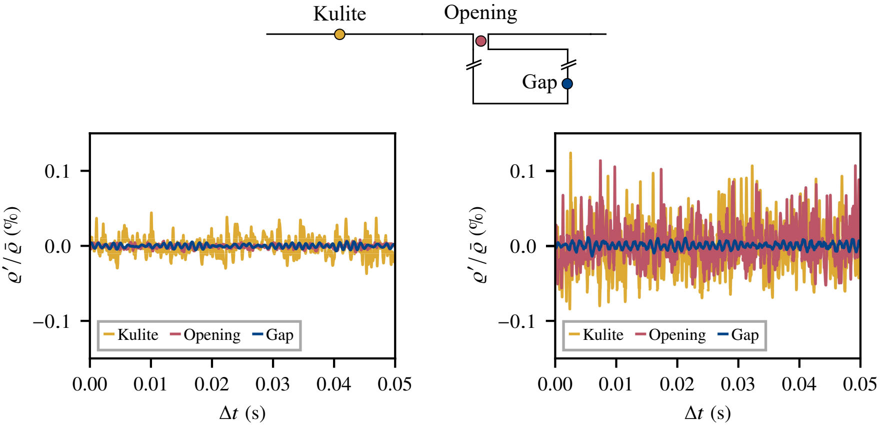

(a) $u_0 = 25\,\mathrm{m\,s^{-1}}$ (b) $u_0 = 40\,\mathrm{m\,s^{-1}}$

Fig. 6.3.12 Relative density variations of the DNC at three different positions and the two free stream velocities.

6.3.3 Computational Costs

Our aeroacoustic simulations were performed on 720 CPUs and the DNC approximately took 8600 CPUh for 0.1 s physical time, and the hybrid simulations were approximately on par with the DNC. This computational performance can be compared to other standard methods that could be applied to the gap acoustics problem. A typical approach for resolving the boundary layer fluctuations in front of a restricted area of interest would be a classical wall-resolved LES that imposes two main requirements: Resolution of the turbulence production scales inside the boundary layer and resolution of the full streamwise expanse of the problem. While the wall-resolved LES, depending on the chosen discretization, is usually expected to give more accurate results in high frequency ranges it is known that the mesh resolution of this approach cannot be significantly reduced to adapt to lower solution requirements. The current comparison is therefore based on the assumption that the presented quality of the results is sufficient and improved results would not generate an additional benefit. According to [78], a spatial streamwise resolution of $\Delta x^+ \approx 50$, a spanwise mesh resolution of $\Delta z^+ \approx 15$ and a wall-normal resolution $y^+ \approx 1$ is required for a wall-resolved LES. Choi and Moin, [16], studied the influence of the timestep size and showed that a time step resolution of $\Delta t^+ = \Delta t u_\tau^2 / \nu = 0.4$ is required to properly resolve the turbulence production. In table 6.5 we use the extracted data at $x = 1165\,\mathrm{mm}$ and $u_0 = 40\,\mathrm{m\,s^{-1}}$ for a comparison with these theoretical requirements.

Table 6.5 Comparison of resolution requirements of wall-resolved LES and our simulation.

	Wall-resolved LES	Hybrid RANS/LES
Δx^+	50	50
y^+	1	1
Δz^+	15	50
Δt^+	0.4	1.35

It should be noted that even the given spatial resolution Δx^+ and Δz^+ is only fulfilled in the mid 15 cm of the spanwise domain size, leading to bigger computational savings in practice than indicated in this analysis. In addition to the savings due to the lower resolution requirements, we do not need to include the whole streamwise expanse of the flat plate in our simulation. We could thus reduce the highly resolved plate length by the first 75 cm of the airfoil, or correspondingly we would need to expand our computational domain about a factor 2.15 for a wall-resolved LES. Furthermore it is assumed, that our used spanwise dimension of 30 cm is necessary to geometrically include the complete gap in the computational domain and to reduce the influence of the side boundaries on the boundary layer - gap interaction. Finally, we assume that a wall-resolved LES could be performed without including the bottom plate of the airfoil. In summary we could thus reduce the computational costs about the factor 24 compared to a classical wall-resolved LES with the same discretization schemes, while we still maintained a well-controlled behavior of the pressure fluctuations inside the boundary layer. What adds to the computational costs of our method is the EB-RSM RANS and the calculation of the ALF coefficents. While the former can be considered a constant offset, much cheaper and independent from the transient simulation, the costs of the latter might be neglected compared to solving the LES equations, as there exists an explicit solution for the linear system, that only requires the computation of matrix-matrix products.[23]

6.3.4 Numerical Robustness of the DNC

To cover the promising results of the DNC and to highlight the need to resolve the turbulent boundary layer fluctuations we perform additional simulations at $u_0 = 40\,\mathrm{m\,s^{-1}}$ of the base case. To reduce the computational costs we now only simulate for $T = 0.3$ s instead of the former 0.6 s. While the experimental results and the quality of the DNC based on the hybrid RANS/LES already indicates the crucial importance of the turbulent boundary layer fluctuations for the gap noise phenomenon also another, simpler simulation might be possible. Based on the same steady RANS it is possible to run a compressible IDDES based e.g. on the Spalart-Allmaras turbulence model. Using the same mesh as before the IDDES switches into the LES branch in the gap opening and thus fluctuations due to the leading edge separation should be resolved. Nevertheless the incoming boundary layer will always remain in a RANS description, i.e. the mean boundary layer profile matches the mean velocity profile and the turbulence information is modeled by the Spalart-Allmaras model parameter $\tilde{\nu}$. The resulting spectrum at the edge microphone is compared to the LES result in fig. 6.3.13. Although the standing wave modes are predicted correctly, the levels are drastically under-predicted, the Helmholtz resonance is not excited and two additional peaks at 180 Hz and 350 Hz are present. This result proves that in fact the present gap noise phenomenon is closely related to the turbulent boundary layer fluctuations and that they are required for any simulation method

Another important possible influence on the results of a sub-domain DNC are the boundary conditions. On the one hand the free stream boundary condition is designed acoustically non-reflecting only if sound and flow hit the boundary perpendicularly. On the other hand, generally, side boundaries can affect the turbulent boundary layer coherence and lead to disturbances. Therefore we perform a calculation on a much larger sub-domain with $600\,\mathrm{mm} \leq x \leq 1600\,\mathrm{mm}$, $y < 450\,\mathrm{mm}$ and $|z| \leq 200\,\mathrm{mm}$ and identical mesh resolution as before. Fig. 6.3.14 shows that the resulting gap acoustics at the edge microphone are nearly independent from the size of the sub-domain and thus the free stream boundary conditions do not significantly influence the results.

We already studied the influence of the spatial and temporal resolution on the turbulent boundary layer fluctuations but we should also clarify their influence on the related gap acoustics. For this purpose we first compare three different mesh refinement steps of the boundary layer, similar to the refinements from chapter 5. In fig. 6.3.15 it is found again that this refinement shifts the high frequency drop to higher frequencies and improves the wall pressure spectra. In a second step we first refine only the gap opening by 0.25 mm cells instead of the original 0.5 mm cells and in a second step we refine the whole cavity volume as described. Interestingly

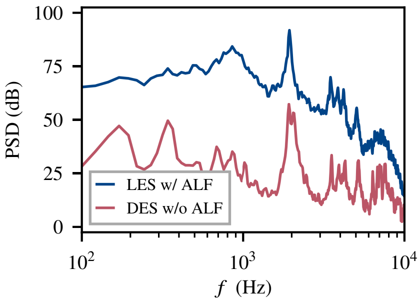

Fig. 6.3.13 Comparison of pressure spectra at the edge microphone at $u_0 = 40\,\mathrm{m\,s^{-1}}$ between the base DNC and a DES.

this refinement does not significantly improve the gap acoustics at the edge microphone, only above 2 kHz a slight increase of the levels and thus less dissipation is found in fig. 6.3.16. Thus the influence of the spatial resolution on the acoustic propagation can be neglected if the hydrodynamic excitation of the boundary layer is not better resolved. As a mesh resolution of 0.5 mm already corresponds to 68 cells per wave length at 10 kHz, the acoustic waves are sufficiently well resolved[89] and this result is expected. A combination of the two refinement approaches is discussed in fig. 6.3.17. Surprisingly, again no significant improvement is found although the incoming boundary layer now matches the experimental spectrum up to higher frequencies. Only the Helmholtz frequency gets sharper (and closer to the experimental shape) as the resolution increases and the first standing wave f_1 gets excited stronger with increasing resolution. However the basic features of the gap acoustics can even be covered on a very coarse mesh without 0.5 mm cells. It appears that the influence of the boundary layer fluctuations on very high frequencies can be somehow neglected, which would confirm the results from the analysis of the hydrodynamic and acoustic contributions from fig. 6.3.9.

Again we compare three different time-step sizes on the base mesh. While it is seen in fig. 6.3.18 that the influence on the wall pressure spectra, especially between the fine and the medium time-step, is very small the gap acoustics spectra now change significantly at high frequencies, see fig. 6.3.19. This indicates that in fact numerical dissipation and dispersion of the acoustic propagation dominate the spectra in this frequency range. At the coarse time-step 2×10^{-5} s the level and frequency resolution begin to drop already at 3 kHz which corresponds to 16.5 time-steps per period. At 8 kHz the fine time-step 5×10^{-6} s still has a temporal resolution of 25 time-steps per period T and thus resolves these frequencies acceptably well with a three-step BD2 scheme. Consequently only at this fine time-step the very high resonance frequencies can be resolved.

Equivalent behavior can be seen when the discretization schemes are changed. While different spatial discretization schemes (see appendix A) affect the wall pressure spectra in fig. 6.3.20 the signals at the edge microphone remain nearly unaffected (see fig. 6.3.21). The influence of the temporal discretization scheme is opposite: While the wall pressure spectra are nearly unchanged (fig. 6.3.22), the high frequency resolution is drastically improved if the less dissipative five-step BD2 scheme is used (fig. 6.3.23). In addition the Helmholtz frequency gets slightly sharper and becomes more accurate in comparison to the experimental data.

A last modification has been applied to the subgrid scale model of the LES. While the particular choice of the basic WALE model was only motivated by its stability and simplicity one could also apply the dynamic Smagorinsky subgrid scale model that should principally help to slightly improve the log-layer mismatch of the resulting boundary layer but that could lead to increased numerical noise due to additional blending. One can see in fig. 6.3.24 that the wall pressure spectrum worsens a little bit as the mid frequency slope is not predicted as precisely as with the WALE model. However the noise inside the gap (fig. 6.3.25) is again quite independent from these uncertainties in the inflow turbulence.

6.4 Summary

In our experimental study we performed detailed measurements of passive gap noise and the boundary layer upstream of the cavity. We were able to confirm experimental results from previous studies but could show that in addition especially the gap's Helmholtz frequency underlies a velocity dependent excitation. We showed by experimental and numerical methods, that this varying excitation involves changing compressibility inside the gap opening on relatively small levels and therefore likely also changing acoustic dissipation due to an interaction of the acoustics with the turbulence of the boundary layer above the gap's opening.

We showed that the hybrid RANS/LES approach consisting of the EB-RSM RANS and ALF produces a transient boundary layer upstream of the cavity whose mean velocity profile and wall pressure spectra compare well with the experimental data. Besides the quality of these significant quantities for the gap acoustics it is found, that a log-layer mismatch occurs at the transition between ALF and classical LES, that is also typically reported for LES on under-resolved meshes. Although this finding has been shown to be unimportant in our case, its impact can increase at higher velocities or gaps with significantly greater shear-layer instability. Additional research and improvement on this topic is needed for a general application. We were able to reduce the computational costs of the passive gap noise problem at least about a factor 24 compared to a numerical simulation with classical wall-resolved LES.

It was shown that the acoustic near field inside the cavity could be successfully simulated using a DNC: Especially the pressure levels at the Helmholtz frequency and the broadband ranges up to $\omega/u_0 = 500\,\mathrm{m}^{-1}$, as well as all resonance frequencies up to 5 kHz could match the experimental 67 % confidence interval. In addition, we could show that current hybrid acoustic simulations are not suitable to predict the pressure levels at the Helmholtz frequency. It is assumed, that the missing interaction of the acoustics with the boundary layer and the shear layer vorticity in our studied approaches is one of the reasons for that issue and further analysis is recommended. Techniques from appendix B could provide a starting point for these studies. Furthermore the hybrid simulations were prone to numerical disturbances above 2.2 kHz.

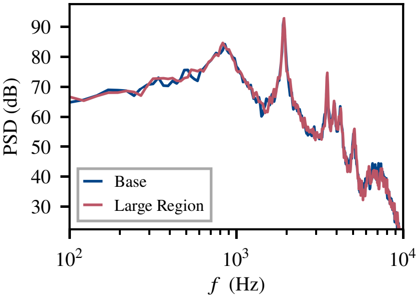

Fig. 6.3.14 Comparison of pressure spectra at the edge microphone at $u_0 = 40\,\mathrm{m\,s^{-1}}$ between different region sizes.

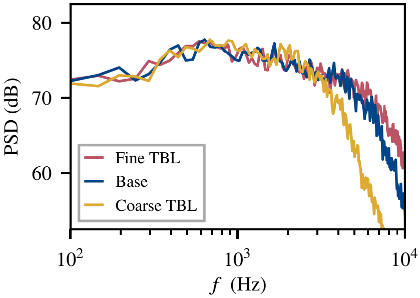

Fig. 6.3.15 Comparison of wall pressure spectra at $u_0 = 40\,\mathrm{m\,s^{-1}}$ between three boundary layer mesh refinements.

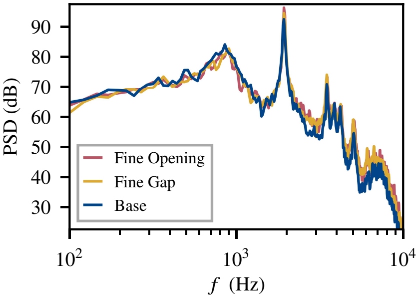

Fig. 6.3.16 Comparison of pressure spectra at the edge microphone at $u_0 = 40\,\mathrm{m\,s^{-1}}$ between three mesh refinements of the gap.

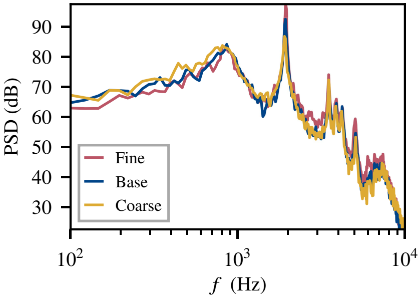

Fig. 6.3.17 Comparison of pressure spectra at the edge microphone at $u_0 = 40\,\mathrm{m\,s^{-1}}$ between three global mesh refinements.

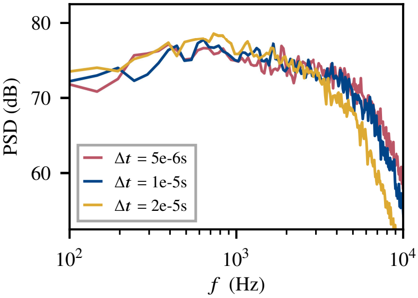

Fig. 6.3.18 Comparison of wall pressure spectra at $u_0 = 40\,\mathrm{m\,s^{-1}}$ under three different time-steps.

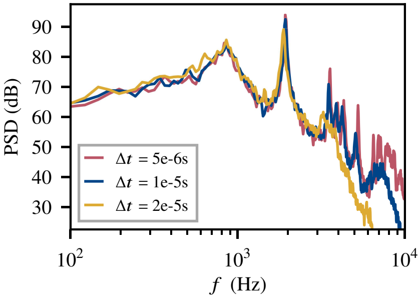

Fig. 6.3.19 Comparison of pressure spectra at the edge microphone at $u_0 = 40\,\mathrm{m\,s^{-1}}$ under three different time-steps.

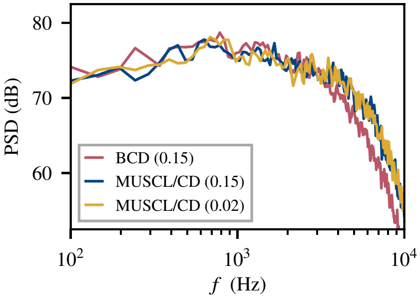

Fig. 6.3.20 Comparison of wall pressure spectra at $u_0 = 40\,\mathrm{m\,s^{-1}}$ under three different spatial discretization schemes.

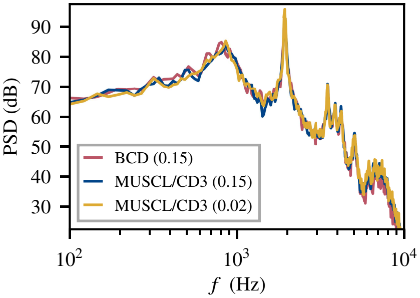

Fig. 6.3.21 Comparison of pressure spectra at the edge microphone at $u_0 = 40\,\mathrm{m\,s^{-1}}$ under three different spatial discretization schemes.

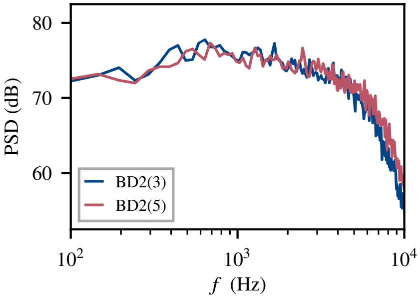

Fig. 6.3.22 Comparison of wall pressure spectra at $u_0 = 40\,\mathrm{m\,s^{-1}}$ under two different temporal discretization schemes.

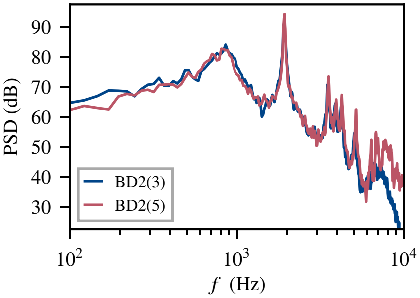

Fig. 6.3.23 Comparison of pressure spectra at the edge microphone at $u_0 = 40\,\mathrm{m\,s^{-1}}$ under two different temporal discretization schemes.

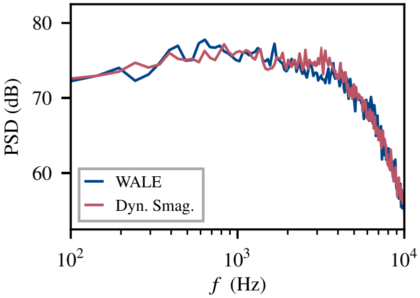

Fig. 6.3.24 Comparison of wall pressure spectra at $u_0 = 40\,\mathrm{m\,s^{-1}}$ under two different subgrid scale models.

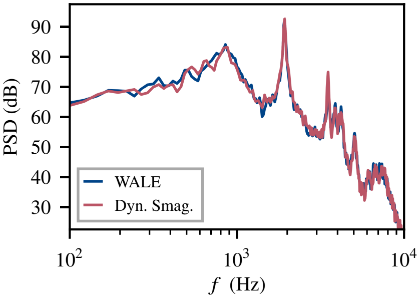

Fig. 6.3.25 Comparison of pressure spectra at the edge microphone at $u_0 = 40\,\mathrm{m\,s^{-1}}$ under two different subgrid scale models.

In summary the DNC gap noise simulations can be well performed with our standard setup. While the boundary layer could be simulated reasonably well with a coarser time-step (although it benefits from a higher order spatial discretization scheme) the acoustic propagation inside the gap requires at least our base time step and is relatively insensitive towards the spatial resolution and the spatial order of discretization. Our base configuration can be considered a compromise between the two different requirements. This study is promising for the planned application to a full-scale vehicle as the simulations on the coarse mesh already delivered acceptable results up to high frequencies.

The results from this chapter are thus seen as a thoroughly validated starting point for additional studies towards gap noise simulation of real cars, i.e. application to advanced modifications in the next chapter and in a second step the application to a full-scale vehicle model.

7 Study of an Idealized Rear Door Gap Model II – Analysis and Simulation of Advanced Modifications

The previously studied reference case allowed us to analyze some basic aspects of automotive gap noise and to establish and validate a DNC for its numerical simulation. However the industrial application of a gap noise simulation approach is more demanding. On the one hand a simulation needs to predict the consequences of design changes of the gap and on the other hand the real flow conditions are more difficult than a ZPG boundary layer. In addition not much is known systematically about the influence of different design parameters and e.g. APG conditions on the gap noise. In this chapter we try to address these issues by systematically increasing the complexity of the reference case and by applying our DNC to several selected cases. First we study the influence of the inflow conditions on the gap noise and then a variety of geometry variations is tested. Rounded leading and trailing edge shapes are introduced, that introduce pressure driven separation or affect the leading edge noise at the gap's downstream edge. We modify the position of the gap opening relative to its resonance volume, introduce vertical offsets of the downstream edge (which is a common issue of the manufacturing process) and systematically modify the gap's opening length to affect the shear layer stability of the system.

7.1 Varying Inflow Conditions

To modify the inflow conditions of the idealized gap we used the rotatable NACA-0012 airfoil described in chapter 6. For these measurements the flat plate was shifted 30 mm from the nozzle's symmetry plane. The rotation axis of the airfoil was fixed 100 mm above the flat plate's upper surface. In this section we compare three different flow conditions: The previous ZPG case, a case called APG-8 where the rotation axis was positioned 855 mm downstream of the flat plate's nose with $\alpha = 8°$ AOA and a case called APG-5 where the rotation axis was fixed 455 mm downstream of the flat plate's nose with $\alpha = 5°$ AOA.

As shown in fig. 7.1.1 the realized pressure distribution of the three cases varies significantly. The ZPG case is characterized by its zero pressure gradient whereas the APG-8 case shows a strong adverse pressure gradient at the measurement module and C_p reaches a relative maximum at 1100 mm. As the airfoil is positioned far more upstream in the APG-5 case its pressure distribution can be principally regarded as a streamwise translation of the APG-8 case, i.e. the measurement modules are located downstream of the relative pressure maximum which leads to nearly ZPG conditions in the vicinity of the gap opening. As discussed in chapter 5 the installation of the NACA-0012 airfoil leads to significant three-dimensional effects that reduce the spanwidth of the free stream core. In fig. 7.1.2 one can see that C_p begins to drop slightly between 50 mm $\leq |z| \leq$ 100 mm indicating the inset of the open jet's turbulent shear layer. Hot wire measurements at $x = 1165$ mm in the spanwise direction at different heights above the flat plate (10 mm $\leq y \leq$ 70 mm) help to understand this phenomenon. It is seen in fig. 7.1.3 for the ZPG conditions that the influence of the shear layer is stronger inside the boundary layer as the mean velocity drops much closer to the symmetry plane than outside of the boundary layer. Even there the two-dimensional inflow region is at least 200 mm wide ($|z| \leq$ 100 mm). Under the APG-8 case (see fig. 7.1.4) the spanwidth of the core is reduced drastically and the usable range is limited by $|z| \leq$ 62.5 mm inside the boundary layer. Nevertheless the free stream core is still wide enough to consider two-dimensional inflow conditions along the spanwidth of the gap opening.

Due to the airfoil the boundary layer is found to thicken significantly and to generate a boundary layer shape factor H with drastically reduced mean flow velocities close to the wall (see fig. 7.1.5) that are typical for APG boundary layers (see table 7.1). The cases APG-5 and APG-8 haven been chosen such that their respective boundary layer thickness δ and momentum thickness θ are very similar while they only differ significantly at the displacement thickness δ^*. Interestingly the APG-5 boundary layer is already relatively relaxed and its shape is quite close to a typical ZPG case. Analysis of the wall pressures confirms these findings. The mid frequency slope of the wall pressure spectra of the APG cases increases with increasing shape factor H, the maximum level increases with the boundary layer thickness δ and H and the maximum frequency is shifted to lower frequencies (see fig. 7.1.6). The streamwise coherence of the two APG cases (fig. 7.1.7 and fig. 7.1.8) again decays faster than the pure ZPG case with APG-5 being much closer the ZPG case ($\alpha = -0.145$) than APG-8 ($\alpha = -0.2$) which highlights the intermediate type of the APG-5 boundary layer.

As a second step the reaction of the gap on the different incoming boundary layers becomes interesting. On the one hand this situation can help to estimate the consequences of thicker boundary layers with comparable shape on gap noise and on the other hand it might help to judge the influence of different shapes and thus flow conditions on the gap noise. In general we would expect that the shear layer of the gap gets further stabilized as the effective velocity inside the opening should become slower. As also the streamwise coherence of the boundary layer is changed we expect the interaction of the acoustics with the shear layer to be affected by

Table 7.1 Experimental boundary layer parameters of the ZPG, APG-5 and APG-8 cases determined at $x = 1165$ mm.

	u_e (m/s)	δ (mm)	δ^* (mm)	θ (mm)	H	u_τ (m/s)	Re_τ	Re_θ
ZPG	41.7	18.7	3.21	2.33	1.38	1.51	1830	6310
APG-5	42.8	34.3	7.79	5.24	1.49	1.27	2830	14560
APG-8	40.9	33.7	9.69	5.47	1.77	0.95	2080	14530

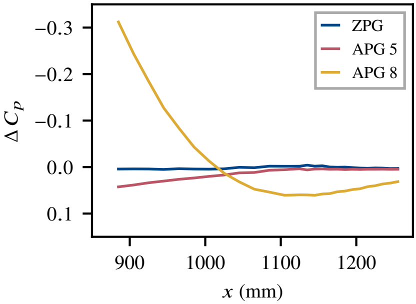

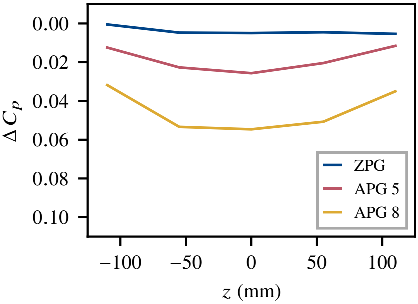

Fig. 7.1.1 Experimental streamwise pressure distribution of the different inflow conditions.

Fig. 7.1.2 Experimental spanwise pressure distribution of the different inflow conditions.

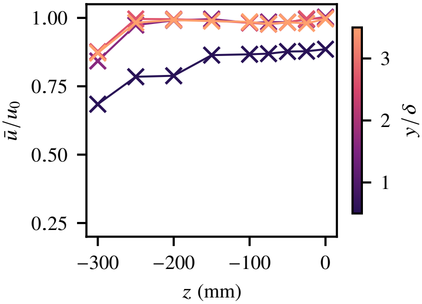

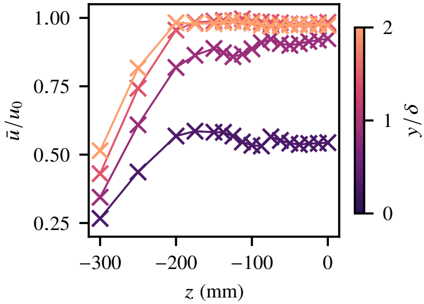

Fig. 7.1.3 Experimental mean velocity $\overline{u_1}$ of the ZPG case along the z-direction at different wall distances.

Fig. 7.1.4 Experimental mean velocity $\overline{u_1}$ of the APG-8 case along the z-direction at different wall distances.

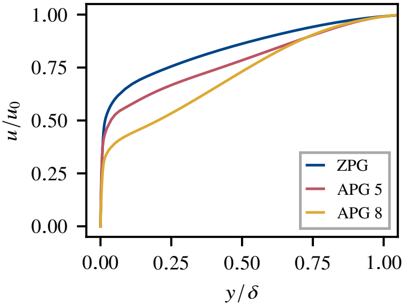

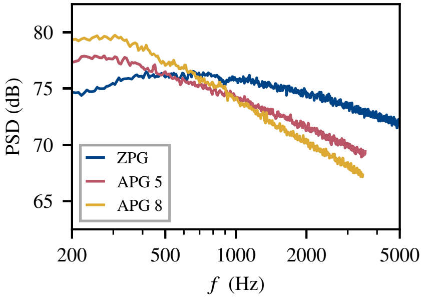

Fig. 7.1.5 Experimental mean velocity boundary layer profiles at $x = 1165$ mm.

Fig. 7.1.6 Experimental wall pressure spectra at $x = 1165$ mm. ($M = 2^{13}$, $^{D}/_{M} = 0.5$).

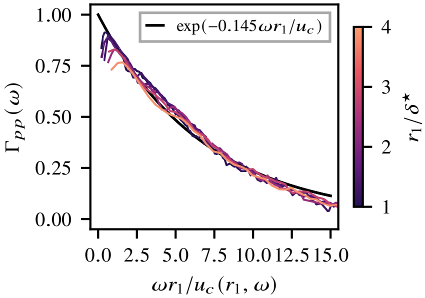

Fig. 7.1.7 Streamwise coherence of the APG-5 case. ($M = 2^{10}$, $^{D}/_{M} = 0.5$)

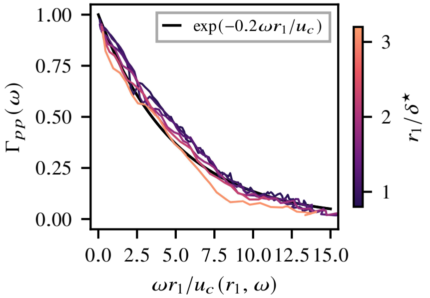

Fig. 7.1.8 Streamwise coherence of the APG-8 case. ($M = 2^{10}$, $^{D}/_{M} = 0.5$)

these changes. Fig. 7.1.9 shows the pressure spectra at the edge microphone of the gap. The changes to the spectrum are quite similar to the changes of the wall pressure spectra. Noise increases at low frequencies where the inflowing boundary layer wall pressure spectra have higher levels. At higher frequencies the levels begin to drop broadbandly. It is found that again the excitation of the first two resonance frequencies depends on the boundary layer. While the levels at the Helmholtz frequency f_H of the ZPG and APG-5 cases are almost identical, the level at the APG-8 case is increased about 5 dB, although the boundary layer wall pressure spectra at f_H are almost on par and approximately 1.5 dB lower than at the ZPG case. At f_1 especially the ZPG and APG-5 case are strongly excited, while the APG-8 case drops in comparison, which confirms the former assumptions on the influence of the boundary layer. We can thus conclude that a precise prediction of the inflow is absolutely crucial for a correct numerical simulation of these passive gap noise phenomena as even the shape of the boundary layer plays a significant role on the spectra and the location of maximum noise. Especially it becomes clear that also the displacement thickness δ^* has a significant influence on the noise inside the gap although typically only the measure θ/L_0 is chosen to classify the stability of the shear layer and accordingly to classify the case, c.f. De Jong[22] and chapter 3. Due to these changes we will also consider different inflow conditions for the planned design modifications of the gap.

The numerical simulation of the different inflow conditions is much more demanding than the previously studied ZPG case. First their respective Reynolds number Re_θ is much higher and second the geometrical situation is more complex. From the experience from the simulation of Hu and Herr's APG-10 case from chapter 5 we will now apply strategies developed in this section to our two APG cases. In fig. 7.1.10 we show principal sketches of the chosen LES sub-domains and the ALF regions. In the APG-5 case the airfoil is positioned so far upstream that it is possible to exclude it from the LES sub-domain and to apply ALF for at least 10δ which is not ideal. From chapter 5 we know that the Reynolds stresses downstream of the airfoil must be expected to be at least 20 % too high compared to experimental values and consequently we decided to scale the ALF target stresses to 80 % of the original RANS results. Due to the large distance between the airfoil's rotation axis and the gap opening it is also possible that the mean boundary layer profile quality of the EB-RSM RANS worsens compared to the experiment. In Hu and Herr's case the results from point x_2 were much better than at x_1, however it is possible that this implies a wrong development tendency that continues further downstream and finally leads to opposite mismatches. In the APG-8 case the NACA-0012 airfoil must be included in the LES sub-domain. Consequently we apply ALF similar to chapter 5 below the airfoil and then let the boundary layer develop in the pure LES region. As the friction velocity is comparably low in this region we expect the mesh to be only slightly under-resolved. However the gap opening is again located further downstream than point x_2 from chapter 5 and thus new uncertainties are possible.

In fact it turns out that the numerical simulation of the incoming boundary layer is difficult in both cases. In fig. 7.1.11 one can see that the simulated mean velocity profiles from the LES do not exactly match the measured profiles. While the ZPG boundary layer analyzed previously only shows the small, located, log-layer mismatch this mismatch extends for the APG-5 case up to a wall distance of 0.3δ. At the APG-8 case the mismatch increases even further and extends up to 0.5δ. An adequate analysis would be required to understand the reasons for these issues. As we assume that they are related to the specific setup of our experiments and as the realized profiles at least resemble the experimental tendencies we will nevertheless accept these results as they are. Especially fig. 7.1.12 shows that the wall pressure spectra of the three cases are not too far off from the experimental results, again with optimal results for the ZPG case. At the APG-5 case the mid frequency slope is a little bit too flat which leads to slightly increased levels around 3 kHz and slightly reduced levels below 1 kHz. However the spectrum lies within a ±3 dB corridor around the experimental values and drops at 5 kHz. The APG-8 spectrum matches the experimental results reasonably well up to 1.5 kHZ. Between 1.5 kHz and the high frequency drop at 4 kHz a hump of approximately 3 dB can be seen. The coherence of the simulated wall pressures is again well matched with the asymptotic experimental curves. At the APG-5 case (see fig. 7.1.13) the simulated results decay a little bit faster than in the experiment but this behavior was already present in the ZPG case and is plausible due to a slight under-resolution. The decay of the coherence curves of the APG-8 case in fig. 7.1.14

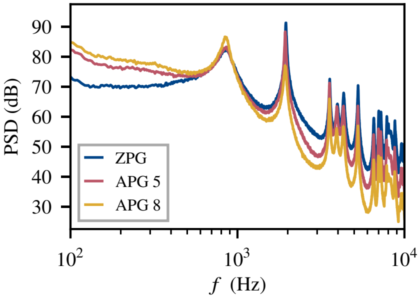

Fig. 7.1.9 Experimental wall pressure spectra of the ZPG, APG-5 and APG-8 cases at the edge microphone. ($M = 2^{14}$, $D/M = 0.5$)

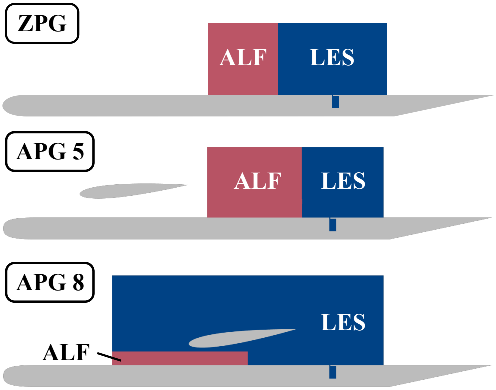

Fig. 7.1.10 Sketch of the LES subdomains and ALF regions in the $z = 0$ plane used for the numerical simulations.

excellently matches the experimental data. As the spectral validation provides good results, we consequently expect that the gap acoustics are not disturbed too much. The momentum thickness of the APG cases is much larger than on the ZPG cases and thus the shear layer in the gap opening should be much more stable than on the original ZPG case which should again decrease the gap's sensitivity towards slightly mismatched velocity profiles.

We can see in fig. 7.1.15 that besides these issues the simulation of the APG-5 case matches the experimental spectrum well up to 4.5 kHz where numerical dispersion and dissipation set in. Especially the increased levels at low frequencies above 250 Hz and the broadband slope of the mid frequency range are predicted correctly. At the APG-8 case (fig. 7.1.16) we see that again the spectrum up to approximately 1.5 kHz is well predicted. This includes the increased lower frequencies and the modified excitation of the Helmholtz frequency. Above 1.5 kHz probably the influence of the hump in the wall pressure spectra sets in and the levels are broadbandly increased up to 7 kHz. In summary the simulation seems to be able to predict the gap's behavior under different incoming boundary layers. If the present issues in the simulation of the boundary layers could be solved we assume that the remaining questions regarding the gap acoustics of the APG-8 case could be solved as well. As especially the frequency range below 1.5 kHz is well predicted for all cases we will have a deeper look on the flow to understand the reasons for the differences between the configurations.

Fig. 7.1.17 shows the turbulent kinetic energy in the $z = 0$ cross-section through the gap opening. It is clearly visible that the turbulence close to the wall and in the opening gets reduced from the ZPG to the APG-8 case, thus with increasing displacement thickness or decreasing friction velocity. This behavior is equivalent to a stabilization of the shear layer. Consequently the main vortex in the gap opening becomes less turbulent from ZPG to APG-8. In fig. 7.1.18 we show $\overline{u_1}$ scaled by the free stream velocity u_0 and the stream lines of the mean flow. It is found that the overall velocity in the opening is reduced which is plausible due to the different boundary layer profiles and in accordance with the calculated turbulent kinetic energy. Additionally one

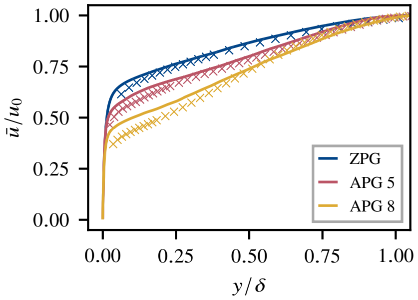

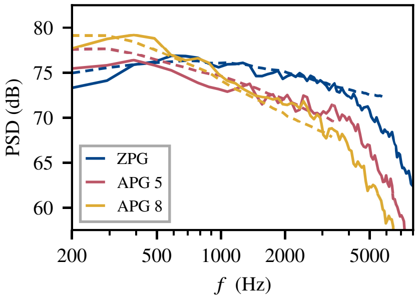

Fig. 7.1.11 Simulated mean velocity boundary layer profiles at $x = 1165$ mm compared to the experimental data.

Fig. 7.1.12 Simulated wall pressure spectra (solid) at $x = 1165$ mm in comparison to the corrected experimental data (dashed). ($M_{\text{exp}} = 2^9$, $M_{\text{sim}} = 2^{10}$, $^D/_M = 0.75$)

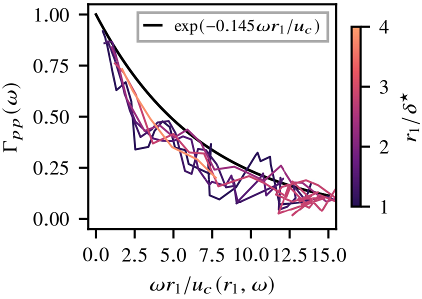

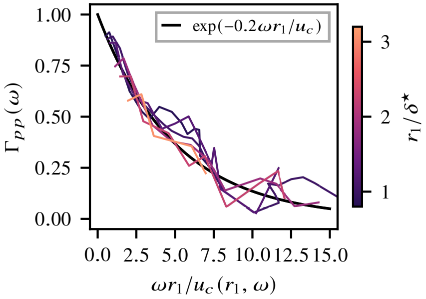

Fig. 7.1.13 Simulated streamwise coherence of the APG-5 case in comparison to the experiment. ($M = 2^9$, $^D/_M = 0.9$)

Fig. 7.1.14 Simulated streamwise coherence of the APG-8 case in comparison to the experiment. ($M = 2^9$, $^D/_M = 0.9$)

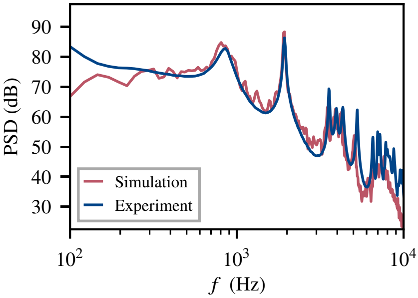

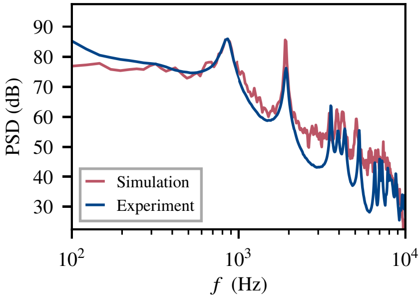

Fig. 7.1.15 Simulated gap acoustics of the APG-5 case in comparison to the experiment. ($M_{\text{exp}} = 2^{11}$, $M_{\text{sim}} = 2^{12}$, $^D/_M = 0.75$)

Fig. 7.1.16 Simulated gap acoustics of the APG-8 case in comparison to the experiment. ($M_{\text{exp}} = 2^{11}$, $M_{\text{sim}} = 2^{12}$, $^D/_M = 0.75$)

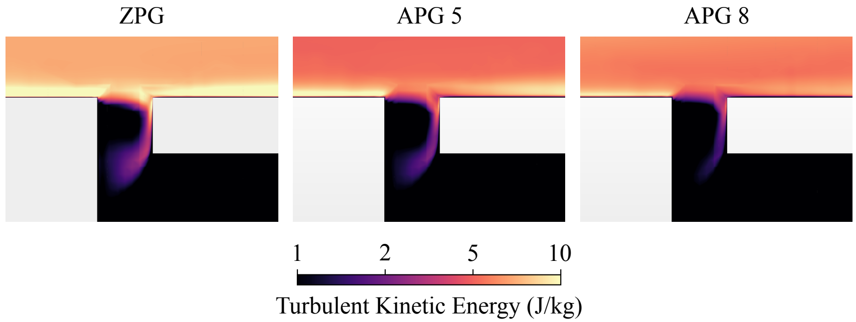

Fig. 7.1.17 Turbulent kinetic energy in the $z = 0$ plane in the gap opening.

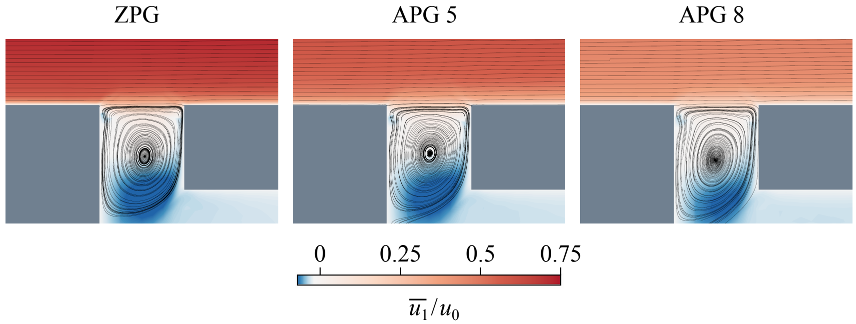

Fig. 7.1.18 Mean flow velocity and mean flow streamlines in the $z = 0$ plane in the gap opening.

can see that only in principle the structure of the main vortex remains constant between the three inflow conditions. With decreasing friction velocity from ZPG to APG-8 the vortex extends further into the cavity and allows a backflow from the gap's resonance volume into the opening which is a significant change to the original ZPG case.

7.2 Geometric Modifications

Above, we established three different inflow conditions and described their respective effects on the gap noise of the previously basic gap noise case. In the following we will use these inflow conditions to study the consequences of geometric modifications of the gap both experimentally and numerically.

7.2.1 Influence of Edge Shapes

Usually real vehicles do not incorporate any sharp edges on their exterior parts. While a certain minimal radius for every edge is required by law and manufacturing processes, bigger radii could be realized which gives the possibility for different designs. To understand the physics of automotive gap noise these rounded egdes however introduce additional difficulties. Pressure driven separation with a fluctuating separation line is possible on the leading edge of the gap and additional interaction with different trailing edge shapes is likely. Schimmelpfennig described the influence of the edge shapes on gap noise on his comparable experiment. Additionally he used a comparison between sharp and rounded edges to analyze physical aspects of gap noise.[90]

In our experiment we were able to interchange the sharp edges with rounded edges with 4 mm radius, which equals the height of the gap opening (see fig. 7.2.7). In fig. 7.2.1 one can see the different spectra of the four different edge shape combinations measured at the edge microphone at $u_0 = 40\,\mathrm{m\,s^{-1}}$. It is found that a similar leading edge shape leads to identical spectra below 1 kHz and the shape of the trailing edge is negligible. The levels of the rounded leading edge in this frequency range are much higher than those of the sharp leading edge and especially the Helmholtz frequency gets excited much stronger with an increase of approximately 30 dB. Above 2 kHz the situation has changed and now the shape of the trailing edge basically determines the levels, with a rounded trailing edge leading to a faster decay at high frequencies. In this frequency range the leading edge shape, especially for a rounded trailing edge, is not completely negligible but the trailing edge certainly plays the decisive role. Between 1 kHz and 2 kHz a transition region is found, the levels of the R – R case begin to drop towards the lower levels and those of the S – S case begin to rise towards the higher levels. Schimmelpfennig analyzed this phenomenon in much detail. He pointed out that in his experiment three physical mechanisms lead to the described behavior. First a rounded leading edge leads to increased separation with a fluctuating separation line, accordingly turbulence in the gap opening's shear layer is increased and gets amplified inside the cavity. Second a sharp trailing edge has a bigger interaction with the turbulent boundary layer and leads to increased turbulence compared to a smooth rounded edge shape. In comparison to the leading edge phenomenon this interaction mechanims is supposed to be quieter. Third and most importantly the transition between the frequency ranges of dominance of the two effects is governed by the surface averaging effect that is well known in the sensor attenuation of wall pressure measurements. The gap opening is $L_0 = 4$ mm long and below a certain wavelength the effective excitation of the gap due to the pure turbulence above its opening is strongly attenuated and thus the influence of the different leading edges cannot be distinguished above this frequency limit. As the major noise source is attenuated at these high frequencies the local interaction of the boundary layer with the trailing edge determines the levels in this region. This behavior gets confirmed by measurements with a 2 mm long gap opening (see fig. 7.2.3). The transition region is now situated between 1.5 kHz and 3 kHz which indicates less attenuation in this case. Above this limiting frequency again the trailing edge shape dominates the spectra.*

One major difference between our experiment and Schimmelpfennig's results is present below the Helmholtz frequency f_H. In our experiment the influence of the leading edge is already visible in this frequency range, while Schimmelpfennig found that this area is completely independent from the edge shapes. However we want to point out that the microphone position in the two experiments were different and that Schimmelpfennig used 1/2-inch microphones instead of 1/4-inch microphones. In chapter 6 we saw that the levels below f_H are completely dominated by hydrodynamic pressure fluctuations and consequently an additional damping in his experiments might be possible.

In addition it is observed that the acoustic radiation of the cavity changes significantly with the round leading edge. One can see in fig. 7.2.2 that in these cases a sharp tonal peak is detected by the Kulite sensors at the Helmholtz frequency while a small detention was present with the sharp leading edge. Also the level of the peak depends significantly from the trailing edge shape with the sharp trailing peak being approximately 5 dB higher than the round trailing edge peak. On the one hand this could be easily explained as the Helmholtz frequency is excited much more effectively and accordingly more noise will be radiated. On the other hand this finding proves that the directivity of the gap's acoustic radiation depends strongly on the realized edge shape. In cases where the external noise plays a role, e.g. if significant parts of the gap noise are transmitted into the vehicle via windows that surround the gap, this phenomenon needs strong consideration in the development process.

A last discussed aspect of the edge modifications under ZPG conditions is the velocity dependency of the Helmholtz resonance shown in fig. 7.2.4. If the edges are both sharp we have already seen, that the Helmholtz frequency remains constant in the velocity range $25\,\mathrm{m\,s^{-1}} \leq u_0 \leq 45\,\mathrm{m\,s^{-1}}$ and only the excitation power of the resonance frequency varies. If the gap's trailing edge is rounded, the excitation power is very similar to the reference case but one can see that the frequency itself begins to shift slightly. If the leading edge is rounded instead, the excitation of the Helmholtz frequency increases rapidly and begins to drop at $u_0 = 45\,\mathrm{m\,s^{-1}}$. Furthermore the frequency shift is comparable to the former case. This frequency shift cannot be explained by a classical feedback mechanism as such mechanisms would show a much larger shift in the studied velocity range. Accordingly we assume that the resulting shear layer varies with the free stream velocity which changes the acoustic impedance condition and the effective opening length of the gap. We can conclude that the excitation strength of the Helmholtz frequency thus depends on the shape of the leading edge and that rounded edges generally lead to a velocity dependent frequency shift of the Helmholtz frequency. For the numerical simulation of the edge modifications we used the mesh with the refined gap opening from the previous parameter study of the simulations of the reference case to capture any possible

---

[*] In these cases a slight frequency shift of the Helmholtz frequency is found when rounded edges are introduced. Due to the rounded edges, the effective opening length is increased which again affects the Helmholtz frequency. As $L_0 = 2\,\mathrm{mm}$ and $r = 4\,\mathrm{mm}$ of the rounded edges the effective opening length gets at least 25 % bigger and thus a visible frequency shift is observed.

Fig. 7.2.1 Experimental pressure spectra of leading and trailing edge variations of the base gap with $L_0 = 4\,\mathrm{mm}$, measured at the edge microphone under ZPG conditions at $u_0 = 40\,\mathrm{m\,s^{-1}}$. ($M = 2^{14}$, $D/M = 0.5$)

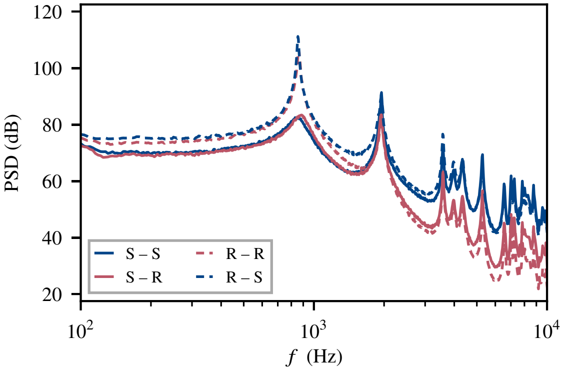

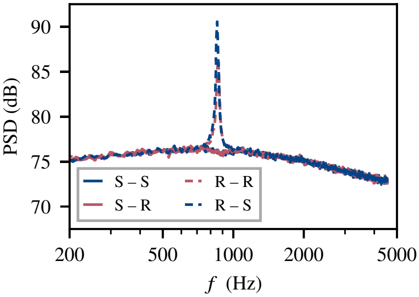

Fig. 7.2.2 Experimental wall pressure spectra at Kulite sensor no. 4, time-synchronously measured to the data from fig. 7.2.1. ($M = 2^{13}$, $D/M = 0.5$)

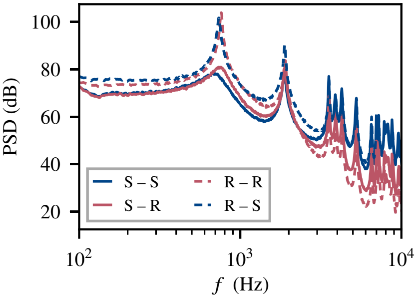

Fig. 7.2.3 Experimental pressure spectra of leading and trailing edge variations of a gap with $L_0 = 2\,\mathrm{mm}$. ($M = 2^{14}$, $D/M = 0.5$)

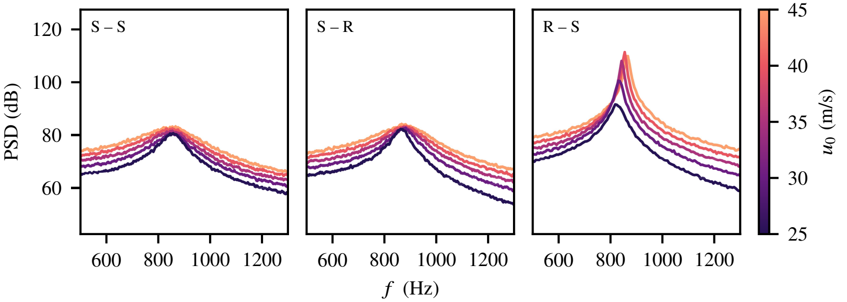

Fig. 7.2.4 Experimental velocity dependency of the Helmholtz resonance under ZPG conditions. Measured at the edge microphone inside the cavity. ($M = 2^{14}$, $D/M = 0.5$)

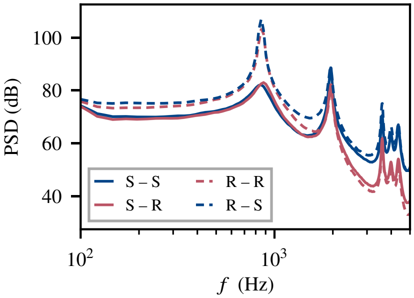

Fig. 7.2.5 Experimental pressure spectra of leading and trailing edge variations of the base gap with $L_0 = 4\,\text{mm}$. ($M = 2^{11}$, $D/M = 0.5$)

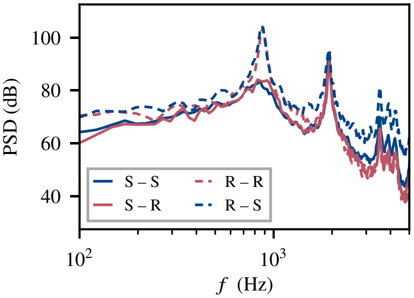

Fig. 7.2.6 Simulated pressure spectra of leading and trailing edge variations of the base gap with $L_0 = 4\,\text{mm}$. ($M = 2^{12}$, $D/M = 0.75$)

local flow effects. The results of these simulations are shown in fig. 7.2.6 and compared to the experimental results with similar frequency resolution from fig. 7.2.5. It is found that the general trends of the phenomenon are again well captured by the simulation. Especially the offset between the leading edge shape in the frequency range below 1 kHz is well predicted. The transition region between 1 kHz and 2 kHz is also well predicted. In the high frequency range some difficulties can be seen. As the spectrum of the reference case was matched quite well with the experiment, we can see that in all cases the rounded edges introduce numerical disturbances at these frequencies. Although the cases with sharp trailing edge both show higher levels than the rounded trailing edge cases, their spectra do not collapse and especially the case R – S shows too high levels. The spectra of the rounded trailing edge cases nearly coincide, as it was seen in the experiment, but overall the difference to the reference case S – S is smaller than in the experiment. From an engineering point of view it is very promising that the method can predict the leading edge dominance where the highest levels are expected.

Thanks to the promising quality of the simulation results we can study again the turbulent kinetic energy (fig. 7.2.7) and the mean flow streamlines (fig. 7.2.8) in the $z = 0$ plane through the gap's opening. The turbulent kinetic energy from our simulations nicely confirms the explanations from Schimmelpfennig. If both edges are sharp, the flow separates more or less tangentially and the turbulence level in the gap opening is low. Close to the trailing edge a relatively strong turbulent interaction region is visible. If the trailing edge is rounded only this interaction region changes: On the one hand it grows but on the other hand the rounded opening covers the gap from the turbulent interaction zone. For the rounded leading edge, the case is very different. The shear layer separates early and spreads significantly which directly leads to a large amount of turbulence inside the gap opening. As the shear layer impinges the trailing edge a large turbulent vortex in the opening is generated. If additionally the trailing edge is rounded we again see the covering effect that transforms the opening vortex and deflects it partially towards the outside of the gap opening. The streamlines provide even more insights: The reference case

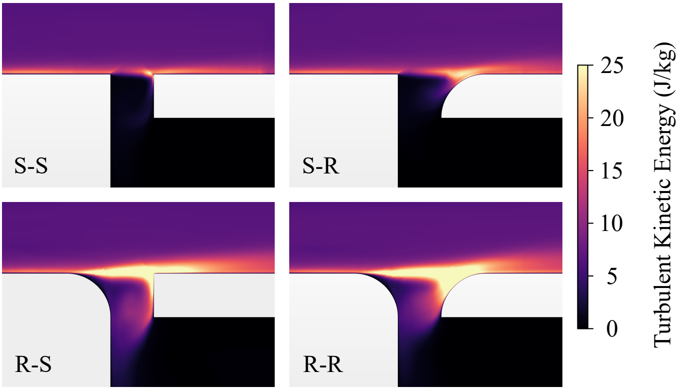

Fig. 7.2.7 Turbulent kinetic energy of the four different edge modifications in the $z = 0$ plane in the gap opening.

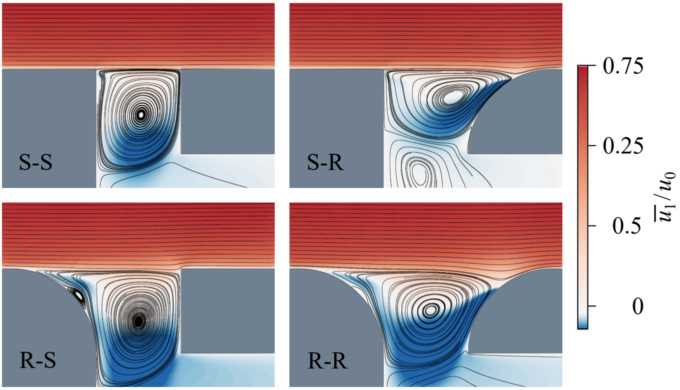

Fig. 7.2.8 Mean flow velocity and mean flow streamlines of the four different edge modifications in the $z = 0$ plane in the gap opening.

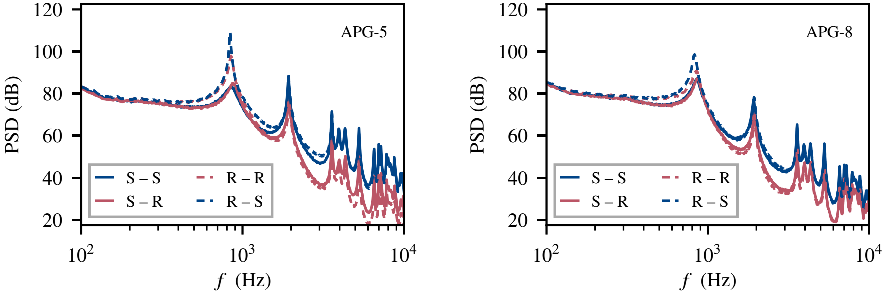

Fig. 7.2.9 Pressure spectra of the leading and trailing edge modifications at the edge microphone at $u_0 = 40\,\mathrm{m\,s^{-1}}$ under APG inflow conditions. ($M = 2^{14}$, $^{D}/_{M} = 0.5$)

is characterized by its large stable vortex in the opening. The rounded trailing edge leads to a compression of this vortex leading to a smaller backflow velocity at the bottom of the opening. Consequently a secondary vortex is formed below the opening that leads to a stabilization of the system. In the case of the rounded leading edge a clear separation bubble is visible and the backflow velocity in the gap opening is significantly increased. One can also notice the non-vanishing backflow from the resonator volume into the opening. The additional rounded trailing edge again weakens these effects as it covers the gap's resonator volume and deflects the opening vortex which also reduces the size of the separation bubble.

Finally our modular experiment gives us the possibility to test the influence of the different inflow conditions on the edge modification. Fig. 7.2.9 shows that in fact the boundary layer has a decisive effect on the influence of the edge shapes. With increasing shape factor (and therefore assumed increased shear layer stability) we see that the influence of the rounded leading edge decreases drastically. Furthermore the positive effect of the rounded trailing edge is reduced with increasing shape factor.

7.2.2 Influence of the Opening Position

In his work De Jong pointed out in detail that also the position of the gap opening relative to the resonator volume can play a significant role for the noise generated in the gap.[22] Although a change of the gap's opening position does not change the acoustic properties of the gap, his experiments proved that an opening at the downstream edge of the resonator volume can lead to the inset of aeroacoustic feedback while a gap opening at an upstream position still remains in a passive mode. Using particle image velocimetry he could prove that the flow in the opening changes significantly between the two opening positions: The upstream position showed a large stable vortex, as seen in our simulations, while the shear layer in the downstream position behaved more like an impinging jet. The inflow conditions in De Jong's work generally lead to much more unstable shear layers ($\theta/L_0 < 0.2$) than in our experiment. Nevertheless we want to study the influence of the gap opening position on our experiment as this design could be adapted on real vehicles.

As shown in fig. 7.2.14 we study four different configurations. For the case with sharp edges and the case with a rounded leading edge, we realized an opening at the upstream edge of the cavity and at the downstream edge, respectively. These cases are referred to as *S-S up*, *S-S down*, *R-S up* and *R-S down*. As we are looking for a change of the shear layer stability we need to investigate the gap noise of these configurations under different velocities. Fig. 7.2.10 shows that switching the opening of our reference case to the downstream position does not affect the spectra at all, which confirms again that in these cases mainly the fluctuations of the turbulent boundary layer get resonantly amplified while the shear layer remains macroscopically stable. With a rounded leading edge the gap becomes very sensitive to the opening position (see fig. 7.2.11). If the opening position is located at the resonator volume's downstream edge the Helmholtz frequency of the gap gets excited much more effectively than at the upstream position. Especially the maximum level with approximately 120 dB is reached at $u_0 = 30\,\mathrm{m\,s^{-1}}$

where the upstream position reaches only 100 dB.[†] In contrary the levels above $u_0 = 40\,\mathrm{m\,s^{-1}}$ behave in an opposite manner and the downstream position shows lower levels than the upstream position. These findings prove that the opening position can have a significant influence on the maximum levels of gap noise as soon as some kind of shear layer instability is involved. Especially on real industrial applications, where edges are usually rounded, the opening position could be an effective design parameter.

Again we applied the same simulation strategy as before to the four presented cases at $u_0 = 40\,\mathrm{m\,s^{-1}}$ and use the refinement of the gap opening. The experimental results of the four cases are summarized in fig. 7.2.12 up to 5 kHz. Fig. 7.2.13 shows the results of the simulation. Up to 2 kHz the simulated results match the experiment very well and even the present frequency shift and the different levels between the two different positions of the rounded leading edge can be predicted. Above 2 kHz the already known numerical disturbances of the rounded edges set in and reduce the quality of the solution but the main effect of the position change could be successfully simulated.

An analysis of the turbulent kinetic energy in 7.2.14 shows that this time indeed no significant changes of the turbulent levels occur between the four modifications. Comparing the two modifications with rounded edges one can see that the opening vortex is smeared out at the downstream position. Especially particles inside this vortex are transported towards the interior of the cavity while they are pushed against the cavity's upstream wall and then again to the opening at the upstream position. The streamlines in fig. 7.2.15 prove this analysis for both cases, sharp and rounded leading edges. At the downstream opening position the backflow velocity is reduced for both leading edges and an inflow into the cavity is present that leads to a reduced stability of the vortex. Especially the separation at the rounded leading edge underlies significant changes. At the downstream position backflow from the cavity into the opening is found that leads to a reduction of the separation bubble.

7.2.3 Influence of Wall-normal Offsets

One of the most important (and often undesired) real-world influence factors on the gap design are wall-normal offsets of either the leading or the trailing edge. Tolerances in the manufacturing process can easily lead to positioning offsets of a few millimeters. While these effects are usually unimportant the dimensions of the gap opening change significantly with every millimeter. Especially a positive wall-normal offset will distort the viscous sublayer and the buffer layer and a negative wall-normal offset will probably lead to a jet like behavior as the trapping potential of the gap opening is reduced. The effects of wall-normal offsets have been addressed briefly in the literature by Schimmelpfennig[90] and by Wickern and Brennberger.[107]

As shown in fig. 7.2.22, we modeled wall-normal trailing edge offsets of +2 mm and −2 mm with respect to the flat plate level. The upstream end of the tailing edge module is positioned

---

[†] The maximum level at $u_0 = 30\,\mathrm{m\,s^{-1}}$ is high enough, that even the first harmonic of the Helmholtz frequency is excited which usually characterizes the inset of non-linear acoustic effects.

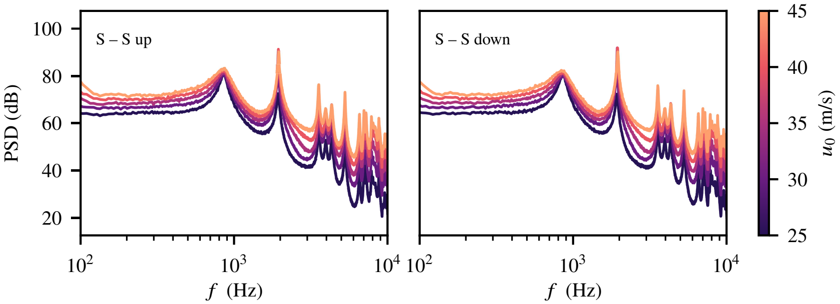

Fig. 7.2.10 Influence of the opening position of the base gap, relative to its resonance volume. Experimental velocity dependency of the pressure spectra at the edge microphone inside the cavity under ZPG conditions. ($M = 2^{14}$, $^{D}/_{M} = 0.5$)

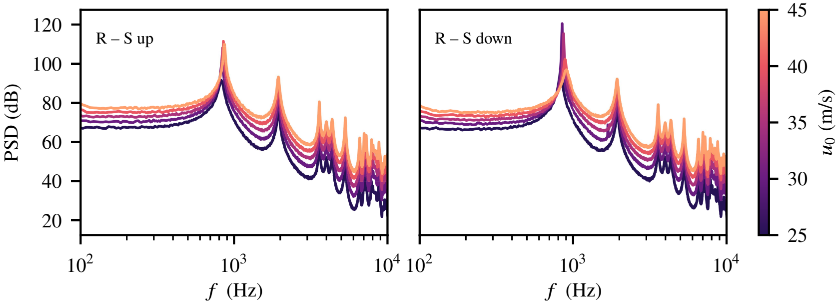

Fig. 7.2.11 Influence of the opening position of the base gap with rounded leading edge, relative its resonance volume. Experimental velocity dependency of the pressure spectra at the edge microphone inside the cavity under ZPG conditions. ($M = 2^{14}$, $^{D}/_{M} = 0.5$)

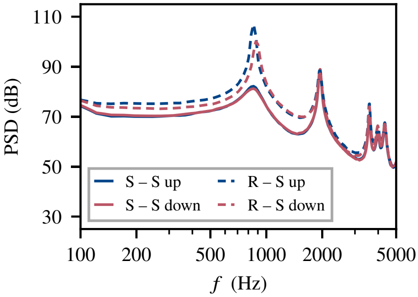

Fig. 7.2.12 Experimental pressure spectra of different opening positions and leading edge shapes at $u_0 = 40\,\mathrm{m\,s^{-1}}$. ($M = 2^{11}$, $^{D}/_{M} = 0.5$)

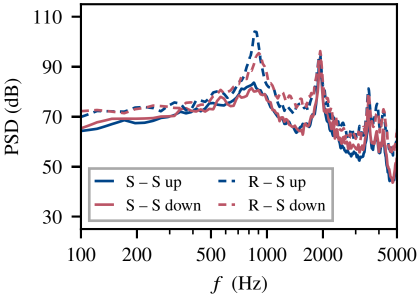

Fig. 7.2.13 Simulated pressure spectra of different opening positions and leading edge shapes at $u_0 = 40\,\mathrm{m\,s^{-1}}$. ($M = 2^{12}$, $^{D}/_{M} = 0.75$)

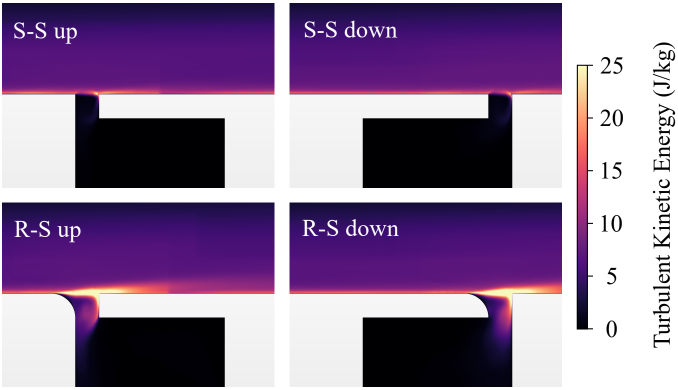

Fig. 7.2.14 Turbulent kinetic energy of the two different leading edges in the up- and downstream position in the $z = 0$ plane in the gap opening.

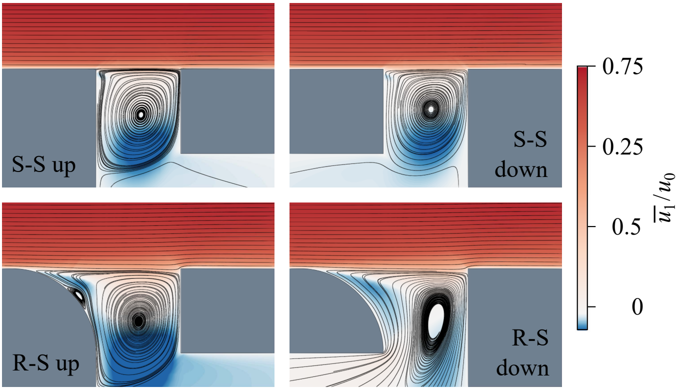

Fig. 7.2.15 Mean flow velocity and mean flow streamlines of the two different leading edges in the up- and downstream position in the $z = 0$ plane in the gap opening.

with the respective offset and the wall is then smoothly ramped downstream to recover the original flat plate level. The measured spectra of these configurations inside the gap are shown in fig. 7.2.16. As expected, the effects on the generated noise are strong: The positive wall-normal offset leads to a broadband increase of approximately 10 dB below 2 kHz. The resonance level at f_1 then recovers to the original levels and only a small increase of noise is found above f_1. Notably, the resonance frequencies f_3 and f_4 are shifted to smaller frequencies as they are based on vertical resonance modes and now the vertical height of the resonator volume is increased by 2 mm. The effect of the negative offset is comparably large: Below 1.5 kHz a slight decrease of the levels can be seen and the Helmholtz frequency is shifted by approximately 200 Hz. This shift can be explained as the effective opening length of the gap is massively increased in this case, which leads to a direct shift of the Helmholtz frequency. The resonance f_1 again recovers the original level of the reference case. Above f_1 the levels begin to drop rapidly as the dominating interaction with the trailing edge is reduced due to the negative vertical offset. Similar to the positive offset the resonance frequencies f_3 and f_4 are now shifted to higher frequencies. Also, one can see in fig. 7.2.17 that under the APG-8 boundary layer these trends remain the same but here the level of the Helmholtz frequency of the negative offset case is about 5 dB higher than the base case. This is only plausible under the assumption that the larger effective opening severely increases the shear layer instability and thus leads to more turbulence above the opening that excites the gap more effectively. The idea of reducing the obstacles in the boundary layer and therefore reducing noise by introducing the negative offset leads to an exact opposite effect.

Previously we saw that the edge shapes also have a significant influence on the generated noise by introducing pressure driven separation or reducing the interaction with the trailing edge. To increase complexity even further this behavior was also depending on the shape of the incoming boundary layer. Consequently, we assume that the edge shapes behave differently if they underlie wall-normal tolerances. Fig. 7.2.18 shows the edge modification at the different wall-normal offsets. The behavior of the base case is reproduced at both vertical offsets. Interestingly the increase of noise at the Helmholtz resonance between the rounded and sharp leading egdes is reduced under both offsets. Especially the maximum level of the rounded leading edge of the positive offset does not significantly excel the maximum of the base case. The influence of the trailing edge nearly vanishes at a negative offset. Under the APG-8 boundary layer (see fig. 7.2.19) the influence of the leading edge shape on the spectra nearly vanishes at both offsets. Notably it appears that even at the Helmholtz frequency the trailing edge shape dominates the spectrum. Again the influence of the trailing edge shape with a negative offset vanishes at high frequencies.

The numerical simulation applying the hybrid RANS/LES is straightforward and we apply a mesh refinement using 0.25 mm cells around the gap opening to capture potential small scale flow effects introduced by the wall-normal offsets. We compare the experimental data in fig. 7.2.20 and the calculated spectra at the edge microphone of the simulations (fig. 7.2.21). Again, the results up to f_1 are in good agreement with the measurements: The different levels of the approaches are calculated correctly as well as the frequency shift of the Helmholtz resonance at

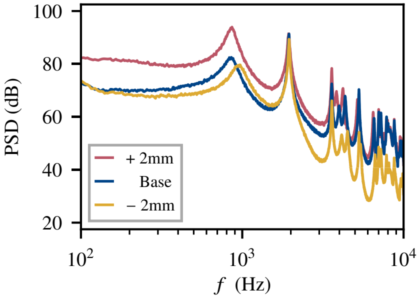

Fig. 7.2.16 Experimental pressure spectra of the base gap with different wall-normal offsets at the edge microphone under ZPG conditions at u_0 = 40 m s^{-1}. ($M = 2^{14}$, $D/M = 0.5$)

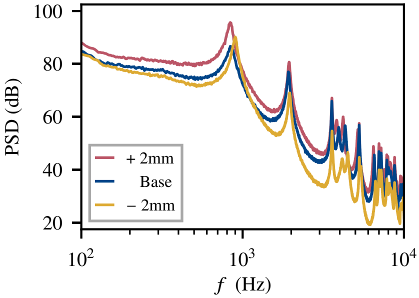

Fig. 7.2.17 Experimental pressure spectra of the base gap with different wall-normal offsets at the edge microphone under APG-8 conditions at u_0 = 40 m s^{-1}. ($M = 2^{14}$, $D/M = 0.5$)

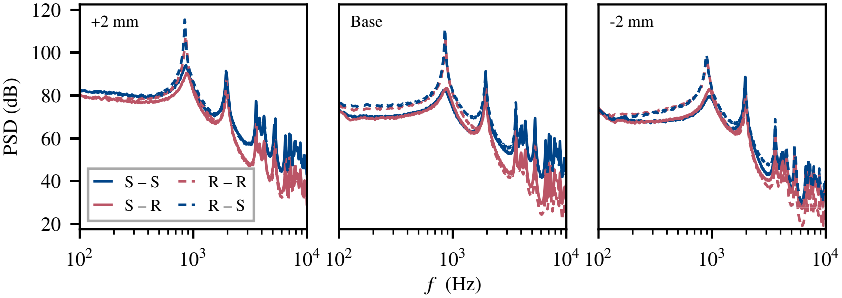

Fig. 7.2.18 Experimental influence of the edge variation on the pressure spectra of gaps with different vertical offsets under ZPG conditions at u_0 = 40 m s^{-1}. ($M = 2^{14}$, $D/M = 0.5$)

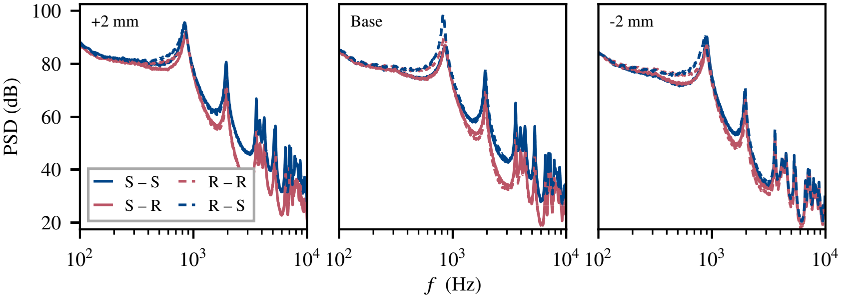

Fig. 7.2.19 Experimental influence of the edge variation on the pressure spectra of gaps with different vertical offsets under APG-8 conditions at u_0 = 40 m s^{-1}. ($M = 2^{14}$, $D/M = 0.5$)

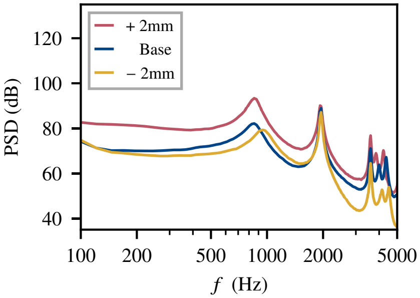

Fig. 7.2.20 Influence of wall-normal offsets: Experimental gap noise pressure spectra at $u_0 = 40\,\mathrm{m\,s^{-1}}$ under ZPG conditions. ($M = 2^{11}$, $^D/_M = 0.5$)

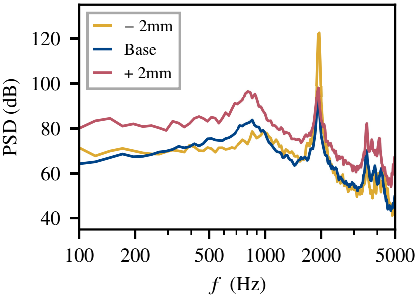

Fig. 7.2.21 Influence of wall-normal offsets: Simulated gap noise pressure spectra at $u_0 = 40\,\mathrm{m\,s^{-1}}$ under ZPG conditions. ($M = 2^{12}$, $^D/_M = 0.75$)

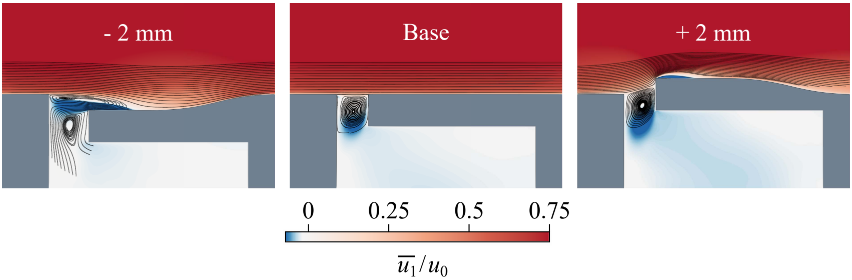

Fig. 7.2.22 Turbulent kinetic energy of the three different wall-normal offsets in the $z = 0$ plane in the gap opening.

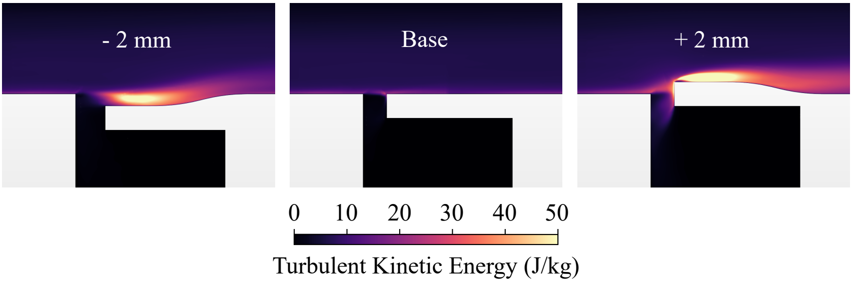

Fig. 7.2.23 Mean flow velocity and mean flow streamlines of the three different wall-normal offsets in the $z = 0$ plane in the gap opening.

the negative offset. At the first standing wave the level of the negative offset modification is extremely over-predicted indicating a strong instability at this frequency. Above f_1 the levels of this modification do not recover to its experimental target and only the base case and the positive offset curve are close to the experiment. Nevertheless the result is very promising in the range of the Helmholtz resonance that is usually considered the most important resonance frequency at industrial applications. Fig. 7.2.22 shows the severe changes to the mean flow. At a negative offset the flow separates tangentially at the gap's leading edge and develops a free shear layer that impinges at the smooth ramp. Below the shear layer a system of two counter-rotating vortices that leads to a strong backflow into the cavity is clearly visible. As the most turbulent region in this case is located above the covering plate (see fig. 7.2.23) the system is now much more unstable and vulnerable to small changes. The positive offset instead leads to a stable flow configuration with a strong vortex in the opening off the gap. However it is seen that the turbulence inside this vortex as well as its extent into the cavity volume has strongly increased. Additionally a strong interaction with the sharp edge and the boundary layer is present in these flow configurations.

We have seen that wall-normal offsets have significant effects on the measured gap noise. On some cases they lead to improvements while on other cases they worsen the noise levels. Our experiments and the simulations indicate that especially for a lowered trailing edge the instability in the shear layer increases dramatically. Therefore, it might be necessary to investigate a wide variety of negative offsets under different relevant inflow conditions to determine the robustness of reduced noise levels. In our opinion, minimum wall-normal tolerances to the planar reference case are thus the most desirable design parameter as the noise levels can be only optimized in these cases.

7.2.4 Influence of the Opening Length

Perhaps the most classical geometric modification in the field of gap noise is the opening length. In most of the literature cavity – inflow combinations that show aeroacoustic feedback are studied in much detail. In our work we already had a deeper look into classical passive cases, as e.g. our reference case. De Jong already discussed the inset of aeroacoustic feedback in a compact manner and found a stability limit $\theta/L_0 \approx 0.18$ to 0.26 that corresponds to results from linear stability theory as briefly discussed before.[22] In this chapter we focus on the inset of the shear layer instability. Tolerance issues in a vehicle's manufacturing process can lead to the previously discussed wall-normal offsets but obviously also to variations of the opening length. It is therefore important to understand the inset of the shear layer instability to judge the vulnerability of a gap design to this issue. Furthermore our developed numerical simulations should be principally able to treat cases with aeroacoustic feedback in the opening but we expect that the influence of the previously discussed log-layer mismatch increases as it affects the shape of the shear layer mean velocity profile. Furthermore the influence of the turbulent boundary layer fluctuations on the gap noise reduces with increasing opening length as the surface averaging effects set in at lower frequencies. Accordingly even numerical simulations based on a DES could lead to appropriate results as long as the RANS/LES transition occurs close enough to the gap's leading edge.

In our experiment we had the possibility to install the gap opening lengths 2, 4, 6, 8, 12 and 16 mm at the upstream position which corresponds to $0.14 \leq \theta / L_0 \leq 1.15$ for the ZPG case. The different opening lengths will always lead to different Helmholtz frequencies which explains shifts of this resonance between the different cases. In fig. 7.2.24 the edge microphone spectra in the operating velocity range of these variants are shown between 100 Hz and 1.5 kHz, where aeroacoustic feedback modes according to equation (2.22) are expected to set in. In the most stable case one can see that the Helmholtz frequency is almost constantly excited compared to the broadband levels around this frequency. As θ / L_0 decreases we see the behavior of our base case, where the excitation of the Helmholtz frequency strongly depends on the inflow velocity, but its frequency remains constant in the measured velocity range. With the 6 mm opening ($\theta / L_0 = 0.38$) we see first signs of shear layer instability. Quite similar to the cases with a rounded leading edge, the resonance frequency is shifted in the velocity range and the peak is sharp at low free stream velocities. With $\theta / L_0 = 0.29$, the 8 mm long opening this behavior increases as both the peak level and its frequency vary stronger in the observed velocity range. With the 12 mm opening length ($\theta / L_0 = 0.19$) suddenly a strong variation in the whole velocity range that is in agreement to the modes from equation (2.22) sets in. One can see two classical feedback modes. The first feedback mode gets shifted from 500 Hz to approximately 1200 Hz. As the feedback frequency gets closer to the geometric Helmholtz frequency the levels begin to increase rapidly as the two resonance mechanisms begin to couple effectively. Accordingly this coupling results in a shifted resonance frequency whose maximum level is reached when the two eigenfrequencies of the feedback mode in the opening and the Helmholtz frequency coincide. Above this frequency the levels of the system's resonance begin to drop again. The second couples to the Helmholtz frequency at very low velocities and leads to a first relatively strong excitation of the resonance and then fades out at higher free stream velocities. A similar but drastically amplified behavior can be seen at $\theta / L_0 = 0.14$ where three feedback modes are visible that independently couple to the Helmholtz resonance. Especially the strongest, first, feedback mode leads to a very sharp peak at the resonant lock-on.

A slightly different result is found under the APG-8 boundary layer in fig. 7.2.25 where we tested the opening lengths 2, 4, 6, 8 and 12 mm corresponding to $0.46 \leq \theta / L_0 \leq 2.74$. Although θ / L_0 is much higher than in the ZPG case the gap's behavior is relatively comparable to the ZPG case. With the 2 mm opening the excitation of the Helmholtz frequency remains nearly constant. At $\theta / L_0 = 1.37$, our base case under the APG-8 boundary layer, we already see a slight frequency shift of the resonance frequencies while again their respective levels remain almost constant. With the 6 mm opening the frequency shift remains quite similar but interestingly the Helmholtz resonance is now especially excited at higher velocities and the shape of the peak varies strongly. At $\theta / L_0 = 0.69$, the 8 mm opening signs of an instability wave are visible at the lowest velocity at approximately 600 Hz. However this small hump fades out and at 30 m s^{-1} the Helmholtz frequency reduces to a very broad "shoulder". As the velocity increases the Helmholtz resonance gets strongly excited again. The most interesting picture

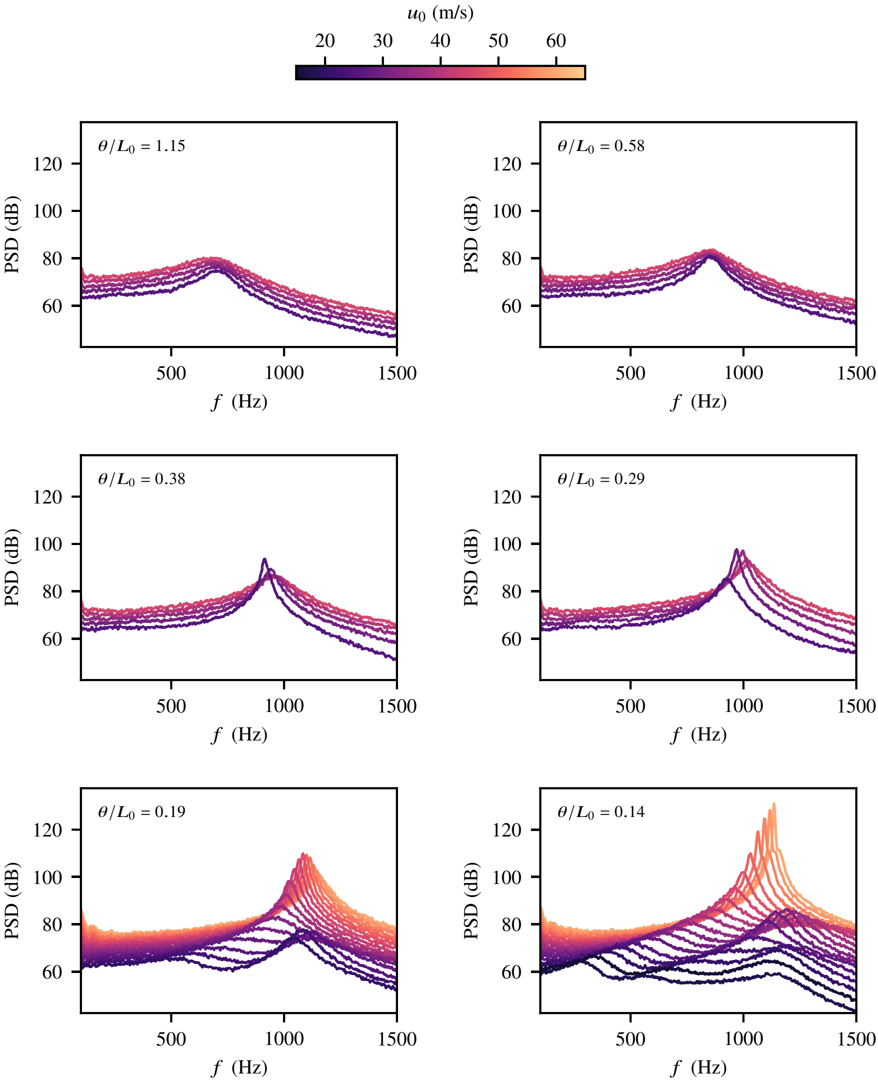

Fig. 7.2.24 Power spectra of the middle microphone at different gap opening lengths under ZPG conditions. Increasing instability of the shear layer leads to the inset of acoustics feedback in the gap opening that couples with the geometric Helmholtz resonance of the resonator volume. ($M = 2^{14}$, ${}^{D}/{}_{M} = 0.5$)

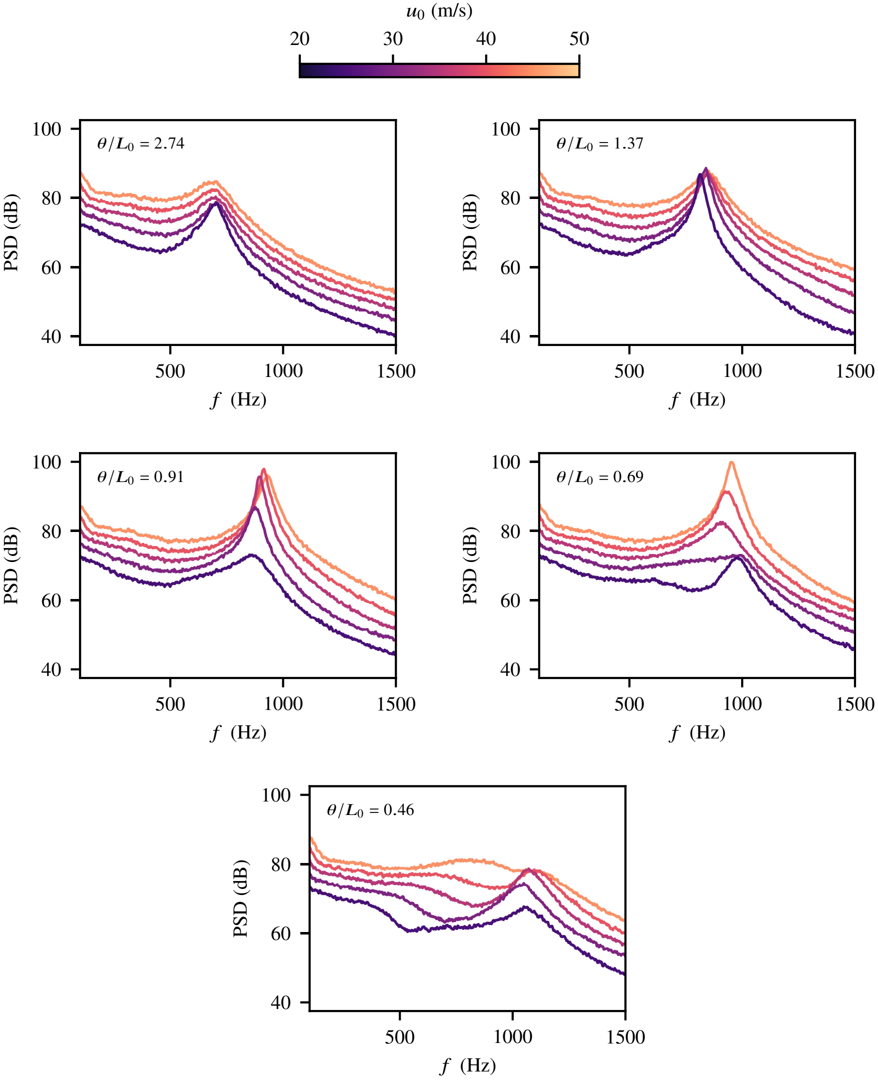

Fig. 7.2.25 Power spectra of the middle microphone at different gap opening lengths under APG-8 conditions. ($M = 2^{14}$, ${}^{D}/{}_{M} = 0.5$)

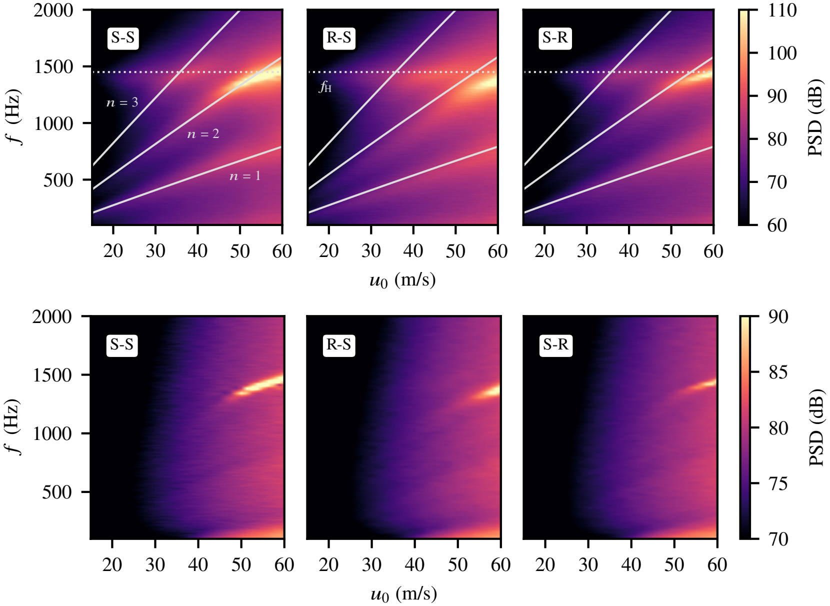

Fig. 7.2.26 Experimental Campbell diagrams of the gap noise (top) and the wall pressure at Kulite sensor no. 4 (bottom) of the deep gap with $L = 25\,\text{mm}$. The three theoretical self-sustained oscillation modes, according to eq. (2.22) with $u_c = 0.35u_0$ are indicated as well as the gap's depth resonance mode f_H.

can be found at $\theta/L_0 = 0.46$, the 12 mm opening. An aeroacoustic feedback mode is clearly visible between 300 Hz and 800 Hz but it is best described by a shoulder followed by a small sink instead of the small peak that it was in the ZPG case. As the shoulder gets closer to the Helmholtz frequency its excitation virtually stops and the levels are even lower than on the shorter opening lengths. This finding indicates that the shear layer of this boundary layer gets unstable but that the consequences of the shear layer instability depend on the inflow boundary layer velocity profile and turbulence.

These findings have good consequences for the development of gaps on vehicles. Usually θ/L_0 on vehicles lies well above 0.5 no matter which gap is studied. Accordingly, we can assume that, independent from its inflow conditions, no significant instability effects will occur in a typical velocity range. Of course there will be an influence of the opening length but with the results from our study of geometric modifications it is clear that the influence of the edge shapes and wall-normal offsets is stronger than tolerance or design issues of the opening length as long as $\theta/L_0 \geq 0.5$ can be secured.

In a last modification we aimed to study pure aeroacoustic feedback of a deep cavity in a very simplistic manner, i.e. representing the other extreme case of complete shear layer instability. We completely removed the gap covering, which corresponds to an opening length of 25 mm or $\theta/L_0 = 0.09$. Furthermore the spanwidth of the cavity is reduced to 30 mm instead of the previously used 100 mm and we varied again the leading and trailing edge shape. Thus only the middle microphone can be used for the experimental validation. The velocity dependent spectra of the middle microphone and the Kulite sensor are shown in fig. 7.2.26 in Campbell diagrams. First we analyze the base case with sharp edges. Again three aeroacoustic feedback modes (highlighted by solid grey lines) that correspond well to the Rossiter modes from equation (2.22) can be found. As these modes reach the geometric depth-mode of the cavity (dashed grey line) resonant lock-on occurs and the levels increase drastically. Additionally the slope of the feedback modes gets distorted as the lock-on occurs. In contrast to the passive cases where no acoustic radiation for the sharp edges could be detected by the Kulite sensors, a sharp peak is visible at the resonant lock-on. If the leading edge is rounded we can see three effects: The background noise level gets increased as the turbulence in the opening is increased. Second, the level of the resonant lock-on is reduced. Most probably this effect is caused by the superposition of the small scale and relatively incoherent shear layer turbulence and the feedback vortices that are very coherent in the spanwise direction. The increased shear layer turbulence reduces the coherence of the feedback eddies and thus the feedback intensity is reduced. Third we can also see a frequency shift of the feedback modes to lower frequencies. Interestingly this frequency shift cannot be detected if the trailing edge is rounded. Consequently it cannot be explained by a change of the effective opening length due to the edge's radius. Instead we assume that the effective convection velocity in the shear layer is reduced due to the turbulent separation at the leading edge which reduces the resulting feedback frequency. At the rounded trailing edge we can also see that the relative levels of the feedback modes to the broadband background noise is reduced. We assume that two effects are related to this result: First the vortex impingement gets smoother as we saw in our previous simulations and consequently we assume that the reflected acoustic wave is less intense and second its directivity towards the upstream edge might be disturbed as well. Accordingly the detected radiation at the Kulite sensor is reduced for both rounded edge variants. In summary, our results are in good accordance with the literature.[22,86]

As described previously our simulation approach should be able to treat aeroacoustic feedback. To test its limitations with a feedback dominated case the developed hybrid RANS/LES and an IDDES without turbulent boundary layer fluctuations have been applied to the $u_0 = 60\,\mathrm{m\,s^{-1}}$ case with sharp edges, where the strong resonant lock-on occurs, by Riedelsheimer in his Master's thesis, [85]. While the details of his simulations were discussed in his thesis, we want to summarize and categorize his main results in the context of the developed hybrid RANS/LES approach based on ALF.

The utilized mesh is comparable to our standard base mesh and thus the resulting flow CFL number of the mesh is increased which corresponds to slightly worse spatial resolution in this case compared to the previous $u_0 = 40\,\mathrm{m\,s^{-1}}$ cases. Consequently, the mean boundary layer profile at $x = 1165\,\mathrm{mm}$, calculated by the hybrid RANS/LES in fig. 7.2.27 shows a

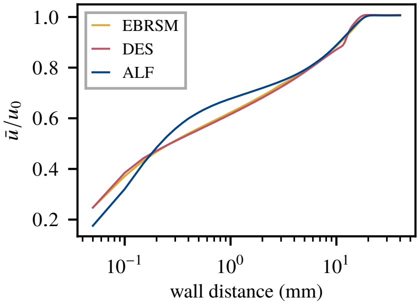

Fig. 7.2.27 Logarithmic scaled mean velocity profiles at $x = 1165$ mm.

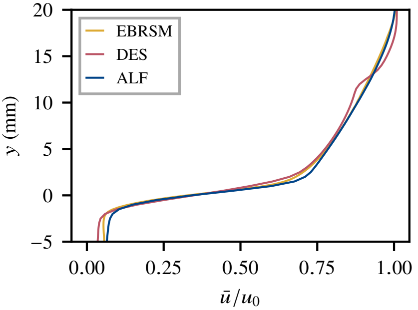

Fig. 7.2.28 Mean velocity profiles in the middle of the gap's opening at $x = 1212$ mm.

Fig. 7.2.29 Experimental and numerical wall pressure spectra at the different Kulite sensor positions at $u_0 = 60\,\mathrm{m\,s^{-1}}$. ($M_{\mathrm{exp}} = 2^{12}$, $M_{\mathrm{sim}} = 2^{13}$, $D/M = 0.5$)

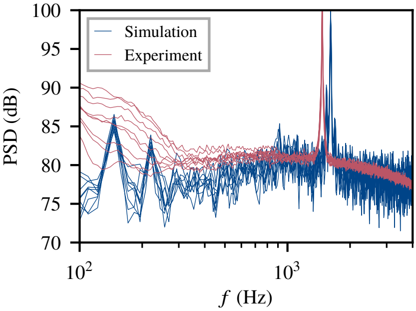

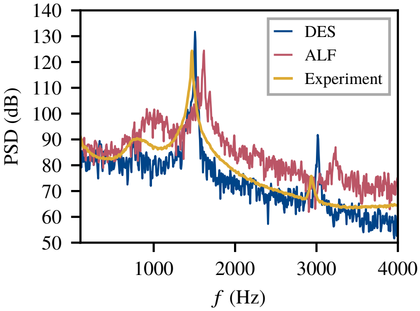

Fig. 7.2.30 Experimental and numerical pressure spectra at the gap microphone position at $u_0 = 60\,\mathrm{m\,s^{-1}}$. ($M_{\mathrm{exp}} = 2^{13}$, $M_{\mathrm{sim}} = 2^{14}$, $D/M = 0.5$)

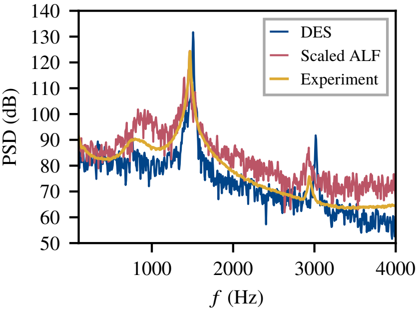

Fig. 7.2.31 Experimental and numerical pressure spectra at the gap microphone position at $u_0 = 60\,\mathrm{m\,s^{-1}}$. ALF results scaled by the theoretically calculated frequency shift. ($M_{\mathrm{exp}} = 2^{13}$, $M_{\mathrm{sim}} = 2^{14}$, $D/M = 0.5$)

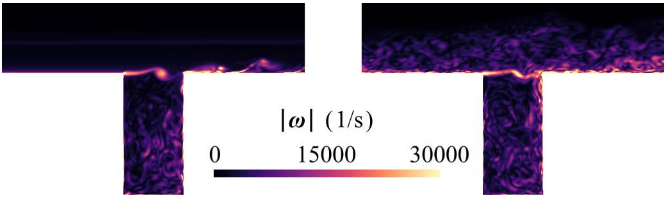

Fig. 7.2.32 Instantaneous vorticity magnitude in the gap in the $z = 0$ cross-section of the DES (left) and the LES with ALF (right).

severe log-layer mismatch of about 10 m s^{-1} in comparison to the EB-RSM RANS results. The corresponding IDDES profile matches the original RANS data very well but a typical shielding issue in the outer layer is present. These issues have consequences on the mean shear layer profiles in the gap opening. The profiles at $x = 1212$ mm in the middle of the gap opening are shown in fig. 7.2.28. It can be seen that the log-layer mismatch of the hybrid RANS/LES leads to higher velocities in the shear layer. Directly above the $y = 0$ plane the velocity is increased by approximately 10 % compared to the EB-RSM.[85] Inside the gap opening the mean velocity is also increased. The IDDES profile again matches the EB-RSM profile quite well with slightly lower mean velocities close to $y = 0$ but the shielding problem of the outer layer is convected into the shear layer. As the feedback frequencies depend strongly on the effective convection velocity in the shear layer, see eq. (2.22), we must assume that the resulting feedback modes of the hybrid RANS/LES are shifted by approximately 10 % to higher frequencies.

A comparison of the wall pressure spectra already shows this consequence (see fig. 7.2.29). Similar to the experimental results a sharp peak is detected at the Kulite position and even its level compares well to the experimental data but it is shifted by approximately 100 Hz to higher frequencies. Furthermore we can see that at these high frequencies the simulation leads to strong low frequency disturbances and equivalently the measurements were very vulnerable against mounting issues and background noise of the wind tunnel.[50] The resulting spectra inside the cavity, fig. 7.2.30, confirm this first impression. The main resonance frequency of the hybrid RANS/LES is shifted again by approximately 100 Hz and the first feedback mode is also shifted to higher frequencies. Although the level of the resonance matches the experiment very well, the broadband noise is approximately 10 dB too high. At least parts of this might be as well explained by the higher shear layer velocity as this certainly leads to higher turbulence in the shear layer that is also partly convected into the cavity (see fig. 7.2.32). Using Rossiter's formula, eq. (2.22), for aerocacoustic feedback with the 10 % increased convection velocity one finds that the feedback mode would be shifted by 9.39 %.[85] If one shifts the spectrum of the hybrid RANS/LES with this value one can see that in fact the main resonance frequencies coincide (see fig. 7.2.31). Consequently the log-layer mismatch appears to be the reason for the frequency shift. In order to obtain improved results it would be necessary to improve this specific issue.

Interestingly the IDDES is able to correctly predict the main resonance frequency and even the broadband levels match the experimental data. However the level at the resonance is approximately 10 dB too high and the first feedback mode is not predicted by this approach. Fig. 7.2.32 again helps to understand this behavior. The vortex rolling up in the shear layer is much more intense than in the hybrid RANS/LES case and obviously it is much more coherent which will lead to more intense feedback modes. As no boundary layer fluctuations are present the general vorticity inside the cavity is lower than on the hybrid RANS/LES solution. The shielding problem leads to a small increase of vorticity in the outer layer of the boundary layer but it does not interact with the cavity opening.

In summary Riedelsheimer found that the log-layer mismatch of the hybrid RANS/LES can lead to significant errors if shear layer instability plays a decisive role in simulated phenomena.[85] We furthermore confirmed our presumption that the tendency to an increased log-layer mismatch increases with the free stream velocity. From the results of the IDDES we see that due to the large opening length the main role of the turbulent boundary layer fluctuations is to disturb the strong spanwise coherence of the feedback vortices and not to generate the background noise level inside the cavity. Accordingly one could interpret the IDDES results such that a typical grey-area is present in the gap opening – the vortex rolls up in a URANS like manner and the IDDES is not able to switch rapidly enough into an LES mode that leads to small-scale fluctuations due to the turbulent shear layer. In consequence a shear-layer improved DDES, e.g. [73], should be applicable to this type of problems which would reduce the required numerical costs as the upstream boundary layer does not need to be resolved. Finally, the present shielding issue in the outer layer is assumed to play a negligible role on the shear layer development inside the restricted cavity opening.

7.3 Summary

In this chapter we described a detailed analysis of different modifications of the reference case of the idealized rear door gap model from chapter 6 and tested our numerical simulation methodology on selected cases. We proved the importance of the incoming boundary layer profiles on the resulting gap noise due to a stabilization of the shear layer as the friction velocity decreases and the boundary layer shape factor H increases. Although it was difficult to correctly calculate the incoming boundary layer in our numerical simulations at least their trends could be represented and the resulting gap noise spectra were in good agreement with the experimental data up to 2 kHz.

We confirmed results from Schimmelpfennig regarding the influence of the gap's edge shapes that can prove the existence of a surface averaging effect in the gap opening. Furthermore we could show that again the incoming boundary layer strongly affects the influence of the edge shapes on the interior gap noise. Again our simulation was in good agreement with the experimental data below 2 kHz. We could also confirm results by De Jong on the influence of the gap opening position on the stability of the shear layer that leads to different gap noise spectra inside the cavity although the acoustic properties of the cavity do not change. The effect of the opening position could again be simulated up to 2 kHz.

Furthermore we studied the influence of wall-normal offsets – a typical tolerance issue in the manufacturing process of vehicles – on the gap noise. Besides first impressions we could prove that especially negative wall-normal offsets lead to a strong destabilization of the flow and accordingly its effects vary strongly under different inflow conditions. We conclude that vertical offsets should not be used as a design parameter as they likely increase the system's vulnerability towards tolerance issues. Although the numerical simulation of the negative offset lead to a strong instability at the resonance frequency f_1 the general effects were well covered up to f_1.

In a series of measurements we studied the influence of the opening length on the shear layer instability in the gap opening. Especially we had a deeper look on the intermediate region between purely passive gap noise and aeroacoustic feedback dominated cases under ZPG and APG conditions. As θ/L_0 is typically high in automotive applications it was found that gaps on vehicles are likely relatively insensitive towards tolerance issues of their respective streamwise opening length.

The results of a final study of a true feedback dominated case of a deep cavity were in good agreement with available results from the literature. In a related Master's thesis, Riedelsheimer could show that the previously described log-layer mismatch of the hybrid RANS/LES leads to a frequency shift of the resonant lock-on of approximately 10 %. Furthermore he studied the applicability of an IDDES to the problem. The results of this study show that the influence of the turbulent boundary layer fluctuations on the background noise in the cavity is likely low and the only role of the boundary layer fluctuations is a disturbance of the streamwise coherence of the shedding vortex in the gap opening. Application of shear layer improved DDES methods should thus lead to good results without resolving the incoming boundary layer.

In summary our experimental data was in good agreement with the literature and could give new insights into more specialized cases related to automotive gap noise. We successfully applied the hybrid RANS/LES to a variety of these cases. Good agreement with the experimental data was consistently reached in the frequency range below 2 kHz where typically the loudest resonances and the highest background noise level is found. Analysis of the turbulent kinetic energy and the mean flow streamlines of the successful simulations could confirm experimentally founded models of gap noise physics from the literature.

8 Rear Door Gap Noise on a Mercedes-Benz E-Class Estate S213

In this chapter we study the applicability of the validated hybrid RANS/LES methodology based on ALF to a close-to-reality case of automotive gap noise. A full-scale model of a Mercedes-Benz E-Class Estate (S213) was prepared to measure the near-field acoustics generated by the car's rear door gap as well as to characterize the inflow conditions in front of the gap at the car's roof. Compared to a small scale basic experiment, this problem introduces the challenges of larger dimensions and higher geometrical complexity but also uncertainties in the acoustic propagation: While a small-scale gap can be easily manufactured from solid aluminum, and can thus be considered as totally acoustically reflecting, the S213 model is built of foam that also resembles most of the rear door gap's inner surface. In comparison to a real vehicle this experiment tries to be a last simplification: The gap's surface is built from the solid, but slightly porous, foam where in reality flexible rubber sealings and thin metal sheets are present. Accordingly, the used foam model is interpreted as intermediate step between modeling and reality. While the inflow conditions are assumed to be very realistic, the gap is modeled as acoustically reflecting as possible under the given technical prerequisites.

Accordingly, we first try to characterize the acoustic properties of the experimental gap model and compare these data to a numerical simulation of this pure acoustic excitation. The transfer of the hybrid RANS/LES from the idealized rear door gap to the full-scale model is straightforward and we discuss in detail the consequences of resolution and uncertainties. We finally check the capability of the numerical simulations at a different inflow velocity and to predict the acoustic behavior of design modifications. The content of the following chapter was originally published in the proceedings of the 25th AIAA/CEAS Aeroacoustics Conference as *A Hybrid RANS/LES for Automotive Gap Noise Simulations*.[32]

8.1 Experimental Setup

The experiment has been carried out at operating velocities in the range $140\,\mathrm{km/h} \leq u_0 \leq 240\,\mathrm{km/h}$ in Daimler's full-scale Aeroacoustic Wind Tunnel in Sindelfingen. The Göttingen Type wind tunnel has a $28\,\mathrm{m}^2$ nozzle area and an anechoic test section with a length of 18.7 m. In the free stream core, the turbulence intensity is below 0.1 %.[13] In the configuration for aeroacoustic measurements neither the installed 5-belt system nor the boundary layer suction for road simulation are used. The utilized full-scale S213 model and a view of the modeled rear door gap can be seen in fig. 8.1.1a and fig. 8.1.1b. In the following x denotes the streamwise direction, y the vertical direction and z the spanwise direction. The origin of the coordinate system is set in the center of the front axis. In the experiment we measured the inflow conditions as well as the gap acoustics using the following measurement techniques:

Static pressure ports module

The static pressure was measured along the roof in the streamwise direction, 15 cm off from the symmetry plane, using pressure ports with a diameter of 0.6 mm (see fig. 8.1.1c).

Wall-pressure module

Directly upstream of the cavity eleven Kulite pressure transducers, model XT-140M with B-screen, with an outer diameter of 2.54 mm were flush-mounted in an L-shaped array. The behavior and the capabilities of these sensors to measure wall pressure spectra beneath turbulent boundary layers have been studied by Hu and Erbig[50] and given the thick boundary layer at the end of the car's roof, accurate results are expected. The sensors in the streamwise direction are positioned in the symmetry plane of the model. The sensors in the spanwise direction were evenly spaced with a distance of 10 mm while the sensors in the streamwise directions had a distance of 8, 10, and 12 mm, respectively. The eleven Kulite sensors in the wall-pressure module are numbered sequentially from 1-11 from the bottom right to the top left position as depicted in fig. 8.1.1d.

Gap Acoustics

The cavity's interior volume is similar to the serial shape of S213. Its sides were closed using small laser sintered panels that lead to a defined resonance volume, but that also introduce a small uncertainty, as their positioning cannot be realized perfectly orthogonal and symmetric. The gap's inner surface consists mainly of a rough foam and only the upper plate is made from laser sintered parts. Fifteen B&K Type 4954-A microphones were flush-mounted in small aluminum panels along the spanwise length of the cavity. The panels themselves are mounted in the cavity's bottom surface. To seal the inner volume we used aluminum tape and wax, which leads to a material mixture inside the cavity, see also fig. 8.1.1e. A model of the gap with its complex geometry and the mounting panels of the microphones is shown in fig. 8.1.2. Notably the cross-section of the rear door gap and the relative position of the gap opening vary significantly with its spanwise extent.

The sampling rate of the time-synchronous measurement of the Kulite sensors and the microphones was set at 51.2 kHz and the data were recorded for 60.6 s. A preamplifier with a gain factor of 259.5 and a high pass filter, that can be approximated as RC filter with a 254 Hz cut-off frequency, was applied to the Kulite sensors. The discussed power spectra are corrected using the filter frequency response curve. The mean velocity boundary layer profile at the roof was measured at the three different positions $x_1 = 1653$ mm, $x_2 = 2454$ mm and $x_3 = 3258$ mm using a pitot tube rake with 26 tubes. The wall distance of the closest tube was set to 3 mm, which lies well inside the logarithmic layer and the rake was positioned in the wall-normal direction.

Besides the influence of the potentially non-negligible wall impedance in the interior of the rear door gap and the uncertainties at its side panels two additional uncertainties are present in

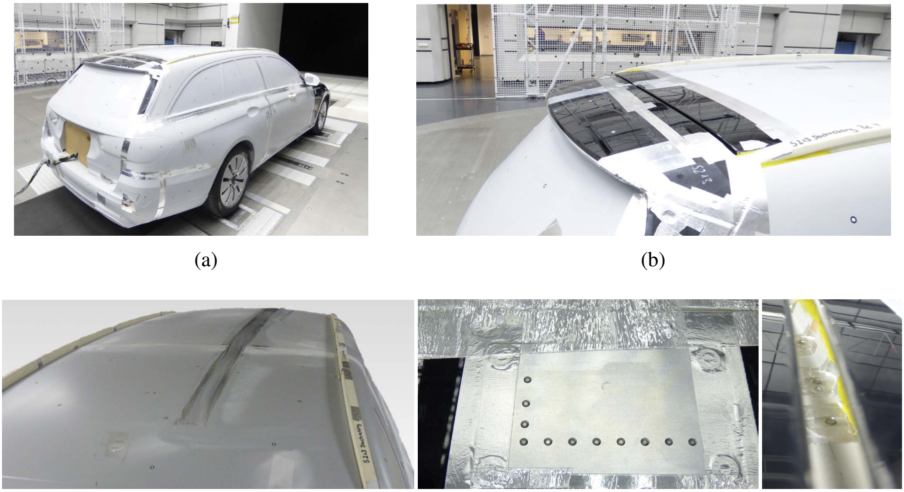

(a) (b)

(c) (d) (e)

Fig. 8.1.1 Experimental Setup: (a) Full-scale S213 model in Daimler's wind tunnel, (b) Outside view of the Rear Door Gap model, (c) 0.6 mm diameter pressure ports inside aluminum panels along S213's roof, (d) Top view of the Kulite array in front of the gap opening. The 4 streamwise sensors lie in the model's symmetry plane, the 8 spanwise sensors are on the right side of the model. The uppermost sensor corresponds to number 11, the rightmost sensor to number 1, (e) View into the gap's resonator volume. Three flush-mounted microphones are visible as well as the wax sealings.

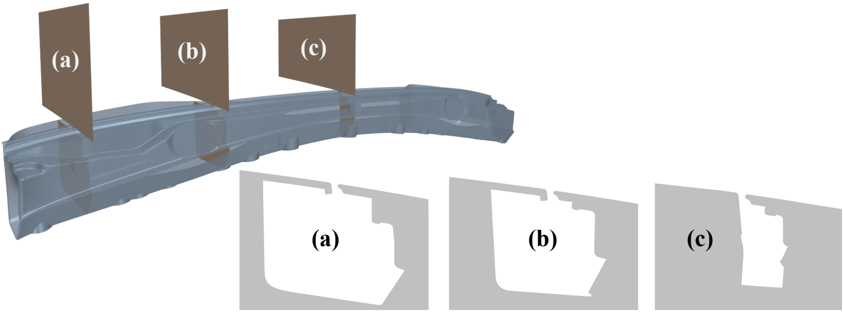

Fig. 8.1.2 Model of the rear door gap's resonator volume and three cross sections, (a) $z = -400$ mm, (b) $z = -225$ mm and (c) $z = 0$ mm.

the current setup. First, the rear door is built from a single, solid part that is connected to the rest of the model by four large screws. Consequently, it is impossible to precisely adjust its position with less than 1 mm accuracy and we decided to fix its position once before the measurements. Second, the main body of the model is built of two parts that are connected at approximately $x = 1.7$ m. In practice this connection leads to a small 1 to 1.5 mm high forward facing step in the spanwise direction at the roof that might lead to small disturbances but that are assumed to decay rapidly.

8.2 Acoustic Properties of the Rear Door Gap

In a first test we want to characterize the acoustic properties of the modeled rear door gap. Wickern and Brennberger[107] and Schimmelpfennig[90] pointed out that due to rubber sealings and complex geometries only a classical Helmholtz frequency is expected for rear door gaps. In our experiment additional, nearly reflecting, side panels are mounted that are expected to introduce additional standing modes to the Helmholtz resonance. The large number of microphones used in our model should allow a clear distinction of different modes, which helps to understand the gap's aeroacoustic behavior. Furthermore a simple acoustic simulation can help to identify geometric differences between the experimental and the numerical model.

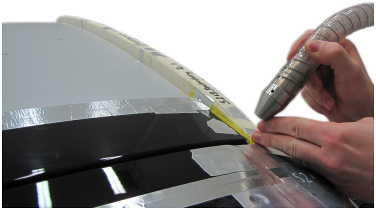

Fig. 8.2.1 Experimentally used broadband noise source at the right edge of the rear door gap.

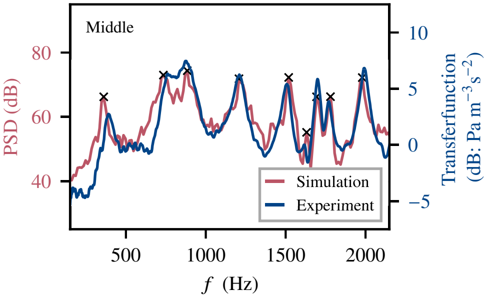

Fig. 8.2.2 Comparison of the experimental transfer function and the pressure spectrum of the numerical simulation ($\Delta f \approx 12$ Hz).

For the acoustic test we positioned a broadband noise source above the left edge of the gap's opening with an incident angle of approximately 50° (see fig. 8.2.1 with the noise source at the right edge). Although the broadband noise source is designed to produce white noise it underlies certain deviations from the ideal case. In addition to the microphones we also record the output signal of the noise source and thus we are able to calculate the transfer function H between the noise source and the chosen microphone. The sampling rate and recording time is equivalent to the previously described settings. In a numerical simulation this experiment can be modeled in a very similar manner: Using the same mesh that will be used for the aeroacoustic simulations (the detailed numerical setup is described in chapter 8.4) we perform simulations with the acoustic wave equation from our hybrid approach. We model a white noise source at the same position as in the experiment by simply setting a volume force in a few cells. The noise source is generated by a pseudo-random number generator to give a nearly uniform distribution of the frequencies. The numerical noise source is much closer to being white noise and accordingly we simply evaluate the power spectral density of the microphones of the numerical simulation.

Fig. 8.2.2 shows a comparison of the experimental transfer function (blue scale) and the numerical spectrum (red scale) at the middle microphone. One can see in the experimental transfer that our model shows at least eight acoustic resonances at this microphone. At the moment the geometrical shape of these modes is still unclear due to the varying geometry and cross-section of the rear door gap but obviously one cannot speak of a simple Helmholtz resonance. Promisingly, the numerical simulation reproduces the overall shape of the transfer function very well. Every resonance frequency can be found in the simulation and only minor differences between the frequencies are present. Especially the 380 Hz and 780 Hz resonance frequencies are predicted at slightly lower frequencies which indicates small differences between the physical and the digital model.

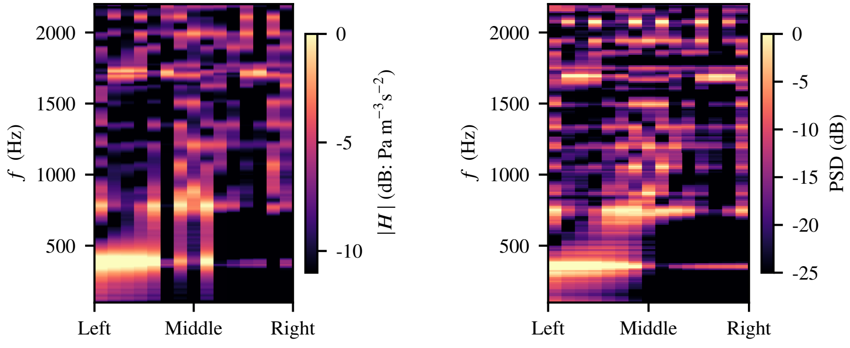

(a) (b)

Fig. 8.2.3 Map of the transfer functions of the 15 cavity microphones: (a) experiment, (b) numerical

A detailed analysis of the structure of the detected resonance frequencies is presented in fig. 8.2.3. The experimental transfer functions and the simulated power spectra of the 15 microphone positions, respectively, are shown as map over the microphone position from the left to the right. In both cases it is seen that the left side of the gap is much stronger excited than the right side as the noise source was positioned on the left. Except of the sixth microphone position from the left, again good coincidence between experiment and simulation is found. It is assumed that this sixth microphone was disturbed in the experiment as its levels were generally very low. In addition to the eight detected resonance frequencies at the middle position a couple of resonances with acoustic nodes at the middle position are found. Overall the geometric structure of the resonance frequencies is very complex with many nodes and anti-nodes. Accordingly it is impossible to predict their underlying mode type based on the discrete data set of localized microphones. As the numerical simulation produces very comparable results an FFT at the gap's surface at the selected resonance would shed some light here. However we feel that first a study of the gap's aeroacoustic behavior is more helpful as the importance of the detected resonance frequencies is yet unclear.

In summary our results of the acoustic excitation show that the geometry model of the rear door gap used for the simulations has some differences to the experimental model, especially factors influencing the two lowest resonance frequencies differ, but overall the similarity is good enough to predict resonance frequencies up to 2 kHz which should represent a good basis for any numerical simulation of aeroacoustic gap noise.

8.3 Experimental Analysis

As we could identify the acoustic resonance frequencies of the rear door gap model it is now possible to analyze the aeroacoustic behavior of the rear door gap. Very similar to the analysis of the idealized rear door gap model we first classified the mean inflow conditions with a masked gap at the operating velocity 140 km/h. Fig. 8.3.1 shows the measured dimensionless pressure along the roof. The three positions of the velocity profile measurements are indicated in this figure. The gap is positioned directly downstream of the end of the pressure measurement module. Consequently we can see that the flow is significantly accelerated between the windscreen and the roof. Shortly downstream, the pressure measurement module is placed and an adverse pressure gradient is detected in the range $1.5\,\mathrm{m} \leq x \leq 2.8\,\mathrm{m}$. Between 2.8 m and the rear door gap the flow underlies zero pressure gradient conditions. These results are in good agreement with the measured mean velocity profiles (fig. 8.3.2 and table 8.1). At measurement point P1 the boundary layer is typical for the influence of an upstream favorable pressure gradient with a shape factor $H = 1.21$ and a very high edge velocity $u_e = 46.8\,\mathrm{m\,s^{-1}}$. The flow then decelerates towards P2 and P3 where finally a shape factor $H = 1.35$ is reached. The boundary layer at P3, directly upstream of the rear door gap's opening has a thickness of 56.8 mm and a momentum thickness of 6.19 mm which already indicates the severe numerical costs indicated with a boundary layer resolving simulation of this problem. In comparison to the idealized rear door gap model especially δ is 65 % larger than the most comparable APG-5 case. Additionally it is found that the corrected wall pressure spectra using the technique from [50] are in very good agreement with Hu's semi-empirical model based on the flow data at point P3, especially the mid frequency slope and the frequency of the maximum are very well matched.* These results indicate that the flow at the end of the vehicle's roof can in fact be estimated by a nearly

---

*Using an alternative, less general, formulation from [52] also the levels are in excellent agreement with the measured data.

two-dimensional ZPG boundary layer. Accordingly, the inflow conditions from the idealized rear door gap experiment from chapter 6 were well suited to approximate the real flow conditions at the end of the roof. The mean opening length of the rear door gap is approximately 8 mm and thus $\theta/L_0 \approx 0.77$ which is well above the critical stability region $\theta/L_0 < 0.25$.

In fig. 8.3.4 one can see the measured power spectral densities at Kulite sensor 10 and the middle microphone in the operating velocity range between 100 km/h and 200 km/h. The results are very similar to the idealized small-scale experiment. The levels of the wall pressure spectra increase broadbandly with the operating velocity and at higher velocities the low frequency content below 200 Hz is disturbed by mounting imperfections. In contrast to the idealized gap model an acoustic radiation of the gap is present not only at one resonance frequency. Instead, the gap radiates sound with varying intensity depending on the flow velocity at three different resonance frequencies. As the wall pressure levels of the incoming boundary layer increase also the broadband content inside the gap increases. Additionally, several resonance frequencies below 3 kHz are found with the maximum levels reached between 800 Hz and 1300 Hz depending on the velocity. Again it is found that the frequencies of the peaks are almost constant through the velocity range and are thus primarily related to an aeroacoustic excitation of the rear door gap's geometric eigenmodes. Small velocity shifts at the 800 Hz and 930 Hz resonance frequencies fall in the range that could be explained in the basic experiment by the rounded edge curvature. The excitation power at the frequencies between 800 Hz and 1100 Hz depends again on the inflow velocity, which is also very similar to the basic experiment. At higher resonance frequencies the excitation does not differ from the broadband regions. In addition to these consistent results, a small peak is found at 100 km/h at approximately 400 Hz which corresponds to the first resonance frequency of the rear door gap. Interestingly this peak fades out rapidly at higher inflow velocities.

In the acoustic excitation study we showed that the associated resonance frequency at 380 Hz has broad anti-nodes (although it is not necessarily a standing wave) in the left and right region of the gap. As such it is very interesting that a peak could be detected in the mid position. In fig. 8.3.5 we try to provide more insights into this excitation by extending the velocity range from 60 km/h to 240 km/h and comparing the left, middle and right microphone. It can be seen, that this first resonance frequency gets excited very effectively below 100 km/h with a maximum at 70 km/h. In this range of maximal excitation a strong asymmetry is detected that leads to almost a 20 dB difference between the left and the right position. Additionally the frequency shift in this velocity range is stronger at the left side of the gap. Above 100 km/h the sharp peak flattens at both sides and the result becomes more symmetric which finally fades out the peak at the mid microphone position. Due to the strong excitation of this peak and the strong frequency shift in a very restricted velocity range this behavior cannot be explained by the findings from the idealized rear door gap experiment. Instead this peak is strongly influenced by the flow and must correspond to a shear layer instability in the gap opening. However an explanation by a classical Rossiter mode, eq. (2.22), in the opening length is not applicable as the first self-sustained oscillation mode at 70 km/h would be expected at approximately 1 kHz far off the frequency region of interest. We assume that a spanwise inflow from the sides of the gap is present that

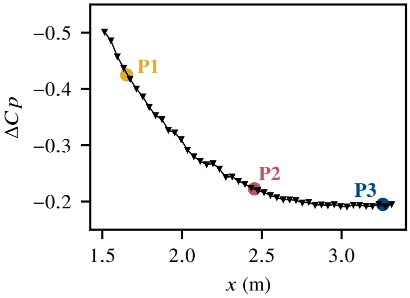

Fig. 8.3.1 Experimental dimensionless pressure distribution along the model's roof. Boundary layer measurement position P1, P2 and P3 are indicated.

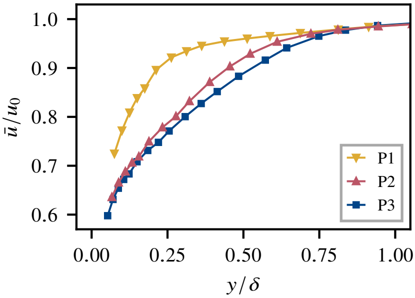

Fig. 8.3.2 Free stream scaled mean boundary layer profiles measured with the pitot rake.

Table 8.1 Experimental characteristic boundary layer parameters.

	u_e (m/s)	δ (mm)	δ^* (mm)	θ (mm)	H	u_τ (m/s)	$\mathrm{Re}_\theta = u_0\theta/\nu$
P1	46.8	43.5	2.88	2.38	1.21	1.87	7233
P2	44.8	50.3	6.02	4.50	1.34	1.50	13072
P3	44.1	56.8	8.35	6.19	1.35	1.42	17717

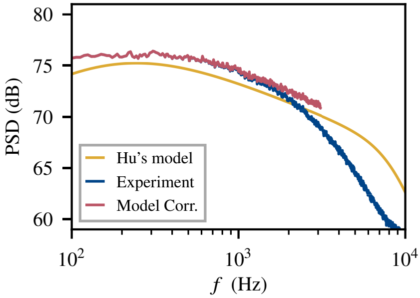

Fig. 8.3.3 Comparison of the measured wall pressure spectrum at Kulite position no. 4, the corrected wall pressure spectrum and Hu's model. ($M = 2^{13}$, $D/M = 0.5$)

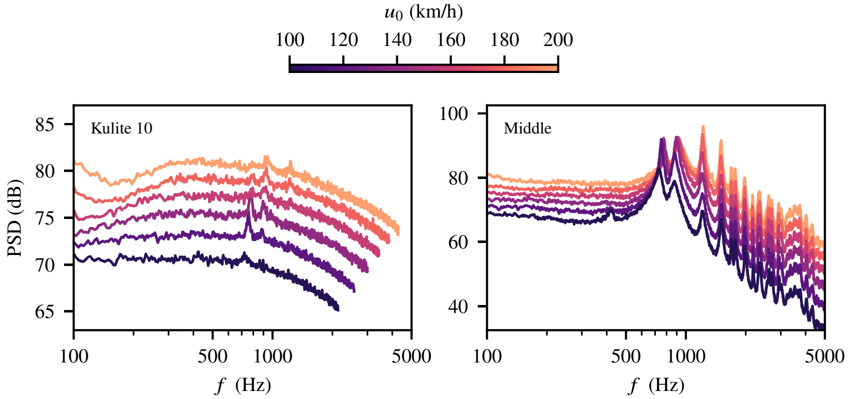

Fig. 8.3.4 Power spectral density of the wall pressure spectra and the gap noise at the middle position at different operating velocities. ($M_{\text{Kulite}} = 2^{14}$, $M_{\text{Mic}} = 2^{15}$, $^{D}/_{M} = 0.5$)

leads to an increased effective opening length. Possible model asymmetries along the roof or at the gap opening at the sides could then lead to different shear layer instabilites at the two sides. Nevertheless this effect is masked above 100 km/h and we thus assume that its effect on the measured spectra at these higher velocities is negligible.

In a last experiment we applied the extremely effective modification of the leading edge shape to the S213 model. As usually the case on real vehicles the base case features a radius $r_{\text{base}} \approx 2.4\,\text{mm}$. Accordingly we manufactured parts with sharp edges and strongly rounded edges with radius $r_{\text{round}} \approx 4\,\text{mm}$. As the vertical positioning of the trailing edge was difficult due to the described insufficiencies of the model's rear door we restricted the measurements to the leading edge modification that effectively influenced the loudest resonance peaks in the simplified experiments from chapter 7.2.1. Fig. 8.3.6 shows the geometric shapes of the three different design modifications and the spectrum at the middle microphone at 140 km/h. The result is again very similar to those of the basic experiment: The larger the radius of the leading edge, the higher are the low frequency broadband levels of the turbulence and the sharper and louder are the resonance peaks below 1 kHz. Above 1 kHz the influence of the leading edge shape suddenly vanishes and the tree designs lead to almost identical spectra. Due to the larger opening length in comparison to the basic experiment the influence of the opening attenuation sets in much earlier.

In summary the rear door gap noise of the S213 model is very similar to the studied idealized rear door gap model. Accordingly this simplified experiment was very well suited to resemble the features of automotive gap noise. In addition to the expected behavior a velocity dependent asymmetric resonant lock-on at approximately 400 Hz was detected below 100 km/h. A difficulty

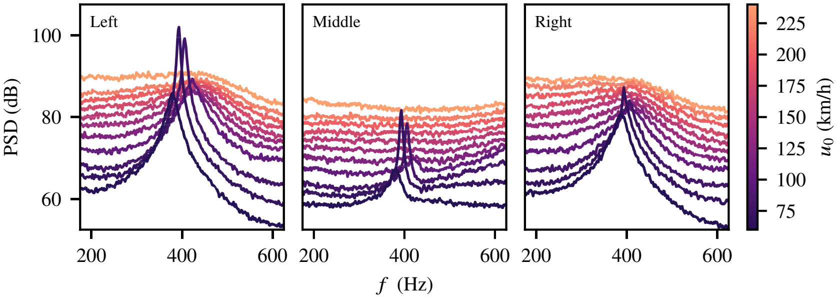

Fig. 8.3.5 Power spectral density of the gap noise at the left, middle and right position at different operating velocities. ($M = 2^{15}$, $^D/_M = 0.5$)

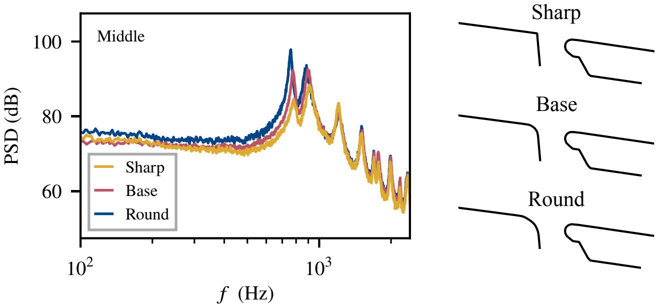

Fig. 8.3.6 Influence of three different leading edge shapes: Gap Noise at the middle microphone inside the rear door gap at $u_0 = 140\,\mathrm{km/h}$. ($M = 2^{15}$, $^D/_M = 0.5$)

in the classification of the resonance frequencies is their complex structure compared to the basic experiment. This knowledge would be required to understand potential development levers to tune the gap noise phenomenon or to affect its levels.

8.4 Numerical Simulation

In this section we will first analyze a set of numerical simulations of the S213 model case at 140 km/h. We want to study the applicability of the hybrid RANS/LES to this problem, especially whether it is stable enough to run a close-to-reality case and whether resolution issues that inevitably arise with the drastically increased geometric dimensions of the problem lower the quality of our results. Furthermore we want to explore how these numerical simulations could be used to improve the understanding of automotive gap noise and to provide new ideas for development processes. Finally, we will apply the numerical simulation approach to the leading edge shape variation and the 70 km/h case with potential inflow from the sides of the gap to push this method closer towards its current limits.

8.4.1 Setup

The numerical setup for these simulations is very comparable to the DNC from chapter 6. In a first step, a 2nd order incompressible steady EB-RSM RANS of the whole model is performed in STAR-CCM+, that is initialized from an incompressible $k - \varepsilon$ Two-Layer RANS. While most of the car's surface is resolved down to $y^+ = 1$, only a few regions around the axles are resolved coarser and utilize a wall-function formulation with $y^+ > 30$. The mesh at the model's roof and windscreen is anisotropically refined in order to smoothly resolve the boundary layer. In total the mesh consists of approximately 213 million cells and a cross section can be seen in fig. 8.4.1a. To stabilize the RANS a permanent local order reduction is applied, if the local flow velocity exceeds 150 m/s. In comparison to the original DNC we now use an incompressible RANS as it significantly increased the stability of the simulations. In contrast to the original experiment, the LES sub-domain is now required to cover the full span of the model's roof and thus we do not cut the roof's boundary layer with the side boundaries of the sub-domain. At the studied velocities significant temperature changes are solely expected inside the boundary layer and accordingly the free stream boundary condition can be approximated with constant temperature. Furthermore the LES can be easily initialized with constant temperature.

In a second step a compressible LES is performed inside a sub-domain around the rear door gap, as visible in fig. 8.4.1b. In this sub-domain, the mean flow velocity is prescribed at the inlet and the bottom boundary and non-reflecting free stream boundaries are used everywhere else. The required data for these b.c.s are mapped from the global RANS. Along the model's roof ALF is used to generate synthetic turbulence that resembles the statistics from the EB-RSM RANS. In fig. 8.4.1c one can see that approximately 20 cm upstream of the rear door gap the artificial volume force is blended out. The LES is based on the WALE subgrid scale model and uses a 2nd order scheme for the temperature equation and a 2nd order bounded central difference scheme for the segregated flow solver. Time is discretized using a second order backward differencing scheme with 10 inner iterations per time step. In the simulation additional Rhie-Chow Type Dissipation is used with a limiting acoustic CFL number 1.5.

The computational trimmed mesh used for the LES consists of 260 million cells with a maximum cell size $\Delta_{\max} = 8\,\mathrm{mm}$. The boundary layer at the roof is resolved by 1 mm cells, that are used up to a wall distance of 60 mm. Below 3 mm wall distance, prism cells are used, that collapse down to a minimum thickness of 10 μm. The gap's interior volume is resolved by 0.5 mm cells in order to capture the strong curvature of the geometry, that can be seen in fig. 8.1.2 and to avoid additional mesh transition regions. A cross section of the mesh can be seen in fig. 8.4.1d. The simulation is performed for a physical time of $T = 0.3\,\mathrm{s}$ using a time-step $\Delta t = 1 \times 10^{-5}\,\mathrm{s}$ and we evaluate spectra within the period $0.05\,\mathrm{s} \leq t \leq 0.3\,\mathrm{s}$. In comparison to the original DNC from chapter 6 these resolutions correspond to $y^+ \approx 0.9$, $\Delta^+ \approx 92$ and

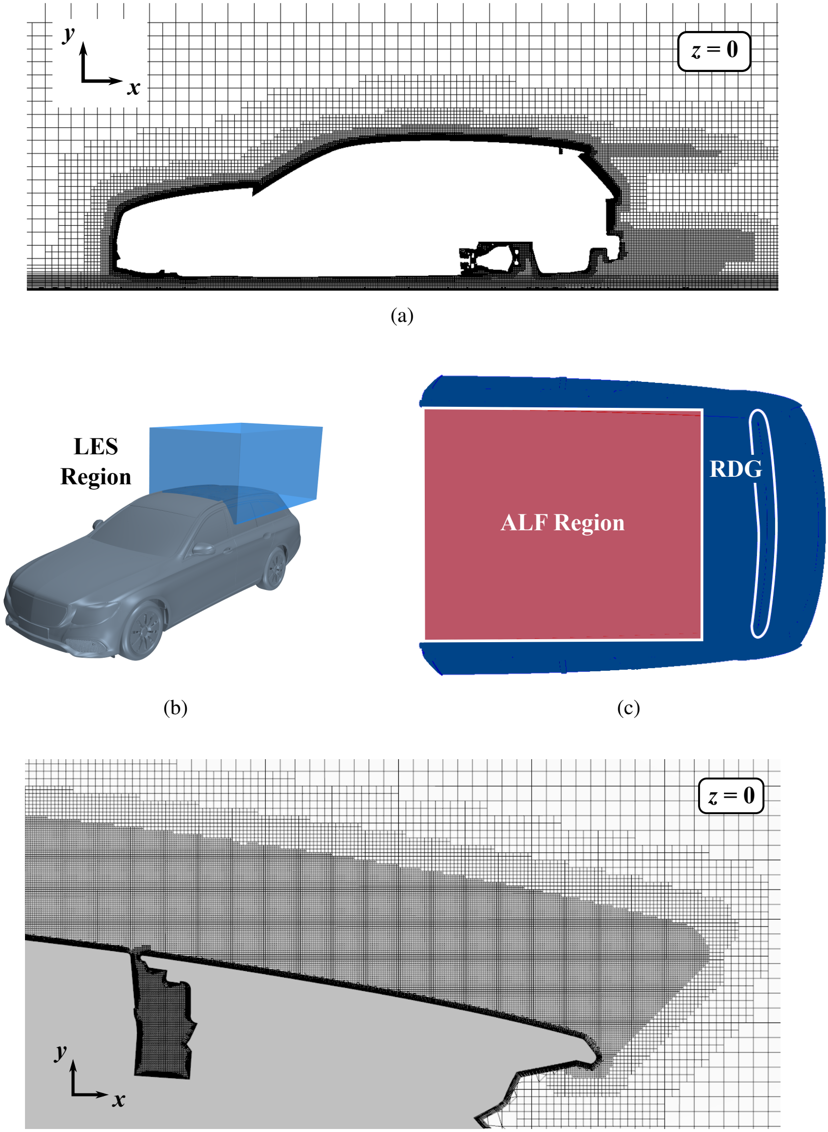

(a)

(b)

(c)

(d)

Fig. 8.4.1 Numerical Setup: (a) RANS mesh, (b) LES region, (c) ALF region, (d) LES mesh

$t^+ \approx 1.3$ at point P3 in front of the gap which is significantly coarser than the previous base settings. However the numerical robustness studies of the simulations showed that gap noise could be simulated with acceptable accuracy under comparable settings although they impose restrictions on the resolved boundary layer fluctuations.

The simulations are performed on 2240 CPUs and take approximately 5.3 days in total. In comparison to a wall-resolved LES of a full-scale car that has been performed by Ambo et al.,[3] these computational costs correspond to an approximate speed-up of a factor 70.

8.4.2 Analysis

In the following we are reviewing the results of the numerical simulation at a free stream velocity of 140 km/h. In fig. 8.4.2 one can see a negative pressure isosurface that clearly shows how our hybrid RANS/LES leads to a transient boundary layer along the roof and the railing of the car. As the mesh is coarsened downstream of the roof's separation edge the vortices are growing considerably fast down to the outlet of the LES sub-domain. It is also visible in fig. 8.4.3 that the attached near wall turbulence resembles the only active excitation source of the rear door gap. The thick turbulent boundary layer is convected past the comparably small gap opening. Although the boundary layer interacts with the leading and trailing edge, which causes some minor pressure fluctuations that decay rapidly, the shear layer remains macroscopically stable and the flow inside the gap opening stays calm.

Again, we first validate the mean inflow of the rear door gap. Although the EB-RSM RANS tends to be very unstable on this case[83] and needs further stabilization by local order reduction, at least the results at the roof are definitely in good agreement with the experiment. Especially the static pressure is well matched with the experiment (see fig. 8.4.4) for both the EB-RSM RANS and the LES. Notably the LES drifts slightly downstream of the ALF region which we assume is due to the coarse mesh resolution in the unforced LES region. Additionally the mean velocity boundary layer profiles are in good agreement with the experimental rake measurement (see fig. 8.4.5). Only relatively close to the wall, in the logarithmic layer, a mismatch between all three data sets is present. Given the coarse mesh we expect a log-layer mismatch between

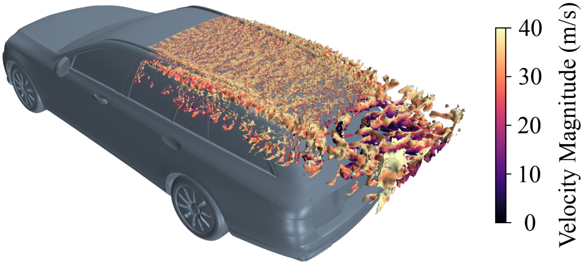

Fig. 8.4.2 Instantaneous isosurface of the negative pressure fluctuations $p' = -10\,\text{Pa}$.

the EB-RSM RANS and the LES. However the EB-RSM is also not capable to completely reproduce the measured data. As the measured data are based on rake measurements even the experimental results in this area should be taken with some care.

As expected due to the coarse mesh resolution the wall pressure spectrum at the Kulite position in fig. 8.4.6 is slightly over-predicted below 600 Hz with a relatively strong amount of noise. At approximately 2 kHz the levels begin to drop due to spatial under-resolution of the scales. In summary, the simulation cannot completely match the 80 % scatter band but is not significantly off the experimental result. Especially the numerical high frequency drop is at a higher frequency than the attenuation due to the surface averaging in the gap opening. Accordingly only the interaction with the trailing edge must be assumed mismatched. Indeed, the pressure spectrum at the middle microphone in fig. 8.4.7 shows good agreement with the experimental data. Below the first resonance frequency matching is excellent. The resonance frequencies up to 2 kHz are correctly predicted, as assumed from the numerical simulation of the acoustic excitation, and the decay of the broadband levels is excellent. As the inflowing turbulence is strongly under-resolved above 2 kHz we must however assume that the high frequency match is more or less good luck. More interestingly the levels of the two resonance frequencies below 1 kHz are predicted too low while the levels of all other resonance frequencies are over-predicted.

This impression gets confirmed by fig. 8.4.8 where we plot the pressure spectra at the 15 microphones over their spanwise position. It is found that the prediction of the resonance frequencies of the simulation is excellent – every experimentally excited mode gets also excited in the simulation. Again the main difference is the excitation strength: The resonance levels below 1 kHz are all under-predicted by the simulation, while the resonance levels above 1 kHz are over-predicted. Consequently, the modes above 1 kHz tend to extend to microphone positions that were not significantly excited in the experiment. Finally the slight mismatch of the lowest resonance frequency that was already observed at the acoustic excitation is still present in this simulation.

A comparison with the simulation of the basic experiment helps to understand this phenomenon. The resonance levels of the basic experiment, especially of the Helmholtz frequency, were generally well predicted, only the first standing wave was sometimes slightly over-predicted. In contrast to the S213 model the gap was made from solid aluminum and could thus be considered fully acoustically reflecting. The S213 gap model consists of a material mixture of rough foam, aluminum tape, wax and a laser sintered coverage and side panels. Accordingly, we must assume that the acoustic impedance boundary condition at these walls is non-trivial and non-negligible which is a major physical difference between the variants. Furthermore it is plausible that such a physical difference will lead to a systematic error in the simulations that is found on all microphone positions. In summary it is thus very likely that these model uncertainties lead to the small issues at the resonance levels.

As the numerical simulation is however capable to predict the resonance frequencies up to 2 kHz very accurately an evaluation of surface FFTs at the gap's surface is valid to interpret their underlying modal structures. As already indicated by the microphone maps in fact no

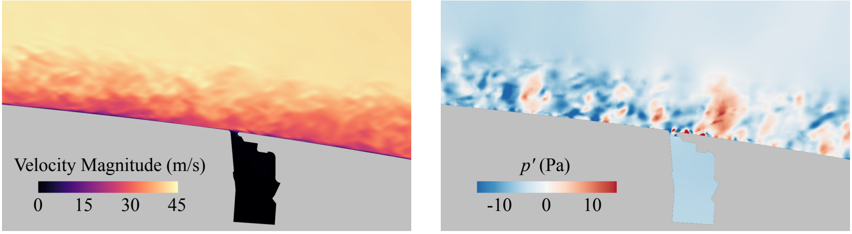

Fig. 8.4.3 Instantaneous velocity $\bar{\boldsymbol{u}}$ and fluctuating pressure p' fields in the $z = 0$ cross-section through the rear door gap opening.

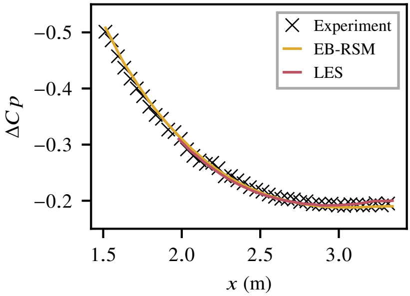

Fig. 8.4.4 Comparison of the calculated dimensionless pressure distribution along the roof to the experimental data.

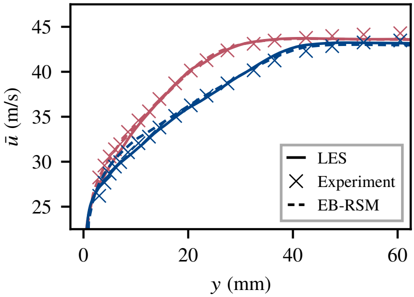

Fig. 8.4.5 Comparison of the mean boundary layer profiles of the EB-RSM RANS and the LES at P2 (red) and P3 (blue) to the experimental data.

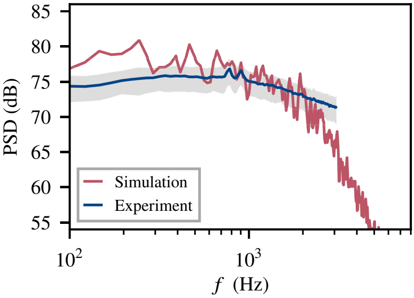

Fig. 8.4.6 Simulated wall pressure spectrum in comparison to the experimental data and scattering band. ($\Delta f \approx 24$ Hz)

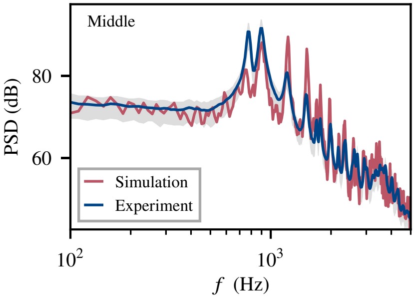

Fig. 8.4.7 Simulated gap noise spectrum at the middle microphone in comparison to the experimental data and scattering band. ($\Delta f \approx 12$ Hz)

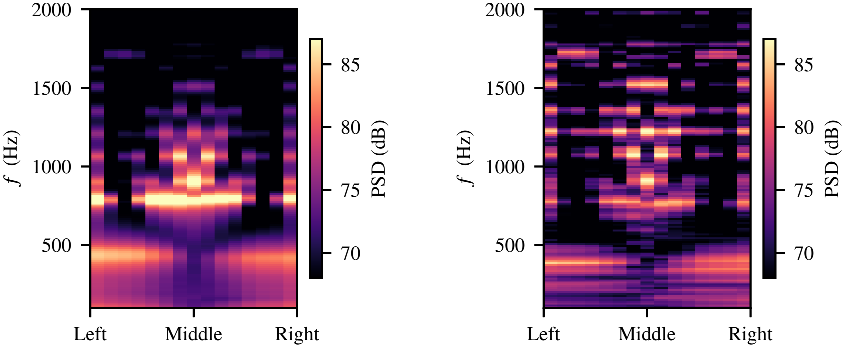

(a)

(b)

Fig. 8.4.8 Map of the gap noise spectra at the 15 microphone positions in the gap: (a) experimental, (b) numerical

classical equivalent to the Helmholtz resonance is present in this experiment and also no classical standing waves with equally spaced nodes are found. Instead we could identify two different types of resonances. The first resonance type is found at the sharpest resonances (compared to their surrounding levels), 400 Hz, 780 Hz, 900 Hz, 1050 Hz and 1700 Hz. As shown in fig. 8.4.9 these resonances feature regions of high acoustic intensity between aerial impedance jumps due to cross-section changes. Especially they do not mainly depend on the reflectance of the walls and the levels close to the gap's side panels are relatively low. The second resonance type (see fig. 8.4.10) is the classical standing wave between the two reflecting side panels of the complex gap. Due to the complex geometry the nodes of these frequencies are not equally distributed. Nevertheless these resonance frequencies depend strongly on the position and the material of the side panels and are thus highly specific to the used model. Especially it is plausible to assume that these resonance frequencies won't be detectable on a real vehicle where no side panels are present and rubber sealings lead to additional damping inside the gap. The first mode type instead is assumed to depend only on the aerial impedance jumps due to the cross-section changes inside the gap and accordingly it should be possible to excite these resonances under the presence of sealings on a real vehicle. As these frequencies depend only on the enclosed volume between the aerial impedance jumps they can be interpreted as a generalization of the classical Helmholtz resonance.

This analysis could be confirmed by measurements on a real S213 E-Class Estate model that was already briefly discussed in the introduction of this thesis. In these experiments we evaluated the top array of the wind-tunnel's measurement system and could localize noise sources in the opening of the rear door gap in fig. 8.4.11. While the main noise source at the

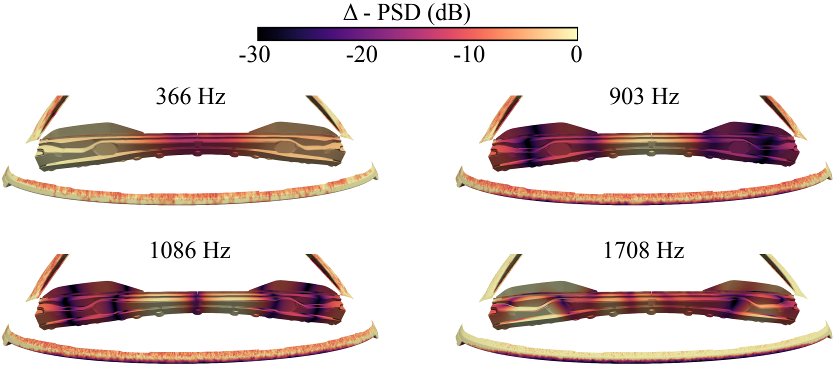

Fig. 8.4.9 Surface FFT at the rear door gap, the roof's spoiler and the railing at four different frequencies that show resonances between aerial impedance jumps (Type 1).

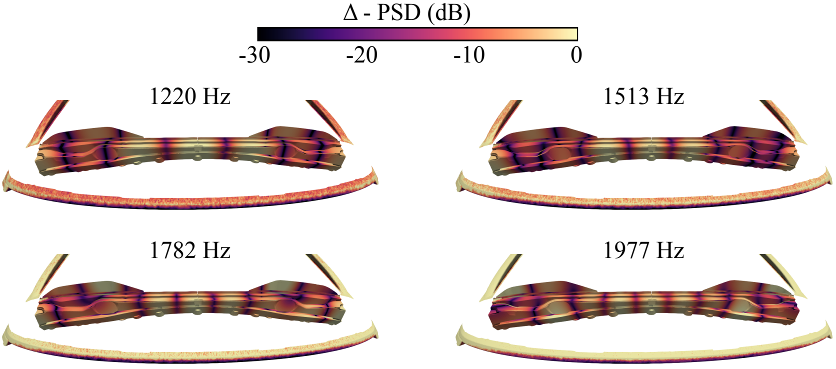

Fig. 8.4.10 Surface FFT at the rear door gap, the roof's spoiler and the railing at four different frequencies that show standing wave resonances between the two SLS side panels (Type 2).

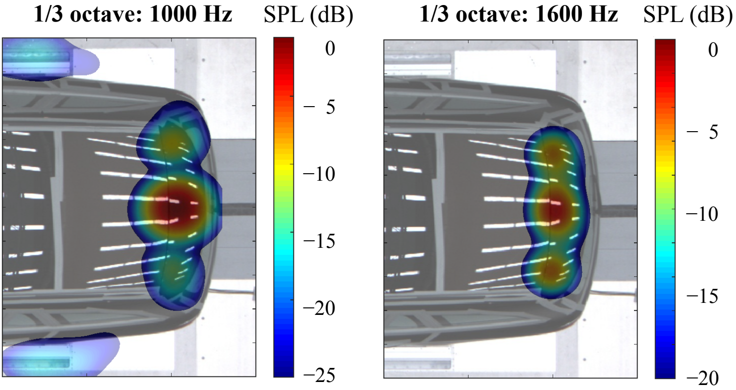

Fig. 8.4.11 Experimental beamforming result of the rear door gap of a real S213 vehicle.

third with base frequency 1 kHz is clearly located in the middle of the gap (which corresponds to the 1080 Hz mode) the noise sources are much more spread in the 1600 Hz third which clearly shows that the 1700 Hz mode is excited as well. Finally the main peak at the driver's ear in these measurements is located at approximately 780 Hz (see fig. 1.4) which coincides extremely well with the loudest 780 Hz mode from the measurements at the S213 model. Consequently, this important resonance frequency could be detuned by adjusting the spanwidth of the small link between the two large cells at the left and the right of the rear door gap. As the coupling between the sealings and the structure of the car is decisive for the final interior noise levels a detuning of the gap could possibly lead to much reduced levels inside the car instead of a pure frequency shift.[47] If the levels of the resonances are not critical, e.g. if a certain resonance frequency is already known to cause problems within the development process, this information could also be gathered by the much cheaper simulation of the pure acoustic excitation.

8.4.3 Numerical Robustness

In order to cover these numerical results, we performed two convergence studies. First we modified only the mesh resolution inside the gap by coarsening the mesh using 1 mm cells instead of 0.5 mm cells. As the inflow does not change between these simulations we can thus study solely the acoustic propagation inside the cavity. The acoustic waves should still be well resolved by the coarse mesh as the wavelength at 5 kHz corresponds to 68 cells per wavelength. It is seen in fig. 8.4.12 that indeed the general behavior does not change but only the levels at the peaks are slightly reduced above 1 kHz. Nevertheless the general behavior remains unchanged and the systematic error persists.

In a second step the resolution of the turbulent boundary layer (that must be considered highly under-resolved in the context of a classical wall-resolved LES) was changed. On the one hand

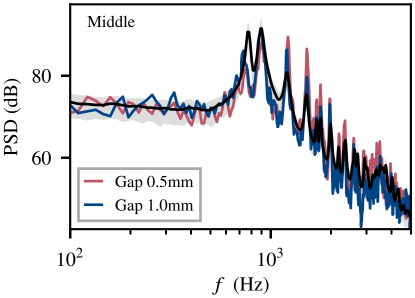

Fig. 8.4.12 Influence of spatial resolution in the gap: Simulated gap noise spectra at the middle microphone in comparison to the experimental data and scattering band. ($\Delta f \approx 12\,\text{Hz}$)

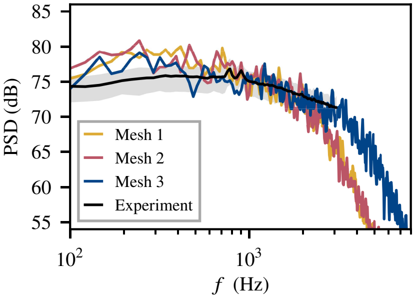

Fig. 8.4.13 Influence of spatial resolution at the roof: Simulated wall pressure spectra at Kulite position no. 4 in comparison to the experimental data and scattering band. ($\Delta f \approx 12\,\text{Hz}$)

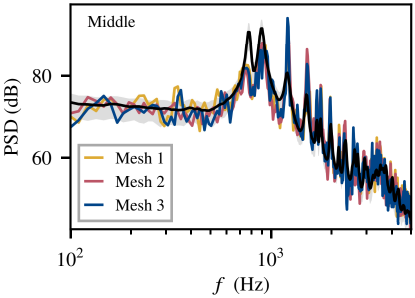

Fig. 8.4.14 Influence of spatial resolution at the roof: Simulated gap noise spectra at the middle microphone in comparison to the experimental data and scattering band. ($\Delta f \approx 12\,\text{Hz}$)

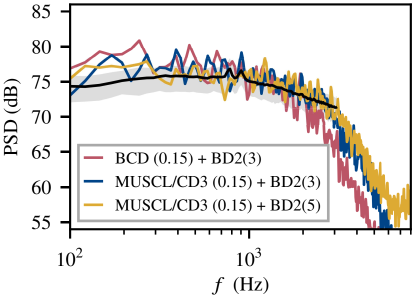

Fig. 8.4.15 Influence of discretization: Simulated wall pressure spectra at Kulite position no. 4 in comparison to the experimental data and scattering band. ($\Delta f \approx 12\,\text{Hz}$)

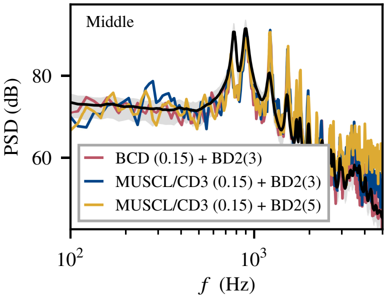

Fig. 8.4.16 Influence of discretization: Simulated gap noise spectra at the middle microphone in comparison to the experimental data and scattering band. ($\Delta f \approx 12\,\text{Hz}$)

we coarsened the outer part of the boundary layer to 2 mm resolution, which results in a total of 180 million cells and on the other hand we introduced a 0.5 mm cell zone in the regions below a wall distance of 5 mm, which leads to a mesh with 545 million cells. In fig. 8.4.13 and fig. 8.4.14 it can be seen that the fine resolution improves the wall pressure spectra at Kulite sensor 4 and the coarse resolution gives very close results to the base case. Again, this finding highlights the capability of ALF to consistently run LES of attached turbulent flows on under-resolved meshes. It is also seen that the acoustic spectra at the mid microphone are basically independent from the upstream resolution as an averaging effect reduces the direct influence of the boundary layer at high frequencies on the acoustic excitation and as the resolution of the gap is always kept at 0.5 mm.

In a last study we modified the used spatial and temporal discretization schemes by testing the originally used MUSCL/CD3 scheme instead of the bounded central scheme and an optimized five step backward differencing scheme instead of the standard three step scheme. It can be seen in fig. 8.4.15 and 8.4.16 that using only the MUSCL/CD3 scheme improves the boundary layer wall pressure spectrum but only changes the high-frequency roll-off of the acoustic spectrum. This shows again the strong dependency from the numerical scheme in this frequency range. When additionally using the optimized BD2 scheme it is found that a high amount of high-frequency noise is introduced in both spectra.

In summary the utilized second order discretization schemes can be consistently used in the simulation of rear door gap noise. Especially, we proved that an improved high frequency roll-off of the boundary layer wall pressure spectra does not imply improvements of the gap noise results. As ALF helps to achieve a consistent behavior on severely under-resolved meshes this finding justifies the usage of a comparably coarse mesh at the vehicle's roof.

8.4.4 Simulation of Case Modifications

Due to the promising results of the hybrid RANS/LES on the S213 model a last hurdle towards near-industrial applicability is the capability to predict the consequences of design modifications and inflow changes. In the experimental analysis we saw that a curvature variation of the leading edge leads to significantly different levels below 1 kHz. We could also show that the gap noise at 70 km/h differs significantly from the previously studied case as a sharp resonance at 400 Hz dominates the spectra. We thus want to stress our method by applying it to these two variations and check whether the systematic error at the resonance frequencies leads to restrictions.

To simulate the noise of the edge design variation we do not change much from our base setup. As we already used a local surface resolution down to 0.25 mm directly at the leading edge, the 0.5 mm cells in the gap and its opening should be fine enough to cover the main flow effects. One can see by comparing fig. 8.4.17 and fig. 8.4.18 that the results of this study are again quite promising. While the base and the sharp variant are on par below 600 Hz, the rounded variant tends to be a few decibels louder in this region. Between 600 Hz and 1100 Hz the expected order from the experimental analysis is clearly present. As the drop of the rounded edge spectra at 1.1 kHz is located at higher frequencies than in the experimental study we must assume, that

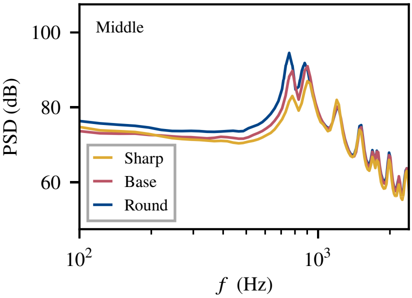

Fig. 8.4.17 Experimental gap noise spectra of the leading edge modifications. ($\Delta f \approx 12\,\mathrm{Hz}$)

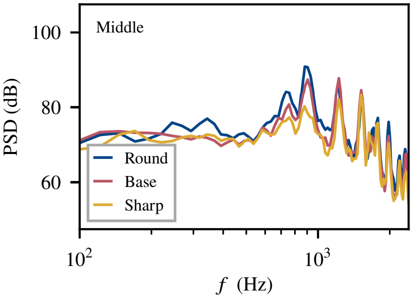

Fig. 8.4.18 Simulated gap noise spectra of the leading edge modifications. ($\Delta f \approx 12\,\mathrm{Hz}$)

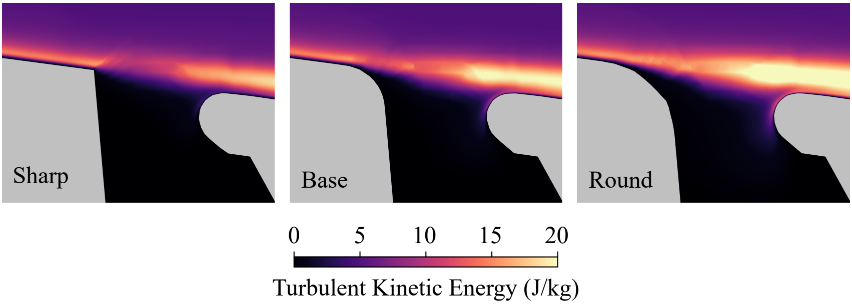

Fig. 8.4.19 Turbulent kinetic energy of the three different leading edges in the $z = 0$ plane in the gap opening.

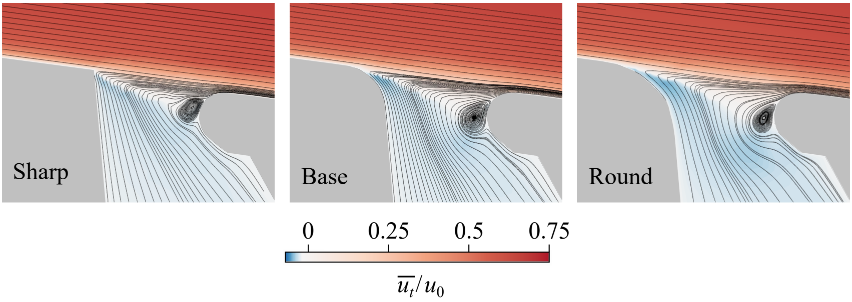

Fig. 8.4.20 Mean flow velocity and mean flow streamlines of the three different leading edges in the $z = 0$ plane in the gap opening.

the gap opening was slightly longer in the experiment, than modeled in our simulations. Above 1.1 kHz the three variants become indistinguishable. Accordingly, the systematic error is equally present for all variants and does not lead to applicability restrictions at this point.

In the basic experiment we saw that a change of the edge shape leads to different flow situations with an unstable, spreading shear layer and accordingly an increased amount of turbulence in the gap's opening. It is found again in fig. 8.4.19 that pressure driven separation sets in with an increased curvature radius of the leading edge and the shear layer begins to spread. Probably due to the thick boundary layer the maximum turbulent kinetic energy in the opening is lower than in the basic experiment. Due to the strongly rounded edge the shear layer's interaction with the trailing edge is also reduced in comparison to the basic experiment from chapter 7.2.1. These findings are confirmed by the mean flow streamlines in fig. 8.4.20. While the flow structure in the basic experiment changed significantly between round and sharp edges, here the structure remains comparable. Due to the increased opening angle of the shear layer, the main vortex moves more into the cavity and the backflow velocity is slightly increased.

As we know from the basic experiment, accurate simulation of aeroacoustic feedback can be hard for our method as the convection velocity in the shear layer is significantly influenced by the potential upstream log-layer mismatch due to spatial under-resolution. Consequently, we assume that an application to the 70 km/h case is a challenging task. Applying the same mesh and time-step choice to this problem first leads to a much faster high-frequency roll-off of the wall pressure spectra. Although this also applies to the surface averaging in the gap opening, it is important to keep this in mind when analyzing the gap acoustics spectra. First, the wall pressure spectrum in front the gap in fig. 8.4.21 is matched with comparable accuracy as the 140 km/h case. Of course the simulation results here begin to drop already at approximately 1 kHz which corresponds again to the same Strouhal number. Interestingly, although being 1 - 2 dB too high, the simulation seems to include the low frequency rise of the levels that cannot be explained by semi-empirical wall pressure models as well as the small peak at 380 Hz. The pressure spectrum at the middle position (fig. 8.4.22) of the gap now features some new properties. While the agreement with the experimental data is generally, and especially in the broadband low-frequency region, quite good again the resonant peaks differ from the experiment. First, the 380 Hz peak is not excited in our simulations. Second, the two resonance frequencies below 1 kHz are severely over-predicted compared to the experiment. And third the levels of the resonances above 1 kHz tend to be closer to the experimental data than at 140 km/h. At least the explanation for this last finding is simple. As the levels of the inflowing boundary layer drop at 1 kHz, the broadband levels at the middle position in this frequency range are lower than the experimental data. Consequently, the relative sharpness of the peaks is comparable to the prior 140 km/h case and only the base level is reduced.

A comparison in the frequency range below 1 kHz between the left, the middle and the right microphone in fig. 8.4.23 can explain at least the 380 Hz issue. While the experimental data showed a strong asymmetry at this resonance frequency between the two sides our simulation result is very symmetric and very close to the data of the right microphone. This indicates that

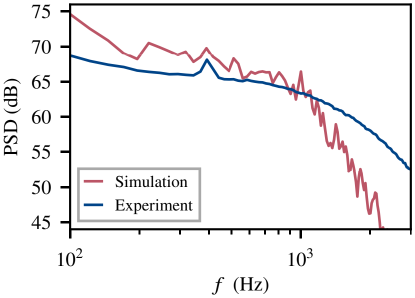

Fig. 8.4.21 Simulated wall pressure spectrum at Kulite position no. 4 in comparison to the experimental data at $u_0 = 70\,\mathrm{km/h}$. ($\Delta f \approx 24\,\mathrm{Hz}$)

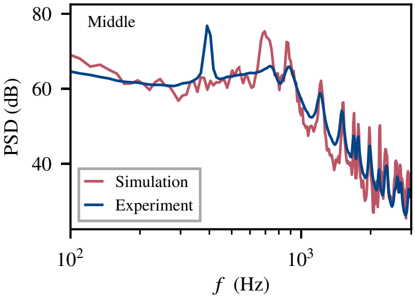

Fig. 8.4.22 Simulated gap noise spectrum at the middle microphone in comparison to the experimental data at $u_0 = 70\,\mathrm{km/h}$. ($\Delta f \approx 12\,\mathrm{Hz}$)

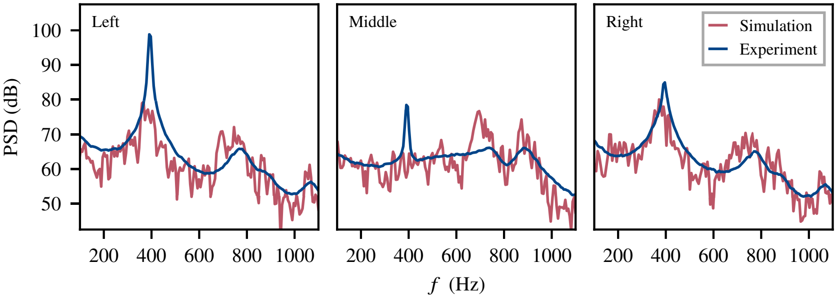

Fig. 8.4.23 Simulated gap noise spectra at the left, middle and right microphone positions in comparison to the experimental data at $u_0 = 70\,\mathrm{km/h}$. ($\Delta f \approx 12\,\mathrm{Hz}$)

in fact the strong excitation at the left side is experimentally introduced by additional shear layer instability due to flow disturbances that are not included in our simulations. Due to the symmetry of the simulation the 380 Hz mode is assumed to vanish at the middle position. Notably also the levels at the two higher frequencies are much closer to the experiment at the left and right position. We can only assume that the strong peak at 380 Hz influences these resonances in the experiment and leads to an attenuation at the middle position.

8.5 Summary

In the preceding chapter we described the transfer of the experiments and simulations of the idealized rear door gap to a full-scale foam model of the rear door gap of a Mercedes-Benz

E-Class Estate S213. The foam model is used to reproduce the realistic geometry and inflow conditions of the gap while still keeping its acoustic boundary conditions as simple as possible. We found that the general behavior of the rear door gap model is very similar to the idealized rear door gap model and accordingly the hybrid RANS/LES can be easily transfered to this realistic case.

It is found that the proposed hybrid RANS/LES is well suited to simulate the turbulent boundary layer induced gap noise of the rear door gap of the S213 model with reasonable computational costs that are approximately 70 times lower than applying a true wall-resolved LES.[3] As a consequence of our numerical and experimental study we can conclude that the current description of the rear door gap of vehicles as pure Helmholtz resonators from Wickern and Brennberger[107] needs further generalization. Depending on the geometry of the rear door gap, resonances between aerial impedance jumps dominate the acoustic spectra in the gap. In the case of simple spanwise shapes this finding coincides with the former formulation of the Helmholtz resonance.[†] For a further development of our numerical method a more accurate treatment of the acoustic impedance at the walls of the rear door gap is required as this physical discrepancy would at least remain as an open question – even if the results could be improved without its addition. In addition we could show that the numerical simulation method is already capable to predict the consequences of velocity dependent sharp resonance peaks as well as the consequences of significant design modifications of the leading edge – even though their impact was comparably small in these cases.

[†] As Wickern and Brennberger used standard 1/2 inch microphones instead of flush-mounted microphones it is also possible that this installation led to an attenuation of the spanwise varying resonance frequencies.

9 Resume and Future Prospects

Based on the current state of research this work aimed to get closer towards a numerical simulation approach for automotive gap noise. To reach these goals we restricted ourselves to a study of the external flow and the noise generated at the rear door gap without the presence of sealings and without analyzing the transport of sound towards the cabin. We wanted to perform experiments that can verify published results, that systematically extend the knowledge of the influence of geometry and inflow variations on gap noise and that create high quality experimental data suitable for the validation of numerical simulations of the external noise. The two bottlenecks for such simulations of automotive gap noise were expected to be a transient representation of the boundary layer pressure fluctuations in the vicinity of the vehicle's gap and the open question whether a DNC might be robust enough for a simulation of the full-scale case or whether a hybrid acoustic simulation based on APE-2 could be applicable to gap noise.

Thus, we experimentally studied automotive gap noise on a strongly idealized model of a car's rear door gap as well as the noise generated at a full-scale foam model of a Mercedes-Benz E-Class Estate's rear door gap. We could clearly prove the similarity between the idealized rear door gap and the full-scale model which allowed to test the importance of several design modifications on the small-scale experiment but most importantly to develop a numerical simulation for the generated gap noise. Our experiments confirmed the proposed mechanisms from the literature that automotive gap noise is essentially a resonant amplification of broadband turbulent boundary layer fluctuations above the gap's opening and especially not dominated by self-sustained oscillations or shear layer instabilities in the opening. We could also show that despite different design changes of the gap the physical mechanism remains relatively stable and only minor velocity dependent frequency shifts of the resonances have been observed. Nevertheless, especially wall-normal offsets and an ill choice of edge curvature can lead to drastically increased noise levels and a velocity dependent cavity response. As the excitation mechanism itself did not change it became however clear that any numerical simulation method for this phenomenon requires a transient representation of the turbulent boundary layer pressure fluctuations.

With a compressible hybrid RANS/LES that is based on the Elliptic Blending Reynolds Stress Model and Anisotropic Linear Forcing we could successfully simulate this phenomenon with respect to accurate boundary layer wall pressure spectra as well as gap noise spectra. The developed method was approximately 70 times faster than a wall-resolved LES of a vehicle.[3] In addition to the restriction of the LES to a smaller computational sub-domain Anisotropic Linear Forcing helped to slightly reduce the strict mesh requirements of the wall-resolved LES. While the quality of the results is reduced on coarse meshes we could still achieve a consistent and stable behavior of the transient simulation. Depending on the used meshes and time-steps its computational costs are thus positioned inbetween a true scale-resolving simulation and stochastic modelling approaches such as the Fast Random Particle Mesh Method and the Stochastic Noise Generation and Radiation methodology. Besides their shear speed these methods are still strongly dependent on empirical model spectra and their application to industrial problems might become critical and restricted to selected situations.

Accordingly, we could prove that Anisotropic Linear Forcing is capable to significantly reduce the numerical costs of turbulent boundary layer simulations on industrial cases. Although the required numerical costs are still comparably high this is a significant step for a problem that has been investigated for years. And although the forcing is only applied to the Reynolds stresses and the mean velocity the resulting pressure fields deliver accurate wall pressure and coherence spectra without introducing a significant amount of spurious noise. Consequently, we want to emphasize that a further mathematical analysis how linear forcing terms in the momentum equation influence the associated pressure fields in the wavenumber and frequency domain is still required. A mathematical justification of the promising and consistent results could help to clarify and strengthen the role of such linear forcing approaches for aeroacoustic applications.

Besides the successful simulation of the externally generated noise at the rear door gap still a significant number of unanswered questions remains. The most interesting quantity for manufacturers is the noise at the passenger positions. To predict spectra at these points the noise simulated inside the gap needs to be transported through the rubber sealings and the metal sheets of the car. Afterwards different possibilities arise: Either the noise is directly radiated into the cabin or it couples first to the structure which could lead to a delocalization of the noise source. The work of Hazir[47] has proven how significant the influence of the sealings on the emitted noise is. Even at very strong external excitations it is possible that the sealing absorbs most of the sound, while it is also possible that a low excitation leads to high levels inside the cabin. Although Hazir already indicated that a one-way coupling to a FE model of the sealing structure using wall-impedance modelling in the fluid domain might be sufficient for simplified cases, clarification is still needed whether a true fluid-structure co-simulation might be required for real gap structures. To increase complexity even further the real position and shape of the sealings is unknown as soon as the doors are closed. Only computer tomography scans could provide the underlying geometry and also discover leakages. We could also show that bad tolerances, especially in the wall-normal direction, can lead to strongly disturbed spectra with increased tonal or broadband noise. Consequently, even the best gap concept can only be assessed correctly within the influence of occurring tolerance issues.

In this context it might be attractive to apply computationally cheap simulation methods in order to get at least rough insights into the physics of automotive gap noise. We could show that the acoustic frequency response test with a white noise excitation could excite all relevant geometric resonance frequencies of the gap. As the computational costs associated with such an approach are much lower than a true aeroacoustic simulation, especially in a frequency domain approach where additionally wall impedances can be implemented in the model, these calculations could develop a valuable standard tool to calculate the gap's transfer function and mode structure. From a steady RANS it is possible to extract the boundary layer profile near the gap opening. This information could then be used to feed a semi-empirical wall pressure spectrum model like Hu's model.[52] As our experiments showed that this model produces good approximations of the wall pressure spectra a combination with the resonance frequencies from the frequency response test could deliver an approximation which resonance frequencies will be strongly excited under aeroacoustic loads.

The transfer of our simulations from the rear door gap to different gaps, such as the side door gaps should be principally possible. Past experimental studies also confirmed the passive excitation type for these gaps, but an accurate match of the inflow conditions for the gap will be more difficult to achieve.[2] As soon as the A-pillar vortex, the side mirror separation and the wake from the front-wheel are involved, the attached boundary layer turbulence will be superposed by detached turbulence. In these cases the applicability of Anisotropic Linear Forcing needs to be studied as both the accuracy of RANS simulations for these inflowing wakes is reduced and the effect of Anisotropic Linear Forcing is strongly reduced for nearly uniform and naturally stable flows. Additionally, the resonance volume of these gaps is much smaller and the influence of rubber sealings in this volume is much bigger.

Especially if wall impedance modeling turned out to be sufficient for automotive gap noise simulations, the simulation with a hybrid acoustic approach would become highly attractive as wall impedance conditions should only act on acoustic waves and not on the hydrodynamic pressure. As we showed in chapter 6, the acoustic wave equation approach based on APE-2 is currently not capable to predict correct levels if the acoustic excitation of a resonance frequency is weak and thus the interaction of the acoustics with the shear layer is strong. We assume that the neglected acoustics – vorticity interaction term from the original APE formulation could improve this behavior. Furthermore we could show that the hybrid simulation is polluted by a high frequency hydrodynamic hump that is strongly affected by the mesh resolution in the corners of the gap. Further research is required to better identify the reasons for this issue.

Finally we showed that currently Anisotropic Linear Forcing is not able to deliver precise results under all conditions. Especially under adverse pressure gradients the EB-RSM RANS tends to strongly over-predict the stresses which necessarily reduces the quality of the target fields for the forcing. On under-resolved meshes and at higher velocities (that usually increase mesh resolution requirements) the LES tends to generate a strong log-layer mismatch. This phenomenon is likely not distinctly due to the LES but more to the used subgrid scale models WALE or Dynamic Smagorinsky that are known to tend to an under-prediction of the friction velocity in such cases. Furthermore, the influence of these issues depends on the observed phenomena. While the influence of the log-layer mismatch on passive gap noise cases is small, an unstable shear layer is significantly affected by its upstream mean boundary layer velocity profile. From our point of view improvements and future work on the EB-RSM RANS and its usability as well as improvements on the log-layer mismatch could help to further improve the method's applicability to other cases while keeping the computational costs as low as possible.

Especially for feedback dominated gap noise applications with comparably large opening we also want to emphasize that the influence of the turbulent boundary layer fluctuations on the gap spectra is typically small due to the surface averaging effect in the gap's opening. Accordingly, (D)DES approaches can become applicable to these kind of problems which would lead to reduced computational costs. Unfortunately the potential grey-area downstream of the gap's leading edge remains an open issue. Approaches like the shear layer improved DDES[73] could be applied successfully to far-field jet noise prediction and might be also applicable to these kind of gap noise cases. Citing Riedelsheimer,[85] we showed that additional shielding errors in the outermost regions of the boundary layer can become an issue with such DES cases and accordingly it might be necessary to understand the influence of the shielding error on the generated gap noise.

For all the above cases, including improvements on the hybrid acoustic wave equation approach, the different variations of the idealized rear door gap experiments and the boundary layer measurements from Hu and Herr can resemble very suitable test cases for validation purposes. Even a superposition of the incoming boundary layer turbulence with the wake of different cylinders was studied and could be used to extrapolate the applicability of the method to different vehicle gaps (c.f. appendix C).

Besides the few present uncertainties we believe that Anisotropic Linear Forcing could be applied successfully to a wide range of different problems that are either intrinsically dependent on the turbulent boundary layer fluctuations or that suffer strongly from grey-area in DES approaches. Possible examples could be: Gap noise under different flow conditions, especially feedback dominated gap noise at airfoils at take-off and landing, airfoil trailing edge and flap noise under large angles of attacks, jet noise, flow noise in ducts that lead to vibrations of the duct, turbulent mixing problems at exhaust systems and probably many more. Although the physically involved frequencies are very low (typically below 50 Hz) even an application of the forcing to sunroof buffeting might be valuable as grey area mitigation in the opening is a strong challenge of such simulations. For all these cases an application strategy for Anisotropic Linear Forcing needs to be developed. Especially the robustness of the forcing region towards complex wall geometries and a comparison of the required time scales for ALF with the time scales of the studied phenomenon will be critical elements of a further generalized application. Finally, the dependency of the phenomena on the potential uncertainties of the method needs to be clarified.

A Discretization Schemes Formulation

In the following we will give a brief summary based on the STAR-CCM+ User Manual v13.06[97] of different discretization schemes compared in this work.

Spatial Discretization

In this thesis we compare the influence of two different spatial discretization schemes of the so-called *convective flux* related to the convective part of the substantial derivative $\mathrm{D}/\mathrm{D}t$. Consider an arbitrary finite volume cell with volume V and surface

$$\partial V := \bigcup_i^n f_i \tag{A.1}$$

with n planar faces f_i and respective face normal vectors $\boldsymbol{n}$ and $\boldsymbol{n}_{f_i}$. The convection of a scalar quantity ϕ is then described by

$$\int_{\partial V} \varrho \boldsymbol{u} \phi \, d\boldsymbol{n} \approx \sum_{f_i}^{n} (\varrho \boldsymbol{u} \phi)_{f_i} \cdot \boldsymbol{n}_{f_i} = \sum_{f_i}^{n} (\dot{m}\phi)_{f_i} = \sum_{f_i}^{n} \dot{m}_{f_i} \phi_{f_i} \tag{A.2}$$

with the mass flow rate $\dot{m}$ and the unknown cell face values ϕ_{f_i}.

In the following, we describe discretization schemes to reconstruct these values within the calculation of the convective flux. Without loss of generality, consider quantity ϕ and a face f, with face center $\boldsymbol{x}_f$ between two neighboring cells with centroids $\boldsymbol{x}_0$ and $\boldsymbol{x}_1$. Especially we are analyzing a standard second order bounded central difference (BCD) scheme and a hybrid bounded third order accurate MUSCL/CD3 scheme. Based on a normalized-variable diagram value ξ both schemes fall back to a first order upwind interpolation under non-smooth flow conditions, where $\xi \notin [0, 1]$.[21,36]

Under smooth flow conditions ($\xi \in [0, 1]$) the convective flux in the BCD scheme is then computed as

$$\phi_{\mathrm{BCD}}(\boldsymbol{x}_f) = \sigma \phi_{\mathrm{CD}}(\boldsymbol{x}_f) + (1 - \sigma)\phi_{\mathrm{SOU}}(\boldsymbol{x}_f) \tag{A.3}$$

with $\sigma \in [0, 1]$ an upwind blending factor. Here ϕ_{CD} is the second order central-difference reconstruction

$$\phi_{\mathrm{CD}}(\boldsymbol{x}_f) = s\phi(\boldsymbol{x}_0) + (1 - s)\phi(\boldsymbol{x}_1) \tag{A.4}$$

with a mesh stretching factor s that equals 0.5 for a uniform mesh. ϕ_{SOU} again is the second order upwind reconstruction of the face flux. Let $\dot{m}_f$ denote the mass flux at $\boldsymbol{x}_f$, $\Delta\boldsymbol{x}_0 := \boldsymbol{x}_f - \boldsymbol{x}_0$ and $\Delta\boldsymbol{x}_1 := \boldsymbol{x}_f - \boldsymbol{x}_1$ then

$$\phi_{\mathrm{SOU}}(\boldsymbol{x}_f) = \begin{cases} \phi(\boldsymbol{x}_0) + \Delta\boldsymbol{x}_0 \cdot (\nabla\phi)_{r,0} & \text{for} \quad \dot{m}_f \geq 0 \\ \phi(\boldsymbol{x}_1) + \Delta\boldsymbol{x}_1 \cdot (\nabla\phi)_{r,1} & \text{for} \quad \dot{m}_f < 0 \end{cases} \tag{A.5}$$

where $(\nabla\phi)_{r,0}$ and $(\nabla\phi)_{r,1}$ are limited reconstruction gradients that depend again on a set of chosen methods and limiters, for more details see [97]. Overall, the BCD scheme provides a compromise between the unstable, more accurate CD scheme and robustness due to its warranted boundedness.

Using the hybrid third order MUSCL/CD3 scheme the convective flux under smooth flow conditions is computed as

$$\phi_{\mathrm{MUSCL/CD3}}(\boldsymbol{x}_f) = \sigma\phi_{\mathrm{MUSCL}}(\boldsymbol{x}_f) + (1-\sigma)\phi_{\mathrm{CD3}}(\boldsymbol{x}_f) \tag{A.6}$$

again with a blending factor σ. The third order central difference reconstruction ϕ_{CD3} is based on two different third order reconstructions ϕ_0 and ϕ_1,

$$\phi_0(\boldsymbol{x}_f) = F\left\{\phi(\boldsymbol{x}_0), (\nabla\phi)_{r,0}, \phi(\boldsymbol{x}_1)\right\} , \tag{A.7}$$

$$\phi_1(\boldsymbol{x}_f) = F\left\{\phi(\boldsymbol{x}_0), (\nabla\phi)_{r,1}, \phi(\boldsymbol{x}_1)\right\} \tag{A.8}$$

using a function F that uses one gradient reconstruction and the two cell center values to estimate a quadratic approximation of ϕ at the face. Then ϕ_{CD3} is calculated as the inverse distance weighted average

$$\phi_{\mathrm{CD3}}(\boldsymbol{x}_f) = \frac{\phi_0(\boldsymbol{x}_f)|\Delta\boldsymbol{x}_1| + \phi_1(\boldsymbol{x}_f)|\Delta\boldsymbol{x}_0|}{|\Delta\boldsymbol{x}_0| + |\Delta\boldsymbol{x}_1|} . \tag{A.9}$$

The third order MUSCL reconstruction ϕ_{MUSCL} is based on [104]. Without loss of generality let cell $\boldsymbol{x}_1$ be downstream of cell $\boldsymbol{x}_0$ and let the cell with centroid $\boldsymbol{x}_{-1}$ be the neighboring cell directly upstream of $\boldsymbol{x}_0$. The principal formulation of the MUSCL scheme then reads

$$\begin{aligned} \phi_{\mathrm{MUSCL}}(\boldsymbol{x}_f) = \phi(\boldsymbol{x}_0) + \frac{1}{4}\Bigg\{&(1+\kappa)\ \varphi\left(\frac{\phi(\boldsymbol{x}_0) - \phi(\boldsymbol{x}_{-1})}{\phi(\boldsymbol{x}_1) - \phi(\boldsymbol{x}_0)}\right)\left[\phi(\boldsymbol{x}_1) - \phi(\boldsymbol{x}_0)\right] + \\ &(1-\kappa)\ \varphi\left(\frac{\phi(\boldsymbol{x}_1) - \phi(\boldsymbol{x}_0)}{\phi(\boldsymbol{x}_0) - \phi(\boldsymbol{x}_{-1})}\right)\left[\phi(\boldsymbol{x}_0) - \phi(\boldsymbol{x}_{-1})\right]\Bigg\} \end{aligned} \tag{A.10}$$

with a suitable blending parameter κ and limiting function φ.

Temporal Discretization

In our simulations an implicit time integration based on second order backward differentiation (BD2) formulas with constant time-step size Δt is used. A minimum number of three time levels is required to achieve second order accuracy and thus the standard scheme used in STAR-CCM+ is the three-step scheme BD2(3), where the temporal derivative of a quantity ϕ at time-step n is governed by

$$\frac{d\phi}{dt} = \frac{1}{\Delta t}\left(\frac{3}{2}\phi_{n+1} - 2\phi_n + \frac{1}{2}\phi_{n-1}\right) \ . \tag{A.11}$$

This BD2(3) scheme is $\mathscr{A}$-stable, which makes it stable enough for multi-purpose applications. According to Dahlquist's theorem an $\mathscr{A}$-stable multistep methode must be of order 2 or lower and thus it is impossible to design higher order backward differencing formulas, that rely on more time levels, without imposing CFL number dependent time-step restrictions.[20] However, incorporating more time levels it is still possible to design $\mathscr{A}$-stable second order backward differencing formulas with significantly reduced error constant compared to the original BD2(3) scheme as a linear combination of different higher order backward differencing schemes.[105] In our studies we especially use the following BD2(5) scheme

$$\mathrm{BD2(5)} = \left(1 - \frac{1}{\sqrt{2}}\right)\mathrm{BD4(5)} - \left(\frac{5}{2} - 2\sqrt{2}\right)\mathrm{BD3(4)} + \left(\frac{1}{\sqrt{2}} + \frac{5}{2} - 2\sqrt{2}\right)\mathrm{BD2(3)} \ , \tag{A.12}$$

where BD3(4) is governed by

$$\frac{d\phi}{dt} = \frac{1}{\Delta t}\left(\frac{11}{6}\phi_{n+1} - 3\phi_n + \frac{3}{2}\phi_{n-1} - \frac{1}{3}\phi_{n-2}\right) \tag{A.13}$$

and BD4(5) by

$$\frac{d\phi}{dt} = \frac{1}{\Delta t}\left(\frac{25}{12}\phi_{n+1} - 4\phi_n + 3\phi_{n-1} - \frac{4}{3}\phi_{n-2} + \frac{1}{4}\phi_{n-3}\right) \ . \tag{A.14}$$

B Vorticity in the Acoustic Wave Equation

In chapter 6 we have seen, that neither the standard Acoustic Wave Equation (4.32), nor the Convective Wave Equation (4.31) is able to correctly predict the levels at weakly excited gap resonance frequencies. It was also found that including the mean flow velocity in the propagation of sound has nearly no influence on the calculated spectra. As the influence of compressibility in the opening increases with increasing velocity but still remains on a low level compared to true compressible cases and as self-sustained oscillations are not present in the observed cases, hybrid acoustic approaches based on APE-2 should be principally applicable. In the derivation of the wave equations we assume $\nabla\bar{\varrho} \to 0$ and neglect several source terms, especially the influence of heat and entropy sources and the linear interaction between the mean flow vorticity and acoustics. While heat and entropy source certainly do not play a decisive role in low Mach-number automotive gap acoustics, we assume that including the vorticity – acoustics interaction can lead to improvements as it is well known that shear layers influence the acoustic propagation, see e.g. [35, 57]. In the following, we derive a very simplistic idea, how this interaction term could be included in the acoustic wave equation. For this purpose, we follow Tosh et al.[103] and recall Ewert's APE-2 equations from chapter 4 in a slightly different form

$$\frac{\partial p'}{\partial t} + c^2\nabla \cdot \left\{\frac{p'}{c^2}\bar{\boldsymbol{u}} + \bar{\varrho}\boldsymbol{u}^{\mathrm{ac}}\right\} = -\, c^2\nabla\bar{\varrho}\cdot\boldsymbol{u}' \tag{B.1}$$

$$\frac{\partial \boldsymbol{u}^{\mathrm{ac}}}{\partial t} + \nabla\left\{\bar{\boldsymbol{u}}\cdot\boldsymbol{u}^{\mathrm{ac}}\right\} + \nabla\frac{p^{\mathrm{ac}}}{\bar{\varrho}} = \nabla q_{\bar{\omega}} \tag{B.2}$$

where $p' := \bar{\varrho}\phi_p + p^{\mathrm{ac}}$ is a pressure fluctuation with the incompressible noise sources ϕ_p and the acoustic pressure p^{ac}. Assuming smoothness of all quantities we can take the substantial derivative $\partial/\partial t + \bar{\boldsymbol{u}}\cdot\nabla$ of equation (B.1) and the divergence of equation (B.2) and get

$$\begin{aligned}\frac{\partial^2 p^{\mathrm{ac}}}{\partial t^2} + \bar{\boldsymbol{u}}\cdot\nabla\frac{\partial p^{\mathrm{ac}}}{\partial t} + c^2\nabla\cdot\left(\bar{\varrho}\frac{\partial\boldsymbol{u}^{\mathrm{ac}}}{\partial t}\right) + c^2\bar{\boldsymbol{u}}\cdot\nabla\left(\nabla\cdot\bar{\varrho}\boldsymbol{u}^{\mathrm{ac}}\right)&\\ + \nabla\cdot\left(\bar{\boldsymbol{u}}\frac{\partial p^{\mathrm{ac}}}{\partial t}\right) + \left(\bar{\boldsymbol{u}}\cdot\nabla\right)\left(\nabla\cdot\bar{\boldsymbol{u}}p^{\mathrm{ac}}\right)&\\ = -\bar{\varrho}\frac{\partial^2\phi_p}{\partial t^2} - \bar{\boldsymbol{u}}\cdot\nabla\left(\bar{\varrho}\frac{\partial\phi_p}{\partial t}\right) - \nabla\cdot\left(\bar{\boldsymbol{u}}\frac{\partial\phi_p}{\partial t}\right) - \left(\bar{\boldsymbol{u}}\cdot\nabla\right)\left(\nabla\cdot\bar{\boldsymbol{u}}\phi_p\right)&\end{aligned} \tag{B.3}$$

$$c^2\nabla\cdot\left(\bar{\varrho}\frac{\partial\boldsymbol{u}^{\mathrm{ac}}}{\partial t}\right) + c^2\nabla\cdot\bar{\varrho}\nabla\left\{\bar{\boldsymbol{u}}\cdot\boldsymbol{u}^{\mathrm{ac}}\right\} + c^2 \bigtriangleup\, p^{\mathrm{ac}} = c^2\nabla\cdot\bar{\varrho}\nabla q_{\bar{\omega}} \tag{B.4}$$

Now assume incompressible flow, i.e. $\nabla \cdot \bar{\boldsymbol{u}} = 0$ and $\nabla \bar{\varrho} \to 0$, and let p^{inc} be an incompressible pressure fluctuation. Then we can furthermore assume

$$\bar{\varrho} \frac{\partial \phi_p}{\partial t} \approx \frac{\partial p^{\mathrm{inc}}}{\partial t} \quad \text{and} \quad \nabla \bar{\varrho} \phi_p \approx \nabla p^{\mathrm{inc}} \,. \tag{B.5}$$

With $\nabla \times \boldsymbol{u}^{\mathrm{ac}} = 0$ and also assuming negligible diffusion of the mean velocity we combine the two equations and obtain a modified form the convective wave equation

$$\begin{aligned} &\frac{1}{c^2}\frac{\partial^2 p^{\mathrm{ac}}}{\partial t^2} + \frac{2}{c^2}\bar{\boldsymbol{u}} \cdot \nabla \frac{\partial p^{\mathrm{ac}}}{\partial t} + \frac{(\bar{\boldsymbol{u}} \cdot \nabla)}{c^2}\left[\nabla \cdot \bar{\boldsymbol{u}} p^{\mathrm{ac}}\right] - \triangle\, p^{\mathrm{ac}} \\ &\qquad = -\left[\frac{1}{c^2}\frac{\partial^2 p^{\mathrm{inc}}}{\partial t^2} + \frac{2}{c^2}\bar{\boldsymbol{u}} \cdot \nabla \frac{\partial p^{\mathrm{inc}}}{\partial t} + \frac{(\bar{\boldsymbol{u}} \cdot \nabla)}{c^2}\left[\nabla \cdot \bar{\boldsymbol{u}} p^{\mathrm{inc}}\right]\right] - \bar{\varrho} \triangle\, q_{\bar{\omega}} \end{aligned} \tag{B.6}$$

With Ewert's definition

$$\Delta\, q_{\bar{\omega}} \coloneqq -\nabla \cdot \left(\bar{\boldsymbol{\omega}} \times \boldsymbol{u}^{\mathrm{ac}}\right) \,. \tag{B.7}$$

and some vector algebra we arrive at

$$\begin{aligned} &\frac{1}{c^2}\frac{\partial^2 p^{\mathrm{ac}}}{\partial t^2} + \frac{2}{c^2}\bar{\boldsymbol{u}} \cdot \nabla \frac{\partial p^{\mathrm{ac}}}{\partial t} + \frac{(\bar{\boldsymbol{u}} \cdot \nabla)}{c^2}\left[\nabla \cdot \bar{\boldsymbol{u}} p^{\mathrm{ac}}\right] - \triangle\, p^{\mathrm{ac}} \\ &\qquad = -\left[\frac{1}{c^2}\frac{\partial^2 p^{\mathrm{inc}}}{\partial t^2} + \frac{2}{c^2}\bar{\boldsymbol{u}} \cdot \nabla \frac{\partial p^{\mathrm{inc}}}{\partial t} + \frac{(\bar{\boldsymbol{u}} \cdot \nabla)}{c^2}\left[\nabla \cdot \bar{\boldsymbol{u}} p^{\mathrm{inc}}\right]\right] + \bar{\varrho}\boldsymbol{u}^{\mathrm{ac}} \cdot (\nabla \times \bar{\boldsymbol{\omega}}) \end{aligned} \tag{B.8}$$

The acoustic velocity $\boldsymbol{u}^a$ is related to the acoustic pressure by the linear Euler equation

$$\bar{\varrho}\, \frac{\partial \boldsymbol{u}^a}{\partial t} = -\, \nabla p^a \tag{B.9}$$

that can be used to close the system. If one allows a slight phase delay of two time-steps, the acoustic velocity $\boldsymbol{u}_n^{\mathrm{ac}}$ at time-step n can be approximated from the original acoustic pressure p^{ac} from equation (4.31) using the second order backward differencing formula

$$\boldsymbol{u}_n^{\mathrm{ac}} = \frac{1}{3}\left[\boldsymbol{u}_{n-1}^{\mathrm{ac}} - \boldsymbol{u}_{n-2}^{\mathrm{ac}} + \frac{2\Delta t}{\bar{\varrho}} \nabla p_n^{\mathrm{ac}}\right] \tag{B.10}$$

which is then used in equation (B.8). Besides this small phase shift, the gradients of the vorticity and the acoustic velocity can become quite large close to the walls and edges in the gap opening and thus still careful gradient limiting as typically used in finite volume codes is likely necessary for a stable simulation.

C Gap Noise in the Wake of a Cylinder

In an additional series of experiments we investigated a superposition of the incoming turbulent boundary layer with the wake of different cylinders on the noise generated by the basic gap from chapter 6. As such a superposition of an attached boundary layer and turbulent wakes is characteristic for most gaps on vehicles it is a central question how the gap responds to increased turbulence levels or tonal noise generated by upstream obstacles or flow phenomena. Applied to the rear door gap, the cylinder can be especially interpreted as an antenna model.

To this purpose we positioned cylinders with diameter d of 10 mm, 20 mm and 60 mm at $x = 950\,\mathrm{mm}$, 150 mm upstream of the cavity at $z = 0\,\mathrm{mm}$, see fig. C.1. The cylinders are 40 mm high, which is thicker than the boundary layer thickness δ, but the influence of the boundary layer on the vortex shedding is still strong. Accordingly we assume that the effective mean free stream velocity for the cylinder flow corresponds more to the boundary layer convection velocity $u_c \approx 0.7u_e$ for a ZPG boundary layer than to u_e. At $u_0 = 40\,\mathrm{m\,s^{-1}}$ the Reynolds number of the cylinder flow is thus in the range $1.8 \times 10^4 \leq \mathrm{Re}_d \leq 1.1 \times 10^5$ which is below the critical range and one can approximate the vortex shedding Strouhal number by St ≈ 0.2.[64]

In fig. C.2 and fig. C.3 one can see the wall pressure spectra measured for the middle position cylinders at Kulite sensor no. 4 that lies directly downstream of the cylinder (radiation angle $\alpha = 0°$) and Kulite sensor no. 9 which is positioned at a radiation angle $\alpha \approx 10.5°$, respectively. At both sensor positions a strong broadband increase of the levels is found compared to the base ZPG case that increases with the cylinder's diameter and becomes smaller at higher frequencies. In case of the thinnest cylinder the levels even coincide with the ZPG wall pressure spectra above 2 kHz and 3.5 kHz, respectively. Especially at $\alpha \approx 10.5°$ different humps and peaks can be seen in the spectra that correspond well to the vortex shedding Strouhal number Sr ≈ 0.2. For the cylinder with diameter $d = 20\,\mathrm{mm}$ also the first harmonic is visbile. At $\alpha = 0°$ only this first harmonic and the very broad hump of the thickest cylinder can be detected in the wall pressure spectra. Fig. C.4 shows the gap noise at the edge microphone of the four variants. Again, a broadband increase of the levels is detected with increasing cylinder diameter and the levels of the spectra get closer as the frequencies increase, which is probably supported by the surface averaging effect in the gap opening. Interestingly only the vortex shedding components visible at $\alpha = 0°$ are present inside the cavity and the cavity's response to these peaks is nearly linear. In his experiments on the influence of a real antenna on the rear door gap noise, Schimmelpfennig argued that the resulting vortices lead to antisymmetric antiphase pressure fluctuations that cannot effectively excite the symmetric gap, if the obstacle is placed in its symmetry plane.[90]

To further test this hypothesis we also positioned the two cylinders with diameters 10 mm and 20 mm at $x = 950\,\mathrm{mm}$ and $z = 50\,\mathrm{mm}$ (see fig. C.5). Kulite sensor no. 4 now corresponds to $\alpha \approx -10.5°$ and Kulite sensor no. 9 to $\alpha \approx -2.7°$. At both radiation angles (fig. C.6 and fig. C.7)

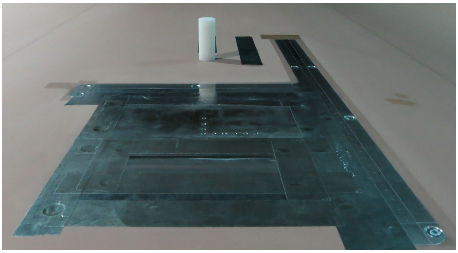

Fig. C.1 Cylinder with diameter $d = 2\,\mathrm{cm}$ positioned 250 mm upstream of the cavity in the symmetry plane of the flat-plate.

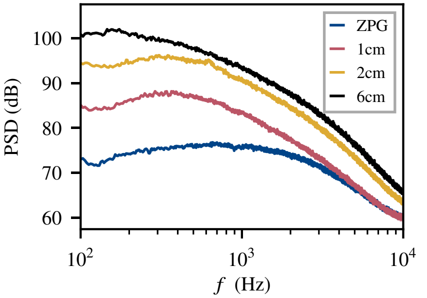

Fig. C.2 Influence of the different cylinders in the symmetry position on the wall pressure spectra at Kulite sensor no. 4, corresponding to $\alpha = 0°$. ($M = 2^{14}$, $^{D}/_{M} = 0.5$)

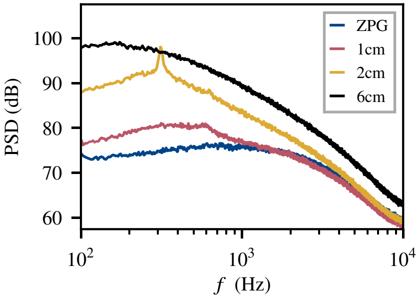

Fig. C.3 Influence of the different cylinders in the symmetry position on the wall pressure spectra at Kulite sensor no. 9, corresponding to $\alpha \approx 10.5°$. ($M = 2^{14}$, $^{D}/_{M} = 0.5$)

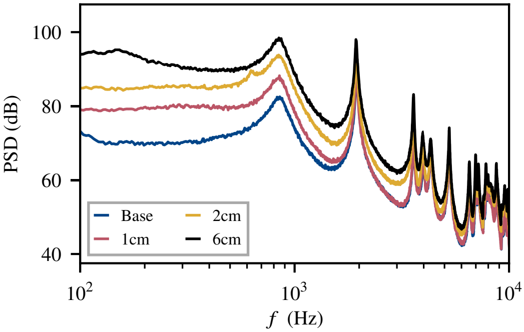

Fig. C.4 Influence of the different cylinders in the symmetry position: Gap noise spectra at the edge microphone. ($M = 2^{14}$, $^{D}/_{M} = 0.5$)

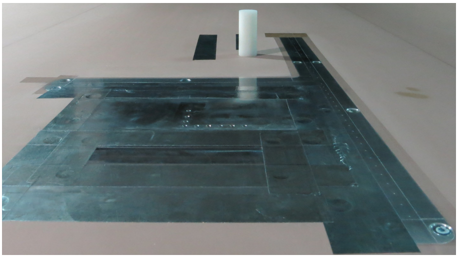

Fig. C.5 Cylinder with diameter $d = 2\,\mathrm{cm}$ positioned 250 mm upstream of the cavity at $z = 50\,\mathrm{mm}$.

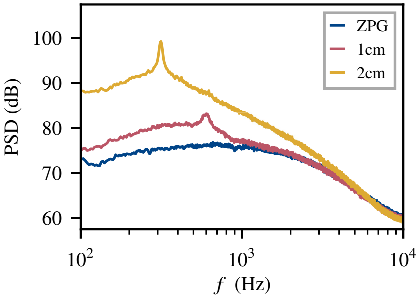

Fig. C.6 Influence of the different cylinders in the $z = 50\,\mathrm{mm}$ position on the wall pressure spectra at Kulite sensor no. 4, corresponding to $\alpha \approx -10.5°$. ($M = 2^{14}$, ${}^{D}/_{M} = 0.5$)

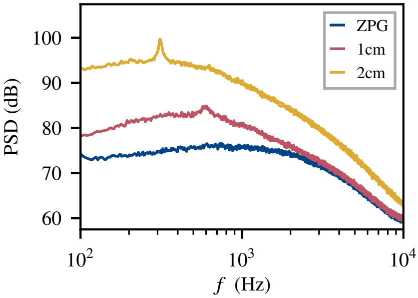

Fig. C.7 Influence of the different cylinders in the $z = 50\,\mathrm{mm}$ position on the wall pressure spectra at Kulite sensor no. 9, corresponding to $\alpha \approx -2.7°$. ($M = 2^{14}$, ${}^{D}/_{M} = 0.5$)

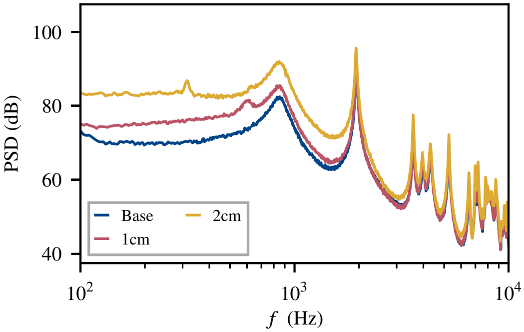

Fig. C.8 Influence of the different cylinders in the $z = 50\,\mathrm{mm}$ position: Gap noise spectra at the edge microphone. ($M = 2^{14}$, ${}^{D}/_{M} = 0.5$)

one can now clearly see the vortex shedding frequency as well as the first harmonic of the 20 mm cylinder. Again the levels at the edge microphone in the cavity in fig. C.8 increase broadbandly as in the symmetric case, but now one can see small tonal peaks of the vortex shedding frequency in the cavity as well. Accordingly, our experiments confirm Schimmelpfennig's hypothesis and emphasize the gap's main role as a passive amplifier of external turbulence and noise – and only under special conditions the gap is not excited effectively.

These results have different consequences for automotive gap noise: First and most obviously, gaps become much louder as the inflowing turbulent fluctuations increase. This finding coincides with Albrecht's results[2] who found, that the lower part of the B-pillar gap, that lies completely within the front wheel's wake, generates most noise at the side door. Secondly one should especially avoid a coincidence of external tonal noise with the geometric resonance frequencies of the gaps, as here the gap's response would lead to a strong amplification of external noise. In any case this experiment clearly proves the importance of a correct resolution of the incoming turbulence independent from the specific inflow conditions. However further studies are required to understand whether a DES might be sufficient for gap noise simulations if the gap's inflow conditions is dominated by detached turbulence.

List of Figures

List of Tables

Nomenclature

Abbreviations

AIAA	American Institute of Aeronautics and Astronautics
ALF	Anisotropic Linear Forcing
AOA	Angle Of Attack
APE	Acoustic Perturbation Equation
APG	Adverse Pressure Gradient
AWB	Acoustic Windtunnel Braunschweig
(C)PSD	(Cross) Power Spectral Density
CAA	Computational Aeroacoustics
CAD	Computer Aided Design
CD	Central Difference
CFD	Computational Fluid Dynamics
CFL	Courant-Friedrichs-Lewy
CPU	Central Processing Unit
DDES	Delayed Detached Eddy Simulation
DES	Detached Eddy Simulation
DLR	German Aerospace Center
DNC	Direct Noise Computation
DNS	Direct Numerical Simulation
EB-RSM	Elliptic Blending Reynolds Stress Model
FFT	Fast Fourier Transform
FPG	Favorable Pressure Gradient
FRPM	Fast Random Particle Mesh Method
IAG	Institute of Aerodynamics and Gasdynamics
IDDES	Improved Delayed Detached Eddy Simulation
LES	Large Eddy Simulation

MUSCL	Monotonic Upwind Scheme for Conservation Laws
NACA	National Advisory Committee for Aeronautics
RDG	Rear Door Gap
S213	Mercedes-Benz E-Class
SGS	Sub-Grid Scale
SLS	Selective Laser Sintering
SNGR	Stochastic Noise Generation and Radiation
SPL	Sound Pressure Level
(T)BL	(Turbulent) Boundary Layer
TKE	Turbulent kinetic energy
(U)RANS	(Unsteady) Reynolds Averaged Navier Stokes
ZPG	Zero Pressure Gradient

Mathematical Operators and Conventions

a	Scalar quantity, completely defined by its magnitude
$\boldsymbol{a}$	Vector $\boldsymbol{a} = (a_1, a_2, a_3)^\mathsf{T} \in \mathbb{R}^3$
$\mathbf{A}$	Second order tensor $\mathbf{A} = (a_{ij})_{i,j=1}^3 \in \mathbb{R}^{3\times 3}$
$\mathbf{A}^\mathsf{T}$	Transpose of tensor $\mathbf{A}$
$\boldsymbol{a} \cdot \boldsymbol{b}$	Scalar (inner) product of $\boldsymbol{a}$ and $\boldsymbol{b}$
$\boldsymbol{a} \times \boldsymbol{b}$	Cross product of $\boldsymbol{a}$ and $\boldsymbol{b}$
$\boldsymbol{a} \otimes \boldsymbol{b}$	Dyadic product of $\boldsymbol{a}$ and $\boldsymbol{b}$
$\mathbf{A} : \mathbf{B}$	Inner product of $\mathbf{A}$ and $\mathbf{B}$
$\partial a / \partial x$	Partial derivative of scalar field a with respect to scalar quantity x
∇a	Gradient of scalar field a
$\nabla \cdot \boldsymbol{a}$	Divergence of vector field $\boldsymbol{a}$
$\nabla \boldsymbol{a}$	Jacobian of vector field $\boldsymbol{a}$
$\nabla \times \boldsymbol{a}$	Curl of vector field $\boldsymbol{a}$
$(\nabla \cdot \boldsymbol{a})\boldsymbol{b}$	Defined as $a_i \partial b_j / \partial x_i \boldsymbol{e}_j$ with the $\mathbb{R}^3$ unit vectors $\boldsymbol{e}_j$
$\nabla \cdot \mathbf{A}$	Divergence of tensor field $\mathbf{A}$
Da/Dt	Substantial derivative $\partial a / \partial t + (\boldsymbol{u} \cdot \nabla) a$ of scalar field a with velocity $\boldsymbol{u}$
$\triangle a$	Laplacian of scalar field a

$\Box a$	Wave operator of scalar field a
$\overline{(\cdots)}$	Temporal averaged quantity
$\langle\cdots\rangle$	Approximation of the temporal averaged quantity
$(\cdots)'$	Fluctuating quantity
$(\cdots)^{\mathrm{inc}}$	Solenoidal incompressible quantity
$\widetilde{(\cdots)}$	Subgrid scale filtered quantity in LES
$(\cdots)^{s}$	Subgrid quantity
$(\cdots)^{\dagger}$	ALF target field
$(\cdots)^{\mathrm{ac}}$	Irrotational acoustic quantity
$(\cdots)^{+}$	Wall (friction velocity) scaled quantity

Latin Symbols

c	Speed of sound
C_p	Pressure coefficient
C_r, C_μ, C_v, C_t	Model constants of ALF
C_s	Model constants of LES subgrid scale models
D	Diameter
D, D_o	Depth, opening depth
e	Specific inner energy
e_t	Specific total energy $e_t = e + \frac{1}{2}\boldsymbol{u}\cdot\boldsymbol{u}$
$\boldsymbol{f}_b$	External body forces
f	Frequency
f_H, f_i	Helmholtz frequency, i-th resonance frequency
H	Shape factor
$\mathbf{I}$	Identity tensor
$\boldsymbol{k}$	Wave vector
k_c	Acoustic wave number
k	Turbulent kinetic energy, wave number
L, L_o	Length, opening length
L_{ALF}	Length of the ALF region
D	Window overlap for Welch's method

M	Sample length for Welch's method
m	Mass
N_{EWA}	ALF temporal filter length
$\mathbf{S}$, S	Strain rate tensor, modulus of the strain rate tensor
$\mathbf{T}$	Viscous stress tensor
p	Pressure
Q	Dynamic pressure
q	Heat flux
$q_{\bar{\omega}}$	Vorticity source term of the APE-2 equations
$\boldsymbol{r}$	Distance
R	Universal gas constant
R_{pp}	Space-time correlation
Re	Reynolds number
S_{pp}	Cross power spectral density
St	Strouhal number
T	Temperature
t	Time
$\boldsymbol{u}$	Velocity
U	Internal energy
u_0	Free stream velocity
u_τ	Friction velocity
u_c	Convection velocity
u_e	Boundary layer edge velocity
W	Width
$\boldsymbol{x}$	Position

Greek Symbols

Δt	Time-step size
Δx	Mesh size
δ	Boundary layer velocity thickness
δ^*	Displacement thickness

δ_{ij}	Kronecker symbol
$\boldsymbol{\Delta}, \Delta$	Filter width, filter length scale
ε	Turbulent dissipation rate
ϕ	Total power spectral density
ϕ_m	Measured total power spectral density
Φ_{pp}	Wavenumber-frequency spectrum
Γ_{pp}	Cross coherence
η	Kolmogorov length scale
λ	Taylor micro-scale
μ	Dynamic viscosity
μ_t	Turbulent viscosity, Subgrid scale viscosity
μ	Kinematic viscosity
ϱ	Density
τ_r, τ_v	ALF time scales
τ_w	Wall-shear stress
θ	Momentum thickness
ω	Angular frequency
$\boldsymbol{\omega}$	Vorticity

Bibliography

[1] *A2MAC1 Automotive Benchmarking*. URL: `https://portal.a2mac1.com/`.

[2] C. Albrecht. “Aeroakustische Untersuchung von Fugen- und Dichtungsgeräuschen am umströmten Fahrzeug”. Master’s thesis. Hochschule für Angewandte Wissenschaften Hamburg, 2011.

[3] K. Ambo et al. “Comparison between Wall-modeled and Wall-resolved Large Eddy Simulations for the prediction of boundary-layer separation around the side mirror of a full-scale vehicle”. In: *2016 AIAA SciTech Forum*. AIAA 2016-2749. 2016.

[4] B. Andersson et al. *Computational fluid dynamics for engineers*. Cambridge: Cambridge University Press, 2012.

[5] G. Araya et al. “A Dynamic Multi-scale Approach for Turbulent Inflow Boundary Conditions in Spatially Developing Flows”. In: *Journal of Fluid Mechanics* 670.3 (2011).

[6] B. Arguillat and D. Ricot. “Measurements of the wavenumber-frequency spectrum of wall pressure fluctuations under turbulent flows”. In: *11th AIAA/CEAS Aeroacoustics Conference*. AIAA 2005-2855. 2005.

[7] W. Béchara et al. “Stochastic approach to noise modeling for free turbulent flows”. In: *AIAA Journal* 32.3 (1994), pp. 455–463.

[8] P. Bernicke et al. “Overset LES of a Solid and Porous NACA0012 Trailing Edge”. In: *2018 AIAA/CEAS Aeroacoustics Conference*. AIAA 2018-3454. 2018.

[9] W. K. Blake and D. M. Chase. “Wavenumber frequency spectra of turbulent boundary!layer pressure measured by microphone arrays”. In: *Journal of the Acoustical Society of America* 49 (1970), pp. 862–877.

[10] D. J. Bodony. “Analysis of sponge zones for computational fluid mechanics”. In: *Journal of Computational Physics* 212.2 (2006), pp. 681–702.

[11] C. Bogey, C. Bailly, and D. Juvé. “Computation of Flow Noise Using Source Terms in Linearized Euler’s Equations”. In: *AIAA Journal* 40.2 (2002), pp. 235–243.

[12] M. Brennberger. “Aeroakustik überströmter Hohlräume”. PhD thesis. Technische Universität München, 2008.

[13] R. Buckisch, H. Tokuno, and H. Knoche. “The New Daimler Automotive Wind Tunnel: Acoustic Properties and Measurement System”. In: *Progress in Vehicle Aerodynamics and Thermal Management. Proceedings of the 10th FKFS-Conference*. 2015.

[14] M. K. Bull. “Wall-pressure fluctuations beneath turbulent boundary layers: Some reflections on forty years of research”. In: *Journal of Sound and Vibration* 190.3 (1996), pp. 299–315.

[15] D. R. Chapman. “Computational aerodynamics development and outlook”. In: *AIAA Journal* 17.12 (1979), pp. 1293–1313.

[16] H. Choi and P. Moin. “Effects of the Computational Time Step on Numerical Solutions of Turbulent Flow”. In: *Journal of Computational Physics* 113.1 (1994), pp. 1–4.

[17] H. Choi and P. Moin. “Grid-point requirements for large eddy simulation: Chapman’s estimates revisited”. In: *Physics of Fluids* 24.1 (2012), p. 011702.

[18] G. M. Corcos. “Resolution of Pressure in turbulence”. In: *Journal of the Acoustical Society of America* 35 (1963), pp. 192–199.

[19] G. M. Corcos. “The structure of the turbulent pressure field in boundary-layer flows”. In: *Journal of Fluid Mechanics* 18.3 (1964), pp. 353–378.

[20] G. G. Dahlquist. “A special stability problem for linear multistep methods”. In: *BIT Numerical Mathematics* 3.1 (1963), pp. 27–43.

[21] M. S. Darwish and F. Moukalled. “Normalized Variable and Space Formulation Methodology for High-Resolution Schemes”. In: *Numerical Heat Transfer, Part B: Fundamentals* 26 (1994), pp. 79–107.

[22] A. T. De Jong. “Aeroacoustic Resonance of Slender Cavities. An experimental and numerical investigation”. PhD thesis. Technische Universiteit Delft, 2012.

[23] B. De Laage de Meux et al. “Anisotropic linear forcing for synthetic turbulence generation in large eddy simulation and hybrid RANS/LES modeling”. In: *Physics of Fluids* 27.3 (2015), p. 035115.

[24] N. Dhamankar, G. A. Blaisdell, and A. Lyrintzis. “An Overview of Turbulent Inflow Boundary Conditions for Large Eddy Simulations (Invited)”. In: *22nd AIAA Computational Fluid Dynamics Conference*. AIAA 2015-3213. 2015.

[25] P. A. Durbin. “Near-wall turbulence closure modeling without “damping functions””. In: *Theoretical and Computational Fluid Dynamics* 3.1 (1991), pp. 1–13.

[26] P. A. Durbin. “A Reynolds stress model for near-wall turbulence”. In: *Journal of Fluid Mechanics* 249.1 (1993), pp. 465–498.

[27] P. A. Durbin and B. A. Pettersson-Reiff. *Statistical theory and modeling for turbulent flows*. 2. ed. Chichester: Wiley, 2011.

[28] G. Eitel-Amor, R. Örlü, and P. Schlatter. “Simulation and validation of a spatially evolving turbulent boundary layer up to $Re_\theta = 8300$”. In: *International Journal of Heat and Fluid Flow* 47.69 (2014), pp. 57–69.

[29] S. A. Elder, T. M. Farabee, and F. C. DeMetz. “Mechanisms of flow-excited cavity tones at low Mach number”. In: *Journal of the Acoustical Society of America* 72.2 (1982), pp. 532–549.

[30] L. Erbig, N. Hu, and S. Lardeau. “Experimental and Numerical Study of Passive Gap Noise”. In: *2018 AIAA/CEAS Aeroacoustics Conference*. AIAA 2018-3595. 2018.

[31] L. Erbig and S. Lardeau. “Hybrid RANS/LES of an Adverse Pressure Gradient Turbulent Boundary Layer Using an Elliptic Blending Reynolds Stress Model and Anisotropic Linear Forcing”. In: *Notes on Numerical Fluid Mechanics and Multidisciplinary Design*. 2020.

[32] L. Erbig and M. Maihöfer. “A Hybrid RANS/LES for Automotive Gap Noise Simulations”. In: *25th AIAA/CEAS Aeroacoustics Conference*. AIAA 2019-2445. 2019.

[33] R. Ewert. “Broadband slat noise prediction based on CAA and stochastic sound sources from a fast random particle-mesh (RPM) method”. In: *Computer & Fluids* 37.4 (2008), pp. 369–387.

[34] R. Ewert and W. Schröder. “Acoustic perturbation equation based on flow decomposition via source filtering”. In: *Journal of Computational Physics* 188 (2003), pp. 365–398.

[35] R. Ewert et al. “A CAA Based Approach to Tone Haystacking”. In: *15th AIAA/CEAS Aeroacoustics Conference (30th AIAA Aeroacoustics Conference)*. AIAA 2009-3217. 2009.

[36] J. H. Ferziger and M. Peric. *Computational Methods for Fluid Dynamics*. 3rd ed. Springer-Verlag Berlin Heidelberg, 2002.

[37] J. Fröhlich. *Large Eddy Simulation turbulenter Strömungen*. 1st ed. Springer, 2006.

[38] M. Germano et al. “A Dynamic Subgrid-Scale Eddy Viscosity Model”. In: *Physics of Fluids A* 3.7 (1991), pp. 1760–1765.

[39] M. Gharib and A. Roshko. “The effect of flow oscillations on cavity drag”. In: *Journal of Fluid Mechanics* 177 (1987), pp. 501–530.

[40] M. B. Giles. “Non-reflecting boundary conditions for Euler equation calculations”. In: *AIAA Journal* 28.12 (1990), pp. 2050–2058.

[41] X. Gloerfelt. *Cavity Noise*. Lecture Notes. Von Karman Institute for Fluid Dynamics, 2009.

[42] X. Gloerfelt. *Noise From Automotive Components*. Lecture Notes. Von Karman Institute for Fluid Dynamics, 2009.

[43] J. Golliard. “Noise of Helmholtz-resonator like cavities excited by a low Mach-number turbulent flow”. Ph.D. thesis. Université de Poitiers, 2002.

[44] M. Goody. “Empirical Spectral Model of Surface Pressure Fluctuations”. In: *AIAA Journal* 42.9 (2004), pp. 1788–1794.

[45] J. C. Hardin and D. S. Pope. “An acoustic/viscous splitting technique for computational aeroacoustics”. In: *Theoretical and Computational Fluid Dynamics* 6 (1994), pp. 323–340.

[46] S. Haxter and C. Spehr. “Up in the Air: In-FlightWavenumber Characterization of Surface Pressure Fluctuations at Transonic Conditions”. In: *2018 AIAA/CEAS Aeroacoustics Conference*. AIAA 2018-3275. 2018.

[47] A. Hazir. “Simulation of the Noise Transmission through Automotive Door Seals”. PhD thesis. Universität Stuttgart, 2016.

[48] B. Henderson. “Category 6 - Sound generation in viscous problems, problem 2 - Sound generation by flow over a cavity”. In: *4th Computational Aeroacoustics Workshop*. Ohio Aerospace Institute. 2004.

[49] M. S. Howe. “Surface pressures and sound produced by turbulent flow over smooth and rough walls”. In: *Journal of the Acoustical Society of America* 95 (1991), pp. 1041–1047.

[50] N. Hu and L. Erbig. “Effect of Sensor Mounting and Flow History on Measured Wall Pressure Spectra”. In: *AIAA Journal* (2020), pp. 1–11.

[51] N. Hu and M. Herr. “Characteristics of Wall Pressure Fluctuations for a Flat Plate Turbulent Boundary Layer with Pressure Gradients”. In: *22nd AIAA/CEAS Aeroacoustics Conference*. AIAA 2016-2749. 2016.

[52] N. Hu. “Empirical Model of Wall Pressure Spectra in Adverse Pressure Gradients”. In: *AIAA Journal* 56.9 (2018), pp. 3491–3506.

[53] N. Hu, N. Reiche, and R. Ewert. “Simulation of turbulent boundary layer wall pressure fluctuations via Poisson equation and synthetic turbulence”. In: *Journal of Fluid Mechanics* 826 (2017), pp. 421–454.

[54] A. Hüppe. “Spektrale finite Elemente für akustische Feldberechnung”. PhD thesis. Technische Universität Wien, 2012.

[55] H. Illy, D. Ricot, and A. Menoret. “Etude expérimentale du mécanisme d’excitation aéroacoustique des césures automobiles”. In: *Acoustiques & Techniques* 50 (2007), pp. 14–20.

[56] N. Jarrin et al. “Reconstruction of turbulent fluctuations for hybrid RANS/LES simulations using a synthetic-eddy Method”. In: *International Journal of Heat and Fluid Flow* 30 (2009), pp. 435–442.

[57] J. Jiao. *Aeroacoustic Wind Tunnel Correction Based on Numerical Simulation*. Tech. rep. Technische Universität Braunschweig, 2017.

[58] J. W. Kim, A. S. H. Lau, and N. D. Sandham. “Proposed Boundary Conditions for Gust-Airfoil Interaction Noise”. In: *AIAA Journal* 48.11 (2010), pp. 2705–2710.

[59] M. Klein, A. Sadiki, and J. Janicka. “A Digital Filter based Generation of In ow Data for Spatially Developing Direct Numerical or Large Eddy Simulations”. In: *Journal of Computational Physics* 186 (2003), pp. 652–665.

[60] T. Knopp. “Model-consistent universal wall-functions for RANS turbulence modelling”. In: *BAIL 2006 International Conference on Boundary and Interior Layers*. 2006.

[61] R. Kraichnan. “Diffusion by a random velocity field”. In: *Physics of Fluids* 13.1 (1970), pp. 22–31.

[62] J. Kreuzinger and S. Schimmelpfennig. “Analyse und Simulation turbulent überströmter Helmholtz-Resonatoren”. In: *Fortschritte der Akustik - DAGA 2016*. DAGA, 2016.

[63] S. Lardeau and R. Manceau. “Computations of canonical and complex flow configurations using a robust formulation of the elliptic-blending Reynolds-Stress model”. In: *10th International ERCOFTAC Symposium on Engineering Turbulence Modelling and Measurements*. Marbella, Spain, 2014.

[64] J. H. Lienhard. *Synopsis of Lift, Drag, and Vortex Frequency Data for Rigid Circular Cylinders*. Bulletin 300. Technical Extension Service, Washington State University, 1966.

[65] M. J. Lighthill. “On sound generated aerodynamically I. General theory”. In: *Proceedings of the Royal Society A* 211.1107 (1952), pp. 564–587.

[66] M. J. Lighthill. “On sound generated aerodynamically II. Turbulence as a source of sound”. In: *Proceedings of the Royal Society A* 222.1148 (1954), pp. 1–32.

[67] D. K. Lilly. “A proposed modification of the Germano subgrid-scale closure method”. In: *Physics of Fluids A* 4.3 (1992), pp. 633–635.

[68] T. Lund, X. Wu, and K. Squires. “Generation of Turbulent In Flow Data for Spatially-Developing Boundary Layer Simulations”. In: *Journal of Computational Physics* 140 (1998), pp. 233–258.

[69] G. Maidanik and D. W. Jorgensen. “Boundary wave-vector filters for the study of the pressure field in a turbulent boundary layer”. In: *Journal of the Acoustical Society of America* 42 (1967), pp. 494–501.

[70] M. Manhart and R. Friedrich. “Towards DNS of Separated Turbulent Boundary Layers”. In: *Direct and Large-Eddy Simulation III*. 1999, pp. 429–440.

[71] J. Mercier. “Etude du bruit de cavités. Application aux césures de portières automobiles”. Master’s thesis. Arts et Métiers ParisTech, 2007.

[72] A. Michalke. “On spatially growing disturbances in an inviscid shear layer”. In: *Journal of Fluid Mechanics* 23.3 (1965), pp. 521–544.

[73] C. Mockett et al. “Industrial prediction of jet-flap interaction noise with advanced hybrid RANS-LES methods”. In: *Notes on Numerical Fluid Mechanics and Multidisciplinary Design*. 2018.

[74] M. Müller. “Aeroakustik überströmter Hohlräume am Fahrzeugheck”. Master’s thesis. Universität Stuttgart, 2008.

[75] C. D. Munz, M. Dumbser, and S. Roller. “Linearized acoustic perturbation equations for low Mach number flow with variable density and temperature”. In: *Journal of Computational Physics* 224 (2007), pp. 352–364.

[76] F. Nicoud and F. Ducros. “Subgrid-Scale Stress Modelling Based on the Square of the Velocity Gradient Tensor”. In: *Flow, Turbulence and Combustion* 62 (1999), pp. 183–200.

[77] M. Pachebat et al. “Problématique et applications dans le domaine des transports terrestres”. In: *Journée » Champs de pression pariétale induits par les écoulements turbulents «*. GDR Bruit des Transports. 2008.

[78] U. Piomelli and J. R. Chasnov. *Large-Eddy Simulations: Theory and Applications*. Vol. 2. ERCOFTAC Series. Springer Dordrecht, 1996.

[79] H. E. Plumbee, J. S. Gibson, and L. W. Lassiter. *Theoretical and experimental investigation of the acoustic response of cavities in an aerodynamic flow*. Technical Report WADD-TR-61-75. U.S. Air Force, 1962.

[80] S. B. Pope. *Turbulent Flows*. 1st ed. Cambridge University Press, 2000.

[81] M. Pott-Pollenske and J. Delfs. “Enhanced Capabilities of the Aeroacoustic Wind Tunnel Braunschweig”. In: *14th AIAA/CEAS Aeroacoustics Conference*. AIAA 2008-2910. 2008.

[82] H. Reichardt. “Vollständige Darstellung der turbulenten Geschwindigkeitsverteilung in glatten Leitungen”. In: *Z. Angew. Math. Mech* 31.7 (1951), pp. 208–219.

[83] P. Renz. “Steady EB-RSM Simulations in the Context of Aeroacoustic Gap Noise Simulations on Vehicles”. Master’s thesis. University of Stuttgart, 2018.

[84] O. Reynolds. *Papers on mechanical and physical subjects. The sub-mechanics of the universe*. First Edition. Cambridge University Press, 1903.

[85] A. Riedelsheimer. “Entwicklung einer Berechnungsmethode zur Vorhersage des Schiebedachwummerns an einem Serienfahrzeug”. Master’s thesis. University of Stuttgart, 2018.

[86] D. Rockwell and E. Naudascher. “Review—Self-Sustaining Oscillations of Flow Past Cavities”. In: *ASME J. Fluids Eng* 2.100 (1978), pp. 152–165.

[87] J. E. Rossiter. *Wind-tunnel experiments on the flow over rectangular cavities at subsonic and transonic speeds*. Reports and Memoranda 3438. Aeronautical Research Council, 1964.

[88] V. Sarohia. “Experimental Investigation of Oscillations in Flows Over Shallow Cavities”. In: *AIAA Journal* 15.7 (1977), pp. 984–991.

[89] A. Schell. “Entwicklung einer Berechnungsmethode zur Vorhersage der Schallausbreitung im Nahfeld eines umströmten Kraftfahrzeugs”. PhD thesis. Universität Stuttgart, 2014.

[90] S. Schimmelpfennig. “Aeroakustik von Karosseriespalten”. PhD thesis. Friedrich-Alexander-Universität Erlangen-Nürnberg, 2015.

[91] S. Schimmelpfennig and R. Lerch. “Helmholtz Resonators Acting as Sound Source in Automotive Aeroacoustics”. In: *Proceedings of the International Conference on Acoustics*. AIA-DAGA, 2013.

[92] P. Schlatter et al. “Turbulent boundary layers up to $\mathrm{Re}_\theta = 2500$ studied through simulation and experiment”. In: *Phys. Fluids* 21 (2009), p. 051702.

[93] H. Schlichting and K. Gersten. *Boundary-Layer Theory*. 9th ed. Springer-Verlag Berlin Heidelberg, 2017.

[94] J. U. Schlüter, H. Pitsch, and P. Moin. “Outflow conditions for integrated large eddy simulation/Reynolds-averaged Navier–Stokes simulations”. In: *AIAA Journal* 43.1 (2005), pp. 156–164.

[95] S. Schoder and M. Kaltenbacher. “Hybrid Aeroacoustic Computations: State of Art and New Achievements”. In: *Journal of Theoretical and Computational Acoustics* 27.04 (2019), p. 1950020.

[96] C. Schram and N. Van De Wyer. “An optimized microphone array for the measurement of turbulent boundary layer wall pressure wavenumber-frequency spectra”. In: *2018 AIAA/CEAS Aeroacoustics Conference*. AIAA 2018-2968. 2018.

[97] *Simcenter STAR-CCM+ v13.06 User Manual*. Siemens PLM Software, 2018.

[98] J. Smagorinsky. “General circulation experiments with the primitive equations: I. The basic experiment”. In: *Monthly Weather Review* 91.3 (1963), pp. 99–164.

[99] A. Smirnov, S. Shi, and I. Celik. “Random Flow Generation Technique for Large Eddy Simulations and Particle-Dynamics Modeling”. In: *Journal of Fluids Engineering* 123.2 (2001), pp. 359–371.

[100] P. R. Spalart and S. R. Allmaras. “A Hybrid Computational Aeroacoustic Method For Low Speed Flows”. In: *30th Aerospace Sciences Meeting & Exhibit*. AIAA-92-0439. 1992.

[101] P. R. Spalart. “Direct simulation of a turbulent boundary layer up to $\mathrm{R}_\theta = 1410$”. In: *J. Fluid Mech.* 187 (1988), pp. 61–98.

[102] C. Speziale, S. Sarkar, and T. Gatski. “Modelling the pressure-strain correlation of turbulence: An invariant dynamical systems approach”. In: *Journal of Fluid Mechanics* 227 (1991), pp. 245–272.

[103] A. Tosh, M. Caraeni, and D. Caraeni. “A Hybrid Computational Aeroacoustic Method For Low Speed Flows”. In: *2018 AIAA/CEAS Aeroacoustics Conference*. AIAA 2018-4096. 2018.

[104] B. Van Leer. “Towards the ultimate conservative difference scheme. V - A second-order sequel to Godunov’s method”. In: *Journal of Computational Physics* 32 (1979), pp. 101–136.

[105] V. Vatsa, M. Carpenter, and D. Lockard. “Re-evaluation of an Optimized Second Order Backward Difference (BDF2OPT) Scheme for Unsteady Flow Applications”. In: *48th AIAA Aerospace Sciences Meeting Including the New Horizons Forum and Aerospace Exposition*. AIAA 2010-122. 2010.

[106] P. D. Welch. “The use of Fast Fourier Transform for the estimation of power spectra: A method based on time averaging over short, modified periodograms”. In: *IEEE Transactions on Audio and Electroacoustics*. Vol. AU-15. 2. 2014, pp. 70–73.

[107] G. Wickern and M. Brennberger. “Helmholtz Resonators Acting as Sound Source in Automotive Aeroacoustics”. In: *SAE Technical Paper*. 2009-01-0183. SAE International, 2009.

[108] D. C. Wilcox. *Turbulence modeling for CFD*. 2. ed., 2. print. La Canada Calif.: DCW Industries, 2000.

[109] W. Willmarth and C. Wooldridge. “Measurements of the fluctuating pressure at the wall beneath a thick turbulent boundary layer”. In: *J. Fluid Mech.* 14 (1952), pp. 187–210.

[110] X. Wu and P. Moin. “Direct numerical simulation of turbulence in a nominally zero-pressure-gradient flat-plate boundary layer”. In: *J. Fluid Mech.* 630 (2009), pp. 5–41.